University of Nevada, Reno

Numerical Investigation of Tsunami-Borne Debris Interaction with Coastal Bridges

A dissertation submitted in partial fulfillment of the
requirements for the degree of Doctor of Philosophy in
Civil and Environmental Engineering

by

Seddigheh Hasanpour Estahbanati

Dr. Denis Istrati (Dissertation Advisor)

Dr. Ian G. Buckle (Dissertation Co-Advisor)

May, 2023

THE GRADUATE SCHOOL

We recommend that the dissertation
prepared under our supervision by

Seddigheh Hasanpour

entitled

Numerical Investigation of Tsunami-Borne Debris Interaction with Coastal Bridges

be accepted in partial fulfillment of the
requirements for the degree of

DOCTOR OF PHILOSOPHY

Denis Istrati
Advisor

Ian G. Buckle
Co-advisor

Ahmad M. Itani
Committee Member

David McCallen
Committee Member

Christos Papachristos
Graduate School Representative

Markus Kemmelmeier, Ph.D., Dean
Graduate School

May, 2023

Abstract

The destructive potential of tsunamis has been well-documented in past events such as the 2004 Indian Ocean and 2011 Great East Japan tsunamis, which resulted in extensive damage to coastal regions including the destruction or damage of numerous bridges. These transportation links are particularly vulnerable to damage from tsunami-driven debris, such as boats, vehicles, and shipping containers, which upon impact can remove a bridge superstructure from its supports. The significance of understanding the effect of floating debris on coastal bridges cannot be overemphasized, as transportation infrastructure plays a vital role in post-disaster response and recovery efforts. Despite the availability of data from several debris-related studies, the majority of them have been focused on buildings, and very limited information is available for bridges. Furthermore, the majority of studies have been experimental, as the numerical investigation of complex multi-physics phenomena involving fluid flow with turbulent wave breaking, and non-linear contact between the debris, the trapped fluid, and the bridge, is quite challenging. Accurate quantification of the forces involved in debris-flow-bridge interaction is important for the design of tsunami-resilient bridges.

The main objectives of this study were to (a) understand the two-fold effect of debris impact and damming on bridges, (b) shed light on the debris dynamics and debris-fluid-bridge interaction and associated loads, (d) quantify the effect of the debris orientation, (d) explore, calibrate and assess the accuracy and limitations of particle-based (SPH) and/or coupled particle-mesh based (SPH-FEM) methods, (e) investigate the role of debris mass, and (e) provide recommendations regarding simplified prescriptive load equations for debris impact for inclusion in the Tsunami Design Guidelines for Coastal Bridges developed by PEER and recently adopted by the AASHTO Committee on Bridges and Structures.

In the present study, a thorough examination of the effect of various factors on debris movement, velocity, and impact force on bridge superstructure was conducted. By utilizing the coupled SPH-FEM numerical technique, it is demonstrated that the trajectory of debris can vary depending on the tsunami flow characteristics, the debris initial orientation, debris mass, and the bridge elevation. Through observation and analysis, three distinct patterns of debris movement around bridge decks are identified and designated as Patterns A, B, and C. Pattern A, the most frequently observed pattern, involves debris impacting the offshore side of the bridge superstructure, followed by movement below the soffit and eventual resurfacing on the onshore side. Additionally, when debris passes below the deck, it may impact the soffit, leading to uplift loads that can surpass the maximum horizontal loads. Pattern B involves debris movement above the deck with or without impact on the top surface. Pattern C -the least frequently observed pattern- involves a debris impacting the offshore side of the superstructure and becoming trapped below the offshore overhang, resulting in repetitive impulsive loads and long-duration damming loads until the end of the inundation.

The study also reveals that the debris exhibits both horizontal and vertical velocities at the instant of primary impact, resulting in applied forces on the bridge in both directions simultaneously. Additionally, the research demonstrates the complexity of the debris dynamics and debris-flow-bridge interaction, with some cases resulting in secondary impacts of greater magnitude than the primary impact. The study further demonstrates that the debris initial orientation has a significant effect, with longitudinal debris reaching higher velocities and resulting in larger impact forces than the transverse one. In addition, it is also shown that the debris mass plays a crucial role in determining its movement, velocity, and impact forces.

The results of this study indicate that the presence of the debris significantly impacts the flow velocities and pressures on bridges relatively to clear-water tsunami conditions. Specifically, it is found that the presence of debris leads to a consistent increase in total horizontal forces. Through

the use of SPH-FEM analyses, the ratio of total forces with transverse debris to total forces without debris (Rx) is found to range between 1.5 and 6.5, with an average value of 2.67. Additionally, the ratio in the vertical direction (Rz) is found to range between 0.9 and 4.7, with an average value of 1.85. Furthermore, it is found that the presence of longitudinal debris leads to an average of 3.64 and 2.13 times larger horizontal and vertical forces respectively, in comparison to cases without debris. These findings highlight the importance of considering the debris in tsunami risk assessment frameworks and the design of bridge structures in tsunami-prone areas.

In summary, the findings of this research are expected to have significant implications for the design and construction of bridges in areas prone to tsunamis and in this regard, a preliminary set of prescriptive equations for the debris impact forces is proposed.

DEDICATION

I dedicate this dissertation to my lovely husband, Reza, who has made countless sacrifices and provided steadfast support throughout my academic endeavors. His love, encouragement, and trust in my abilities have been invaluable. I am also deeply grateful to my beloved parents, brother, and sister for their unconditional love and support. Their belief in my capabilities and dedication to my success has been a constant source of inspiration. Without their help, this accomplishment would not have been possible. I express my sincere gratitude and appreciation to them.

ACKNOWLEDGMENTS

The work described in this dissertation was supported by the State of California through the Transportation System Research Program of the Pacific Earthquake Engineering Research Center (PEER). Any opinions findings and conclusions or recommendations expressed in this material are those of the author(s) and do not necessarily reflect those of the funding agency.

I would like to extend my gratitude to my dissertation committee, Dr. Ahmad Itani, Dr. David McCallen, and Dr. Christos Papachristos for their invaluable input and guidance throughout this research. Their thoughtful suggestions and evaluations have significantly contributed to the success of this dissertation.

I am also grateful to Zachary Newell, a research computing engineer at the Nevada System of Higher Education (NSHE), for his support in granting me access to High-Performance Computing (HPC) systems. I appreciate his dedication and efforts in making this research a success.

Lastly, I would like to express my sincerest appreciation to my advisors, Dr. Denis Istrati and Dr. Ian Buckle, for their exceptional guidance, support, and mentorship throughout the duration of my graduate studies. Their expertise and unwavering dedication to my research have been invaluable, and I am deeply grateful for the insights, advice, and encouragement they have provided. Their support and guidance were integral to the successful completion of this dissertation, and I am honored to have had the opportunity to work with such esteemed professionals. I am truly grateful for their invaluable contributions and guidance.

Table of Contents

1. Introduction 2
1.1. Literature review and motivation 2
1.2. Research statement and objectives 8
1.3. Numerical method 9
1.3.1. Background 9
1.3.2. Coupled SPH-FEM modeling technique 12
1.3.3. SPH governing equations 13
1.3.4. SPH for viscous fluid 16
1.3.5. Equation of state (EOS) 18
1.3.6. Contact 19
1.4. Organization of the dissertation 20
1.5. References 23
2. Coupled SPH-FEM Modeling Tsunami-Borne Large Debris Flow and Impact on Coastal Structures 29
2.1. Introduction 30
2.2. Numerical method 35
2.2.1. SPH governing equations 35
2.2.2. SPH for viscous fluid 38
2.2.3. Sorting 40
2.2.4. Equation of state (EOS) 40
2.2.5. Time integration 41
2.2.6. Contact definitions 41
2.3. Experimental work 42
2.4. Coupled SPH-FEM modeling 44
2.4.1. Numerical settings 44
2.4.2. Accuracy of numerical modeling 47
2.5. Role of debris restraints 55
2.6. Effect of hydrodynamic conditions on debris movement and impact forces 59
2.6.1. Tsunami flow characteristics 59
2.6.2. Initial water depth 65
2.7. Summary and conclusions 71
2.8. Acknowledgements 75

2.9. Appendix 75
2.10. References 76
3. Multi-Physics Modeling of Tsunami Debris Impact on Bridge Decks 83
3.1. Introduction 84
3.2. Methodology 86
3.2.1. Description of numerical model 86
3.2.2. Validation for container impact on coastal structure 90
3.2.3. Numerical modeling of debris impact on a box-girder bridge 94
3.3. Results and discussion 95
3.3.1. Tsunami-debris-deck interaction and flow patterns around deck 95
3.3.2. Debris impact loads on bridge deck 103
3.4. Conclusions 105
3.5. Acknowledgements 107
3.6. References 107
4. Three-Dimensional Investigation of Floating Debris Effects on Bridge Superstructures During Tsunamis 112
4.1. Introduction 113
4.2. Methodology 118
4.2.1. Description of numerical method 118
4.2.2. Validation with experiments of container impact on coastal structure 122
4.2.3. Three-dimensional numerical model of single debris impact on a box-girder bridge . 126
4.3. Tsunami flow characteristics 128
4.4. Debris movement and debris-fluid-bridge intercation 130
4.4.1. General trends 130
4.4.2. Debris displacements and rotations 134
4.4.3. Debris velocities 137
4.5. Impact force on bridge superstructure 145
4.6. Role of debris 152
4.7. Conclusions and recommendations 156
4.8. Acknowledgments 159
4.9. References 160
5. Effect of Debris Orientation on the Debris-Tsunami-Bridge Interaction and Induced Forces 166
5.1. Introduction 167

5.2. Methodology 171
5.3. Tsunami flow characteristics 174
5.4. Debris movement and debris-flow-bridge interaction 175
5.5. Impact force on bridge superstructure 183
5.6. Role of debris orientation 187
5.7. Role of debris 195
5.8. Conclusions 197
5.9. Acknowledgement 199
5.10. References 199
6. SPH-FEM Investigation of Floating Container Impact on Bridge Superstructures: Role of Debris Mass 204
6.1. Introduction 204
6.2. Methodology 209
6.2.1. Numerical models of debris impact with varying masses on a box-girder bridge 209
6.3. Debris-bore-bridge interaction 210
6.3.1. General trends 210
6.3.2. Debris displacements and rotations 212
6.3.3. Debris velocities 215
6.4. Impact forces on bridge superstructures 217
6.5. Summary and conclusions 222
6.6. Acknowledgment 224
6.7. References 224
7. Prescriptive Design Equations 228
7.1. Background 228
7.2. Prescriptive equations for debris impact loads on buildings 228
7.3. Comparison of results from simplified equations for buildings with numerical simulations of bridges 229
7.3.1. Results 229
7.3.2. Discussion 230
7.4. Recommendations for bridges 235
7.5. References 236
8. Summary, Conclusions, and Future Work 238
8.1. Summary 238
8.2. Conclusions 239

8.3. Recommendations for future work 241

List of Tables

Table 4-1 Hydrodynamic conditions.....128
Table 4-2 Debris-deck interaction for the investigated bore cases 133
Table 4-3 Ratio of the total forces with and without debris in the two directions 156
Table 5-1 Hydrodynamic conditions and maximum magnitude of bore height, free-surface and fluid velocity at Z=0.25m and at free-surface 175
Table 5-2 Debris-tsunami-bridge interaction for transverse debris [40] and longitudinal debris 188
Table 5-3 Ratio of the debris forces: longitudinal and transverse orientations in the two directions 193
Table 5-4 Ratio of the total forces: longitudinal and transverse orientations in the two directions 194
Table 6-1 Debris-tsunami-bridge interaction.....211
Table 7-1 Average values of the debris horizontal impact force calculated by numerical simulations and estimated by the simplified equations 235

List of Figures

Figure 2-1 Cross-section of the Large Wave Flume (LWF) depicting the bathymetry, column location and flume instrumentation of the experiments of Ko and Cox [65] used for the validation study 44
Figure 2-2 Numerical models with large debris: side-views of the debris, the column and the wave maker 45
Figure 2-3 Variation of the free surface and fluid velocity at different locations along the flume. Experimental [65] and numerical results for h1 = 2.496 m and Terf = 30 s 48
Figure 2-4 Maximum free-surface values of experiments [65] and numerical simulations for h1 = 2.496 m, and three wave cases with Terf = 30, 40 and 45 s 49
Figure 2-5 Maximum fluid velocities of experimental tests [65] and numerical simulations for h1 = 2.496 m, and three wave cases with Terf = 30, 40, and 45 s 50
Figure 2-6 Debris velocity histories: Estimated based on the experimental tests of [65] and results from the numerical simulations for h1 = 2.496 m, Terf = 30 s 52
Figure 2-7 Comparison of the debris impact forces: experimental tests [65] and numerical simulations for h1 = 2.496 m, and two wave cases with Terf = 30 s and 45 s 54
Figure 2-8 Maximum values of debris impact force on column: experimental tests [65] and numerical simulation for h1 = 2.496 m, and three wave cases with Terf = 30, 40, and 45 s 55
Figure 2-9 Selected instants of the debris−wave interaction and impact on the column of the free debris. Numerical results for the hydrodynamic case with h1 = 2.496 m, h2 = 0.13 m and Terf = 30 s 56
Figure 2-10 Debris trajectory (left) and rotation (right) for the restrained debris and free debris. Numerical results for the hydro-dynamic case with h1 = 2.496 m, and h2 = 0.13 m and Terf = 30 s 58
Figure 2-11 Debris velocity (left) and forces on the column (right). Experimental and numerical results (of restrained and free de-bris) for the hydrodynamic case h1 = 2.496 m and Terf = 30 s 59
Figure 2-12 Variation of free surface (left) and fluid velocity (right)at x = 62 m: Numerical results for h1 = 2.496 m and three wave cases with Terf = 30, 40, and 45 s 60
Figure 2-13 Snapshots of debris−-tsunami interaction and impact on the column. Numerical results for h1 = 2.496 m and two wave cases with Terf = 30 s (top) and 45 s (bottom) 61
Figure 2-14 Numerical results of the free debris: vertical displacement (left) and rotation (right), for h1 = 2.496 m and three wave cases with Terf = 30, 40, and 45 s 61
Figure 2-15 Free debris histories (left) and maximum values of debris impact on the column vs. the impact velocity (right). Numerical results for h1 = 2.496 m h2 = 0.13 m, and Terf = 30, 40, and 45 s 64
Figure 2-16 Time histories of the free surface, fluid velocity, motion of the debris (y displacement and rotation), debris velocity and debris impact force on the column. Numerical results of free debris for Terf = 40 s and three water depths with h1 = 2.496, 2.664 68
Figure 2-17 Snapshots of debris-tsunami interaction and impact on the column. Numerical results of free debris for Terf = 40 s and three water depths with h1 = 2.496 (top), 2.664 (center) and 2.8 m (bottom) 69
Figure 2-18 Maximum values of the debris impact force as a function of the impact velocity for three water depths and nine tsunami bores 71

Figure 3-1 Cross section of the LWF depicting the bathymetry, column location and flume instrumentation of the experiments of Ko & Cox (2012) [25] 91
Figure 3-2 Variation of the free surface (top) and fluid velocity (bottom) at different locations along the flume: Experimental [25] and numerical results for h1 = 2.664m m and Terf = 25s 93
Figure 3-3 Variation of debris impact forces on coastal pier: Experimental [25] and numerical results for h1 = 2.664m and Terf = 25 s 94
Figure 3-4 Cross section of the computational domain (top), numerical models with debris and bridge (bottom) including the side-views of the wave maker, the debris and the bridge deck 95
Figure 3-5 Free-surface (left) and fluid velocity histories (right) of tsunami flow in front of the debris for h1=2.664m and Terf = 20 s 96
Figure 3-6 Tsunami-debris-deck interaction for a container in longitudinal direction and two bridge elevations, 0.60m (left) and 0.50m (right) 98
Figure 3-7 Tsunami-debris-deck interaction for a container in transverse direction and deck elevation 0.50m 99
Figure 3-8 Debris horizontal and vertical displacement histories for three cases, including longitudinal and transverse container impact 102
Figure 3-9 Debris rotations for three cases, including longitudinal and transverse container impact 102
Figure 3-10 Debris velocities in the horizontal (left) and vertical (right) direction for three cases, including longitudinal and transverse container impact 102
Figure 3-11 Applied horizontal and vertical force histories for three cases: Long_zb=0.6m (top), Long_zb= 0.5m (center) and Transv_zb =0.5m (bottom) 104
Figure 4-1 Cross section of the computational domain (top), numerical models with the gate, the debris, and the column 123
Figure 4-2 Variation of the free surface and fluid velocity at different locations along the flume. Experimental [68] and numerical results for the strong bore (B3) 125
Figure 4-3 Comparison of the disk debris velocity and impact force: experimental test [68]and numerical simulation for the strong bore (B3) 125
Figure 4-4 Cross section of the computational domain (top), numerical models with the debris and the bridge 127
Figure 4-5 Free-surface (left) and fluid particle velocity histories (right) of tsunami flow in front of the debris location for strong bores and Z=0.25 m 129
Figure 4-6 Maximum free-surface values (left) and fluid velocities (right) of tsunami flow in front of the debris location for all the investigated bores and three elevations with Z=0.15, 0.20 and 0.25 m 129
Figure 4-7 Tsunami-debris-bridge interaction for case B4Zb; strong bore and bridge elevation of 0.30 m 130
Figure 4-8 Debris-tsunami and debris-tsunami-bridge interaction for three scenarios: B2Zb (left, weak bore and bridge elevation of 0.30 m), B3Zb (center, strong bore and bridge elevation of 0.30 m), and B5Za (right, strong bore and bridge elevation of 0.20 m) 132
Figure 4-9 Debris vertical displacement histories (top) and trajectories (bottom) for two bridge elevations (0.20 m (Za) and 0.30 m (Zb)) and different bore strengths 135
Figure 4-10 Debris maximum vertical displacement for all the investigated cases 136

Figure 4-11 Debris rotation histories for two bridge elevations (0.20 m (Za) and 0.30 m (Zb)) and different bore strengths..... 137
Figure 4-12 Debris offshore and onshore corners velocities in the horizontal (top) and vertical (bottom) directions for three strong bore cases and different bridge elevation, including B3Za (bridge elevation of 0.20 m), B4Zb (bridge elevation of 0.30 m), and B5Zc (bridge elevation of 0.35 m) 139
Figure 4-13 Debris velocities in the horizontal (left) and vertical (right) directions for two selected cases with similar bridge elevation (0.20 m) and different bore strengths, including B1Za (weak bore), and B3Za (strong bore) generate 141
Figure 4-14 Debris velocities in the horizontal (top) and vertical (bottom) directions for four selected strong bores with similar bridge elevation (0.30 m) and different initial water levels, including B3Zb (d=0.10 m), B4Zb (d=0.15 m), B5Zb (d=0.20 m), and B6Zb (d=0.25 m) 141
Figure 4-15 Debris velocities in the horizontal (left) and vertical (right) directions for three selected cases with similar bore properties and different bridge elevations, including B4Za (bridge elevation of 0.20 m), B4Zb (bridge elevation of 0.30 m), and B4Zc (bridge elevation of 0.35 m) 142
Figure 4-16 Maximum values of the debris velocities in the horizontal (top) and vertical (bottom) directions at the instant of primary impact and throughout propagation..... 144
Figure 4-17 Ratio of the primary impact velocities for all investigated cases 145
Figure 4-18 Applied horizontal and vertical force histories for four cases with similar bridge elevation of 0.30m and bore strength and different initial water depths, including B3Zb (d=0.10 m), B4Zb (d=0.15 m), B5Zb (d=0.20 m), and B6Zb (d=0.25 m) 147
Figure 4-19 Time histories of the debris horizontal and vertical forces, total horizontal and vertical forces, and the maximum values of the debris and total horizontal and vertical forces for four cases with similar bridge elevation of 0.30 m and bore strength and different initial water depth, including B3Zb (d=0.10 m), B4Zb (d=0.15 m), B5Zb (d=0.20 m), and B6Zb (d=0.25 m)..... 149
Figure 4-20 Applied horizontal and vertical force histories for three cases with similar bore properties and different bridge elevations, including B4Za (bridge elevation of 0.20 m), B4Zb (bridge elevation of 0.30 m), and B4Zc (bridge elevation of 0.35 m) 150
Figure 4-21 Maximum values of the debris, fluid, and total horizontal and vertical forces for three cases with similar bore properties and different bridge elevations, including B4Za (bridge elevation of 0.20 m), B4Zb (bridge elevation of 0.30 m), and B4Zc (bridge elevation of 0.35 m) 151
Figure 4-22 Maximum values of the hydrodynamic forces in the horizontal and vertical directions on the bridge superstructure for the investigated cases and two scenarios; with and without debris 153
Figure 4-23 Maximum values of the total impact forces in the horizontal and vertical directions on the bridge superstructure for the investigated cases and two scenarios; with and without debris 155
Figure 5-1 Cross section of the computational domain (top), three-dimensional and top views of numerical models with the debris and the bridge (bottom) 173
Figure 5-2 Bore height (left) and fluid particle velocity histories (right) of tsunami flow in front of the debris location for the strong bores and Z=0.25 m..... 175

Figure 5-3 Top view of tsunami-debris-bridge interaction for case B6Zb; strong bore and bridge elevation of 0.30m 176
Figure 5-4 Debris-tsunami and debris-tsunami-bridge interaction for three scenarios: (a): top, debris becomes trapped below the offshore overhang, (b): center, debris moves above the deck, (c): bottom, debris moves below the bridge 177
Figure 5-5 Debris vertical displacement histories (left) and trajectories (right) for selected cases 178
Figure 5-6 Debris pitch rotation and yaw rotation time-histories for selected cases 179
Figure 5-7 Debris offshore and onshore corners velocities in the horizontal (top) and vertical (bottom) directions for the same bridge elevation and bore strength but initial water level, including B3Zc (d=0.10 m), B4Zc (0.15 m) 180
Figure 5-8 Debris velocities in the horizontal (top) and vertical (bottom) directions for four selected strong bores with the same bridge elevation (0.30 m) but different initial water level, including B3Zb (d=0.10 m), B4Zb (d=0.15 m), B5Zb (d=0.20 m), and B6Zb (d=0.25 m) 182
Figure 5-9 Debris velocities in the horizontal (left) and vertical (right) directions for selected cases with the same bore properties but different bridge elevation, including B2Za (bridge elevation of 0.20 m) and B2Zb (bridge elevation of 0.30 m) 183
Figure 5-10 Applied horizontal and vertical debris and fluid force histories for four cases with similar bridge elevation of 0.30 m and bore strength and different initial water depths, including B3Zb (d=0.10 m), B4Zb (d=0.15 m), B5Zb (d=0.20 m), and B6Zb (d=0.25 m) 185
Figure 5-11 Maximum values of the debris and total horizontal and vertical forces for four cases with the same bridge elevation of 0.30m and bore strength, but different initial water depths, including B3Zb (d=0.10 m), B4Zb (d=0.15 m), B5Zb (d=0.20 m), and B6Zb (d=0.25 m) 186
Figure 5-12 Applied horizontal and vertical debris, fluid, and total force histories for cases with the same bore properties but different bridge elevations, including B2Za (bridge elevation of 0.20 m) and B2Zb (bridge elevation of 0.30 m) 187
Figure 5-13 Debris maximum vertical displacement for two debris orientations; transverse and longitudinal 190
Figure 5-14 Time histories of the horizontal (top left) and vertical (top right) debris velocities, horizontal (bottom left) and vertical (bottom right) debris forces for case B1Za and two different debris orientations 191
Figure 5-15 Maximum values of the debris impact forces and velocities in the horizontal and vertical directions on the bridge superstructure for the investigated cases and two debris orientations 192
Figure 5-16 Maximum values of the total forces in the horizontal and vertical directions on the bridge superstructure for the investigated cases and two debris orientations 194
Figure 5-17 Maximum values of the hydrodynamic and total forces in the horizontal and vertical directions on the bridge superstructure for the investigated cases and two scenarios; with and without debris 196
Figure 5-18 Ratio of the maximum total force with and without debris in the two directions 196
Figure 6-1 Debris-flow-bridge interaction for transverse debris and case B6: (a) 9.2% mass, (b) 75% mass 210
Figure 6-2 Debris vertical displacement histories (top) and trajectories (bottom) for case B5 for two orientations with variable masses 213
Figure 6-3 Debris maximum vertical displacement for two orientations with variable masses .. 214

Figure 6-4 Time histories of debris pitch rotation for case B5 and two orientations with variable masses 215
Figure 6-5 Debris velocities in the horizontal (top) and vertical (bottom) directions for case B4 for two debris orientations and variable masses 216
Figure 6-6 Maximum values of debris velocities in the horizontal (left) and vertical (right) directions for all studied cases including two different orientations and variable masses .. 217
Figure 6-7 Time histories of debris impact forces in the horizontal (top) and vertical (bottom) directions for case B6 for two debris orientations and variable masses 219
Figure 6-8 Maximum values of debris impact forces in the horizontal (left) and vertical (right) directions for all studied case including two different orientations and variable masses 219
Figure 6-9 Time histories of total impact forces in the horizontal (top) and vertical (bottom) directions for case B6 for two debris orientations and variable masses 221
Figure 6-10 Maximum values of total.3 impact forces in the horizontal (left) and vertical (right) directions for all studied case including two different orientations and variable masses 222
Figure 7-1 Comparison of longitudinal debris impact force for 50% mass and bridge elevation of 0.20m (Z_a) 231
Figure 7-2 Comparison of longitudinal debris impact force for 50% mass and bridge elevation of 0.30 m (Z_b) 232
Figure 7-3 Comparison of longitudinal debris impact force for 50% mass and bridge elevation of 0.35 m (Z_c) 232
Figure 7-4 Comparison of longitudinal debris impact force for 9.2% mass and bridge elevation of 0.30 m (Z_b) 232
Figure 7-5 Comparison of longitudinal debris impact force for 75% mass and bridge elevation of 0.30 m (Z_b) 233
Figure 7-6 Comparison of transverse debris impact force for 50% mass and bridge elevation of 0.20 m (Z_a) 233
Figure 7-7 Comparison of transverse debris impact force for 50% mass and bridge elevation of 0.30 m (Z_b) 233
Figure 7-8 Comparison of transverse debris impact force for 50% mass and bridge elevation of 0.35 m (Z_c) 234
Figure 7-9 Comparison of transverse debris impact force for 9.2% mass and bridge elevation of 0.30 m (Z_b) 234
Figure 7-10 Comparison of transverse debris impact force for 75% mass and bridge elevation of 0.30 m (Z_b) 234

Chapter 1

1. Introduction

1.1. Literature review and motivation

After the recent major tsunamis generated by earthquakes including the Indian Ocean Tsunami in 2004 and the Great East Japan Tsunami in 2011, which caused tremendous structural damages and significant destruction of coastline infrastructure and enormous financial losses [1], tsunamis have gained a great deal of attention. Due to the enormous amount of energy, tsunami waves can travel many kilometers, pose significant threats to coastal communities, and take away lives. In spite of the low frequency of the occurrence of such events, due to population growth, the urbanization trend, and sea level rise, the exposure of coastal environments to extreme water hazards is increasing. Past tsunamis revealed that much of the nearshore infrastructure located in tsunami-prone areas are highly vulnerable to hydrodynamic loads. The tsunami waves inundated a large number of bridges, damaged the connections, and washed away the superstructures. Failure of coastal bridges is critical (due to the significant role of these structures in emergency services aftermath of the event) and possess a huge obstacle for the transportation system. According to field surveys, a total of 1,100 km of coastline was affected and 81 bridges were washed away as a result of the 2004 Indian Ocean tsunami [2]. The Great East Japan tsunami resulted in widespread damage of about USD211 billion and about 252 bridges were washed away [3-4]. On-site reconnaissance surveys after the 2004 Indian Ocean tsunami revealed that a number of bridges were subjected not only to large hydrodynamic loads but also to debris and floating objects, such as boats and shipping containers resulting in an increase in the impact force and significant lateral displacement or washout of the structure [5-7]. FEMA outlined the catastrophic effect of debris and reported that about 27% of the total disaster recovery costs in the United States are accounted for by the existence of water-borne debris [8].

Several numerical simulations and experimental studies have been carried out to date to advance the understanding of tsunami forces on coastal structures. In an experimental attempt to estimate the tsunami-induced load combinations on shoreline structures, Palermo et al. (2009) [9] reported that hydrodynamic and surge components are a function of the velocity and water depth. The results of a series of 1:100 scale experimental tests for evaluating the impact of tsunami-induced bores on buildings showed that the applied forces on the projected area of an octagonal building are reduced by about 20% compared with the square building [10]. Honda et al. (2014) [11] carried out an experimental investigation on the tsunami pressure acting on Piloti-type buildings and reported that the applied forces on the floor slabs are affected by the location of the shaft with respect to the front face of the super-structure. Foster et al. (2017) [12] carried out a 1:50 scale experimental study and proposed a semi-empirical equation for predicting tsunami induced-forces on a rectangular building. Tomiczek et al. (2019) [13] performed experimental measurements on a 1:10 scale physical model to estimate the peak horizontal forces and pressure distribution on an elevated coastal structure due to nonbreaking, breaking, and broken wave conditions and modified Goda equation. Hasanpour and Istrati (2021) [14] conducted three-dimensional numerical simulations to evaluate the wave impact on two types of buildings, with a slab on the ground and an elevated one. The results of the analyses demonstrated that as the lowest floor elevation increases, the applied horizontal force becomes negligible, while significant uplift force is applied on the elevated slab. In addition, the generation of a large overturning moment with simultaneously large uplift forces could increase the uplift demand in offshore structural elements and cause failure of the building. More recently, Hasanpour and Istrati (2022) [15] investigated extreme wave storm impact on elevated coastal buildings with different widths and the results demonstrate that while increasing the structure width has a negligible effect on the maximum applied horizontal force, it plays an important role for the uplift force. Moreover, it was also shown that by increasing the width, the

building has to withstand the uplift force for a longer duration, which could potentially increase the likelihood of failure.

To quantify the wave-in-deck loads, Bea et al. (1999) [16] proposed a procedure to determine wave-in-deck force considering the buoyant, drag, slamming, lift, and inertial forces. Araki et al. (2010) [17] investigated solitary wave forces on a bridge model and found that the fluid forces in the case of a post breaking wave were smaller than those in the case of a just breaking wave. The results of a series of 1:5 scale of bridge superstructure suggested that the large pressure amplitude, induced by wave impact had a negligible effect on horizontal and vertical forces on a bridge superstructure [18]. Lau et al. (2011) [19] carried out experimental research to evaluate the imposed tsunami forces on an inland coastal bridge. The results revealed that the induced vertical forces during inundation are followed by approximately constant downward force when the wave overtopped the bridge superstructure. Azadbakht and Yim (2015) [20] examined the role of forces and overturning moments on California coastal bridges. Based on the simulation results, a design approach to compute the maximum induced forces was proposed. Istrati et al. (2018) [21] conducted large-scale hydrodynamic experiments on tsunami wave impact on a bridge with open girder. The experimental data revealed that maximum stream-wise and uplift forces did not occur simultaneously and a significant overturning moment was generated at the initial impact when the slamming forces were maximized. Some studies evaluated the effects of different wave forms on coastal decks, including unbroken, breaking, and post-breaking waves and bores, and revealed fundamental differences in the effects caused by the two wave types. In fact, Istrati et al. (2017) [22] demonstrated that turbulent bores applied horizontal forces that were larger than the uplift forces by up to a factor of 2.2, while the unbroken waves exhibited an opposite trend with a ratio of horizontal/uplift force decreasing down to 0.54. This highlighted the need to be able to identify a priori the tsunami wave type that is expected to impact a specific coastal area in order to design

properly a new structure or strengthen an existing one at that location. Fortunately, several simplified predictive load equations have been developed in the literature for a range of different types of structures, for both bores [23] and unbroken solitary waves [24-25].

Other critical aspects related to the hydrodynamic effects on coastal structures that have been identified by previous studies include the high aleatory variability of bore impact on structures [26-27], the importance of structural flexibility and dynamic fluid–structure interaction [27-29], the critical role of trapped air below elevated decks [30-33], and the demand on individual connections and columns [21]. For example, Robertson et al. (2008) [7] found significant variability in the impulsive uplift pressures applied by a turbulent bore on the slab soffit of a vertical wall with an overhang, with the maximum pressures at selected locations ranging between 3 and 7.5 kPa among the different repetitions of the same bore. Similarly, Istrati (2017) [27] showed large aleatory variability in the bore-induced horizontal force on a bridge deck with the standard deviation in the experimental tests being equal to approximately 20% of the average value. However, after the decomposition of the total force into a slamming and quasi-static component, it was revealed that the variability is generated by the slamming component. Moreover, several studies found that the air entrapment below elevated decks with girders can significantly increase the maximum total uplift forces generated by solitary waves [24, 30]. However, the trapped air can also increase the overturning moment, while it has a complex and inconsistent effect on the total slamming and on the uplift demand in the offshore bearings and columns generated by bores [21].

The majority of the past studies mainly focused on clear-water condition to develop an understanding of wave-structure interaction and the applied loadings. However, field surveys conducted in the aftermath of major events including the 2004 Indian Ocean Tsunami and the 2011 Japan Tsunami revealed that the cause of damage to coastal structures in tsunami-prone areas is not limited to water wave hydrodynamic loads and water-borne debris loading is one of the critical

types of loading which should be considered in the design of tsunami-resistant structures ([1, 6]). Therefore, it is crucial to predict the movement and assess the impact of water-borne debris under extreme hydrodynamic events. In recent years, several studies have been carried out to investigate the dynamics and impact of water-borne debris. According to experimental studies carried out by Haehnel and Daly (2004) [33] and Matsutomi (2009) [34], the maximum debris impact force depends on the debris mass, the impact velocity, and the effective stiffness. Arikawa et al., (2007) [35] carried out an experimental study to explore the impact of the 1:5 scale model of a shipping container under air and tsunami conditions and proposed an empirical formula based on the Hertz theory to calculate the impact force. The performance of RC columns against the impact loads from water-borne shipping containers was investigated by Madurapperuma and Wijeyewickrema (2012) [36] and a linear relationship between the maximum impact force and container velocity up to 2m/s was reported. Ko et al., (2015) [37] conducted a series of experiments to study the impact of a 1:5 scale shipping container on a column and concluded that the peak impact force in water was about 1.2 times the corresponding impact force in the air and has a longer duration. However, in another experimental study, it was observed that the cushioning of trapped water between the debris and the vertical wall reduced the impact energy and force [38]. Shafiei (2016) [39] carried out a series of dam-break tests and reported that the vertical component of the impact force is about 60% of the horizontal component which was attributed to the debris impact angle at the instant of impact. Goseberg et al., (2016) [40] conducted an experimental study focusing on the motion of a 1:40 scaled model of a shipping container and observed that the debris tends to rotate toward an equilibrium position as it propagates inland with the long axis perpendicular to the flow direction. Derschum et al., (2018) [41] conducted a 1:40 scaled experimental study to investigate the impact of a shipping container on a vertical structure and reported that the initial orientation of the debris did not have a considerable effect on the debris impact load on the structure.

Bridges are an important part of the infrastructure and damage or failure of them leads to disruption of the transportation network and consequently the recovery process after a tsunami event. Therefore, the tsunami-borne debris loads on bridges need to be quantified. Yang (2016) [42] used the material point method to investigate the demands on bridge superstructures by tsunami-borne debris. The results showed that the existence of floating debris leads to an increase in demand for bridges. It is also reported that the debris impact forces in water could be up to 35% higher than the corresponding in-air cases. Oudenbroek et al., (2018) [43] conducted numerical and experimental investigations to study the debris damming failure of bridge decks and piers. It was reported that the bridge stability is affected by the presence of debris via introducing additional drag and uplift forces. Istrati et al., (2020) [44] carried out three-dimensional computational fluid dynamic analyses to investigate tsunami-borne debris damming loads on a coastal bridge. The results of the analyses demonstrated that debris damming does not have a significant effect on the applied horizontal and vertical forces. However, it has a major effect on the overturning moment which could transfer to additional vertical forces and cause the failure of the offshore structural components. In addition, the exact location of the trapped container plays a critical factor in the design of the structural component. i.e., if the container is trapped close to the supports of the span, due to the 3D effects, additional yow and roll moments are generated, which should be accounted for in the design of the structural components to avoid potential damage or collapse. Ruffini et al., (2021) [45] used the open-source DualSPHysics and reported that the model is accurate to regenerate the floating debris dynamics (trajectory and velocity). Hasanpour et al. (2021) [46] employed the novel smoothed particle hydrodynamic coupled finite element method (SPH-FEM) modeling technique to simulate tsunami-borne debris transport and impact on the coastal structure. The results of the analyses revealed the accuracy of this modeling approach to capture the debris transport and impact. Moreover, a high level of debris pitching which transferred to the non-normal impact on the coastal structure, and the resultant reduced contact area and impact force was observed. It was reported

that the level of debris pitching is a function of tsunami flow characteristics and initial water depth and a non-linear force-velocity trend for small water depth was documented. In another study, Hasanpour et al., (2022) [47] investigated the tsunami debris impact on a bridge deck utilizing the coupled SPH-FEM and the results demonstrated that the debris has both a horizontal and vertical velocity at the instant of the initial impact on the offshore side of the bridge deck and consequently exerts impulsive loads simultaneously in both directions, and the debris-fluid-deck interaction is quite complex and can accelerate the debris as it moves below the box-girder bridge, leading to secondary impacts on the soffit with significant magnitudes. much larger than the ones of the primary impact on the offshore side of the deck. More recently, Istrati and Hasanpour (2022) [48] numerically investigated the water-borne debris impact loads on piers and reported that the debris impulsive loads are 6 to 10 times larger than the fluid force.

In comparison to the tsunami propagation and inundation mechanisms, limited investigations and discussions have been made to expand the knowledge of tsunami-borne debris movement and associated impact forces on coastal bridges. Considering the increasing rate of natural hazards and their associated disruptions, the critical role of the transportation network and the catastrophic effect of water-borne debris which could cause considerable damage to infrastructure, it is critical to decipher the complex wave-debris-bridge interaction and quantify the associated loads.

1.2. Research statement and objectives

Widespread damage to coastal bridges in recent tsunamis (Indian Ocean, 2004, and East Coast Japan, 2011) have shown the vulnerability of these structures to tsunami overtopping and the crippling socioeconomic impact of their loss on both emergency response and long-term recovery of the affected communities. Developing design guidelines for coastal bridges subject to tsunami overtopping has therefore become a priority and large-scale experimental and numerical simulations have been conducted to develop and validate tsunami design equations. But this work

has been limited to clear-water conditions. The goal of the present effort is to study the effect of tsunami-borne debris on design loads for bridges using a coupled Finite Element (FE) and Smoothed Particle Hydrodynamics (SPH).

The objectives of this study are to:

1. Understand the two-fold effect of debris impact and damming on bridges.

2. Decipher debris-wave interaction during tsunami propagation inland and debris-wave-bridge interaction and associated loads for different debris orientations (longitudinal and transverse).

3. Explore and calibrate novel particle-based (SPH) and/or coupled mesh-particle based (SPH-FEM) methods of analysis.

4. Investigate role of debris mass.

5. Developing prescriptive load equations for debris impact for inclusion in the Tsunami Design Guidelines for Coastal Bridges developed by PEER and recently adopted by the AASHTO Committee on Bridges and Structures.

1.3. Numerical method

1.3.1. Background

The *Smoothed Particle Hydrometric* (SPH) is a Lagrangian-based meshless technique, in which continuum properties of the fluid are discretized by a set of non-connected particles, which carry individual material properties describing the medium such as position, velocity, mass, density, pressure, and other physical quantities [49]. Besides representing the problem domain and acting as information carriers, the particles act as the computational frame for the filed function approximations. Each particle moves and interacts with others within the computational domain

according to conservation governing equations derived from the Navier-Stokes equation. SPH was created to deal with gas dynamic problems of astronomical interests [50, 51] and later extended to solve computational fluid dynamics (CFD) problems to avoid the limitations of mesh tangling encountered in extreme deformation problems with the finite element method, governed by the Navier–Stokes equations [52]. In this method, conservation governing equations is discretized and depends on smoothing functions at one particle using a weighted average of the properties of its neighboring particles. The Lagrangian nature of the SPH would lead this method to be well suited to problems with large deformations and distorted free-surface. The major advantage of using SPH is in dealing with free-surface problems where there is no need for special treatments for the free-surface to simulate highly nonlinear and potentially violent flows. This property makes it a robust computational tool to simulate a wide range of coastal and ocean engineering applications such as solitary waves on beaches [53], breaking waves [54-55], wave-structure interaction [56-58], wave overtopping on the offshore platforms [59].

Monaghan (1994) [52] presented some examples of SPH applications for dam break problems and propagation of waves toward a beach. The approach was based on the observation that real fluids such as water are compressible, but with a speed of sound that is very much greater than the speed of bulk flow. The results showed that SPH can be used to simulate free surfaces without any difficulty where the particles are moved with the0 correct velocity. Crespo et al. (2008) [59] analyzed a dam break evolution over dry and wet beds with smoothed particle hydrodynamics method. The model was shown to accurately fit both experimental dam break profiles and the measured velocities. Cummins et al. (2012) [60] studied three-dimensional Navier–Stokes SPH computations of a dam-break flow with a rectangular column located downstream. The simulations demonstrated the ability of SPH to reproduce the complex transient loading characteristics on the column. The results approached the existing experimental data as the particle resolution increased

and were in good agreement with the experimental data for the finest resolution simulation. In particular, oscillations in the column forces after the secondary impact were captured for the higher resolutions.

Monaghan and Kos (1999) [53] numerically and experimentally studied solitary waves propagating onto and over a dry beach and returning after striking a vertical wall. They showed that the solitary wave can be successfully modeled with SPH. The SPH simulations reproduced the shape and position of the surface in a fairly good agreement. Groenenboom et al. (2016) [61] simulated the interactions between a tsunami bore using a solitary wave approach and an idealized timber structure by SPH based software. The results demonstrated the ability of the SPH method to provide impact pressure distributions in a great level of detail both spatially and temporally. Aristodemo et al. (2017) [62] analyzed the horizontal and vertical hydrodynamic forces induced by solitary waves on a submerged horizontal circular cylinder, by means of experimental and SPH numerical study. The good agreement between experimental and SPH forces allowed, as a result, the proposal of empirical formulas to calculate the hydrodynamic coefficients.

Monaghan et al. (2003) [55] used SPH to study numerically the impact between a rigid body and water and compared the results with their experiments for a rectangular box. The SPH simulation technique reproduced the qualitative features of the entire process and gave satisfactory results compared to the experiments. Gómez-Gesteira and Dalrymple (2005) [57] evaluated the collision of a wave with a tall stationary structure by conducting a three-dimensional version of the SPH method. They reported that the SPH can be used successfully to study three-dimensional wave problems like those related to the collision between waves and structures. The interaction between a large wave and a coastal structure was studied with a three-dimensional (3D) SPH model by Crespo et al. (2007) [59]. The role of protecting barriers (dikes and seawalls) to mitigate the force and moment exerted on the structure was analyzed. ST-Germain et al. (2014) [63] used a single-

phase three-dimensional (3D) weakly compressible smoothed particle hydrodynamics (WCSPH) model to investigate the hydrodynamic forces, induced by the impact of rapidly advancing tsunami like hydraulic bores, on a freestanding column of a square cross section and the results agreed with a physical model and in-situ data. Altomare et al. (2015) [58] validated a SPH-based technique for wave loading on coastal structures. Regular and random waves were simulated and good agreements were achieved. Wei et al. (2015) [64] applied the SPH method to investigate the impact of a tsunami bore on bridge piers. The influences of bridge pier shape and orientation on free surface evolution and hydrodynamic loading are carefully examined. Dynamic interactions between a tsunami bore and bridge piers were simulated, and the model showed a good capability to capture the free surface evolution in front of bridge piers. Furthermore, the model was able to accurately compute the tsunami bore hydrodynamic force on different piers. Sarfaraz and Pak (2017) [65] used the Lagrangian mesh-free method of SPH to simulate the forces applied by tsunami waves on the superstructure of the coastal bridges. The method showed a good level of accuracy to predict the free surface configuration and the induced loads on the coastal structures.

1.3.2. Coupled SPH-FEM modeling technique

The SPH technique employed in this research was implemented in the LS-Dyna software, from Livermore Software Technology Corporation (LTSC). The SPH model in LS-Dyna is based on weakly compressible smoothed particle hydrodynamics (WCSPH). LS-Dyna enables the coupling of mesh-based (FEM) and mesh-less methods (SPH). Pelfrene (2011) [66] studied the SPH method for the simulation of free surface water flow with a focus on a regular and breaking wave. It was found that the SPH solver in LS-Dyna is able to simulate free surface flow, and capture the main features of plunging breaking waves.

1.3.3.SPH governing equations

The SPH formulation can be divided in two key steps: the integral representation is used for filed approximation, known as the kernel approximation and the particle approximation. The particle approximation replaces the integral in the kernel approximation by summations over all neighboring particles in the so-called support domain. As the particle position and the magnitude of the individual properties varies with time, the summation of the particle approximation is performed at each time step.

Kernel approximation

In the SPH method, the computational domain is discretized into a set of particles, which carries individual material properties ([63]). This method is based on a quadrature formula on moving particles. Traditional SPH formulation exhibits very substantial pressure oscillation when modelling fluid flow. Instead of using the traditional computational grid, the conservation laws of continuum mechanics are defined by partial equations. For any SPH pseudo-particle, the function describing the field Ω is approximated in the form of "kernel function", which is stated as the integral form of the product of any function and kernel function [52]:

$$< f(x) >= \int_{\Omega} f(x')W(x - x', h)dx' \qquad \text{Equation 1.1}$$

where x and x' are the position vector of the material points in a domain Ω; $f(x)$ is the continuous function of the field corresponding to the coordinate x; $f(x')$ is the value of quantity at the point x'; $W(x - x', h)$ is the bell-shaped smooth kernel function, where h is the smoothing length, defining the influence volume of the smooth function which varies in time and in space.

The smoothing function determines the range of computation with other particles and therefore has a significant effect on precision and accuracy of the analyses. The kernel function can be constructed taking in account a number of conditions and should satisfy the following properties [67]:

The smoothing function is normalized:

$$\int_{\Omega} W(x - x', h)dx' = 1 \qquad \text{Equation 1.2}$$

There is a compact support for the smoothing function:

$$W(x - x', h) = 0, for\ |x - x'| > \kappa h \qquad \text{Equation 1.3}$$

where κ is the constant determines the effective area of the smoothing function. This area is called the support domain.

$W(x - x', h)$ is non-negative for any x' within the support domain. This is necessary to achieve physically meaningful results in hydrodynamic computations.

The smoothing length increases as particles separate and reduces as the concentration increases.

With the smoothing length approaching zero, the kernel approaches the Dirac delta function:

$$\lim_{h \to 0} W(x - x', h) = \partial(x - x') \qquad \text{Equation 1.4}$$

The smoothing function should be an even function.

The forms of kernel functions usually include quantic spline function, cubic spline function Gaussian kernel function [51]. The kernel function must be normalized over its support domain regardless of the type and should satisfy the Dirac delta function [67]. By balancing the calculation accuracy and efficiency and considering that the commercial software LS-Dyna was used for the simulations throughout this study, the following B-spline spline smoothing function was adopted [68]:

$$W(x,h) = \frac{1}{h(x)^d}\theta(x) \qquad \text{Equation 1.5}$$

where d is the number of space dimensions (2 or 3) and $\theta(x)$ is the cubic B-spline function defined by ([69]):

$$\theta(x) = C * \begin{cases} 1 - \frac{3}{2}{x_{ij}}^2 + \frac{3}{4}{x_{ij}}^3 & for\ x_{ij} \le 1 \\ \frac{1}{4}(2 - x_{ij})^3 & for\ 1 < x_{ij} \le 2 \\ 0 & for\ \ 2 < x_{ij} \end{cases} \qquad \text{Equation 1.6}$$

where C a constant for normalization, depending on the number of space dimensions and x_{ij} is the relative distance of particles *i* and *j*.

Particle approximation

The second key aspect in SPH formulations is the particle approximation, which enables the system to be represented by a finite number of particles that carry an individual mass and occupy an individual space. For the SPH method, Equation 1.1 can be transformed into discretized forms by

the summing up the values of the filed function within the support domain defined by the smoothing length h as follows [52]:

$$< f(x_i) >= \sum_{j=1}^{n} \frac{m_j}{\rho_j} f(x_i)\, W(x_i - x_j, h) = \sum_{j=1}^{n} \frac{m_j}{\rho_j} f(x_j)\, W_{ij,} \qquad \text{Equation 1.7}$$

where $< f(x_i) >$ is the kernel approximation operator, $f(x_j)$ is the physical value at the *j*th position, i is the number of any particle in the domain; n is the total number of particles within the influence area of the particle at i; and m_j and ρ_j are the mass and density associated with particle j. Thus, the value of particle i is approximated using the weighted average of the function values at all particles within the support domain of particle j. The partial approximation of the spatial derivation of a function can be expressed as:

$$< \nabla . f(x_i) >= -\sum_{j=1}^{n} \frac{m_j}{\rho_j} f(x_i) . \nabla W_{ij} \qquad \text{Equation 1.8}$$

where

$$\nabla W_{ij} = \frac{x_i - x_j}{r_{ij}} \frac{\partial W_{ij}}{\partial r_{ij}} \qquad \text{Equation 1.9}$$

1.3.4. SPH for viscous fluid

The smoothing kernel and particle approximation can be used for discretization of partial differential equations (PDE's). The SPH formulation is derived by discretizing the Navier- Stokes equations spatially, thus leading to a set of ODE's which can be solved via time integration. Substituting the SPH approximations for a function and its derivative to the partial differential equations governing the physics of fluid flows, the discretization of these governing equations can be written as follows [69]:

$$\frac{d\rho_i}{dt} = \sum_{j=1}^{n} m_j \ (x_i^\beta - x_j^\beta) \ \frac{\partial W_{ij}}{\partial x_i^\beta}$$

$$\frac{dv_i^\alpha}{dt} = \sum_{j=1}^{n} m_j \ (\frac{\sigma_i^{\alpha\beta}}{\rho_i^2} + \frac{\sigma_j^{\alpha\beta}}{\rho_j^2}) \frac{\partial W_{ij}}{\partial x_i^\beta}$$

$$\frac{dv_i^\alpha}{dt} = \sum_{j=1}^{n} m_j \ (\frac{\sigma_i^{\alpha\beta}}{\rho_i\rho_j} . \frac{\partial W_{ij}}{\partial x_i^\beta} - \frac{\sigma_j^{\alpha\beta}}{\rho_i\rho_j} . \frac{\partial W_{ij}}{\partial x_j^\beta})$$

Equation 1.10

$$\frac{de_i}{dt} = -\frac{p_i + \Pi_{ij}}{\rho_i^2} \sum_{j=1}^{n} m_j \ (v_i - v_j) \ \frac{\partial W_{ij}}{\partial x_i^\beta}$$

$$\frac{dx_i^\alpha}{dt} = v_i + \varepsilon \sum_{j=1}^{n} \frac{m_j}{\rho_j} (v_i - v_j) \, W_{ij}$$

where the superscripts α and β are the coordinate directions; g is the acceleration of gravity;σ is the particle stress; v is the particle velocity; e is the internal energy per unit mass; ε is the shear strain rate ($\varepsilon \cong 0.5$) and Π_{ij} is the Monaghan artificial viscosity [50]. In the analysis of the interaction between waves and structures, Π_{ij} can prevent the non-physical shock of the solution results in the impact area and effectively prevent the non-physical penetration of particles when they are close to each other. The role of artificial viscosity is to smoothen the shock over several particles and to allow the simulation of viscous dissipation, the transformation of kinetic energy to heat. Therefore, to consider the artificial viscosity, an artificial viscous pressure term Π_{ij} is added.

From Equation 1.10, the following particle body forces can be derived:

$$F_i^{pressure} = -\sum_j \ m_j \frac{p_i + p_j}{2\rho_j} \nabla W(r_{ij}, h)$$

$$F_i^{viscosity} = \mu \sum_j \ m_j \frac{v_i + v_j}{2\rho_j} \nabla^2 W(r_{ij}, h)$$

Equation 1.11

where $r_{ij} = x_i - x_j$, μ is the viscosity coefficient of the fluid. The pressure p_i are computed via the constitutive equation:

$$p_i = K\,(\rho_i - \rho_0) \qquad \text{Equation 1.12}$$

where k is the stiffness of the fluid and ρ_0 is the initial density.

The acceleration of particle i is derived from:

$$a_i = \frac{1}{\rho_i\,(F_i^{pressure} + F_i^{viscosity} + F_i^{external})} \qquad \text{Equation 1.13}$$

where $F_i^{external}$ are external forces such as body forces and forces due to contacts.

1.3.5. Equation of state (EOS)

When the SPH method is applied in solving the FSI problems, the fluid is treated as weakly compressible, which means that an equation of state is utilized to determine the dynamic fluid pressure based on the variation in density and internal energy of particles. The equation of state is originally applied to SPH by Monaghan (1994) [52] to model free surface flows for water, which is stated in the following form:

$$P = k_0[(\frac{\rho}{\rho_0})^{\Upsilon} - 1] \qquad \text{Equation 1.14}$$

where ρ_0 denotes the reference water density, ρ is the current density, Υ is a constant parameter and often set to 7 for water, and k_0 is used to govern the maximum fluctuations of pressure, and is usually taken as follows [63]:

$$c_0 = \sqrt{\frac{\Upsilon k_0}{\rho_0}} \geq 10\, v_{max} \qquad \text{Equation 1.15}$$

where c_0 is the speed of sound in water at the reference density. In order to satisfy the Courant-Friedrichs-Lewy (CFL) condition, the real speed of sound and is typically chosen to be at least 10 times faster than the maximum fluid velocity. Satisfying this criterion will keep the density variations to within less than 1% and ensure low compressibility while allowing for a relatively large time step size.

1.3.6. Contact

Penalty-based contact algorithms are utilized to define the interface between the SPH and FE parts, in which the particles are treated as the slave and other elements as the master. To treat the interaction between SPH and FE parts, the particles are considered as nodes, and the FE parts as surface. When the fluid particles come into contact with the surface, each slave node is searched for penetration and if the slave node penetrates, a resisting force is applied to eliminate further penetration. The resisting force is stated by [68]:

$$f=kdn \qquad \text{Equation 1.16}$$

where d is the penetration distance, n is the surface normal vector and k is a penalty factor. The stiffness factor k for master segment s_i is given in terms of the bulk modulus K_i, the volume V_i, and the face area A_i of the element that contains s_i as

$$k_i = \frac{A_i K_i f_{si}}{max\ (shell\ diagonal)} \qquad \text{Equation 1.17}$$

where f_{si} is a scale factor for the interface stiffness and is defined equal 10. The constant k should be set large to minimize penetration and instabilities, but it should not be too large that it generates artificially large forces. As the contact location and the direction may be difficult to predict, the automatic contacts are recommended, since they can detect the penetration at each time step, irrespective of whether it is coming from the slave or master part. The automatic contacts determine

the contact surface by projecting normally from the shell mid-plane to a distance equal to half of the contact thickness. It must be noted that the solver can simulate the contact between flexible structures, rigid and flexible structures, or between rigid bodies only. Interestingly, even in the case of rigid bodies where the deformations are not calculated, it is possible to define a bulk modulus at the material level, which enables the user to adjust the contact parameters (e.g., contact stiffness) and avoid numerical spikes in the contact forces.

The interaction between the FE elements with each other is defined through a two-way treatment of contact in which both slave and master segments are checked for penetration. This type of contact is symmetric and the definition of the slave and master surfaces are arbitrary. As the prediction of the contact location and the direction may be difficult to conclude, the automatic contacts are recommended, since they can detect the penetration at each time-step, irrespective of whether it is coming from the slave or master part. The automatic contacts determine the contact surface by projecting normally from the shell mid-plane to a distance equal to half of the contact thickness.

1.4. Organization of the dissertation

This dissertation follows a paper-based format that encompasses five standalone papers besides three introductory, prescriptive design equations, and concluding chapters. Thus, the dissertation is organized into a total of eight chapters as follows. Chapter 1 presents the introduction including a literature review, research statement and objectives, and a detailed explanation of the utilized numerical method. In the second Chapter 2 (standalone paper#1), a coupled SPH-FEM modeling approach is introduced which simulates the fluid as particles, and the flume, the debris, and the structure with mesh-based finite elements. The validity of this approach is demonstrated through comparisons with large-scale experimental data from the literature. These comparisons showed that the method is able to accurately capture the interactions between debris, wave, and structure in two-dimensional simulations. In the third chapter (standalone paper#2), the results of two-dimensional

simulations of tsunami debris impacting a box girder bridge are presented. The multi-physics modeling approach used in these simulations allowed for a preliminary investigation of the interaction between the debris, tsunami and, bridge, as well as the impact loads on the superstructure under different orientations of a floating container and varying deck elevations. In chapters 4 and 5 (standalone papers#3 and 4), an extensive numerical investigation is conducted to gain a more comprehensive understanding of the underlying physics of three-dimensional debris-wave and debris-wave-bridge interactions. The influence of various factors, including bore strength, initial water depth, bridge elevation, and initial debris orientation, on debris dynamics, impact forces, and loading sequences are examined. In Chapter 6 (standalone paper#5), the effect of the mass of debris on its dynamic and impact forces are analyzed for two different debris orientations, using a variety of debris mass values. Chapter 7 presents a comparison of the results of numerical simulations with available simplified equations and provides recommendations for bridges. This comparison aims to assess the accuracy and reliability of the simplified equations in predicting the impact forces. Finally, the last chapter summarizes the key findings of this study followed by research recommendations for future studies.

A chapter-by-chapter summary of the content of this dissertation is therefore as follows:

Chapter 1:

Title: Introduction

Chapter 2:

Title: Coupled SPH-FEM Modeling of Tsunami-Borne Large Debris Flow and Impact on Coastal Structures.

Publication Status: Published in the *Journal of Marine Science and Engineering*

Citation: Hasanpour, A., Istrati, D., & Buckle, I. (2021). Coupled SPH–FEM modeling of tsunami-borne large debris flow and impact on coastal structures. *Journal of Marine Science and Engineering*, *9*(10), 1068. doi: 10.3390/jmse9101068

Chapter 3:

Title: Multi-physics Modeling of Tsunami Debris Impact on Bridge Decks

Publication Status: Presented at 3rd International Conference on Natural Hazards & Infrastructure-Has been indexed in Scopus.

Citation: Hasanpour, A., Istrati, D., & Buckle, I. G. (2022, July). Multi-physics modeling of tsunami debris impact on bridge decks. In *Proceedings of the 3rd International Conference on Natural Hazards & Infrastructure, Athens, Greece* (pp. 5-7).

Chapter 4:

Title: Three-Dimensional Investigation of Floating Debris Effects on Bridge Superstructures During Tsunamis

Publication Status: has been submitted to Coastal Engineering: An International Journal for Coastal, Harbour, and Offshore Engineers, Published by Elsevier

Citation: Hasanpour A., Istrati D., Buckle I. (2023). "Three-Dimensional Investigation of Floating Debris Effects on Bridge Superstructures During Tsunamis", *Coastal Engineering.*

Chapter 5:

Title: Effect of Debris Orientation on the Debris-Tsunami-Bridge Interaction and Induced Forces

Publication Status: To be submitted to a peer-reviewed journal.

Citation: Hasanpour A., Istrati D., Buckle I. (2023). "Effect of Debris Orientation on the Debris-Tsunami-Bridge Interaction and Induced Forces", (*to be submitted to a peer-reviewed journal)*

Chapter 6:

Title: SPH-FEM Investigation of Floating Container Impact on Bridge Superstructures: Role of Debris Mass

Publication Status: To be submitted to a peer-reviewed journal.

Citation: Hasanpour A., Istrati D., Buckle I. (202x). "SPH-FEM Investigation of Floating Container Impact on Bridge Superstructures: Role of Debris Mass", (*to be submitted to a peer-reviewed journal)*

Chapter 7:

Title: Prescriptive Design Equations

Chapter 8:

Title: Summary, Conclusions, and Future Work

1.5. References

1. Yeh, H.; Sato, S.; Tajima, Y. The 11 March 2011 East Japan earthquake and tsunami: Tsunami effects on coastal infrastructure and buildings. *Pure Appl. Geophys.* 2013, *170*, 1019–1031, https://doi.org/10.1007/s00024-012-0489-1.
2. Unjoh S. (2007). Bridge damage caused by tsunami. B Japan Assoc Earthquake Eng, 2007, 6: 6–28.
3. Aglipay, M.R.I., Kyokawa, H., Konagai, K., 2011. Bridges washed away by tsunami in minamisanriku, miyagi prefecture in the March 11th 2011 Great East Japan earthquake. Seisan Kenkyu 63 (6), 723–727.
4. Kajitani Y, Chang S, Tatano H (2013): Economic Impacts of the 2011 Tohoku-Oki Earthquake and Tsunami.*Earthquake Spectra*, 29 (S1), S457-S478. [https://doi.org/10.1193%2F1.4000108]
5. Ghobarah, A.; Saatcioglu, M.; Nistor, I. The impact of the 26 December 2004 earthquake and tsunami on structures and infrastructure. Eng. Struct. 2006, 28, 312–326.
6. Rossetto, T., et al., 2007. The Indian Ocean tsunami of December 26, 2004: observations in Sri Lanka and Thailand. Nat. Hazards 42 (1), 105–124.
7. Robertson, I.; Riggs, H.R.; Yim, S.C.; Young, Y.L. Lessons from Hurricane Katrina storm surge on bridges and buildings. J. Waterw. Port Coast. Ocean Eng. 2007, 133, 463–483.

8. FEMA, Public Assistance—Debris Management Guide, Dept. of Homeland Security, Washington, DC, 2007.
9. Palermo, Dan, Ioan Nistor, Younes Nouri, and Andrew Cornett. "Tsunami loading of near-shoreline structures: a primer." *Canadian Journal of Civil Engineering* 36, no. 11 (2009): 1804-1815.
10. Chinnarasri, C., Thanasisathit, N., Ruangrassamee, A., Weesakul, S., Lukkunaprasit, P., 2013. The impact of tsunami-induced bores on buildings. Proc. ICE-Marit. Eng. 14–24.
11. Honda, Takahide, Yukinobu Oda, Kazunori Ito, Masaaki Watanabe, and Tomoyuki Takabatake. "AN EXPERIMENTAL STUDY ON THE TSUNAMI PRESSURE ACTING ON PILOTI-TYPE BUILDINGS." *COASTAL ENGINEERING* (2014): 2.
12. Foster, A. S. J., T. Rossetto, and W. Allsop. "An experimentally validated approach for evaluating tsunami inundation forces on rectangular buildings." *Coastal Engineering* 128 (2017): 44-57.
13. Tomiczek, Tori, Amy Wyman, Hyoungsu Park, and Daniel T. Cox. "Modified Goda Equations to Predict Pressure Distribution and Horizontal Forces for Design of Elevated Coastal Structures." *Journal of Waterway, Port, Coastal, and Ocean Engineering* 145, no. 6 (2019): 04019023.
14. Hasanpour, A., & Istrati, D. (2021). Reducing extreme flooding loads on essential facilities via elevated structures. In *Lifelines 2022* (pp. 755-766).
15. Hasanpour, A., & Istrati, D. (2022, July). Extreme Storm Wave Impact on Elevated Coastal Buildings. In *Proceedings of the 3rd International Conference on Natural Hazards & Infrastructure (ICONHIC2022), Athens, Greece* (pp. 5-7).
16. Bea, R. G., T. Xu, J. Stear, and R. Ramos. "Wave forces on decks of offshore platforms." *Journal of Waterway, Port, Coastal, and Ocean Engineering* 125, no. 3 (1999): 136-144.
17. Araki, S.; Ishino, K.; Deguchi, I. Stability of girder bridge against tsunami fluid force. In Proceedings of the 32th International Conference on Coastal Engineering (ICCE), Shanghai, China, June 30- July 5, 2010.
18. Bradner, Christopher, Thomas Schumacher, Daniel Cox, and Christopher Higgins. "Experimental setup for a large-scale bridge superstructure model subjected to waves." *Journal of waterway, port, coastal, and ocean engineering* 137, no. 1 (2011): 3-11.
19. Lau, Tze Liang, Tatsuo Ohmachi, Shusaku Inoue, and Panitan Lukkunaprasit. "Experimental and numerical modeling of tsunami force on bridge decks." *Tsunami—a growing disaster. InTech* 6 (2011): 105-130.
20. Azadbakht, M., Yim, S.C., 2015. Simulation and estimation of tsunami loads on bridge superstructures. J. Waterw. Port. Coast. Ocean. Eng. 141 (2), 20.
21. Istrati, Denis, Ian Buckle, Pedro Lomonaco, and Solomon Yim. "Deciphering the tsunami wave impact and associated connection forces in open-girder coastal bridges." *Journal of Marine Science and Engineering* 6, no. 4 (2018): 148.
22. Istrati, D.; Buckle, I.G.; Itani, A.; Lomonaco, P.; Yim, S. Large-scale FSI experiments on tsunami-induced forces in bridges. In Proceedings of the 16th World Conference on Earthquake, 16WCEE, Santiago, Chile, 9–13 January 2017; pp. 9–13. Available online: http://www.wcee.nicee.org/wcee/article/16WCEE/WCEE2017-2579.pdf (accessed on 15 July 2021).
23. Chock, G.Y.; Robertson, I.; Riggs, H.R. Tsunami structural design provisions for a new update of building codes and performancebased engineering. Solut. Coast. Disasters 2011, 423–435.
24. McPherson, R.L. Hurricane Induced Wave and Surge Forces on Bridge Decks. Ph.D. Thesis, Texas A&M University, College Station, TX, USA, 2008.
25. Xiang, T.; Istrati, D.; Yim, S.C.; Buckle, I.G.; Lomonaco, P. Tsunami loads on a representative coastal bridge deck: Experimental study and validation of design equations. J. Waterw. Port Coast. Ocean Eng. 2020, 146, 04020022.

26. Robertson, I.N.; Riggs, H.R.; Mohamed, A. Experimental results of tsunami bore forces on structures. In Proceedings of the International Conference on Offshore Mechanics and Arctic Engineering, Shanghai, China, 6–11 January 2008; pp. 509–517.
27. Istrati, D. Large-Scale Experiments of Tsunami Inundation of Bridges Including Fluid-Structure-Interaction. Ph.D. Thesis, University of Nevada, Reno, NV, USA, 2017. Available online: https://scholarworks.unr.edu//handle/11714/2030 (accessed on 15 July 2021).
28. Choi, S.J.; Lee, K.H.; Gudmestad, O.T. The effect of dynamic amplification due to a structure's vibration on breaking wave impact. Ocean Eng. 2015, 96, 8–20.
29. Bozorgnia, M.; Lee, J.J.; Raichlen, F. Wave structure interaction: Role of entrapped air on wave impact and uplift forces. In Proceedings of the International Conference on Coastal Engineering, 30 June–5 July 2010
30. Seiffert, B.; Hayatdavoodi, M.; Ertekin, R.C. Experiments and computations of solitary-wave forces on a coastal-bridge deck. Part I: Flat plate. Coast. Eng. 2014, 88, 194–209.
31. Xu, G.; Cai, C.S.; Chen, Q. Countermeasure of air venting holes in the bridge deck–wave interaction under solitary waves. J. Perform. Constr. Facil. 2017, 31, 04016071.
32. Istrati, D.; Buckle, I. Role of trapped air on the tsunami-induced transient loads and response of coastal bridges. Geosciences 2019, 9, 191.
33. Haehnel, R. B., & Daly, S. F. (2004). Maximum impact force of woody debris on floodplain structures. *Journal of Hydraulic Engineering*, *130*(2), 112-120.
34. Matsutomi, H. (2009). Method for estimating collision force of driftwood accompanying tsunami inundation flow. *Journal of Disaster Research*, *4*(6), 435-440.
35. ARIKAWA, T., OHTSUBO, D., Nakano, F., SHIMOSAKO, K., & ISHIKAWA, N. (2007). Large model tests of drifting container impact force due to surge front tsunami. In *Proceedings of coastal engineering, JSCE* (Vol. 54, pp. 846-850). Japan Society of Civil Engineers.
36. Madurapperuma, M. A. K. M., and Wijeyewickrema, A. C. (2012). "Inelastic dynamic analysis of an RC building impacted by a tsunami water-borne shipping container." *J. Earthquake Tsunami*, 6, 1250001. [https://doi.org/10.1142/S1793431112500017]
37. Ko, H., Cox, D., Riggs, H., and Naito, C. (2015). "Hydraulic experiments on impact forces from tsunami-driven debris." J. Waterway, Port, Coastal, Ocean Eng., 10.1061/(ASCE)WW.1943-5460.0000286, 04014043.
38. Ikeno, M., Takabatake, D., Kihara, N., Kaida, H., Miyagawa, Y., & Shibayama, A. (2016). Improvement of collision force formula for woody debris by airborne and hydraulic experiments. *Coastal Engineering Journal*, *58*(04), 1640022.
39. Shafiei, S., Melville, B. W., Shamseldin, A. Y., Adams, K. N., & Beskhyroun, S. (2016). Experimental investigation of tsunami-borne debris impact force on structures: Factors affecting impulse-momentum formula. *Ocean Engineering*, *127*, 158-169.
40. Goseberg, N., Stolle, J., Nistor, I., & Shibayama, T. (2016). Experimental analysis of debris motion due the obstruction from fixed obstacles in tsunami-like flow conditions. *Coastal Engineering*, *118*, 35-49. [https://doi.org/10.1016/j.coastaleng.2016.08.012
41. Derschum, C., Nistor, I., Stolle, J., & Goseberg, N. (2018). Debris impact under extreme hydrodynamic conditions part 1: Hydrodynamics and impact geometry. *Coastal Engineering*, *141*, 24-35. [https://doi.org/10.1016/j.coastaleng.2018.08.016]
42. Yang, W.C. Study of Tsunami-Induced Fluid and Debris Load on Bridges using the Material Point Method. Ph.D. Thesis, University of Washington, Seattle, WA, USA, 2016. Available online: http://hdl.handle.net/1773/37064 (accessed on 15 July 2021).
43. Oudenbroek, Kevin, Nader Naderi, Jeremy D. Bricker, Yuguang Yang, Cor Van der Veen, Wim Uijttewaal, Shuji Moriguchi, and Sebastiaan N. Jonkman. "Hydrodynamic and debris-damming failure of bridge decks and piers in steady flow." *Geosciences* 8, no. 11 (2018): 409. [https://doi.org/10.3390/geosciences8110409]

44. Istrati, D.; Hasanpour, A.; Buckle, I. Numerical Investigation of Tsunami-Borne Debris Damming Loads on a Coastal Bridge. In Proceedings of the 17 World Conference on Earthquake Engineering, Sendai, Japan, 13–18 September 2020.
45. Ruffini, G., Briganti, R., De Girolamo, P., Stolle, J., Ghiassi, B., & Castellino, M. (2021). Numerical Modelling of Flow-Debris Interaction during Extreme Hydrodynamic Events with DualSPHysics-CHRONO. *Applied Sciences*, *11*(8), 3618.
46. Hasanpour, A., Istrati, D., & Buckle, I. (2021). Coupled SPH–FEM Modeling of Tsunami-Borne Large Debris Flow and Impact on Coastal Structures. *Journal of Marine Science and Engineering*, *9*(10), 1068. [https://doi.org/10.3390/jmse9101068]
47. Hasanpour, A., Istrati, D., & Buckle, I. G. (2022, July). Multi-Physics Modeling of Tsunami Debris Impact on Bridge Decks. In *Proceedings of the 3rd International Conference on Natural Hazards & Infrastructure, Athens, Greece* (pp. 5-7).
48. Istrati, D., & Hasanpour, A. (2022, September). Advanced numerical modelling of large debris impact on piers during extreme flood events. In *Proceedings of the 7th IAHR Europe Congress, Athens, Greece* (pp. 7-9).
49. Liu, M.B.; Liu, G.R. Smoothed particle hydrodynamics (SPH): An overview and recent developments. Arch.
50. Gingold, R. A., and Monaghan, J. J. (1977). "Smoothed particle hydrodynamics: Theory and application to non-spherical stars." Mon. Not. R. Astron. Soc., 181, 375–389.
51. Lucy, L. B. (1977). "A numerical approach to the testing of the fission hypothesis." Astron. J., 82, 1013–1024.
52. Monaghan, J. J. (1994), Simulating free surface flows with SPH, Journal Computational Physics, 110: 399-406.
53. Monaghan, J.J., & Kos, A., 1999. Solitary waves on a cretan beach. J. Waterw. Port Coast. Ocean Eng. 125, 145–155.
54. Colagrossi, A., and Landrini, M. (2003). Numerical simulation of interfacial flows by smoothed particle hydrodynamics." Journal of Computational Physics, 191, 448-475.
55. Monaghan, J. J., and Kos, A., Issa, N. (2003). "Fluid motion generated by impact." Journal of Waterway, Port, Coastal and Ocean Engineering, 129(6) 250- 259.
56. Dalrymple, R. A., Knio, O., Cox, D. T., G_omez-Gesteira, M., and Zou, S. (2002). Using a Lagrangian particle method for deck overtopping." Proc. of Waves, ASCE., 1082-1091
57. Gomez-Gesteira, M., Cerqueiro, D., Crespo, C., and Dalrymple, R. A. (2005). Green water overtopping analyzed with a SPH model." Ocean Engineering, 32, 223-238.
58. C. Altomare, J.M. Domínguez, A.J.C. Crespo, T. Suzuki, I. Caceres, M. Gómez- Gesteira, Hybridization of the wave propagation model SWASH and the meshfree particle method SPH for real coastal applications, Coast. Eng. J. 57 (2015) 1550024.
59. Crespo, A. J., Gómez-Gesteira, M., & Dalrymple, R. A. (2007). Modeling dam break behavior over a wet bed by a SPH technique. *Journal of waterway, port, coastal, and ocean engineering*, *134*(6), 313-320.
60. Cummins, S. J., Silvester, T. B., & Cleary, P. W. (2012). Three-dimensional wave impact on a rigid structure using smoothed particle hydrodynamics. *International journal for numerical methods in fluids*, *68*(12), 1471-1496.
61. Groenenboom, P.; Siemann, M. Fluid-structure interaction by the mixed SPH-FE method with application to aircraft ditching. Int. J. Multiphys. 2016, 9, 249–265.
62. Aristodemo A, Tripepi G, Meringolo DD, Veltri P (2017) Solitary wave-induced forces on horizontal circular cylinders: laboratory experiments and SPH simulations. Coast Eng 129:17–35. https ://doi. org/10.1016/j.coast aleng .2017.08.011
63. St-Germain, Philippe, Ioan Nistor, Ronald Townsend, and Tomoya Shibayama. "Smoothed-particle hydrodynamics numerical modeling of structures impacted by tsunami bores." *Journal of Waterway, Port, Coastal, and Ocean Engineering* 140, no. 1 (2014): 66-81.

64. Wei Z, Dalrymple RA, Hérault A, Bilotta G, Rustico E, Yeh H (2015) SPH modeling of dynamic impact of tsunami bore on bridge piers. Coast Eng 104:26–42
65. Sarfaraz, Mohammad, and Ali Pak. "SPH numerical simulation of tsunami wave forces impinged on bridge superstructures." *Coastal Engineering* 121 (2017): 145-157.
66. Pelfrene, J. Study of the SPH Method for Simulation of Regular and BreakingWaves. Master's Thesis, Gent University, Ghent, Belgium, 2011.
67. Liu, G.R.; Liu, M.B. Smoothed Particle Hydrodynamics: A Meshfree Particle Method; World Scientific: Singapore, 2003.
68. Hallquist, J.O. LS-DYNA theory manual. Liverm. Softw. Technol. Corp. 2006, 3, 25–31.
69. Petschek, A.G.; Libersky, L.D. Cylindrical smoothed particle hydrodynamics. J. Comput. Phys. 1993, 109, 76–83.

Chapter 2

2. Coupled SPH-FEM Modeling Tsunami-Borne Large Debris Flow and Impact on Coastal Structures

Abstract

Field surveys in recent tsunami events document the catastrophic effects of large waterborne debris on coastal infrastructure. Despite the availability of experimental studies, numerical studies investigating these effects are very limited due to the need to simulate different domains (fluid, solid), complex turbulent flows and multi-physics interactions. This study presents a coupled SPH–FEM modeling approach that simulates the fluid with particles, and the flume, the debris and the structure with mesh-based finite elements. The interaction between the fluid and solid bodies is captured via node-to-solid contacts, while the interaction of the debris with the flume and the structure is defined via a two-way segment-based contact. The modeling approach is validated using available large-scale experiments in the literature, in which a restrained shipping container is transported by a tsunami bore inland until it impacts a vertical column. Comparison of the experimental data with the two-dimensional numerical simulations reveals that the SPH–FEM models can predict (i) the non-linear transformation of the tsunami wave as it propagates towards the coast, (ii) the debris–fluid interaction and (iii) the impact on a coastal structure, with reasonable accuracy. Following the validation of the models, a limited investigation was conducted, which demonstrated the generation of significant debris pitching that led to a non-normal impact on the column with a reduced contact area and impact force. While the exact level of debris pitching is highly dependent on the tsunami characteristics and the initial water depth, it could potentially result in a non-linear force–velocity trend that has not been considered to date, highlighting the need for further investigation preferably with three-dimensional models.

Keywords: tsunami; wave; bore; flooding; debris; SPH; numerical modeling; SPH-FEM coupling; fluid-structure interaction; coastal structures

2.1. Introduction

After the Indian Ocean Tsunami in 2004 and Great East Japan Tsunami in 2011, which resulted in significant destruction of coastline infrastructure and enormous financial losses [1], tsunamis have gained a great deal of attention. Due to the enormous amount of energy, tsunami waves can travel many kilometers and pose significant threats to coastal communities, taking away lives, and causing serious damage to coastal structures. In spite of the low frequency of the occurrence of such events, due to population growth, the urbanization trend and sea level rise, the exposure of coastal environments to extreme water hazards is increasing. Past tsunamis revealed that much of the nearshore infrastructure located in tsunami-prone areas is highly vulnerable to hydrodynamic loads. Extensive damage to coastal buildings, bridges, seawalls, and breakwaters was reported after the 2004 Indian tsunami and the 2011 Tohoku tsunami [2–5]. FEMA P-646 [3] reported that the Indian tsunami generated by a Mw9.1 subduction earthquake [3] caused extensive damage to critical infrastructure and total loss of life over 310,000 [6]. Flooding caused by the 2011 Tohoku tsunami affected areas that were 7 miles away from the shore and damaged over 162,000 buildings and more than 300 bridges [5–9].

Several numerical simulations and experimental studies have been carried out to date to advance the understanding of tsunami forces on coastal structures. Palermo et al. [10] described the tsunami-induced force components on nearshore structures and reported that the hydrodynamic and surge components were a function of the instantaneous velocity and water depth. Other studies focused on the experimental testing of tsunami bore loads on rectangular buildings [11], piloti-type buildings [12], walls with overhangs [13] and coastal bridges [14–17]. Some studies evaluated the effects of different wave forms on coastal decks, including unbroken, breaking and post-breaking waves and bores [14,18], and revealed fundamental differences in the effects caused by the two wave types. In fact, Istrati et al. [18] demonstrated that turbulent bores applied horizontal forces

that were larger than the uplift forces by up to a factor of 2.2, while the unbroken waves exhibited an opposite trend with a ratio of horizontal/uplift force decreasing down to 0.54. This highlighted the need to be able to identify a priori the tsunami wave type that is expected to impact a specific coastal area in order to design properly a new structure or strengthen an existing one at that location. Fortunately, several simplified predictive load equations have been developed in the literature for a range of different types of structures, for both bores [19, 20] and unbroken solitary waves [21, 22].

Other critical aspects related to the hydrodynamic effects on coastal structures that have been identified by previous studies include the high aleatory variability of bore impact on structures [13, 17], the importance of structural flexibility and dynamic fluid–structure interaction [17, 23, 24], the critical role of trapped air below elevated decks [21,25–28] and the demand on individual connections and columns [29]. For example, Robertson et al. [13] found a significant variability in the impulsive uplift pressures applied by a turbulent bore on the slab soffit of a vertical wall with an overhang, with the maximum pressures at selected locations ranging between 3 and 7.5 kPa among the different repetitions of the same bore. Similarly, Istrati [17] showed a large aleatory variability in the bore-induced horizontal force on a bridge deck with the standard deviation in the experimental tests being equal to approximately 20% of the average value. However, after the decomposition of the total force into a slamming and quasi-static component, it was revealed that the variability is generated by the slamming component. Moreover, several studies found that the air entrapment below elevated decks with girders can significantly increase the maximum total uplift forces generated by solitary waves [21, 30]. However, the trapped air can also increase the overturning moment, while it has a complex and inconsistent effect on the total slamming and on the uplift demand in the offshore bearings and columns generated by bores [28].

In addition to the adverse tsunami-induced effects on coastal structures documented by the aforementioned studies focusing on ‘clear-water’ conditions, field surveys after recent tsunamis revealed the presence of waterborne debris (e.g., containers, cars, wooden poles), which can result in an increase in the uplift and drag forces and lead to significant lateral displacement and potential instability of the structure [1, 31, 32]. Consequently, the quantification of the impact forces caused by the waterborne debris attracted the attention of several research studies, both numerical [33–35] and experimental [36–39]. According to Haehnel and Daly [36], the peak debris impact force is a function of the impact velocity, the mass of the debris, and the effective stiffness. Como and Mahmoud [35] evaluated the debris impact on interior and exterior wood structural panels using fluid–structure interaction analyses and reported that the debris impact forces on an exterior panel increased with the wave height, while this was not the case for the interior panels. Ko [37] investigated experimentally the impact of a shipping container on a column and reported that the in-water applied load was 1.2-fold larger than the corresponding in-air condition, and had a longer duration. An equation to estimate the debris velocity based on the relative distance of debris pick-up location and the structure was developed in Shafiei et al. [38]. Derschum et al. [40] investigated the debris impact on structures and reported that the initial impoundment depth had a significant effect on the impact angle. Moreover, the same study observed a non-linear movement of the debris with a reduced impact velocity close to the structure, which was attributed to the formation of splitting streamlines and a stagnation zone in front of the coastal structure.

Yang [41] studied the tsunami-induced debris loading on bridge decks using the material point method. The results of the analyses showed that the presence of debris increases the applied loads on bridges, with the in-water analyses giving up to 35% larger debris impact forces than the in-air cases. Oudenbroek et al. [42] carried out an experimental and numerical study to evaluate the failure mechanism of selected bridges in Japan. The results confirmed that debris accumulation had

significant effects on the hydraulic demand on bridges by increasing the uplift and drag forces, which could lead to the structural failure of the bridge. Istrati et al. [43] carried out a three-dimensional (3D) numerical investigation on the effects of tsunami-borne debris damming on coastal bridges. The results demonstrated that a shipping container trapped below the offshore overhang of a bridge has a negligible effect on the horizontal load but it can increase the overturning moment (pitching), which could consequently increase the probability of failure of the offshore bearings and connections that have to withstand this moment. If the container is trapped at locations offset from the mid-length of the span (e.g., close to the supports of the span), significant yaw and roll moments are generated due to 3D effects, which could lead to unequal distribution of the loads to the structural components of the two bent caps or abutments.

The majority of the numerical studies conducted to date on tsunami and extreme flooding effects on structures used mesh-based solvers that employed the finite volume [26, 42] or the finite element method [23, 44], while some of them used particle-based methods including smoothed particle hydrodynamics [45–47] or hybrid particle-finite methods such as PFEM [48]. SPH is a Lagrangian-based meshless technique, in which continuum properties of the fluid are discretized by a set of non-connected particles that carry individual material properties describing the medium, including, position, velocity, mass, density, pressure, and other physical quantities [49]. The Lagrangian nature of the SPH makes this method well suited to problems with large deformations and distorted free surface. The major advantage of using SPH is in dealing with free-surface problems where there is no need for special treatments for the free surface in order to simulate highly non-linear and potentially violent flows [50]. In recent years, SPH has been widely utilized to simulate a wide range of coastal and ocean engineering applications, such as solitary waves on beaches [51], breaking waves [52–55], wave–structure interaction and impact on coastal structures [45–47, 56–60], and wave overtopping on offshore platforms [61]. Although the SPH method is one of the most

matured forms of meshless techniques for cases of large deformations, such as during the breaking process of a wave, the computational accuracy and efficiency in simulating small deformation of solid bodies are lower than that of the FEM approach [62]. However, in the context of coastal structures and their dynamic response to large wave loads, the hybrid SPH–FEM approach could be utilized to take advantages of the ability of: (a) the SPH method to simulate complex free-surface flows and large fluid deformations, and (b) the FEM to simulate the dynamics of the structure [63, 64].

The number of available numerical studies of tsunami-borne debris loading on coastal structures is quite limited, which can be attributed to the challenging multi-physics nature of the phenomenon. This phenomenon involves a complex fluid flow with turbulent wave breaking, a non-linear debris–fluid interaction with large deformations, a contact between the debris, the fluid and the coastal structure, and a dynamic structural response. Given (i) the catastrophic effects of large tsunami-borne debris, such as containers, in past tsunami events, and (ii) the good performance of SPH in other coastal engineering applications, the aim of this manuscript is to present a coupled SPH–FEM numerical modeling approach and evaluate its accuracy in simulating both the debris flow and the impact on a coastal structure. Therefore, this paper presents first a detailed explanation of the governing equations and modeling approach. Then, a comprehensive comparison of the coupled SPH–FEM models against experimental data available in the literature [37, 65] is presented in terms of wave propagation and tsunami inland flow, debris motion and impact on a downstream coastal structure. Following the verification phase, a preliminary investigation focusing on the role of the debris restraints, the tsunami characteristics, and the initial water depth is conducted in order to shed light on the underlying physics of the debris–fluid interaction and impact on structures, and identify some critical parameters that govern this complex phenomenon.

2.2. Numerical method

The SPH technique employed in this research is available in LS-DYNA [66] and is based on weakly compressible smoothed particle hydrodynamics (WCSPH). Several numerical investigations of fluid–structure interaction (FSI) were conducted using the SPH formulation in LS-DYNA to study large deformation problems [55, 65, 67]. For example, Pelfrene [55] used the SPH method for the simulation of free-surface water flow with focus on regular and breaking wave, and found that the solver is able to simulate the free-surface flow and capture the main features of the plunging breaking wave. Moreover, Grimaldi et al. [67] and Panciroli et al. [68] used the same method to investigate the impact of a solid body on water and both of them showed a good comparison with experimental results, justifying the selection of this solver for the numerical investigation conducted in the current study.

2.2.1. SPH governing equations

Kernel approximation

In the SPH method, the particles are the computational framework on which the governing equations are resolved. This method is based on a quadrature formula on moving particles. Traditional SPH formulation exhibits very substantial pressure oscillation when modelling fluid flow. Instead of using the traditional computational grid, the conservation laws of continuum mechanics are defined by partial equations. For any SPH pseudo-particle, the function describing the field Ω is approximated in the form of a "kernel function", which is stated as the integral form of the product of any function and kernel function [66, 69]:

$$< f(x) >= \int_{\Omega} f(x')W(x - x', h)dx', \qquad \text{Equation 2.1}$$

where x and x' are the position vectors of the material points in a domain Ω; $f(x)$ is the continuous function of the field corresponding to the coordinate x; $f(x')$ is the value of quantity at the point x'; $W(x-x',h)$ is the bell-shaped smooth kernel function, where h is the smoothing length, defining the influence volume of the smooth function which varies in time and in space.

The smoothing function determines the range of computation with other particles and therefore has a significant effect on precision and accuracy of the analyses. The kernel function can be constructed taking in account a number of conditions and should satisfy the following properties [49]:

The smoothing function is normalized:

$$\int_{\Omega} W(x-x',h)dx' = 1, \qquad \text{Equation 2.2}$$

There is a compact support for the smoothing function:

$$W(x-x',h) = 0, for\ |x-x'| > \kappa h, \qquad \text{Equation 2.3}$$

where κ is the constant that determines the effective area of the smoothing function. This area is called the support domain.

$W(x-x',h)$ is non-negative for any x' within the support domain. This is necessary to achieve physically meaningful results in hydrodynamic computations.

The smoothing length increases as particles separate and reduces as the concentration increases.

With the smoothing length approaching zero, the kernel approaches the Dirac delta function:

$$\lim_{h\to 0} W(x-x',h) = \partial(x-x'), \qquad \text{Equation 2.4}$$

The smoothing function should be an even function.

The forms of kernel functions usually include a quantic spline function [70], a cubic spline function [71] and a Gaussian kernel function [72]. By balancing the calculation accuracy and efficiency and considering that the commercial software LS-DYNA was used for the simulations throughout this study, the following B-spline smoothing function was adopted [66]:

$$W(x,h) = \frac{1}{h(x)^d}\theta(x), \qquad \text{Equation 2.5}$$

where *d* is the number of space dimensions (2 or 3) and $\theta(x)$ is the cubic B-spline function defined by:

$$\theta(x) = \begin{cases} 1 - \frac{3}{2}{x_{ij}}^2 + \frac{3}{4}{x_{ij}}^3 & for\ x_{ij} \le 1 \\ C * \frac{1}{4}(2 - x_{ij})^3 & for\ 1 < x_{ij} \le 2 \\ 0 & for\ \ 2 < x_{ij} \end{cases} \qquad \text{Equation 2.6}$$

where *C* is a constant for normalization, depending on the number of space dimensions and x_{ij} is the relative distance of particles *i* and *j*.

Particle approximation

The second key aspect in SPH formulations is the particle approximation, which enables the system to be represented by a finite number of particles that carry an individual mass and occupy an individual space. For the SPH method, Equation (1) can be transformed into discretized forms by summing up the values of the field function within the support domain defined by the smoothing length h as follows [69]:

$$< f(x_i) >= \sum_{j=1}^{n} \frac{m_j}{\rho_j} f(x_i)\, W(x_i - x_j, h) = \sum_{j=1}^{n} \frac{m_j}{\rho_j} f(x_j)\, W_{ij},$$ Equation 2.7

where $< f(x_i) >$ is the kernel approximation operator; $f(x_j)$ is the physical value at the jth position, i is the number of any particle in the domain; n is the total number of particles within the influence area of the particle i; and m_j and ρ_j are the mass and density associated with particle *j*. Thus, the value of particle i is approximated using the weighted average of the function values at all particles within the support domain of particle j. The partial approximation of the spatial derivation of a function can be expressed as in Das and Holm [73]:

$$< \nabla . f(x_i) >= \sum_{j=1}^{n} \frac{m_j}{\rho_j} f(x_i) . \nabla W_{ij},$$ Equation 2.8

where

$$\nabla W_{ij} = \frac{x_i - x_j}{r_{ij}} \frac{\partial W_{ij}}{\partial r_{ij}}$$ Equation 2.9

2.2.2. SPH for viscous fluid

The smoothing kernel and particle approximation can be used for discretization of partial differential equations (PDEs). The SPH formulation is derived by discretizing the Navier–Stokes equations spatially, thus leading to a set of ODEs which can be solved via time integration. Substituting the SPH approximations for a function and its derivative to the partial differential equations governing the physics of fluid flows, the discretization of these governing equations can be written as follows [74]:

$$\frac{d\rho_i}{dt} = \sum_{j=1}^{n} m_j \ (x_i^\beta - x_j^\beta) \ \frac{\partial W_{ij}}{\partial x_i^\beta},$$

$$\frac{dv_i^\alpha}{dt} = \sum_{j=1}^{n} m_j \ (\frac{\sigma_i^{\alpha\beta}}{\rho_i^2} + \frac{\sigma_j^{\alpha\beta}}{\rho_j^2}) \frac{\partial W_{ij}}{\partial x_i^\beta},$$

$$\frac{dv_i^\alpha}{dt} = \sum_{j=1}^{n} m_j \ (\frac{\sigma_i^{\alpha\beta}}{\rho_i\rho_j}.\frac{\partial W_{ij}}{\partial x_i^\beta} - \frac{\sigma_j^{\alpha\beta}}{\rho_i\rho_j}.\frac{\partial W_{ij}}{\partial x_j^\beta}), \qquad \text{Equation 2.10}$$

$$\frac{dv_i^\alpha}{dt} = \sum_{j=1}^{n} m_j \ (\frac{\sigma_i^{\alpha\beta}}{\rho_i\rho_j}.\frac{\partial W_{ij}}{\partial x_i^\beta} - \frac{\sigma_j^{\alpha\beta}}{\rho_i\rho_j}.\frac{\partial W_{ij}}{\partial x_j^\beta}),$$

$$\frac{dx_i^\alpha}{dt} = v_i + \varepsilon \sum_{j=1}^{n} \frac{m_j}{\rho_j} (v_i - v_j) \ W_{ij},$$

where the superscripts α and β are the coordinate directions; g is the acceleration of gravity; σ is the particle stress; v is the particle velocity; e is the internal energy per unit mass; ε is the shear strain rate ($\varepsilon \cong 0.5$) and Π_{ij} is the Monaghan artificial viscosity [75]. In the analysis of the interaction between waves and structures, Π_{ij} can prevent the non-physical shock of the solution results in the impact area and effectively prevent the non-physical penetration of particles when they are close to each other. The role of artificial viscosity is to smoothen the shock over several particles and to allow the simulation of viscous dissipation, the transformation of kinetic energy to heat. Therefore, to consider the artificial viscosity, an artificial viscous pressure term Π_{ij} is added.

From Equations set 2.10, the following particle body forces can be derived [76]:

$$F_i^{pressure} = -\sum_j \ m_j \frac{p_i + p_j}{2\rho_j} \nabla W(r_{ij}, h) \qquad \text{Equation 2.11}$$

$$F_i^{viscosity} = \mu \sum_j m_j \frac{v_i + v_j}{2\rho_j} \nabla^2 W(r_{ij}, h)$$

where $r_{ij} = x_i - x_j$, and μ is the viscosity coefficient of the fluid. The pressure p_i is computed via the constitutive equation:

$$p_i = K\,(\rho_i - \rho_0)$$ Equation 2.12

where *K* is the stiffness of the fluid and ρ_0 is the initial density.

The acceleration of particle i is derived from:

$$a_i = \frac{1}{\rho_i\,(F_i^{pressure} + F_i^{viscosity} + F_i^{external})}$$ Equation 2.13

where $F_i^{external}$ represents external forces such as body forces and forces due to contacts.

2.2.3. Sorting

In the SPH method, the location of neighboring particles is important. The sorting consists of finding which particles interact with which others at a given time. A bucket sort is used that consists of partitioning the domain into boxes where the sort is performed. With this partitioning, the closest neighbors will reside in the same box or in the nearest boxes. This method reduces the number of distance calculations and therefore the computational time [66].

2.2.4. Equation of state (EOS)

When the SPH method is applied in solving the FSI problems, the fluid is treated as weakly compressible, which means that an equation of state is utilized to determine the dynamic fluid pressure based on the variation in density and internal energy of particles. The equation of state is originally applied to SPH by Monaghan [69] to model free-surface flows for water, which is stated in the following form:

$$P = k_0[(\frac{\rho}{\rho_0})^{\Upsilon} - 1]$$ Equation 2.14

where ρ_0 denotes the reference water density, ρ is the current density, Υ is a constant parameter and often set to 7 for water, and k_0 is used to govern the maximum fluctuations of pressure, and is usually taken as follows [45]:

Equation 2.15

$$c_0 = \sqrt{\frac{\Upsilon k_0}{\rho_0}} \geq 10\ vmax$$

where c_0 is the speed of sound in water at the reference density. In order to satisfy the Courant–Friedrichs–Lewy (CFL) condition, the real speed of sound should be at least 10-fold faster than the maximum fluid velocity. Satisfying this criterion will keep the density variations to within less than 1% and ensure low compressibility while allowing for a relatively large time step size.

2.2.5. Time integration

The CFL condition requires the time step to be proportional to the smallest spatial particle resolution, which in SPH is represented by the smoothing length. LS-DYNA uses a simple and first-order scheme for integration. The time step is calculated by the following expression [66]:

$$\delta t = C_{CFL}\ min_i(\frac{h_i}{c_i + v_i})$$ Equation 2.16

2.2.6. Contact definitions

The interaction between the SPH and FE elements is defined using a penalty-based contact algorithm in which the SPH is always defined to be the slave part and the finite elements are defined to be the master. When a node is in contact with the surface, each slave node is checked for penetration. If the slave node penetrates, a restoring force is applied to prevent further penetration. This magnitude of this force is proportional to the penetration distance into the shell or solid

element and acts in the direction normal to the master surface. The restoring force is defined by [66]:

$$f = kdn \qquad \text{Equation 2.17}$$

where d is the penetration distance, n is the surface normal vector and k is a penalty factor, comparable to a spring constant. The stiffness factor k for master segment s_i is given in terms of the bulk modulus K_i, the volume V_i, and the face area A_i of the element that contains s_i as:

$$k_i = \frac{A_i K_i f_{si}}{max\ (shell\ diagonal)} \qquad \text{Equation 2.18}$$

where f_{si} is a scale factor for the interface stiffness and is normally defaulted to 10. The constant K should be set large enough to minimize penetration and instabilities, but it should not be too large that it generates artificially large forces. As the contact location and the direction may be difficult to predict, the automatic contacts are recommended, since they can detect the penetration at each time step, irrespective of whether it is coming from the slave or master part. The automatic contacts determine the contact surface by projecting normally from the shell mid-plane to a distance equal to half of the contact thickness. It must be noted that the solver can simulate the contact between flexible structures, rigid and flexible structures, or between rigid bodies only. Interestingly, even in the case of rigid bodies where the deformations are not calculated, it is possible to define a bulk modulus at the material level, which enables the user to adjust the contact parameters (e.g., contact stiffness) and avoid numerical spikes in the contact forces.

2.3. Experimental work

The experimental study described in Ko and Cox [65], and Ko [37] was adopted for benchmarking the numerical SPH-FE modeling approach. These experiments had been conducted in the Large Wave Flume (LWF) at O.H. Hinsdale Wave Research Laboratory (HWRL) at Oregon State

University. The flume is 104.24 m in length, 3.66 m in width, and 4.57 m in depth, and is shown in Figure 2-1. The LWF is equipped with a piston-type dry-back wavemaker that has a 4 m maximum hydraulic stroke actuator and a maximum speed of 4 m/s, which can generate both regular and random waves, as well as solitary waves, to simulate hurricane and tsunami waves. The LWF has adjustable bathymetry made of 20 square configurable concrete slabs. The flume includes a series of bolted holes with vertical patterns every 3.66 m along the flume for supporting test specimens, as well as, the concrete bathymetry slabs.

The coastal structure was represented by a column assembly located between bays 17 and 18, and was equipped with a load cell to measure the debris impact force. An aluminum 1:5 scale model of the standard intermodal container was used as the debris specimen. Given the fact that a standard container has dimensions of 6.1 m in length, 2.44 m in width, and 2.9 m in height, at 1:5 scale, the model had dimensions of 1.22 m × 0.49 m × 0.58 m, while the draft of the empty container was 9.1 cm. The longitudinal orientation is defined so that the major axis of the debris is parallel to the x axis and the direction of tsunami propagation. The debris specimen is located 3.5 m away from the column in the x direction. In order to control the movement of the debris and maintain the debris' orientation, guide wires had been installed in the LWF between bays 15 and 18. The debris specimen was allowed to move freely in the x and z directions, i.e., horizontal and vertical directions, but it was restrained in the y direction, which means that there was no translation across the flume width and no yaw.

To measure the free-surface time history and fluid velocity in the x direction, several resistance and ultrasonic wave gages, and acoustic doppler velocimeter (ADV) had been installed along the flume. The error function method proposed by Thomas and Cox [77] was used to generate the wave paddle displacement in the aforementioned experiments. To maximize the volume and duration of the

tsunami inundation process, the full 4 m stroke of the wave maker had been used. The time for the wave paddle to travel the full 4 m stroke, i.e., error function period, is denoted as $T_{erf.}$

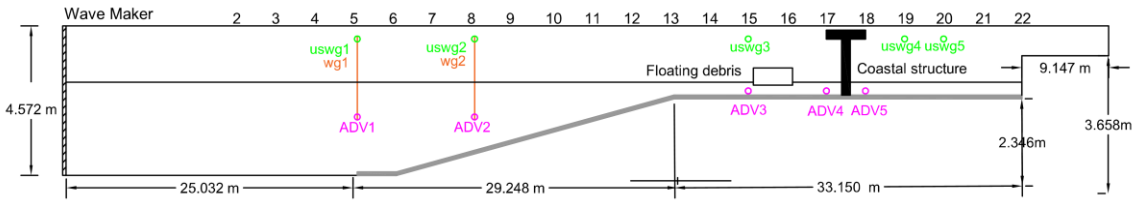

Figure 2-1 Cross-section of the Large Wave Flume (LWF) depicting the bathymetry, column location and flume instrumentation of the experiments of Ko and Cox [65] used for the validation study

2.4. Coupled SPH-FEM modeling

2.4.1. Numerical settings

A numerical model of the experimental setup was developed using particles (SPH) for the fluid, and finite elements (FEM) for the flume walls, the debris specimen and the column. The bathymetry and experimental setup shown in Figure 1 was simulated via a two-dimensional model that represented a slice crossing through the mid-width of the flume, and cutting the debris and the column in two equal halves. This assumption was possible due to the debris restraints used in the experiments, which eliminated the movement of the debris across the flume width (normal to the tsunami flow). In this model, the wavemaker was represented with rigid shell elements with a prescribed horizontal motion equal to the input wavemaker displacements of the experiments found in Ko and Cox [65].

The influence of different SPH particle sizes on the computational time and numerical results was investigated by comparing sizes of 1, 2 and 3 cm, as shown in Appendix A. Decreasing the initial particle size improves the accuracy of the numerical results; however, too small sizes could cause numerical instability [78]. Considering the computational time, numerical accuracy, and calculation efficiency, the particle size of 1 cm was selected in the final numerical models presented herein. The debris and the column were generated using shell elements that had the same size with

the fluid particles (1 cm), as shown in Figure 2-2. The final 2D numerical model consisted of 14,571 shell elements and 1,193,075 SPH particles. Given the fact that no significant deformations of the debris were observed in the selected experimental results [65] during the debris–flow interaction and impact on the structure, the debris was simulated as a rigid body. In the case of a 'rigid' assumption the properties of the rigid shell elements are not considered in the calculation of the time step of the explicit analyses, meaning that the time step is determined only by the remaining elements and particles. This in turn allows the explicit solver to use a significantly larger time step and reduce the required computational time per analysis.

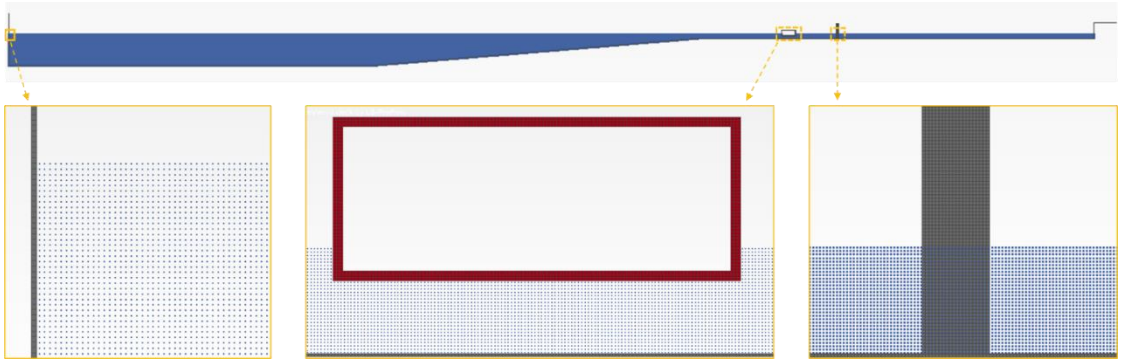

Figure 2-2 Numerical models with large debris: side-views of the debris, the column and the wave maker

Given the 2D nature of the numerical model, several additional calculations and assumptions had to be made in order to ensure compatibility with the actual experiments. First, the 2D geometries of the container and the column were simulated (see Figure 2). However, since the sides of the container were not simulated in the 2D model, its thickness and density were adjusted in order to simultaneously satisfy the required draft of 9.1 cm and exhibit a rotational inertia that was equivalent to the one of the experimental specimens. Then, by assuming that the ratio of the debris' mass to the column's mass is identical in both the numerical and experimental models, the density of the column was determined accordingly. With the beneficial effect of the 'rigid' assumption in mind (in terms of computational time), and the expected small effect of the steel column deformation on the overall phenomenon (e.g., fluid flow around the column and the debris–fluid–

column interaction), the column was assumed to be rigid as well. Despite this assumption, since the objective of this paper was to investigate the accuracy of predicting the impact forces, the contact stiffness was reasonably calculated by the solver via the bulk modulus (defined at the material level) and Equation (18) to avoid artificially high numerical spikes generated by a rigid-to-rigid body contact.

Key parts in the development of the numerical models included the definitions of the SPH–FEM and FEM–FEM contacts interfaces. In fact, different contact algorithms were employed to define the interaction (i) between the fluid (SPH) and the flume wall, the wavemaker and the debris specimen (FE), and (ii) between the debris and the column. The interaction between the FE and the SPH particles was defined in the numerical simulation via the *CONTACT_2D_NODES_TO_SOLID contact card, with the master-slave penalty algorithm, in which the shell elements were assigned the role of the master part and the SPH particles the slave part. Moreover, the contact between the floating debris and the column was determined via the *2D_AUTOMATIC_SURFACE_TO_ SURFACE contact type, which is a segment-based two-way contact. Such segment-based contacts are preferred over node-based contacts, since the penetration can be easily traced even if it happens at locations far from existing nodal locations, and consequently tend to be more accurate but computationally more expensive. It must be noted that the contact between the fluid and the column was not simulated in the 2D model because it would generate a reflection of the bore when it reached the structure, which is not realistic given the fact that in the actual experiments the bore can escape from the sides of the column.

Despite the speed-up of the numerical analyses due to the aforementioned assumptions, it was not feasible to run the 2D model on a regular desktop and therefore all the computational analyses were run on the high-performance computing (HPC) cluster at the University of Nevada, Reno, using up

to 80 cores per analysis. The analysis time ranged between 15 and 21 h depending on the hydrodynamic characteristics (i.e., water depth), which affected the total number of SPH particles.

2.4.2. Accuracy of numerical modeling

Free surface and fluid velocities

In order to quantify the accuracy of the numerical model, the results of the free-surface and fluid velocity histories at two different distances from the wavemaker, were compared with those measured in Ko and Cox [65]. Wave gage 1 (wg1) and adv1 are the closest to the wavemaker and are located at the end of the first horizontal part, with x = 24.930 m for both instruments and z = 1.240 m for the adv. In addition to this location where the wave has propagated only over a horizontal slab, the numerical results are also compared with the experimental results at x = 35.890 m (see wg2 and adv2), which is located along the sloped part. The z coordinate of adv2 is 1.236 m. Figure 2-3 shows the variation of free-surface at (a) wg1 and (b) wg2 and fluid velocity at (c) adv1 and (d) adv2 for all trials of the experimental tests with parameters of h_1 = 2.496 m and h_2 = 0.13 m, and T_{erf} = 30 s from [65], where h_1 and h_2 corresponds to the initial water depth offshore (at wavemaker location) and on the coast close to the debris, respectively. It can be observed that both the free-surface and fluid velocity histories computed by the numerical model are in good agreement with the experimental data, both in terms of the peak values and temporal evolution. There are some underpredictions of the maximum wave height and some overpredictions of the velocity but those do not exceed 6% for the selected wave. In addition to this good agreement, the encouraging thing is that the numerical model can predict the relative increase between wg2 and wg1 of the maximum free surface, indicating that the SPH–FEM coupled approach can capture the interaction of the fluid with the sloped part of the flume and result in a similar non-linear transformation of the wave during the shoaling process.

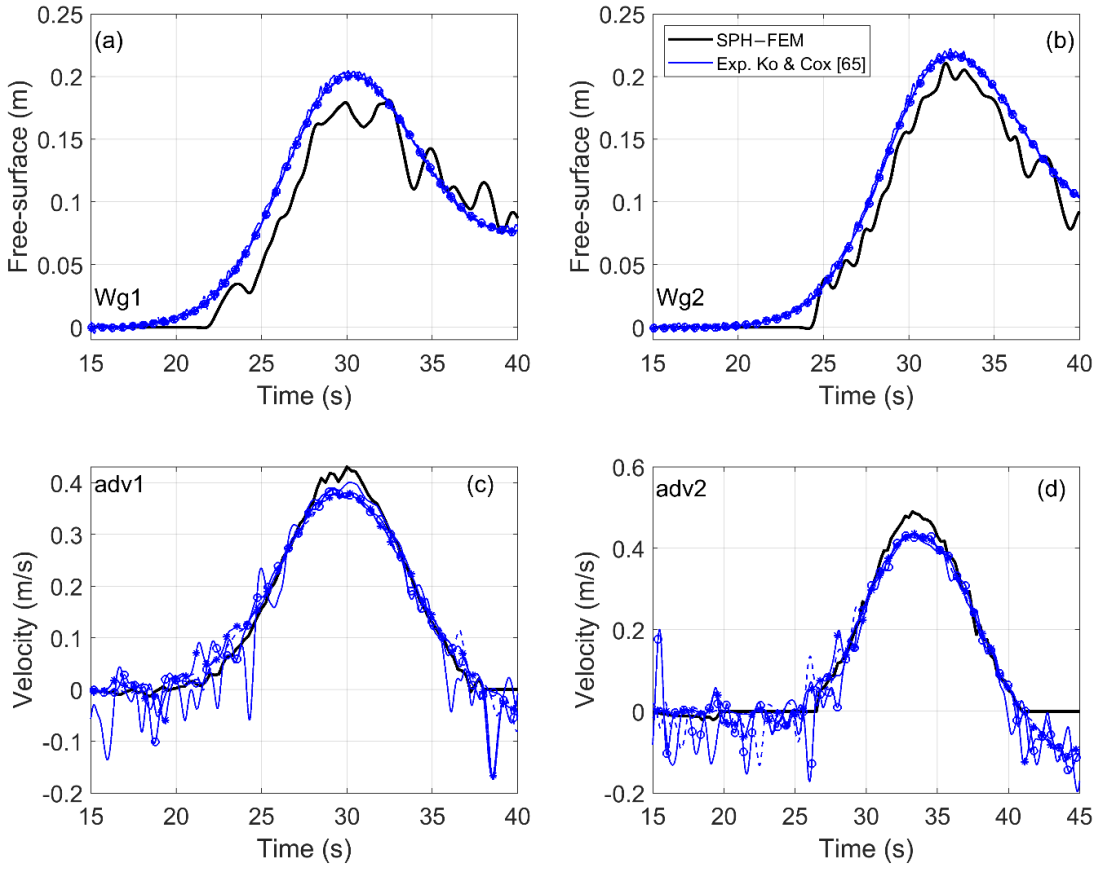

Figure 2-3 Variation of the free surface and fluid velocity at different locations along the flume. Experimental [65] and numerical results for h1 = 2.496 m and Terf = 30 s

Figure 2-4 shows a comparison of the numerically predicted maximum values of the free surface at the locations (a) wg1 and (b) wg2 with the experimental data for all the tested tsunami waves (T_{erf} = 30 s, 40 s, 45 s) for h_1 = 2.496 m and h_2 = 0.13 m. Promising agreement with the experimental was achieved, with the maximum deviation from the average value of the measured data at wg1 being 6.3%, 11.7%, and 13.7% for T_{erf} = 30, 40 and 45 s, respectively. At wg2, the maximum differences are 4%, 15.9%, and 15.2%. As expected, both the numerical and experimental data show that the shorter $T_{erf,}$ i.e., T_{erf} = 30 s gives greater inundation depths at the two locations. This also seems to be true for the peak velocities, especially those measured at adv2, as shown in Figure 2-5. The latter figure presents the experimentally and numerically recorded maximum velocities at

the (a) adv 1 and (b) adv2 for the same hydrodynamic conditions as in Figure 2-4 (h_1 = 2.496 m). Similarly, to the free surfaces, the SPH–FEM approach can predict reasonably the maximum fluid velocities with maximum deviations of 3%, 4.7%, and 2% at adv1 for the three different tsunami bores (T_{erf} = 30, 40, and 45 s), respectively. At adv2, the maximum differences are 6%, 14%, and 22%, respectively. It is noteworthy that (i) the experimentally recorded peak fluid velocities in Ko and Cox [65] had significantly larger variability than the measurements of the free surface, and (ii) the most sensitive experimental results corresponded to the measured velocities of the slower flows (e.g., for T_{erf} = 45 s), for which the numerical modeling yielded the largest deviations (underprediction of approximately 25%).

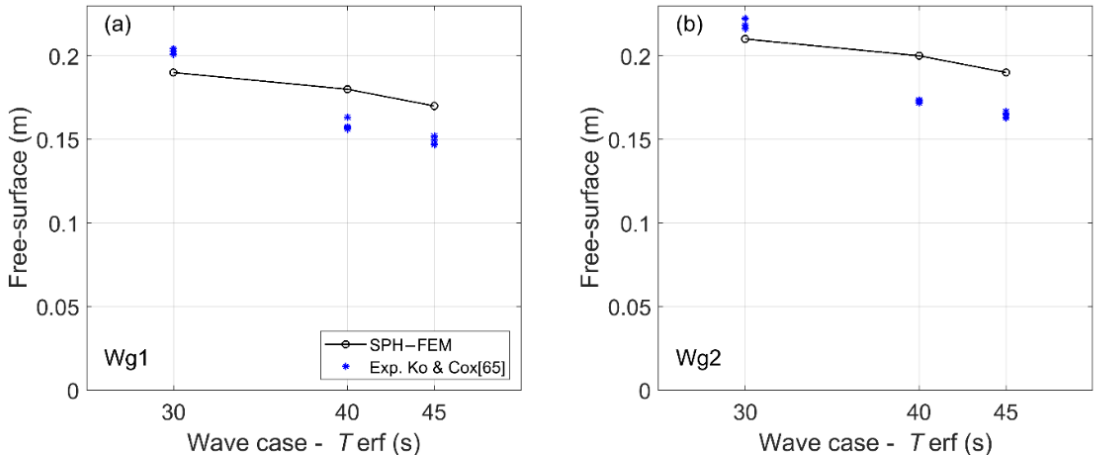

Figure 2-4 Maximum free-surface values of experiments [65] and numerical simulations for h1 = 2.496 m, and three wave cases with Terf = 30, 40 and 45 s

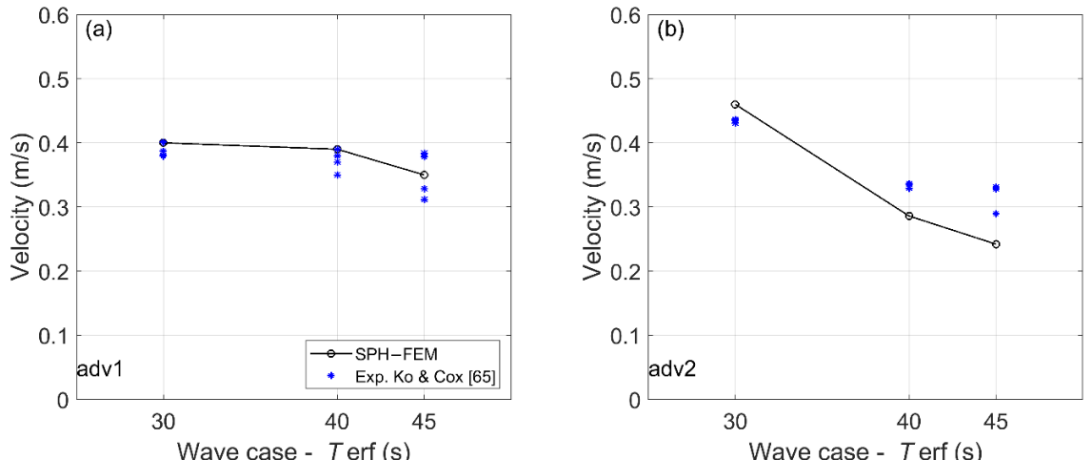

Figure 2-5 Maximum fluid velocities of experimental tests [65] and numerical simulations for h1 = 2.496 m, and three wave cases with Terf = 30, 40, and 45 s

Debris motion

Although the reasonable predictions of the free surface and fluid velocities achieved by the numerical simulations increase the confidence in the SPH solver and the coupled SPH–FEM approach, one of the most critical aspect for future risk assessment studies is the ability to estimate the debris transport and propagation overland. To this end, Figure 6 shows the velocity history of the debris specimen for one of the hydrodynamic conditions with h_2 = 0.13 m and T_{erf} = 30 s. The debris velocity was generated based on the publicly available videos on DesignSafe (i.e., Ko and Cox [65]), using a color-based tracking algorithm. However, it must be noted that the estimated velocities (from the videos of the experiments) could potentially entail some errors due to the fact that the ceiling cameras could not be perpendicular to the top surface of the debris for the whole propagation process (from its initial position up to the coastal structure). A more accurate estimate would require a perspective correction, as in Ko [37], which was not done herein due to the lack of adequate information.

Since the debris specimen was modeled as a solid body, in order to evaluate the accuracy of the debris velocity from the SPH–FEM simulation, the velocity was output at four nodes of the debris,

which corresponded to the external corners. Figure 2-6 presents the nodal velocities at the lower right and left corner together with the experimental velocity and a reasonable agreement is observed. The numerical and experimental simulations seem to give similar debris velocities when the bore reaches the container and starts transporting it. However, as the debris propagation continues, the numerical model seems to accelerate more and reach a larger velocity than the experimental specimen before the impact on the column. This in turn causes the numerical model of the container to cross the 3.5 m (initial distance between debris-column) faster and impact the column earlier than the experiment.

One of the possible explanations for the observed differences lies in the 2D formulation of the current numerical model, which implies that the pressures applied from the bore on the offshore face of the debris (i.e., the mechanism causing the debris movement) are uniform across the debris width. However, in the actual experiments the pressures on the offshore face of the debris (and below its bottom side) are expected to be smaller at locations close to the sidewalls than the mid-width due to 3D effects. In other words, some of the bore pressures on the debris are relieved close to the vertical sides of the debris since the bore can propagate along these sides, given that there is a large area between the flume walls and the debris. Moreover, it must be clarified than in the presented numerical results the debris was restrained to move only in the horizontal direction, i.e., the direction of the bore propagation, eliminating any pitching that could potentially attenuate the debris transport.

The decision to restrain the debris was made based on the findings of Ko [37], who stated that there was significant variability in the experimentally recorded impact forces due to: (i) the “off-centered” impact of the debris on the load cell, and (ii) the effect of the pitch angle that was present in some trials but not in others. For example, it can be estimated from the figures of Ko and Cox [65] that for a debris velocity of approximately 1.4–1.5 m/s the ‘off-centered” impact can give

maximum impact forces that are reduced by approximately 40% relative to the centered case. This explains why in the aforementioned study was decided to consider only the centered experimental results, and why in the present numerical investigation the debris was not allowed to pitch during the validation phase.

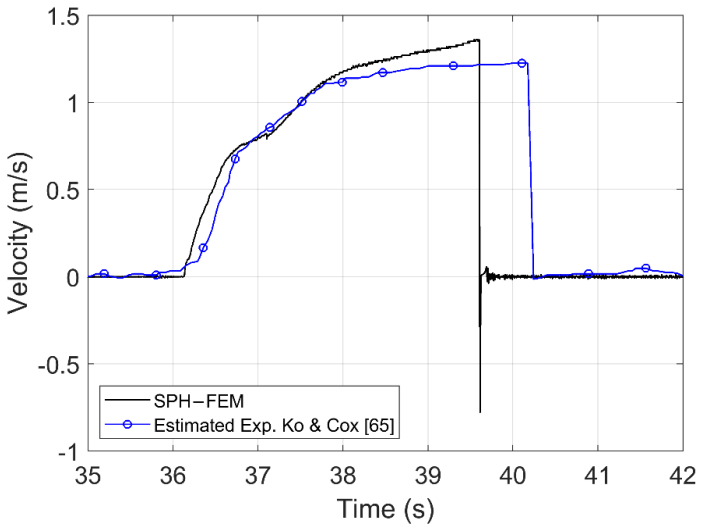

Figure 2-6 Debris velocity histories: Estimated based on the experimental tests of [65] and results from the numerical simulations for h1 = 2.496 m, Terf = 30 s

Debris impact force

Figure 2-7 shows the time histories of the debris impact forces on the column for two selected hydrodynamic conditions, with T_{erf} = 30 s and T_{erf} = 45 s for the same initial water depth $h2$ = 0.13 m. Subfigures (a) and (b) correspond to the T_{erf} = 30 s for numerical and experimental data, respectively, and subfigures (c) and (d) show the results of T_{erf} = 45 s from numerical and experimental analyses, respectively. The agreement between the computations and the different trials of the physical tests is reasonable, both in terms of the peak impact force and in the overall trends. For instance, for the case of T_{erf} = 30 s, the SPH–FEM models predict a relatively higher impact force than the experiments by approximately 15%. However, this can be explained by the fact that as shown in Figure 6 the numerically predicted impact velocity was approximately 20%

higher than the experimental one. Given the fact that the majority of the available simplified equations for debris impact loads, such as those presented in FEMA P646 [3] and ASCE [79], are a linear function of the impact velocity, it is reasonable to obtain larger impact forces from the numerical simulations since they predict larger velocities. Apart from the similarities in the results, there are also two noticeable differences:

In the numerical simulations, the impact force on the column is applied earlier for T_{erf} = 30 s and later for T_{erf} = 45s compared to the physical tests. However, these differences in the instants could be justified by the differences in the debris velocities, which were most likely overpredicted and underpredicted, respectively, as indicated by the trends in the maximum values. In other words, it is reasonable for the debris impact to occur earlier when the numerical models overpredict the magnitude of the impact, because the reason is the larger debris velocity.

Immediately after the primary impact force, the column in the physical tests experienced a second short-duration impact force, which is relatively small compared to the main impact. However, this trend was not observed in the numerical results. In contrast, the simulations show a long duration load after the initial impact, which seems to have a nearly constant magnitude. This difference can be attributed again to the 2D simplification made in the numerical models, which are unable to allow the fluid to escape from the sides of the debris after the initial impact on the column and relieve the pressures applied on its offshore face. This leads consequently to the stagnation of the flow in front of the offshore face, resulting in a nearly steady-state horizontal damming load.

The trends of the peak values of the impact forces observed in the previous figure are also verified in Figure 2-8, which plots the corresponding maximum values from the experiments and the computational models for all three hydrodynamic flows (T_{erf} = 30, 40, and 45 s) with h_1 = 2.496 m and h_2 = 0.13 m. In fact, this figure reveals that the maximum deviation from the measured values

is 14%, 25%, and 19% for the three flows, respectively, which is promising given the differences in the debris velocities. Moreover, another observation that reinforces the confidence in the SPH–FEM modeling approach is that it presents similar trends with the physical tests (as a function of $T_{erf,}$) since both of them give larger debris velocities and impact forces for the smallest T_{erf} = 30 s representing the more transient flow with the largest fluid velocities.

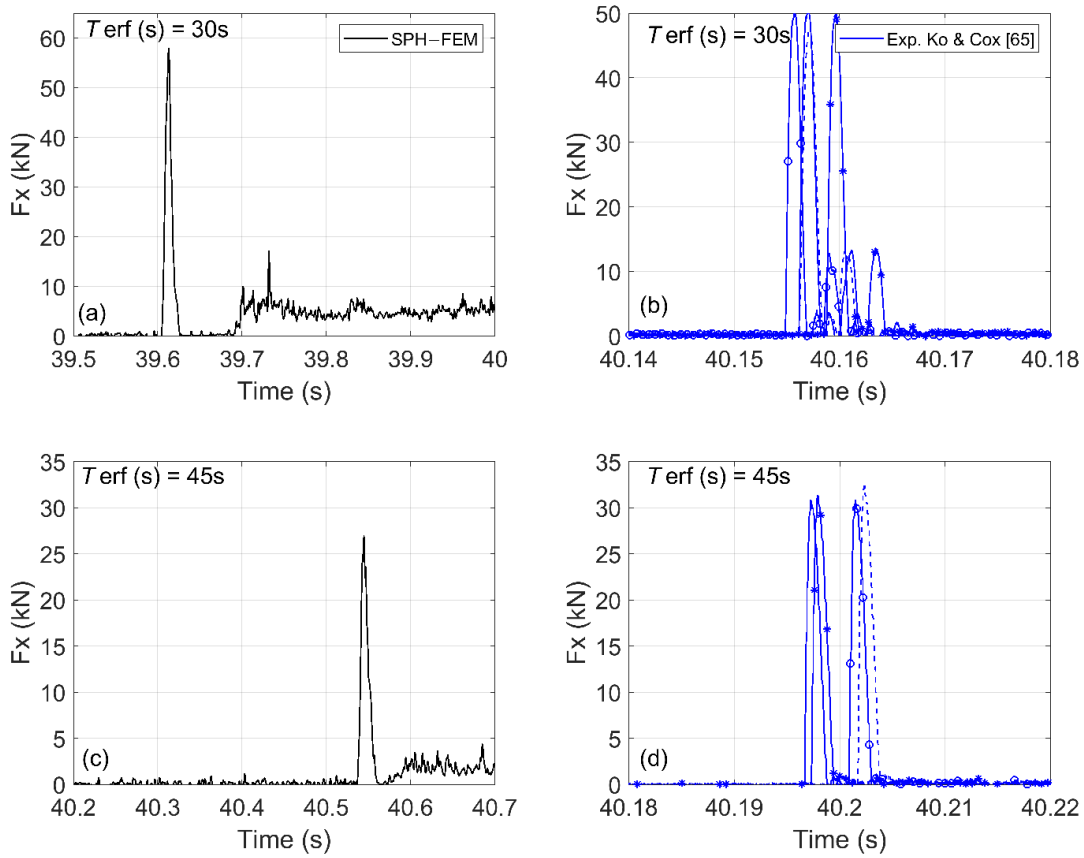

Figure 2-7 Comparison of the debris impact forces: experimental tests [65] and numerical simulations for h1 = 2.496 m, and two wave cases with Terf = 30 s and 45 s

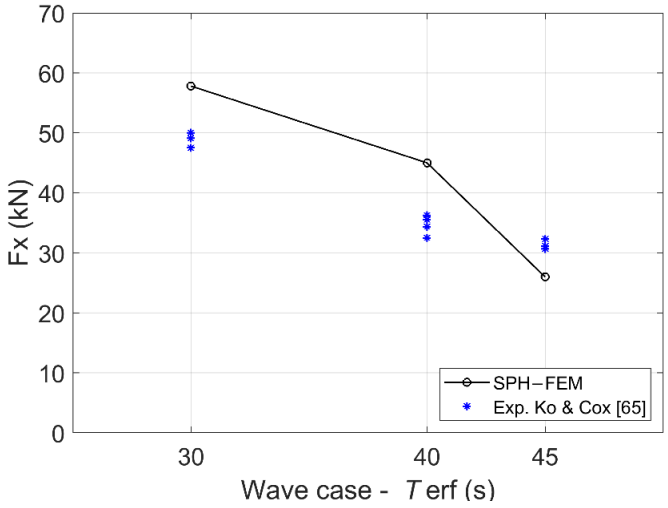

Figure 2-8 Maximum values of debris impact force on column: experimental tests [65] and numerical simulation for h1 = 2.496 m, and three wave cases with Terf = 30, 40, and 45 s

2.5. Role of debris restraints

Given the fact that in the validation section the debris was restrained in order to make it more consistent with the experiments, it is essential to assess the role of the restraint for the debris–wave interaction, the debris transport overland and the impact on the structure. To this end, the restrained model of the previous section was compared with another model that allowed the debris to move freely in the 2D plane (horizontal and vertical displacement, and pitching). Figure 2-9 presents several selected snapshots of the tsunami flow with T_{erf} = 30 s for h_2 = 0.13 m as the free debris propagates towards the column location, from the instant that the bore starts moving the debris up to the instant of the second impact. Among these snapshots, ‘e’, ‘f’, ‘g’ corresponds to following instants: (i) slightly before the first impact on the column, (ii) after the 1st impact, and (iii) at the instant of the 2nd impact on the column, respectively. As shown, the debris starts pitching in the clockwise direction up to the point that the onshore bottom corner tends to touch the bottom of the flume, after which it immediately changes the direction of pitching. It is also revealed that the large counter-clockwise pitching continues until the debris reaches the column location, which results in a non-normal impact angle and a consequently non-uniform contact of the onshore vertical face of

the debris with the column, affecting the contact area and consequently the maximum impact forces. After the initial impact, the debris bounces back and re-impacts the column with a clockwise pitching angle, which generates a smaller magnitude impulse.

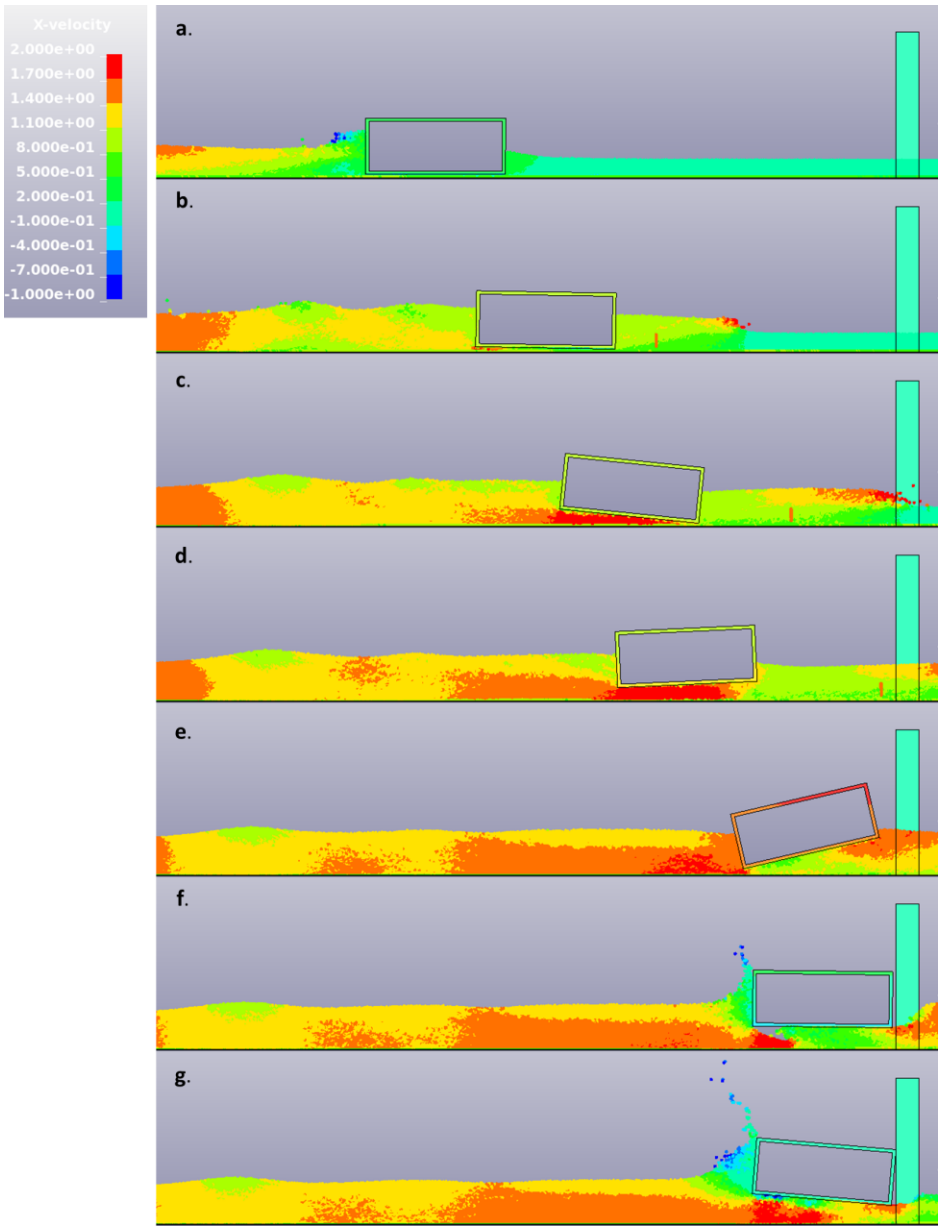

Figure 2-9 Selected instants of the debris−wave interaction and impact on the column of the free debris. Numerical results for the hydrodynamic case with h1 = 2.496 m, h2 = 0.13 m and Terf = 30 s

Figure 2-10 presents a quantitative comparison between the debris motion of the two cases. In the case of the free debris four locations are selected for presentation, including, the lower left corner

(C1), the lower right corner (C2), the upper right corner (C3), and the upper left corner (C4). The x-displacement vs. y displacement curves for the free movement debris reveals that the two lower corners move in the opposite y direction as the debris moves along the x direction. A similar motion trend is observed for the two upper corners as well. The opposite movement in the y direction indicates the initiation of the debris rotation. To evaluate the level of the pitching, the rotation angle of the debris is calculated using the corner displacements and is presented on the right subplot of Figure 2-10. Based on this figure it becomes evident that the debris starts rotating clockwise after the bore reaches its location (negative rotation), then as it transports inland it changes the direction of rotation until it reaches the maximum rotation of approximately 37° slightly before the primary impact on the column, and then rotates in the opposite direction as it interacts with the column, until it stabilizes at a zero angle and the long duration damming process is initiated.

The debris velocity and impact forces histories for the free and restrained container models are presented in Figure 2-11. Interestingly, although it was expected the peak impact velocity to be affected by the pitching, the expectation was that the free debris would exhibit a more significant wave–structure interaction (due to the larger vertical displacements and rotation), which would dissipate more of the energy of the bore leading to a smaller horizontal debris velocity and a delayed arrival at the column location. While the delayed arrival did happen as expected and the debris velocity was indeed smaller than the respective velocity of the restrained model, this was true only at some instants during the debris transport inland and not at the instant of the impact on the column. The impact velocity of the free debris was surprisingly larger than the restrained one, which highlights the complexity and non-linearity of the debris interaction with the turbulent flow.

Another interesting finding can be reached from the subplot of the impact forces, according to which, the column experiences a significantly larger impact force from the restrained debris than the free case, although the latter one impacts the column with a larger velocity. The debris restraint seems to increase the maximum impact force by approximately a factor of 2.3 relative to the free case and reach the experimentally recorded values. The above trend could be attributed to the presence of debris pitching that affects the impact angle on the column, since as was observed in the swinging in-air tests of Ko [37] the cases with a zero-pitch angle tended to give larger impact forces than the larger pitch angles, even when the debris impact velocities were the same.

The above finding indicates that future predictive equations might have to be a function of not only the impact velocity but also the impact angle, while design methodologies and risk assessment frameworks should be able to predict these two parameters. Ideally, the location of the impact on the coastal structure should also be estimated since the structural damage caused by the container could be very localized (close to the point of contact) if the debris impacts a coastal structure with a non-normal pitching angle.

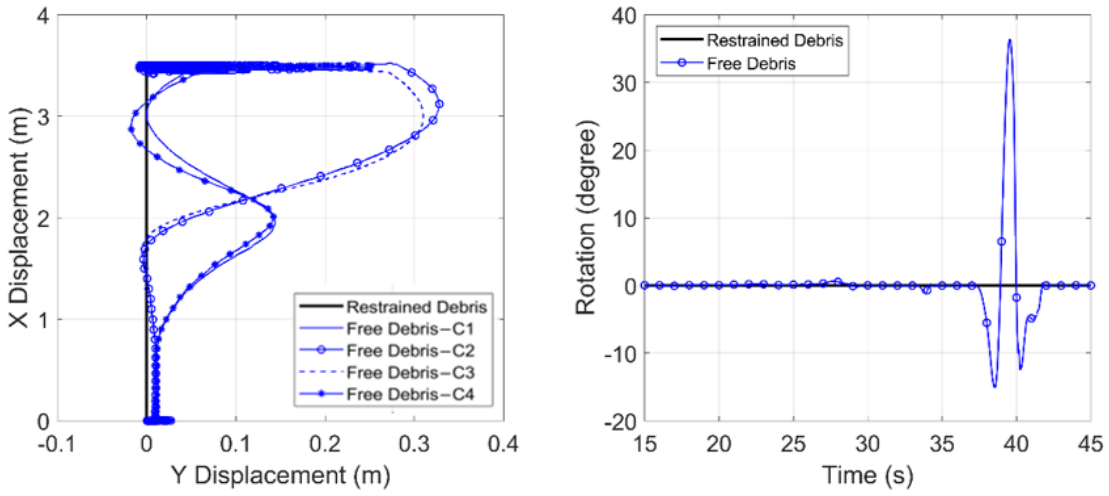

Figure 2-10 Debris trajectory (left) and rotation (right) for the restrained debris and free debris. Numerical results for the hydro-dynamic case with h1 = 2.496 m, and h2 = 0.13 m and Terf = 30 s

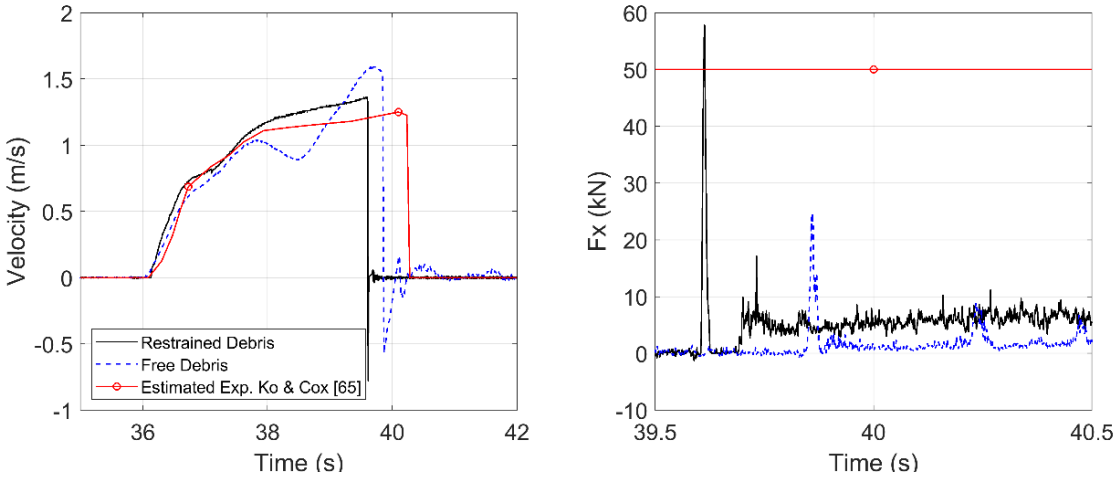

Figure 2-11 Debris velocity (left) and forces on the column (right). Experimental and numerical results (of restrained and free de-bris) for the hydrodynamic case h1 = 2.496 m and Terf = 30 s

2.6. Effect of hydrodynamic conditions on debris movement and impact forces

2.6.1. Tsunami flow characteristics

To gain further insight into the debris–flow interaction and impact on coastal structures, this section will evaluate the effects of the flow characteristics by considering the three different cases with T_{erf} = 30 s, T_{erf} = 40 s, and T_{erf} = 45 s for h_1 = 2.496 m and h_2 = 0.13 m tested in [37]. In this section, the debris will be considered free in the 2D plane since it is considered more realistic, despite the fact that the restrained model captured better the experimental data. Comparison of the free surface and fluid velocity at a location close to the container, i.e., x = 62 m, is depicted in Figure 2-12. As discussed in [37], the error function (T_{erf}) affects the wave characteristics, and particularly the wave height and fluid velocity. The new figure shows that although there are similarities in the free-surface histories for all three waves, the smallest T_{erf} (which corresponds to the faster movement of the wavemaker) exhibits the largest peak values for the free surface and the fluid velocity, with the most noticeable differences observed in the fluid velocities. Interestingly, as the T_{erf} increases the flow height and fluid velocity is reducing, while the duration of the inundation is elongated, which indicates that the flow is switching from a highly transient bore to a more steady-state flow.

Figure 2-13 presents two selected snapshots of the debris–fluid interaction as the container propagates inland for two selected tsunami waves with T_{erf} = 30 s, and T_{erf} = 45 s, respectively. While both waves present similar trends in the debris motion, which comprises of a clockwise rotation followed by a counter-clockwise one, the faster moving bore results in larger particle velocities around the debris that in turn cause larger pitching of the container. This would indicate that the pitching of the debris is mainly caused by the larger velocities, and not that much by the differences in the free surface, which are much smaller. Figure 2-14 plots the vertical movement of the lower-right corner of the container and its rotation throughout the propagation inland. This figure illustrates that the debris flow is indeed highly dependent on the tsunami characteristics and that the fastest bore (T_{erf} = 30 s) can cause pitching angles that are approximately 85% larger than those of the slowest wave (T_{erf} = 45 s). This larger rotation leads to an increase in the upward vertical movement of the offshore face of the container, which enables it to impact structural locations at higher elevations.

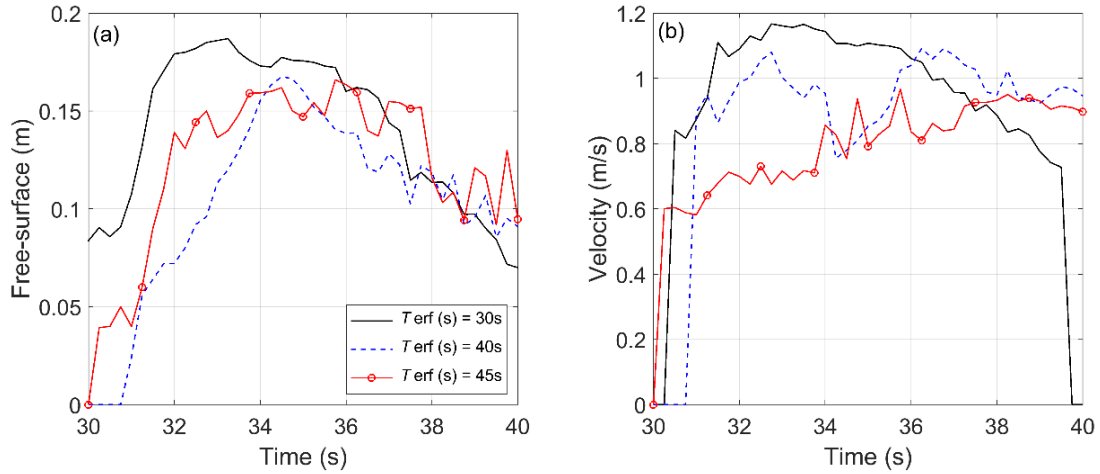

Figure 2-12 Variation of free surface (left) and fluid velocity (right)at x = 62 m: Numerical results for h1 = 2.496 m and three wave cases with Terf = 30, 40, and 45 s

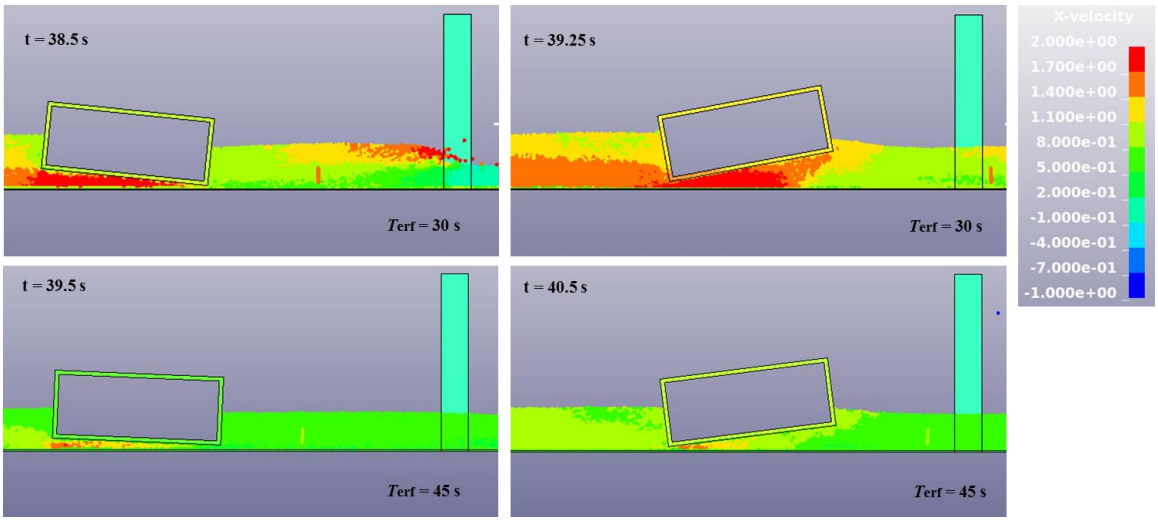

Figure 2-13 Snapshots of debris−-tsunami interaction and impact on the column. Numerical results for h1 = 2.496 m and two wave cases with Terf = 30 s (top) and 45 s (bottom)

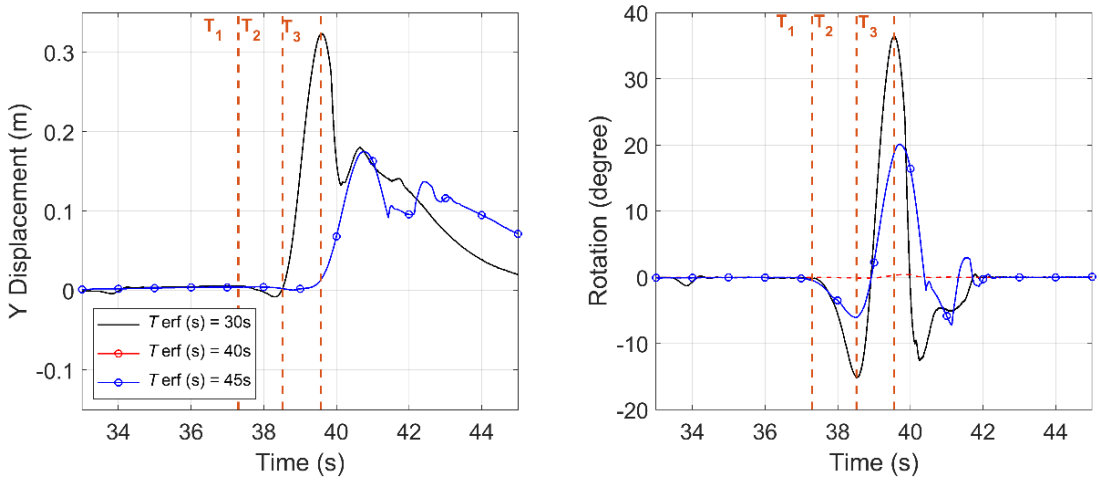

Figure 2-14 Numerical results of the free debris: vertical displacement (left) and rotation (right), for h1 = 2.496 m and three wave cases with Terf = 30, 40, and 45 s

Combining the trends of the previous figures and snapshots, it is possible to identify three characteristic time instants in the motion of the debris for the case of T_{erf} = 30 s, as shown below:

- T1: This time instant represents the initiation of the debris rotation. It occurs slightly after the tsunami has started pushing the debris inland. After that initial contact with the bore, the debris starts accelerating and as the flow below the debris increases and the bore front

surpasses the debris, the latter one starts rotating clockwise (see also snapshots b. and c. in Figure 2-10).

- T2: This instant corresponds to the largest clockwise rotation, at which point the lower right (onshore) corner has displaced downward so much that it impacts the floor of the flume. When this impact takes place, a restoring force is applied to the debris causing it to start rotating in the opposite direction (counter-clockwise).

- T3: After the primary debris impact on the flume floor and the initiation of the counter-clockwise rotation, the debris continues rotating in this direction until it reaches the maximum pitch angle, which tends to occur slightly before the primary debris impact on the column. At this instant, it is possible for the lower left (offshore) corner of the debris to touch the floor of the flume before it impacts the column. However, this will depend on the initial relative distance between the debris and the coastal structure, as well as, the hydrodynamic conditions. This means that instant T3 represents the maximum clockwise pitching angle, which might be close to the impact angle, but not necessarily the same. Future studies should investigate different debris–structure relative distances, and a larger range of hydrodynamic conditions in order to determine the dependence of the maximum pitching angle and the impact angle on these parameters. Ideally, such studies should employ three-dimensional models, which are expected to be more accurate than two-dimensional models.

The debris impact forces on the column, including both time histories and the peak value versus the impact velocity, are presented in Figure 2-15 for all the tsunami waves of h_2 = 0.13 m. As expected, larger tsunami waves have more energy and higher particle velocities, which lead to higher values of the debris impact velocities and impulsive forces on the column. This is why the

wave with T_{erf} = 30 s exerts the largest impact force on the column. Interestingly, the largest/fastest tsunami bores also result in higher damming loads, with T_{erf} = 30 s giving almost 3-fold larger values than T_{erf} = 45 s. However, this observation must be taken with caution, since, as explained earlier, the 2D nature of the numerical models can lead to over-prediction of the damming loads. Last but not least, the right subplot of Figure 15 reveals that contrary to the existing simplified equations of debris loads (e.g., FEMA P626 [3]), the impact forces might not necessarily be a linear function of the impact velocity, at least for the specific hydrodynamic conditions. In fact, when the debris velocity increases above a certain limit (e.g., 1.1 m/s for this water depth) the rate of the increase in the impact force with the velocity decreases, resulting in a non-linear increase in the force. This behavior can be explained by the trends observed in the previous figures, according to which, the largest impact velocity corresponds to the fastest bore (T_{erf} = 30 s) that cause significant pitching of the debris and non-normal impact on the column. Ultimately, the results presented herein indicate that the debris impact forces might be a function of both the debris velocity and pitching angle at the instant of the impact on the coastal structure. However, this indication must be further verified with validated three-dimensional models. Ideally, such future models should simulate the debris and the coastal structure as flexible bodies, since that will enable a more realistic prediction of the impact duration and determine its dependence on the debris velocity and pitch angle.

The above findings seem to extend and complement the findings of previous studies, which have demonstrated the critical role of the relative tsunami–structure or debris–structure angle, in the estimation of hydrodynamic and debris loads, respectively. For example, Istrati and Buckle [44,80] demonstrated the dependence of the maximum tsunami loads on the skew angle of a bridge and the angle of attack (obliqueness of the wave), respectively, while Haehnel and Daly [36] and Derschum et al. [40] revealed experimentally the dependence of the debris loads on the yaw angle of the

impact on the structure, for wooden logs and shipping containers, respectively. The former research study proposed a reduction coefficient for cases of oblique debris impact on a structure, and was later on the basis for the development of the orientation coefficient (equal to 0.65) in the Tsunami chapter of ASCE 7-16 [79]. Interestingly, the debris rotation and oblique collisions between adjacent containers were suggested as a critical factor in Stolle et al. [81], since these could result in energy losses and consequently reduce the impact forces on coastal structures. The latter authors simplified the estimation of the impact loads induced by multiple debris, by assuming them to be a function of an area coefficient that accounted for the impact debris geometry and compactness. However, they noted that accounting for the impact angle of the agglomeration in future studies, would be physically more realistic. Last but not least, the experimental observations of Shafiei et al. [38] are perhaps the closest in agreement with the findings of the current study, since they observed that the debris always impacted the vertical structure at non-zero pitching angle, which ranged between 3 and 10° and 15 and 30° for a rigid rectangular box and a disc, respectively. This pitching angle had a major effect because it governed the variability of the impact accelerations and caused a large vertical load (in the case of a horizontal tsunami flow) that was approximately 60% of the horizontal one.

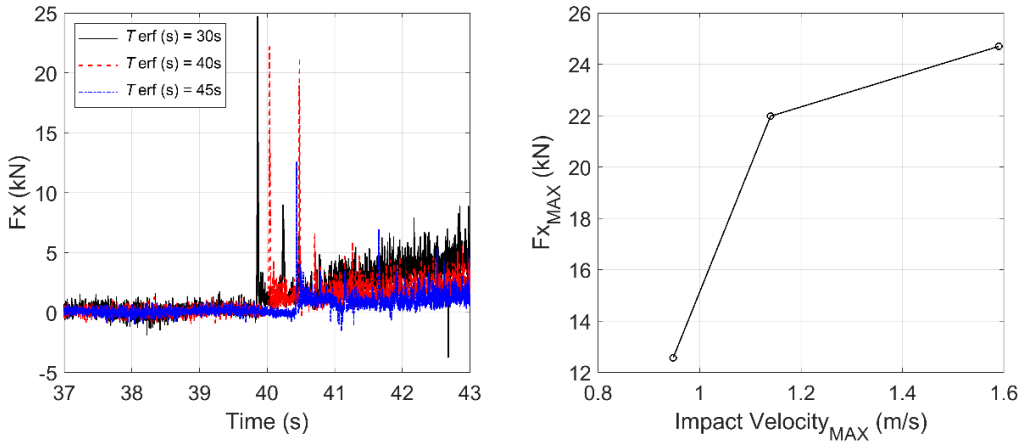

Figure 2-15 Free debris histories (left) and maximum values of debris impact on the column vs. the impact velocity (right). Numerical results for h1 = 2.496 m h2 = 0.13 m, and Terf = 30, 40, and 45 s

2.6.2. Initial water depth

In addition to the effect of the tsunami characteristics, it is of interest to evaluate the effect of the initial water depth on the debris motion, and the debris interaction with the column and the bottom of the flume. For this purpose, two of the water depths tested in Ko [37], i.e., h_1 = 2.496 and 2.664 m and a new depth with h_1 = 2.8 m were considered for a range of tsunami flows. These offshore water depths translated into local initial water depths of 0.13, 0.30 and 0.43 m, respectively, at the debris location. Figure 2-16 illustrates the (a) variation of the free surface, (b) fluid velocity, (c) debris vertical displacement, (d) debris rotation, (e) debris velocity and (f) impact force. The free-surface histories are plotted close to the offshore side of the debris, at x = 62 m, and are calculated relative to the initial water level, while the fluid velocities are plotted at the same x coordinate at the level of the initial free surface (i.e., 9.1 cm above the bottom of the debris). This means that the absolute elevation of the locations at which the fluid velocities are plotted are different for each water depth, but the relative distance from the bottom of the debris is the same. The figure reveals small differences in the maximum bore heights and nearly negligible differences in the fluid velocity histories close to the debris location, for three water depths. There are some differences in the free-surface history of the shallower water level relative to the two larger depths, with the most obvious difference in the bore front and the instant of the arrival at x = 62 m. In the case of the deeper water, the tsunami waves are arriving slightly faster, which is attributable to the increase in the wave celerity offshore caused by the increase in the water depth. Nonetheless, the tsunami bores at the debris location are similar enough for the three water depths, enabling the proper investigation of the effect of this parameter. Interestingly, despite the smaller bore height in the case of the h_1 = 2.496 m relative to the other depths, this case exhibits the largest vertical displacement of the debris (at its onshore corner) and the largest pitching. In fact, the maximum pitching angle seems to consistently decrease with the increase in the water depth, with the shallowest case inducing an

approximately 5-fold larger maximum pitching angle relative to the deepest case of 2.8 m. This demonstrates that the rotation of the debris is highly dependent on the initial water depth. Moreover, in addition to the differences in the magnitudes, it can be observed that the previously identified pattern in the debris motion, which involved an initial clockwise debris rotation followed by a counter-clockwise one before the impact on the column, is not consistent for all the water depths. For larger initial depths it is possible to notice an opposite sequence of debris rotations (i.e., for h_1 = 2.66 m) or just a clockwise rotation before the initial debris contact with the column (i.e., for h_1 = 2.8 m). Last but not least, in contrast to the differences in the vertical displacement and rotation of the debris, the debris horizontal velocities present more similarities. The major difference is observed in the fact that the deeper cases exhibit a gradual increase in the debris velocity, which becomes nearly constant as it approaches the coastal structure, while in the shallowest case more abrupt increases in the debris velocity are observed that result in a larger impact velocity on the column. Despite the larger debris impact velocity for h_1 = 2.496 m (for the specific tsunami bore), this case gives similar impact forces with the large water depths, which can be justified by the higher level of pitching in the former case.

Figure 2-17 presents selected snapshots for the three water depths and T_{erf} = 40 s, as the debris moves inland and impacts the coastal structure. This visual representation of the phenomenon verifies the previously observed trends, with the two larger water depths being associated with nearly a consistent debris orientation (small rotation) contrary to the shallow water that is dominated by debris pitching effects. Moreover, despite the similar bore velocities at x = 62 m (a few meters from the debris) observed in Figure 16, the fringe plots of the fluid particle velocities reveal that there are significant differences in the flow around the debris, since in the shallow case the flow seems to accelerate more below the debris. This is probably due to the fact that in the latter case the bore is more restricted and does not have as much space to propagate below the debris as

in deeper waters, resulting in faster flows horizontally that tend to uplift on one side of the debris and consequently rotate it. Another major difference lies in the fact that when the initial water level is low, the pitching of the debris can move one of its corners downwards so much that it impacts the bottom of the flume. This contact between the debris and the flume complicates further the debris–fluid interaction and is a distinguishable feature of the small water depths only. Last, but not least the snapshots reveal major differences in the fluid flow below the debris after the initial impact on the column, which affects the number of secondary impacts and their magnitude, as well as, the damming loads. For example, smaller damming loads can be noticed in the case of larger water depths, because less of the bore gets reflected on the structure and more of it propagates onshore by moving below the debris. However, these differences might be exaggerated by the 2D assumption made in the development of the numerical models.

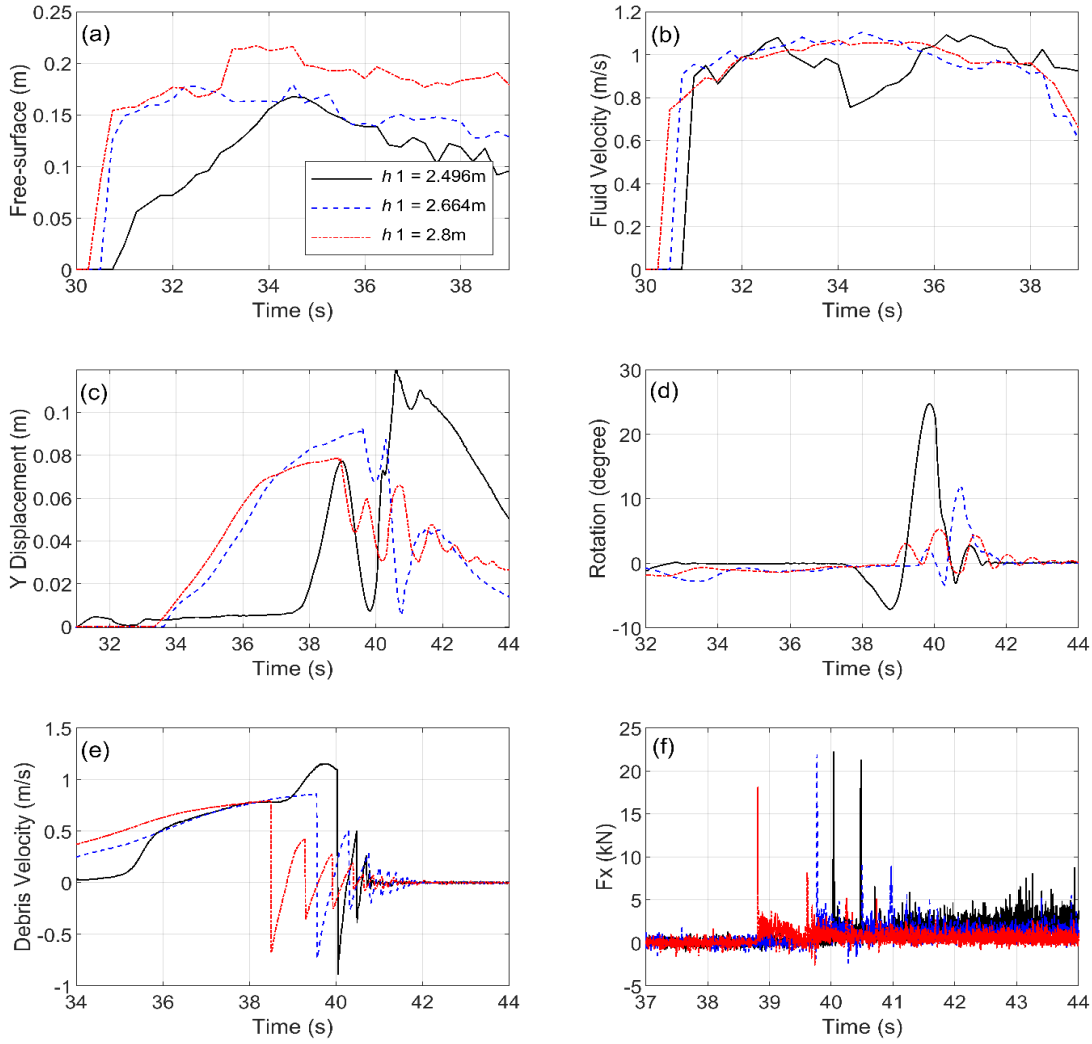

Figure 2-16 Time histories of the free surface, fluid velocity, motion of the debris (y displacement and rotation), debris velocity and debris impact force on the column. Numerical results of free debris for Terf = 40 s and three water depths with h1 = 2.496, 2.664

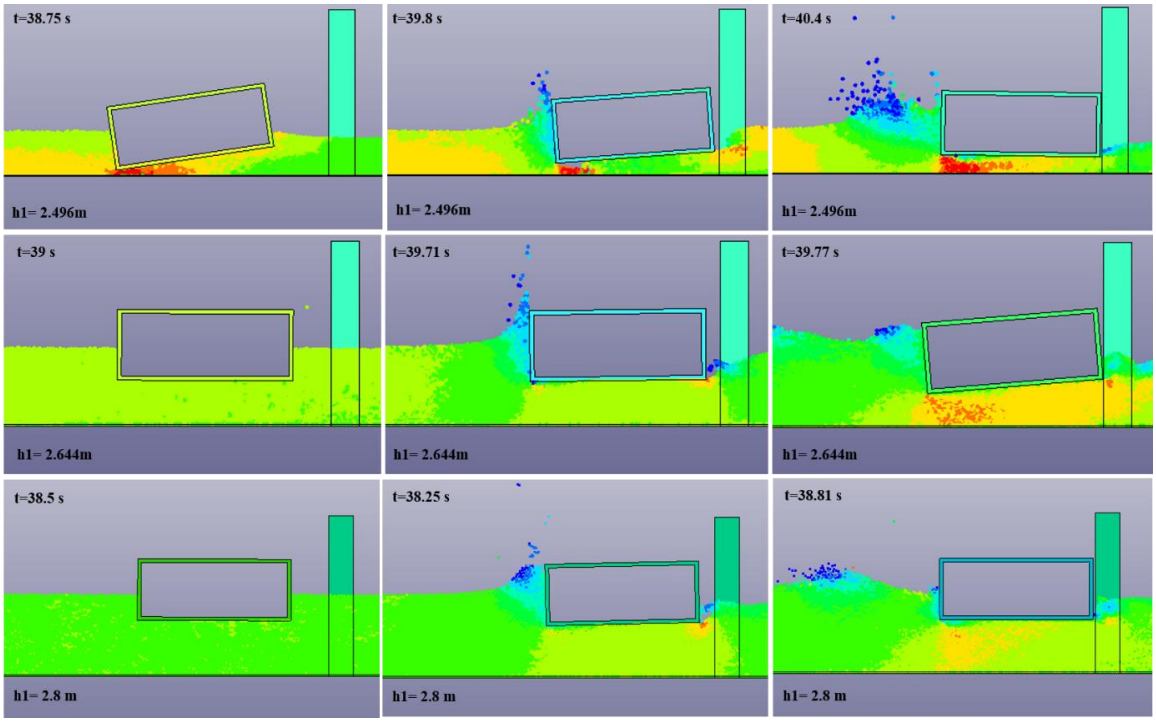

Figure 2-17 Snapshots of debris-tsunami interaction and impact on the column. Numerical results of free debris for Terf = 40 s and three water depths with h1 = 2.496 (top), 2.664 (center) and 2.8 m (bottom)

The maximum debris impact forces as a function of the impact velocities for all the water depths and bores, are presented in Figure 2-18. This figure reveals, that although for larger water depths (e.g., h_1 = 2.66 and 2.8 m) the relationship between the maximum debris impact force and impact velocity is nearly linear, which agrees with existing predictive equations (e.g., FEMA P646 [3] and ASCE [79]), for small water depth the trend seems to be non-linear. In fact, in the latter case, after the exceedance of the debris velocities above a certain limit, the impact force increases less than what a linear force–velocity assumption would suggest, indicating that predictive equations that utilize such an assumption might yield conservative results. To investigate whether such an indication is true, additional parametric investigations are required, followed by direct comparisons with available simplified equations, which is beyond to scope of this manuscript. However, the results presented herein raise the question on whether future predictive equations of debris loads should: (i) be a function of the water depth, so that for large initial water depths a linear impact

force–velocity relationship is used and for shallow depths a non-linear one that will account for the possibility of debris pitching and non-normal impact angle on the structure, especially if the structure is located close to the location of the debris entrainment, and (ii) limit the applicability of the linear force–velocity equations to a certain velocity limit, above which, the rate of the force increase with the velocity will drop significantly.

As explained earlier, the indications of this preliminary numerical investigation should be verified with follow-up expanded studies that will include a wider range of hydrodynamic conditions (e.g., faster flows and more water depths) and different relative distances between the debris and the coastal structure. The latter parameter is especially crucial, since as observed in Goseberg et al. [82] the debris tended to yaw towards an equilibrium position as it propagated inland, in which the long axis was perpendicular to the flow direction. It would be interesting to see if the pitching of the debris will be damped out in the case where it could propagate for a longer distance before impacting the structure. If such a behavior was true, then the significance of pitching effects documented herein might be applicable only to locations near the debris entrainment by the bore, and disappear after a certain propagation distance. Moreover, although the current 2D SPH–FEM models were validated against the restrained debris experiments of Ko [37] and Ko and Cox [65], future studies should employ 3D numerical models that will be able to simulate both the yaw and roll of the debris, in order to ensure that the influence of the pitching angle on the impact forces identified by the current study is not affected by the 2D assumption. Last but not least, given the observed complex interaction of the debris with a simplified vertical coastal structure, it would be interesting for future studies to investigate how to debris will interact with more complex structural geometries, such as elevated decks with overhangs, piloti-type buildings with columns or multiple structures in urban environments.

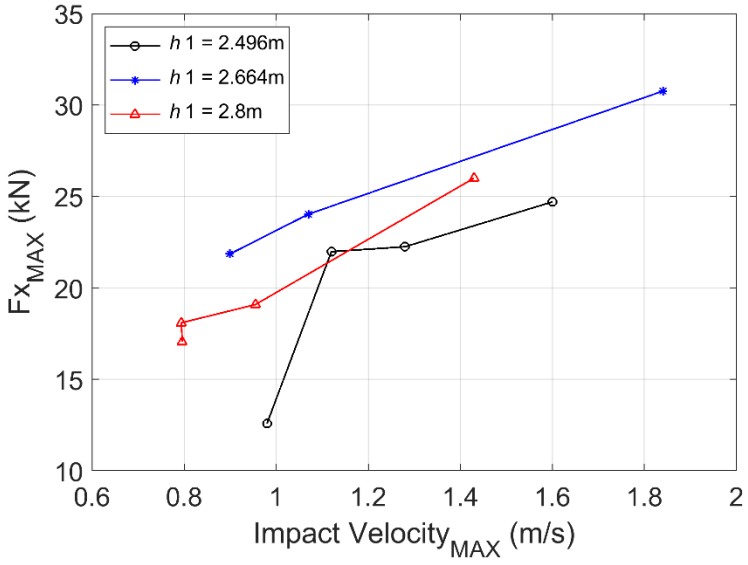

Figure 2-18 Maximum values of the debris impact force as a function of the impact velocity for three water depths and nine tsunami bores

2.7. Summary and conclusions

Given the documented catastrophic effects of large debris in past tsunamis, and the difficulty of simulating numerically such effects, this study presents a coupled SPH–FEM modeling approach and evaluates its capability to predict both the debris–fluid interaction and the impact on a coastal structure. In this modeling approach the fluid was modeled via particles, based on the weakly compressible smoothed particle hydrodynamics, while the wavemaker, flume, debris and structure were modeled with mesh-based finite elements. The interaction between the fluid and solid bodies was defined via node-to-solid contacts, while the interaction of solid bodies (e.g., debris–flume, debris–structure) was defined via a two-way segment-based contact that could trace the impact at any location of the body. For the validation of the coupled modeling, the large-scale experimental data from Ko and Cox [65] and Ko [37] were selected as a benchmark. In these experiments, a tsunami-like wave was generated offshore via a wavemaker, which then propagated over a complex bathymetry, forming a transient flow on the coast that entrained the debris and propagated it onshore until it impacted a vertical column. The fact that the debris was restrained experimentally

to move only in the direction of the flow (i.e., no yaw and no movement across the flume width) enabled the development of a two-dimensional (2D) numerical model instead of a 3D one, which reduced consequently the required computational time.

The comparison between the experimental and numerical results revealed an overall acceptable accuracy of the SPH–FEM coupled modeling approach, with some parameters being estimated more accurately than other, as explained below:

- The free surface and fluid velocities had good agreement with the experimentally recorded results, both offshore and during the wave propagation along the slope. The deviation of the maximum wave height from the average value of the experimental tests ranged between 4% and 15.2%, while the deviation of the maximum fluid velocities was between 2% and 22%, depending on the location along the flume and the tsunami flow. These results showed that the numerical model can predict the relative increase in the free surface and fluid velocities as the wave propagates over the sloped part and undergoes a non-linear transformation, indicating that the fluid–flume contact worked properly.

- The SPH–FEM models estimate similar debris velocities with the experiments, especially when the bore reaches the container and starts transporting it. However, as the debris propagation inland continues, the numerical model tends to accelerate more and reach an impact velocity that is approximately 20% larger than in the experiments, leading consequently to some differences in the arrival time at the column location. One possible explanation for these differences lies in the 2D formulation of the current numerical model, which implies that the pressures applied from the bore on the offshore face of the debris is uniform across the debris width, which is not necessarily the case in real 3D environments.

- The deviation of the numerically predicted maximum debris impact forces on the column from the experimental data was in the range of 14–25% for the investigated hydrodynamic flows. However, these differences are consistent with the observed differences in the debris impact velocities. Overall, the numerical results presented similar trends with the physical tests since both gave larger impact forces for the more transient and faster tsunami flows.

Following the verification of the numerical modeling, a preliminary investigation was conducted with the aim to gain an insight into (i) the sensitivity of the results to the debris restraints, and (ii) the role of the hydrodynamic conditions. The analyses of the 2D free debris revealed that for small water depths, the debris starts rotating clockwise upon the arrival of the bore, then as it transports inland, it changes the direction of rotation until it reaches the maximum counter-clockwise pitching angle slightly before the primary impact on the column. The prominent pitching effect during the debris transport inland resulted in higher impact velocities relatively to the restrained debris, which was unexpected, highlighting the complexity and non-linearity of the debris interaction with the turbulent flow. Moreover, despite the larger impact velocity of the free debris, the applied impact forces were smaller by approximately 56% relative to the restrained one. This is attributed to the fact that the free debris continues pitching until it reaches the column location, which results in a non-normal impact angle and a consequently non-uniform contact. This non-normal pitching angle reduces the contact area between the debris and the column, and consequently the maximum impact forces.

The comparison of different tsunami flows revealed that the 2D motion of the debris is highly dependent on the tsunami characteristics, with the largest wave (i.e., faster flow inland) causing pitching angles that were approximately 85% larger than the smallest wave. In fact, there was some indication that the pitching of the debris was caused mainly by the high velocities of the turbulent flow passing below the debris, justifying why faster bores caused more debris pitching. Moreover,

the comparison of similar tsunami flows for three different water depths demonstrated that the debris–fluid interaction is also dependent on the initial water level at the debris location, with the debris pitching decreasing consistently with the increase in the water depth. When the water level is low the bottom corners of the debris can impact the bottom of the flume if the pitching angle is large, complicating further the debris–fluid interaction and impact on the column. Interestingly, although for larger water depths the relationship between the maximum debris impact force and impact velocity is nearly linear, which agrees with existing predictive equations, for the small water depth a non-linear trend was observed. In fact, in the latter case, after the exceedance of the debris velocity above a certain limit, the impact force increased less than what a linear force–velocity relationship would suggest.

Despite the limited investigated hydrodynamic conditions, the observed trends raise the question on whether debris load equations should: (i) be a function of the water depth, so that for large initial water depths a linear impact force–velocity relationship is used and for shallow depths a more complex equation is developed that will account for the debris pitching angle at the instant of impact, and/or (ii) limit the applicability of the linear force–velocity equations to a certain velocity range, above which, the rate of the force as a function of the impact velocity will drop. Future studies should consider a wider range of hydrodynamic conditions (e.g., faster flows, more water depths) and different relative distances between the debris and the coastal structure in order to determine if the pitching effects observed herein are going to be damped out as the debris propagates over longer distances. Such studies should employ 3D numerical models that will be able to simulate both the yaw and roll of the debris, in order to ensure that the influence of the pitching angle is not exaggerated by the 2D SPH–FEM models used in this study.

2.8. Acknowledgements

The authors acknowledge Michael Scott from Oregon State University and Christos Papachristos from the University of Nevada, Reno for their support of the research project, and the Engineering Computing Team at the University of Nevada, Reno for providing computational support and resources that have contributed to the research results reported within this paper.

2.9. Appendix

The sensitivity of the numerical results to the SPH particle size was investigated for the fastest bore with T_{erf} = 30s. This appendix shows the numerically predicted free surface, debris velocity and impact force for particle sizes equal to 1, 2 and 3 cm.

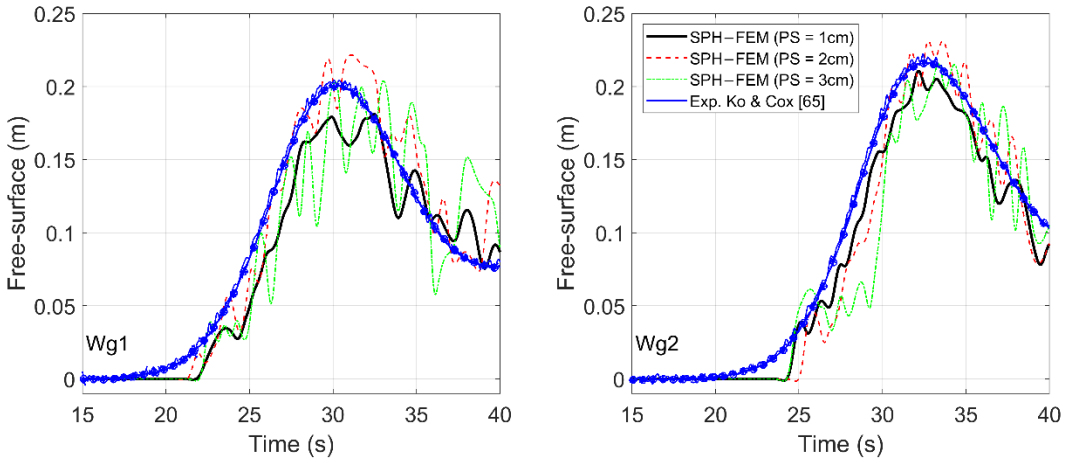

Figure 2-A1 Variation of the free surface at different locations along the flume. Experimental [65] and numerical results for three particle sizes, for h1 = 2.496 m and Terf = 30 s

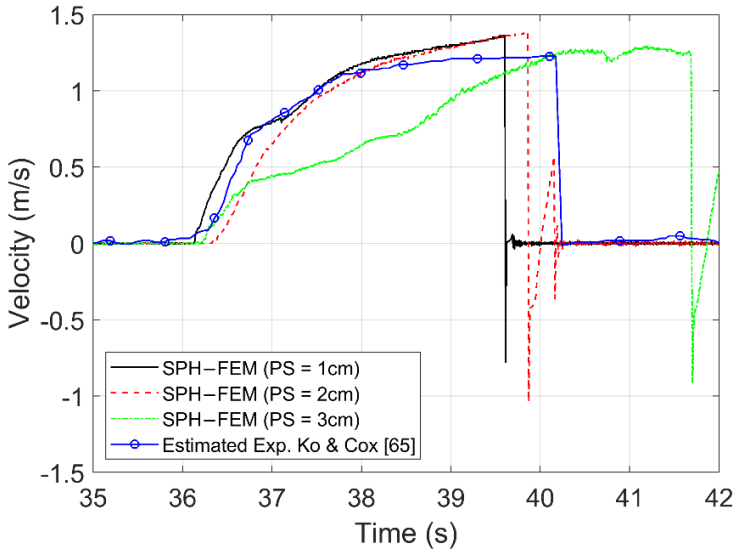

Figure 2-A2 Debris velocity histories. Estimated based on the experimental tests of [65] and numerical results for three particle sizes, for h1 = 2.496 m and Terf = 30 s

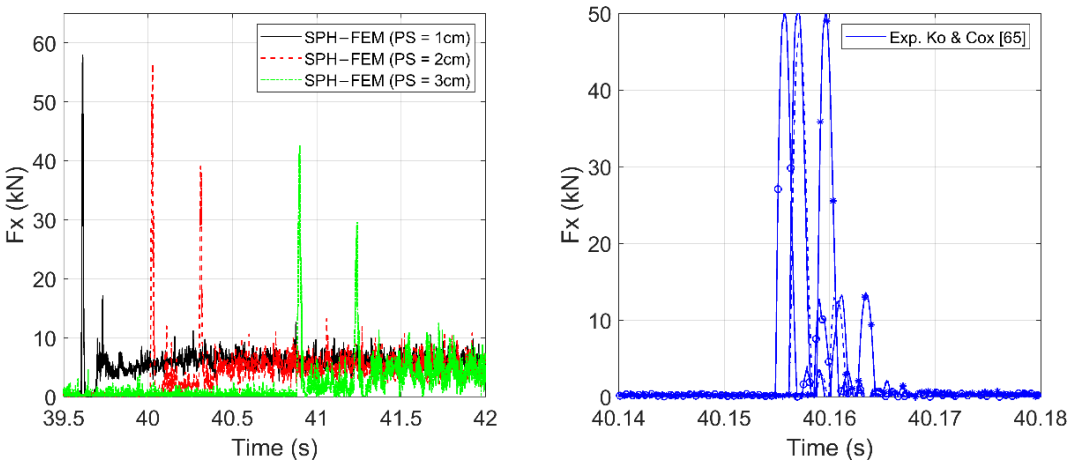

Figure 2-A3 Debris velocity histories. Estimated based on the experimental tests of [65] and numerical results for three particle sizes, for h1 = 2.496 m and Terf = 30 s

2.10.References

1. Yeh, H.; Sato, S.; Tajima, Y. The 11 March 2011 East Japan earthquake and tsunami: Tsunami effects on coastal infrastructure and buildings. *Pure Appl. Geophys.* 2013, *170*, 1019–1031, https://doi.org/10.1007/s00024-012-0489-1.
2. Earthquake Engineering Research Center (EERI). The Tohoku, Japan, Tsunami of March 11, 2011: Effects on Structures, Special Earthquake Report; EERI: 2011, California, USA.

3. FEMA P646. *Guidelines for Design of Structures for Vertical Evacuation from Tsunami*; Federal Emergency Management Agency: Washington, DC, USA, 2012.
4. Takahashi, S. Urgent survey for 2011 great east Japan earthquake and tsunami disaster in ports and coasts. *Tech. Note Port Airpt. Res. Inst.* 2011, *1231*, 75–78.
5. Mikami, T.; Shibayama, T.; Esteban, M.; Matsumaru, R. Field survey of the 2011 Tohoku earthquake and tsunami in Miyagi and Fukushima prefectures. *Coast. Eng. J.* 2012, *54*, 1250011-1–1250011-26, https://doi.org/10.1142/S0578563412500118.
6. Canadian Association of Earthquake Engineering (CAEE). *Reconnaissance Report on the December 26, 2004 Sumatra Earthquake and Tsunami*; CAEE: 2005, British Columbia, CA.
7. Akiyama, M.; Frangopol, D.M.; Strauss, A. Lessons from the 2011 Great East Japan Earthquake: Emphasis on life-cycle structural performance. In Proceedings of the Third International Symposium on Life-Cycle Civil Engineering, Vienna, Austria, October 3-6 2012; pp. 13–20.
8. Kawashima, K.; Buckle, I. Structural performance of bridges in the Tohoku-oki earthquake. *Earthq. Spectra* 2013, *29*, 315–338, https://doi.org/10.1193%2F1.4000129.
9. Maruyama, K.; Tanaka, Y.; Kosa, K.; Hosoda, A.; Arikawa, T.; Mizutani, N.; Nakamura, T. Evaluation of tsunami force acting on bridge girders. In Proceedings of the Thirteenth East Asia-Pacific Conference on Structural Engineering and Construction, Sapporor, Japan, September 11-13, 2013. Available online: http://hdl.handle.net/2115/54508 (accessed on July 15, 2021).
10. Palermo, D.; Nistor, I.; Nouri, Y.; Cornett, A. Tsunami loading of near-shoreline structures: A primer. *Can. J. Civ. Eng.* 2009, *36*, 1804–1815, https://doi.org/10.1139/L09-104.
11. Foster, A.S.J.; Rossetto, T.; Allsop, W. An experimentally validated approach for evaluating tsunami inundation forces on rectangular buildings. *Coast. Eng.* 2017, *128*, 44–57, https://doi.org/10.1016/j.coastaleng.2017.07.006.
12. Honda, T.; Oda, Y.; Ito, K.; Watanabe, M.; Takabatake, T. An experimental study on the tsunami pressure acting on Piloti-type buildings. *Coast. Eng. Proc.* 2014, *1*, 1–11.
13. Robertson, I.N.; Riggs, H.R.; Mohamed, A. Experimental results of tsunami bore forces on structures. In Proceedings of the International Conference on Offshore Mechanics and Arctic Engineering, Shanghai, China, January 6-11,2008; pp. 509–517, https://doi.org/10.1115/OMAE2008-57525.
14. Araki, S.; Ishino, K.; Deguchi, I. Stability of girder bridge against tsunami fluid force. In Proceedings of the 32th International Conference on Coastal Engineering (ICCE), Shanghai, China, June 30- July 5, 2010.
15. Lau, T.L.; Ohmachi, T.; Inoue, S.; Lukkunaprasit, P. *Experimental and Numerical Modeling of Tsunami Force on Bridge Decks*; InTech: Rijeka, Croatia, 2011; pp. 105–130.
16. Hoshikuma, J.; Zhang, G.; Nakao, H.; Sumimura, T. Tsunami-induced effects on girder bridges. In Proceedings of the International Symposium for Bridge Earthquake Engineering in Honor of Retirement of Professor Kazuhiko Kawashima, Tokyo, Japan, March 2013.
17. Istrati, D. Large-Scale Experiments of Tsunami Inundation of Bridges Including Fluid-Structure-Interaction. Ph.D. Thesis, University of Nevada, Reno, NV, USA, 2017. Available online: https://scholarworks.unr.edu//handle/11714/2030 (accessed on July 15, 2021).
18. Istrati, D.; Buckle, I.G.; Itani, A.; Lomonaco, P.; Yim, S. Large-scale FSI experiments on tsunami-induced forces in bridges. In Proceedings of the 16th World Conference on Earthquake, 16WCEE, Santiago, Chile, January 9-13, 2017; pp. 9–13. Available online: http://www.wcee.nicee.org/wcee/article/16WCEE/WCEE2017-2579.pdf (accessed on July 15, 2021).
19. Chock, G.Y.; Robertson, I.; Riggs, H.R. Tsunami structural design provisions for a new update of building codes and performance-based engineering. *Solut. Coast. Disasters* 2011, 423–435, https://doi.org/10.1061/41185(417)38.

20. Azadbakht, M.; Yim, S.C. Simulation and estimation of tsunami loads on bridge superstructures. *J. Waterw. Port Coast. Ocean Eng.* 2015, *141*, 04014031, https://doi.org/10.1061/(ASCE)WW.1943-5460.0000262.
21. McPherson, R.L. Hurricane Induced Wave and Surge Forces on Bridge Decks. Ph.D. Thesis, Texas A&M University, College Station, TX, USA, 2008.
22. Xiang, T.; Istrati, D.; Yim, S.C.; Buckle, I.G.; Lomonaco, P. Tsunami loads on a representative coastal bridge deck: Experimental study and validation of design equations. *J. Waterw. Port Coast. Ocean Eng.* 2020, *146*, 04020022. https://doi.org/10.1061/(ASCE)WW.1943-5460.0000560.
23. Istrati, D.; Buckle, I.G. Effect of fluid-structure interaction on connection forces in bridges due to tsunami loads. In Proceedings of the 30th US-Japan Bridge Engineering Workshop, Washington, DC, USA, October 21-23, 2014. Available online: https://www.pwri.go.jp/eng/ujnr/tc/g/pdf/30/30-10-2_Buckle.pdf (accessed on July 15, 2021).
24. Choi, S.J.; Lee, K.H.; Gudmestad, O.T. The effect of dynamic amplification due to a structure′ s vibration on breaking wave impact. *Ocean Eng.* 2015, *96*, 8–20, https://doi.org/10.1016/j.oceaneng.2014.11.012.
25. Bozorgnia, M.; Lee, J.J.; Raichlen, F. Wave structure interaction: Role of entrapped air on wave impact and uplift forces. In Proceedings of The International Conference on Coastal Engineering, June 30- July 5, 2010.
26. Seiffert, B.; Hayatdavoodi, M.; Ertekin, R.C. Experiments and computations of solitary-wave forces on a coastal-bridge deck. Part I: Flat plate. *Coast. Eng.* 2014, *88*, 194–209, https://doi.org/10.1016/j.coastaleng.2014.01.005.
27. Xu, G.; Cai, C.S.; Chen, Q. Countermeasure of air venting holes in the bridge deck–wave interaction under solitary waves. *J. Perform. Constr. Facil.* 2017, *31*, 04016071, https://doi.org/10.1061/(ASCE)CF.1943-5509.0000937.
28. Istrati, D.; Buckle, I. Role of trapped air on the tsunami-induced transient loads and response of coastal bridges. *Geosciences* 2019, *9*, 191. https://doi.org/10.3390/geosciences9040191.
29. Istrati, D.; Buckle, I.; Lomonaco, P.; Yim, S. Deciphering the tsunami wave impact and associated connection forces in open-girder coastal bridges. *J. Mar. Sci. Eng.* 2018, *6*, 148. https://doi.org/10.3390/jmse6040148.
30. Seiffert, B.R.; Cengiz Ertekin, R.; Robertson, I.N. Effect of entrapped air on solitary wave forces on a coastal bridge deck with girders. *J. Bridge Eng.* 2016, *21*, 04015036, https://doi.org/10.1061/(ASCE)BE.1943-5592.0000799.
31. Rossetto, T.; Peiris, N.; Pomonis, A.; Wilkinson, S.M.; Del Re, D., Koo, R.; Gallocher, S. The Indian Ocean tsunami of december 26, 2004: Observations in Sri Lanka and Thailand. *Nat. Hazards* 2007, *42*, 105–124, https://doi.org/10.1007/s11069-006-9064-3.
32. Robertson, I.N.; Carden, L.; Riggs, H.R.; Yim, S.; Young, Y.L.; Paczkowski, K.; Witt, D. Reconnaissance following the September 29, 2009 tsunami in Samoa. *Research Rep.* 2010. Available online: https://www.eeri.org/site/images/eeri_newsletter/2010_pdf/Samoa-Rpt.pdf (accessed on July 15, 2021).
33. Yeom, G.S.; Nakamura, T.; Mizutani, N. Collision analysis of container drifted by runup tsunami using drift collision coupled model. *J. Disaster Res.* 2009, *4*, 441–449, https://doi.org/10.20965/jdr.
34. Madurapperuma, M.A.K.M.; Wijeyewickrema, A.C. Inelastic dynamic analysis of an RC building impacted by a tsunami water-borne shipping container. *J. Earthq. Tsunami* 2012, *6*, 1250001, https://doi.org/10.1142/S1793431112500017.
35. Como, A.; Mahmoud, H. Numerical evaluation of tsunami debris impact loading on wooden structural walls. *Eng. Struct.* 2013, *56*, 1249–1261, https://doi.org/10.1016/j.engstruct.2013.06.023.
36. Haehnel, R.B.; Daly, S.F. Maximum impact force of woody debris on floodplain structures. *J. Hydraul. Eng.* 2004, *130*, 112–120. https://doi.org/10.1061/(ASCE)0733-9429(2004)130:2(112).
37. Ko, H. Hydraulic Experiments on Impact Forces from Tsunami-Driven Debris. Master's Thesis, Oregon State University, Corvallis, OR, USA, 2013.

38. Shafiei, S.; Melville, B.W.; Shamseldin, A.Y.; Adams, K.N.; Beskhyroun, S. Experimental investigation of tsunami-borne debris impact force on structures: Factors affecting impulse-momentum formula. *Ocean Eng.* 2016, *127*, 158–169, https://doi.org/10.1016/j.oceaneng.2016.09.008.
39. Stolle, J.; Goseberg, N.; Nistor, I.; Petriu, E. Debris impact forces on flexible structures in extreme hydrodynamic conditions. *J. Fluids Struct.* 2019, *84*, 391–407, https://doi.org/10.1016/j.jfluidstructs.2018.11.009.
40. Derschum, C.; Nistor, I.; Stolle, J.; Goseberg, N. Debris impact under extreme hydrodynamic conditions part 1: Hydrodynamics and impact geometry. *Coast. Eng.* 2018, *141*, 24–35, https://doi.org/10.1016/j.coastaleng.2018.08.016.
41. Yang, W.C. Study of Tsunami-Induced Fluid and Debris Load on Bridges using the Material Point Method. Ph.D. Thesis, University of Washington, Seattle, WA, USA, 2016. Available online: http://hdl.handle.net/1773/37064 (accessed on July 15, 2021).
42. Oudenbroek, K.; Naderi, N.; Bricker, J.D.; Yang, Y.; Van der Veen, C.; Uijttewaal, W., Moriguchi, S.; Jonkman, S.N. Hydrodynamic and debris-damming failure of bridge decks and piers in steady flow. *Geosciences* 2018, *8*, 409, https://doi.org/10.3390/geosciences8110409.
43. Istrati, D.; Hasanpour, A.; Buckle, I. Numerical Investigation of Tsunami-Borne Debris Damming Loads on a Coastal Bridge. In Proceedings of the 17 World Conference on Earthquake Engineering, Sendai, Japan, September 13-18, 2020. Available online: https://www.researchgate.net/profile/Denis-Istrati/publication/342027873_Numerical_Investigation_of_Tsunami-Borne_Debris_Damming_Loads_on_a_Coastal_Bridge/links/5f71a957299bf1b53efa468f/Numerical-Investigation-of-Tsunami-Borne-Debris-Damming-Loads-on-a-Coastal-Bridge.pdf (accessed on July 15, 2021).
44. Istrati, D.; Buckle, I.G. Tsunami Loads on Straight and Skewed Bridges—Part 1: Experimental Investigation and Design Recommendations (No. FHWA-OR-RD-21-12). Oregon Department of Transportation. Research Section, 2021. Available online: https://rosap.ntl.bts.gov/view/dot/55988 (accessed on July 15, 2021).
45. St-Germain, P.; Nistor, I.; Townsend, R.; Shibayama, T. Smoothed-particle hydrodynamics numerical modeling of structures impacted by tsunami bores. *J. Waterw. Port Coast. Ocean Eng.* 2014, *140*, 66–81, https://doi.org/10.1061/(ASCE)WW.1943-5460.0000225.
46. Pringgana, G.; Cunningham, L.S.; Rogers, B.D. Modelling of tsunami-induced bore and structure interaction. *Proc. Inst. Civ. Eng.-Eng. Comput. Mech.* 2016, *169*, 109–125, https://doi.org/10.1680/jencm.15.00020.
47. Sarfaraz, M.; Pak, A. SPH numerical simulation of tsunami wave forces impinged on bridge superstructures. *Coast. Eng.* 2017, *121*, 145–157, https://doi.org/10.1016/j.coastaleng.2016.12.005.
48. Zhu, M.; Elkhetali, I.; Scott, M.H. Validation of OpenSees for tsunami loading on bridge superstructures. *J. Bridge Eng.* 2018, *23*, 04018015, https://doi.org/10.1061/(ASCE)BE.1943-5592.0001221.
49. Liu, G.R.; Liu, M.B. Smoothed Particle Hydrodynamics: A Meshfree Particle Method; World Scientific: Singapore, 2003.
50. Violeau, D. Fluid Mechanics and the SPH Method: Theory and Applications; Oxford University Press: Oxford, UK, 2012.
51. Monaghan, J.J.; Kos, A. Solitary waves on a Cretan beach. *J. Waterw. Port Coast. Ocean Eng.* 1999, *125*, 145–155, https://doi.org/10.1061/(ASCE)0733-950X(1999)125:3(145).
52. Colagrossi, A.; Landrini, M. Numerical simulation of interfacial flows by smoothed particle hydrodynamics. *J. Comput. Phys.* 2003, *191*, 448–475, https://doi.org/10.1016/S0021-9991(03)00324-3.
53. Monaghan, J.J.; Kos, A.; Issa, N. Fluid motion generated by impact. *J. Waterw. Port Coast. Ocean Eng.* 2003, *129*, 250–259, https://doi.org/10.1061/(ASCE)0733-950X(2003)129:6(250).

54. Crespo, A.J.C.; Gómez-Gesteira, M.; Dalrymple, R.A. 3D SPH simulation of large waves mitigation with a dike. *J. Hydraul. Res.* 2007, *45*, 631–642, https://doi.org/10.1080/00221686.2007.9521799.
55. Pelfrene, J. Study of the SPH Method for Simulation of Regular and Breaking Waves. Master's Thesis, Gent University, Ghent, Belgium, 2011.
56. Dalrymple, R.A., Knio, O.; Cox, D.T.; Gesteira, M.; Zou, S. Using a Lagrangian particle method for deck overtopping. *Ocean Wave Meas. Anal.* 2002, 1082–1091, https://doi.org/10.1061/40604(273)110.
57. Gómez-Gesteira, M.; Dalrymple, R.A. Using a three-dimensional smoothed particle hydrodynamics method for wave impact on a tall structure. *J. Waterw. Port Coast. Ocean Eng.* 2004, *130*, 63–69, https://doi.org/10.1061/(ASCE)0733-950X(2004)130:2(63).
58. Barreiro, A.; Crespo, A.J.C.; Domínguez, J.M.; Gómez-Gesteira, M. Smoothed particle hydrodynamics for coastal engineering problems. *Comput. Struct.* 2013, *120*, 96–106, https://doi.org/10.1016/j.compstruc.2013.02.010.
59. Altomare, C.; Crespo, A.J.; Domínguez, J.M.; Gómez-Gesteira, M.; Suzuki, T.; Verwaest, T. Applicability of Smoothed Particle Hydrodynamics for estimation of sea wave impact on coastal structures. *Coast. Eng.* 2015, *96*, 1–12, https://doi.org/10.1016/j.coastaleng.2014.11.001.
60. Aristodemo, F.; Tripepi, G.; Meringolo, D.D.; Veltri, P. Solitary wave-induced forces on horizontal circular cylinders: Laboratory experiments and SPH simulations. *Coast. Eng.* 2017, *129*, 17–35, https://doi.org/10.1016/j.coastaleng.2017.08.011.
61. Gómez-Gesteira, M.; Cerqueiro, D., Crespo, C.; Dalrymple, R.A. Green water overtopping analyzed with a SPH model. *Ocean Eng.* 2005, *32*, 223–238, https://doi.org/10.1016/j.oceaneng.2004.08.003.
62. Yang, Y.; Li, J. SPH-FE-Based Numerical Simulation on Dynamic Characteristics of Structure under Water Waves. *J. Mar. Sci. Eng.* 2020, *8*, 630, https://doi.org/10.3390/jmse8090630.
63. Hu, D.; Long, T.; Xiao, Y.; Han, X.; Gu, Y. Fluid–structure interaction analysis by coupled FE–SPH model based on a novel searching algorithm. *Comput. Methods Appl. Mech. Eng.* 2014, *276*, 266–286, https://doi.org/10.1016/j.cma.2014.04.001.
64. Thiyahuddin, M.I.; Gu, Y.; Gover, R.B.; Thambiratnam, D.P. Fluid–structure interaction analysis of full-scale vehicle-barrier impact using coupled SPH–FEA. *Eng. Anal. Bound. Elem.* 2014, *42*, 26–36, https://doi.org/10.1016/j.enganabound.2013.10.007.
65. Ko, H.; Cox, D. OSU: 1-D Hydraulic Experiment, Aluminum, Water depth = 249.6 cm. *DesignSafe-CI* 2012, https://doi.org/10.4231/D3KH0DZ8Z.
66. Hallquist, J.O. LS-DYNA theory manual. *Liverm. Softw. Technol. Corp.* 2006, *3*, 25–31.
67. Grimaldi, A.; Benson, D.J.; Marulo, F.; Guida, M. Steel structure impacting onto water: Coupled finite element-smoothed-particle-hydrodynamics numerical modeling. *J. Aircr.* 2011, *48*, 1299–1308, https://doi.org/10.2514/1.C031258.
68. Panciroli, R.; Abrate, S.; Minak, G.; Zucchelli, A. Hydroelasticity in water-entry problems: Comparison between experimental and SPH results. *Compos. Struct.* 2012, *94*, 532–539, https://doi.org/10.1016/j.compstruct.2011.08.016.
69. Monaghan, J.J. Simulating free surface flows with SPH. *J. Comput. Phys.* 1994, *110*, 399–406, https://doi.org/10.1006/jcph.1994.1034.
70. Wu, Z. Compactly supported positive definite radial functions. *Adv. Comput. Math.* 1995, *4*, 283–292, https://doi.org/10.1007/BF03177517.
71. Monaghan, J.J.; Lattanzio, J.C. A refined particle method for astrophysical problems. *Astron. Astrophys.* 1985, *149*, 135–143.
72. Gingold, R.A.; Monaghan, J.J. Smoothed particle hydrodynamics: Theory and application to non-spherical stars. *Mon. Notices R. Astron. Soc.* 1977, *181*, 375–389.
73. Das, J.; Holm, H. On the improvement of computational efficiency of smoothed particle hydrodynamics to simulate flexural failure of ice. *J. Ocean Eng. Mar. Energy* 2018, *4*, 153–169, https://doi.org/10.1007/s40722-018-0114-1.

74. Petschek, A.G.; Libersky, L.D. Cylindrical smoothed particle hydrodynamics. *J. Comput. Phys.* 1993, *109*, 76–83, https://doi.org/10.1006/jcph.1993.1200.
75. Monaghan, J.J.; Gingold, R.A. Shock simulation by the particle method SPH. *J. Comput. Phys.* 1983, *52*, 374–389, https://doi.org/10.1016/0021-9991(83)90036-0.
76. Xu, J.; Wang, J. Node to node contacts for SPH applied to multiple fluids with large density ratio. In Proceedings of the 9th European LS-DYNA Users' Conference, Manchester, UK, June 3, 2013; pp. 2–4.
77. Thomas, S.; Cox, D. Influence of finite-length seawalls for tsunami loading on coastal structures. *J. Waterw. Port Coast. Ocean Eng.* 2012, *138*, 203–214, https://doi.org/10.1061/(ASCE)WW.1943-5460.0000125.
78. Swegle, J.W.; Attaway, S.W.; Heinstein, M.W.; Mello, F.J.; Hicks, D.L. An analysis of smoothed particle hydrodynamics (No. SAND-93-2513). *Sandia Natl. Labs* 1994, https://doi.org/10.2172/10159839.
79. American Society of Civil Engineers (ASCE). *Minimum Design Loads and Associated Criteria for Buildings and Other Structures; ASCE/SEI 7-16*; American Society of Civil Engineers (ASCE): Reston, VA, USA, 2016.
80. Istrati, D.; Buckle, I.G. Tsunami Loads on Straight and Skewed Bridges—Part 2: Numerical Investigation and Design Recommendations (No. FHWA-OR-RD-21-13). Oregon Department of Transportation. Research Section, 2021. Available online: https://rosap.ntl.bts.gov/view/dot/55947 (accessed on July 15, 2021).
81. Stolle, J., Nistor, I., Goseberg, N., & Petriu, E. Multiple Debris Impact Loads in Extreme Hydrodynamic Conditions. *J. Waterw. Port Coast. Ocean Eng.* 2020, *146*, 04019038.

Chapter 3

3. Multi-Physics Modeling of Tsunami Debris Impact on Bridge Decks

Abstract

Recent tsunamis revealed the vulnerability of coastal infrastructure, including bridges and transportation networks. On-site reconnaissance surveys found that a number of coastal structures and bridges were heavily damaged or destroyed by the loads generated by debris and floating objects, such as, boats, vehicles and shipping containers, which were carried inland by the tsunami-induced flow. Although several studies have been conducted to date, the majority of them focused on buildings, with very limited information currently available for bridges. Moreover, the majority of the studies were experimental, since the numerical investigations are quite challenging due to the multi-physics nature of the phenomena, which involves: a complex fluid flow with turbulent wave breaking, a nonlinear debris-fluid interaction with large deformations, a contact between the debris, the trapped fluid and the bridge, and a dynamic structural response. To overcome these challenges the authors used a multi-physics modeling approach, in which the fluid flow is simulated via the Smoothed Particle Hydrodynamics Method (SPH), while the debris and the bridge are simulated via the Finite Element Method (FEM). The fact that both the fluid and the structural parts are represented via Lagrangian methods facilitates the simulation of the interaction of the different parts via a penalty-based contact. Following the description of the numerical approach and the validation study with previous large-scale experiments of debris impact on a column, a preliminary numerical investigation is presented herein in order to obtain an insight into the debris-fluid-deck interaction and impact loads on a bridge superstructure. The SPH-FEM results demonstrate that (i) the elevation of deck and the initial orientation of the debris has a significant effect on the debris movement, velocity and impact force, (ii) the debris has both a horizontal and a vertical velocity at the instant of the initial impact on the offshore side of the bridge deck and consequently exerts impulsive loads simultaneously in both directions, and (iii) the debris-fluid-deck interaction is quite

complex and can accelerate the debris as it moves below the box-girder bridge, leading to secondary impacts on the soffit with magnitudes much larger than the ones of the primary impact on the offshore side of the deck.

Keywords: tsunami, bridge, debris, SPH

3.1. Introduction

Recent major tsunamis generated by earthquakes including the 2004 Indian Ocean, 2010 Chile and 2011 Japan caused tremendous structural damages to buildings, bridges and infrastructure across the affected coastal regions. The tsunami waves inundated a large number of bridges, damaged the connections and washed away the superstructures. The failure of coastal bridges due to tsunami wave impact possess a huge obstacle for the transportation system. Based on the post-tsunami surveys, the 2011 Great East Japan Earthquake and Tsunami impacted more than 300 bridges. Most of these bridges survived the earthquake but they were collapsed due to the tsunami-induced loading [1]. On-site reconnaissance surveys after the 2004 Indian Ocean tsunami revealed that a number of bridges were subjected not only to large hydrodynamic loads, but also to debris and floating objects, such as, boats and shipping containers resulting in an increase of the impact force and significant lateral displacement or washout of the structure [2- 4].

Given the critical role of coastal bridges and observed poor performance in previous tsunami events, several experimental and numerical studies have been carried out to investigate (i) the tsunami inundation mechanism of bridge decks and the corresponding hydrodynamic forces [1], [5-10], (ii) the role of the air-entrapment below the deck of open-girder bridges [11-13] and efficiency of air-venting [14] (iii) the fluid-structure interaction [15, 16], (iv) the differences between unbroken, breaking and broken waves/bores [5, 17], (v) the three-dimensional effects during the tsunami impact on skewed bridges [18, 19] or the oblique impact on straight bridges

[20], and (vi) the development of simplified predictive load equations [21, 22] and design methodologies with multiple load cases [23]. Despite the extensive investigation of the aforementioned challenging aspects of the tsunami inundation of bridges in previous studies, the majority of them were focused on clear-water conditions, with very few studies currently available on the topic of water-borne debris impact on bridge superstructures.

Some studies have investigated the tsunami-borne debris transport and impact on coastal structures, but they were focused on buildings [24] or simplified vertical structures and columns [25-28]. Yang (2016) [29] studied the tsunami-induced debris loading on bridge decks using the material point method. The results of the analyses showed that presence of debris increases the applied loads on bridges and that the in-water analyses give up to 35% larger debris impact forces than the in-air cases. Oudenbroek et al, (2018) [30] carried out an experimental study to evaluate the failure mechanism of a selected bridge in Japan. Their results confirmed that debris accumulation in front of the superstructure has significant effects on the fluid loads, particularly, increasing the uplift and drag force, which could lead to the failure of the structure. More recently, Istrati et al, (2020) [31] evaluated the effects of tsunami-borne debris damming loads on coastal bridges using three-dimensional numerical simulations. The results demonstrated that a trapped container below the offshore overhang has a negligible effect on the horizontal load but a larger effect on the vertical load and overturning moments that could increase the probability of failure of the offshore bearings and connections.

The majority of the numerical simulation of tsunami impacts on coastal structures were performed using mesh-based solvers that utilized the finite volume or finite element technique [11, 21, 28, 32], particle-based methods, such as, the smoothed particle hydrodynamics, i.e. SPH, [33], and hybrid methods, such as, the particle finite element method, i.e. PFEM [10]. The meshless nature of the SPH makes it ideal for problems dealing with large deformations, which explains why the

method has been successfully applied to different applications of coastal engineering, including the propagation of solitary waves on beaches [34], the breaking of waves [35], the wave-structure interaction [36] and the wave overtopping of offshore platforms [37]. Recently, Hasanpour et al, (2021) [28] employed a coupled SPH-FEM approach to study the tsunami-borne large debris transport and impact on a vertical coastal structure, revealing the accuracy of this modeling approach and giving an insight into some of the underlying physics, such as, the occurrence of significant debris pitching in the case of shallow initial water depths and the nonlinear relationship between the debris' horizontal velocity and impact load.

Considering the poor performance of coastal bridges in past tsunamis, the critical role of transportation networks following natural disasters, and the demonstrated catastrophic debris effects on other types of coastal structures, it is of great importance to advance the understanding of the water-borne debris impact on bridges in order to improve their resilience. To this end, the main objective of this paper is to investigate the effects of tsunami debris loading on a representative bridge superstructure by utilizing a coupled finite element (FE) and smoothed particle hydrodynamics (SPH) modeling approach.

3.2. Methodology

3.2.1. Description of numerical model

The smoothed particle hydrodynamics was originally invented to deal with astronomical problems [38, 39]. SPH is a Lagrangian meshless technique, in which the fluid domain is represented by a set of non-connected particles. The particles carry individual material properties and move and interact with others within the computational domain according to conservation governing equations derived from the Navier-Stokes equations (NS). The SPH technique employed in this research is available in LS-DYNA [40] and is based on weakly compressible smoothed particle hydrodynamics.

Kernel approximation

For any SPH pseudo-particle, the function describing the field Ω is approximated in the form of "kernel function", which is stated as the integral form of the product of any function and kernel function [41]:

$$< f(x) >= \int_{\Omega} f(x')W(x - x', h)dx' \qquad \text{Equation 3.1}$$

where x and x' are the position vector of the material points in a domain Ω; f(x) is the continuous function of the field corresponding to the coordinate x; $f(x')$ is the value of quantity at the point x'; $W(x - x', h)$ is the bell-shaped smooth kernel function, where h is the smoothing length, defining the influence volume of the smooth function which varies in time and in space.

Particle approximation

The second key aspect in SPH formulations is the particle approximation, which enables the system to be represented by a finite number of particles that carry an individual mass and occupy an individual space. For the SPH method, equation 1 can be transformed into discretized forms by the summing up the values of the filed function within the support domain defined by the smoothing length h as follows [41]:

$$< f(x_i) >= \sum_{j=1}^{n} \frac{m_j}{\rho_j} f(x_i)\, W(x_i - x_j, h) = \sum_{j=1}^{n} \frac{m_j}{\rho_j} f(x_j)\, W_{ij,} \qquad \text{Equation 3.2}$$

where $< f(x_i) >$ is the kernel approximation operator, $f(x_j)$ is the physical value at the jth position, i is the number of any particle in the domain; n is the total number of particles within the influence area of the particle at i; and m_j and ρ_j are the mass and density associated with particle j.

SPH formulation

The SPH formulation is derived by discretizing the Navier–Stokes equations spatially, thus leading to a set of ODEs which can be solved via time integration. Substituting the SPH approximations for a function and its derivative to the partial differential equations governing the physics of fluid flows, the discretization of these governing equations can be written as follows [42]:

$$\frac{d\rho_i}{dt} = \sum_{j=1}^{n} m_j \left(x_i^\beta - x_j^\beta\right) \frac{\partial W_{ij}}{\partial x_i^\beta},$$

$$\frac{dv_i^\alpha}{dt} = \sum_{j=1}^{n} m_j \left(\frac{\sigma_i^{\alpha\beta}}{\rho_i^2} + \frac{\sigma_j^{\alpha\beta}}{\rho_j^2}\right) \frac{\partial W_{ij}}{\partial x_i^\beta},$$

$$\frac{dv_i^\alpha}{dt} = \sum_{j=1}^{n} m_j \left(\frac{\sigma_i^{\alpha\beta}}{\rho_i\rho_j} . \frac{\partial W_{ij}}{\partial x_i^\beta} - \frac{\sigma_j^{\alpha\beta}}{\rho_i\rho_j} . \frac{\partial W_{ij}}{\partial x_j^\beta}\right), \qquad \text{Equation 3.3}$$

$$\frac{dv_i^\alpha}{dt} = \sum_{j=1}^{n} m_j \left(\frac{\sigma_i^{\alpha\beta}}{\rho_i\rho_j} . \frac{\partial W_{ij}}{\partial x_i^\beta} - \frac{\sigma_j^{\alpha\beta}}{\rho_i\rho_j} . \frac{\partial W_{ij}}{\partial x_j^\beta}\right),$$

$$\frac{dx_i^\alpha}{dt} = v_i + \varepsilon \sum_{j=1}^{n} \frac{m_j}{\rho_j} \left(v_i - v_j\right) W_{ij},$$

where the superscripts α and β are the coordinate directions; g is the acceleration of gravity; σ is the particle stress; v is the particle velocity; e is the internal energy per unit mass; ε is the shear strain rate ($\varepsilon \cong 0.5$) and Π_{ij} is the Monaghan artificial viscosity [43].

From Equations 3.3, the following particle body forces can be derived [44]:

$$F_i^{pressure} = -\sum_j \; m_j \frac{p_i + p_j}{2\rho_j} \nabla W(r_{ij}, h)$$

$$F_i^{viscosity} = \mu \sum_j m_j \frac{v_i + v_j}{2\rho_j} \nabla^2 W(r_{ij}, h) \qquad \text{Equation 3.4}$$

where $r_{ij} = x_i - x_j$, and μ is the viscosity coefficient of the fluid. The pressure p_i is computed via the constitutive equation:

$$p_i = K\,(\rho_i - \rho_0) \qquad \text{Equation 3.5}$$

where K is the stiffness of the fluid and ρ_0 is the initial density.

The acceleration of particle i is derived from:

$$a_i = \frac{1}{\rho_i\,(F_i^{pressure} + F_i^{viscosity} + F_i^{external})} \qquad \text{Equation 3.6}$$

where $F_i^{external}$ represents external forces such as body forces and forces due to contacts.

Contact

The interaction between the SPH and FE elements is defined using a penalty-based contact algorithm in which the SPH is always defined to be the slave part and the finite elements are defined to be the master. When a node is in contact with the surface, each slave node is checked for penetration, and if it penetrates a restoring force is applied to prevent further penetration. The magnitude of this force is proportional to the penetration distance into the shell or solid element and acts in the direction normal to the master surface. The restoring force is defined by [40]:

$$f=kdn \qquad \text{Equation 3.7}$$

where d is the penetration distance, n is the surface normal vector and k is a penalty factor, comparable to a spring constant. The stiffness factor k for master segment si is given in terms of the bulk modulus Ki, the volume Vi and the face area Ai of the element that contains si as

$$\mathrm{k_i} = \frac{\mathrm{A_i\,K_i\,f_{si}}}{\max\,(\text{shell diagonal})} \qquad \text{Equation 3.8}$$

where f_{si} is a scale factor for the interface stiffness and is normally defaulted to 10. The constant *k* should be set large enough to minimize penetration and instabilities, but it should not be too large that it generates artificially large forces.

The interaction between the FE elements with each other is defined through a two-way treatment of contact in which both slave and master segments are checked for penetration. This type of contact is symmetric and the definition of the slave and master surfaces are arbitrary. As the prediction of the contact location and the direction may be difficult to conclude, the automatic contacts are recommended, since they can detect the penetration at each time-step, irrespective of whether it is coming from the slave or master part. The automatic contacts determine the contact surface by projecting normally from the shell mid-plane to a distance equal to half of the contact thickness.

3.2.2. Validation for container impact on coastal structure

In order to validate the employed SPH-FE numerical technique, the experimental study presented by Ko & Cox (2012) [25] and Ko (2013) [45] was selected as the benchmark. Those experiments were carried out in the Large Wave Flume (LWF) at the O.H. Hinsdale Wave Research Laboratory (HWRL) at Oregon State University. Details of the flume is presented in Figure 3-1. The flume is 104.24m long, 3.66m wide and 4.57m deep and is equipped with a piston-type wavemaker. Free-surface and fluid velocity had been measured in the aforementioned experiments via several wave gages and acoustic doppler velocimeters along the flume. As it is shown, the coastal structure was represented by a column, while an aluminum 1:5 scale model of the standard intermodal container with dimensions of 1.22m * 0.49m * 0.58m and draft of 9.1cm was utilized as the floating debris. The debris was allowed to move freely in the horizontal and vertical directions, but it was restrained to translate across the flume width (no yaw) which made it possible to develop a two-dimensional model representing a slice crossing through the mid-width of the flume, the debris and the column.

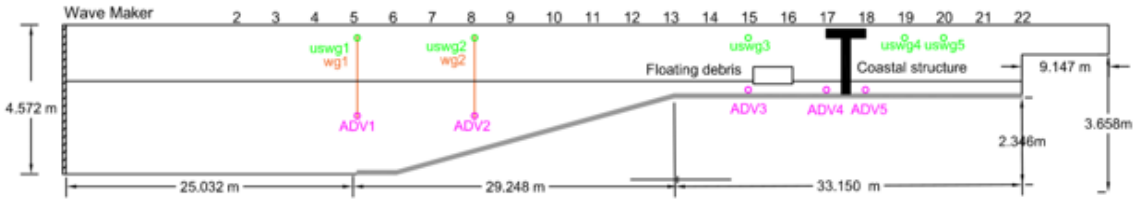

Figure 3-1 Cross section of the LWF depicting the bathymetry, column location and flume instrumentation of the experiments of Ko & Cox (2012) [25]

A two-dimensional numerical model of the experimental setup was generated using finite elements (FE) for the flume walls, the column and the floating debris and SPH for the fluid. Extensive numerical investigations were carried out to evaluate the effect of different SPH particle sizes and the FE mesh sizes on the numerical accuracy and the computational time and particle size and FE mesh size of 1cm were selected for the final numerical models presented herein. To define the interaction between the fluid particles and the FE parts, the CONTACT_2D_NODES_TO_SOLID was employed. In addition, a 2D automatic surface to surface contact was selected to define the interaction between the debris and the column. To model the movement of the wavemaker the error function method was used, in which the time for the wave paddle to travel the full stroke is denoted by T_{erf} [46]. More detailed information about the developed numerical models can be found in Hasanpour et al, (2021) [32].

In order to evaluate the accuracy of the numerical model, the results of the free-surface and fluid velocity histories at two different distances from the wavemaker, were compared with those measured in Ko & Cox (2012). Wave gage 1 (wg1) and adv1 are the closest to the wavemaker with x = 24.930 m for both instruments and z = 1.240 m for the adv. Moreover, the free-surface history is also compared with the experimental results at x = 35.890 m (see wg2), which is located along the sloped part.

Figure 3-2 presents the variation of free-surface at wg1 and wg2 and fluid velocity at adv1 for all the trials of the experimental tests with parameters of $h_1 = 2.664$m and $T_{erf} = 25$s from Ko & Cox (2012) [25], where h_1 corresponds to the initial water depth offshore. The figure reveals that the free-surface and fluid velocity histories have good agreement with experimentally recorded data in terms of the peak values and temporal evolution, both offshore and during the wave propagation along the slope. The interesting finding is that the coupled SPH-FEM technique can predict the relative increase between wg2 and wg1 of the maximum free-surface, demonstrating that this approach can capture the interaction between the fluid and the slope and result in a similar non-linear transformation of the wave during the shoaling process. The maximum deviation from the average value of the experimental data at wg1 and wg2 being 6.1% and 7.6%, respectively. As it can be observed, the measured fluid velocity had significantly larger variability than the recorded free-surface. Nonetheless, the SPH–FEM approach can predict reasonably the fluid velocities with maximum deviations of 30% at adv1.

Figure 3-3 plots the time histories of the debris impact force on the column for the same hydrodynamic condition as in the previous figures. The left subfigure shows the numerical result and the right subfigure shows all trials from the experimental tests. It can be observed that the impact force computed by the numerical model is in good agreement with the experimental data, both in terms of the peak impact force and the overall trends. The numerical model under-predicts the impact force by approximately 8.6%. This under-prediction could be correlated to the under-prediction of the maximum fluid velocity shown in Figure 3-2, since the majority of the available simplified equations for debris impact loads, such as those presented in FEMA P646 (2012) [47] and ASCE (2016) [48] are a linear function of the impact velocity.

Therefore, the overall good prediction of the tsunami wave propagation towards to the shore in terms of free-surface and fluid velocity, and the debris impact forces on the structure, verifies the

ability of the coupled SPH-FEM to simulate such multi-physics phenomena related to coastal hazards.

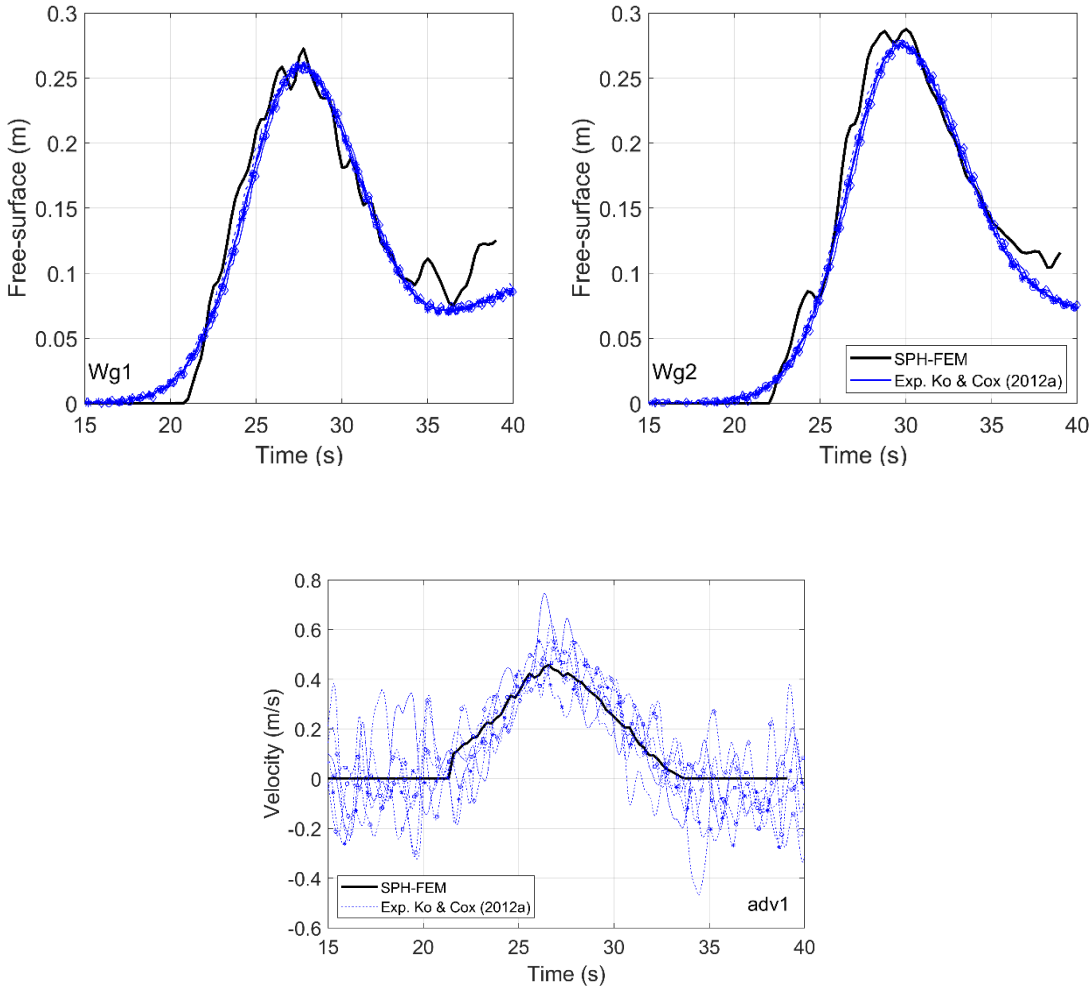

Figure 3-2 Variation of the free surface (top) and fluid velocity (bottom) at different locations along the flume: Experimental [25] and numerical results for h1 = 2.664m m and Terf = 25s

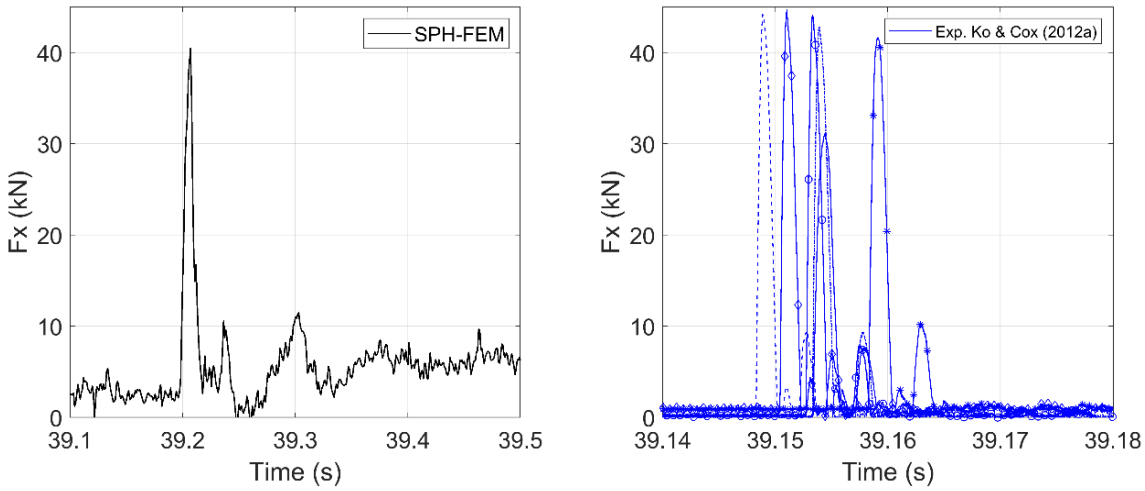

Figure 3-3 Variation of debris impact forces on coastal pier: Experimental [25] and numerical results for h1 = 2.664m and Terf = 25 s

3.2.3. Numerical modeling of debris impact on a box-girder bridge

In order to evaluate the performance of coastal bridges against tsunami-borne debris flow and impact, the developed numerical model of the validation study was modified. There are two main differences; the column was replaced by a bridge deck and the debris and the bridge deck were scaled-down to a 1:10 scale, so that the same tsunami waves could be leveraged in the new analyses. The bridge has a width of 0.96m and height of 0.13m, which follow the dimensions of the deck used in the large-scale hydrodynamic tests [9]. The scaled dimensions of the debris are 0.61m * 0.249m * 0.29m as shown in Figure 3-4. The final numerical model consisted of 17,077 shell elements and 1,328,633 SPH particles. Using up to 96 cores of a high-processing computing system available at UNR, each analysis was completed within 19 hours.

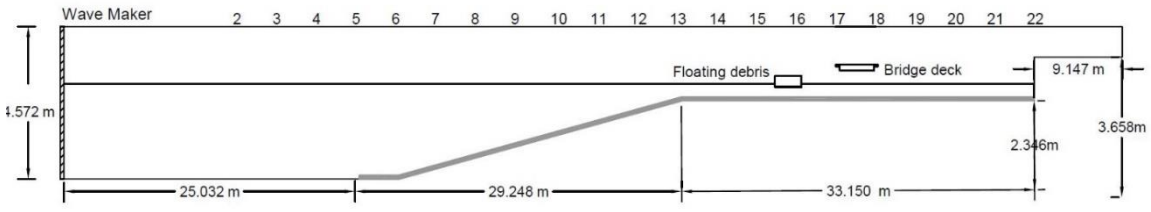

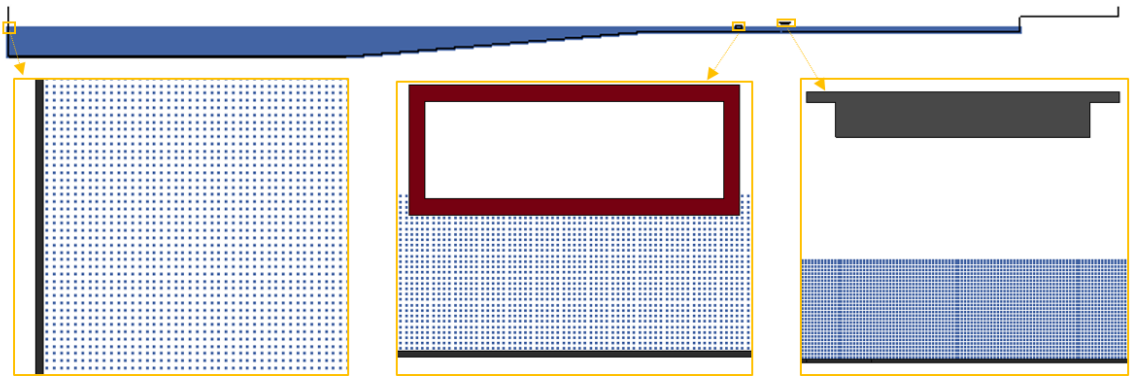

Figure 3-4 Cross section of the computational domain (top), numerical models with debris and bridge (bottom) including the side-views of the wave maker, the debris and the bridge deck

3.3. Results and discussion

3.3.1. Tsunami-debris-deck interaction and flow patterns around deck

Tsunami flow characteristics

Figure 3-5 shows the variation of the free-surface and fluid velocity for the case with h_1=2.664m and T_{erf} = 20s. The free-surface histories are plotted close to the offshore side of the debris, at x=62m, and are calculated relative to the initial water level, while the fluid velocities are plotted at the same x coordinate at the level of the initial free-surface. The figure shows that the tsunami bore at the debris location has a relatively long duration (about 10 seconds), which should be enough for the debris to transport from its initial location, impact the bridge deck and interact with it, and reasonable velocities (4.3m/s at full-scale) for tsunami-like conditions.

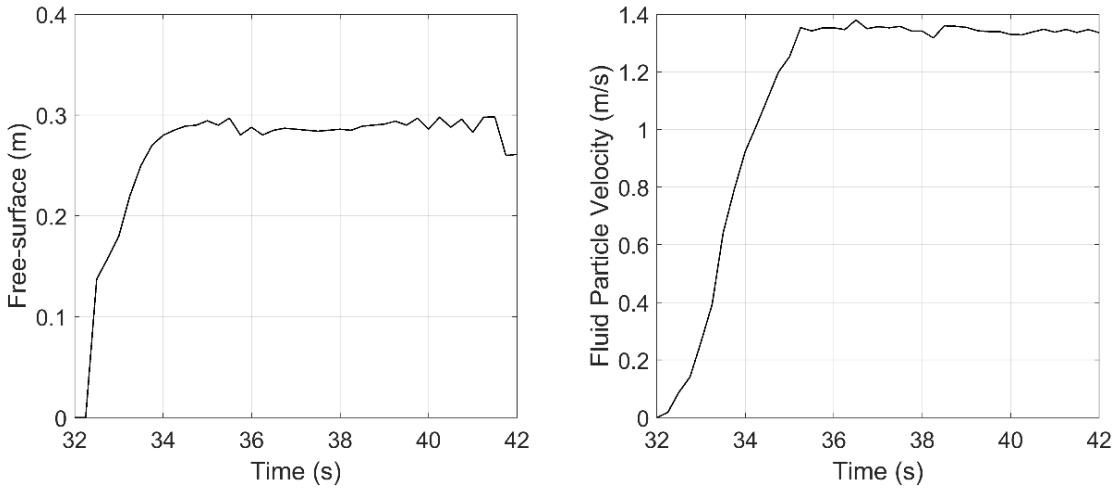

Figure 3-5 Free-surface (left) and fluid velocity histories (right) of tsunami flow in front of the debris for h1=2.664m and Terf = 20 s

Snapshots of tsunami-debris-deck interaction

Figure 3-6 presents some selected snapshots of the x-velocities for the container in longitudinal direction, and for two bridge elevations (0.6m and 0.5m), as the container moves inland and impacts the bridge superstructure. In this case the long axis of the debris is parallel to the flume length and direction of tsunami propagation. The visual presentation of the phenomenon demonstrates that the tsunami bore reaches the deck before the debris, which implies that the impulsive tsunami bore forces will not coincide with the debris impact force. In case of the largest deck elevation, as the container reaches the offshore side of the deck, it impacts the offshore web and then moves below the deck by exhibiting a complex flow pattern with significant rotation and multiple impacts on the soffit. However, in case of the smallest bridge elevation (0.5m), the container impacts the concrete slab of the offshore overhang and after multiple follow-up impacts at lower locations of the offshore web, the debris is trapped below the overhang until the end of the inundation. The snapshots reveal that the elevation of the deck is a critical parameter that affects the movement of the debris below the deck and the debris-wave-deck interaction that determines sequence of the loading on the deck.

Figure 3-7 shows a visualization of the sequence of the flow-debris-deck interaction for the container in the transverse direction, i.e. the long axis of the debris is perpendicular to the flume length, for the case with a 0.50m deck elevation. As the debris moves inland and starts to interact with the deck, the debris rotates and hits the concrete slab which is followed by several impacts on the offshore overhang and the web. Then, the debris moves below the deck and applies multiple impacts on the soffit. As the debris reaches to the onshore side of the deck, the onshore overhang experiences an impact force from the debris which does not happen in the longitudinal direction as shown in the bottom snapshot. Therefore, the transverse debris could overload and damage both the offshore and onshore overhangs. Overall, the snapshots demonstrate that for the same tsunami bore the longitudinal and transverse container exhibit a totally different debris-tsunami-deck interaction and flow patterns around deck. The longitudinal debris gets trapped below the offshore overhang while the transverse debris moves below the deck. Therefore, in addition to the bridge elevation, the initial orientation of the debris plays a significant role on the debris transport and the debris-tsunami-deck interaction.

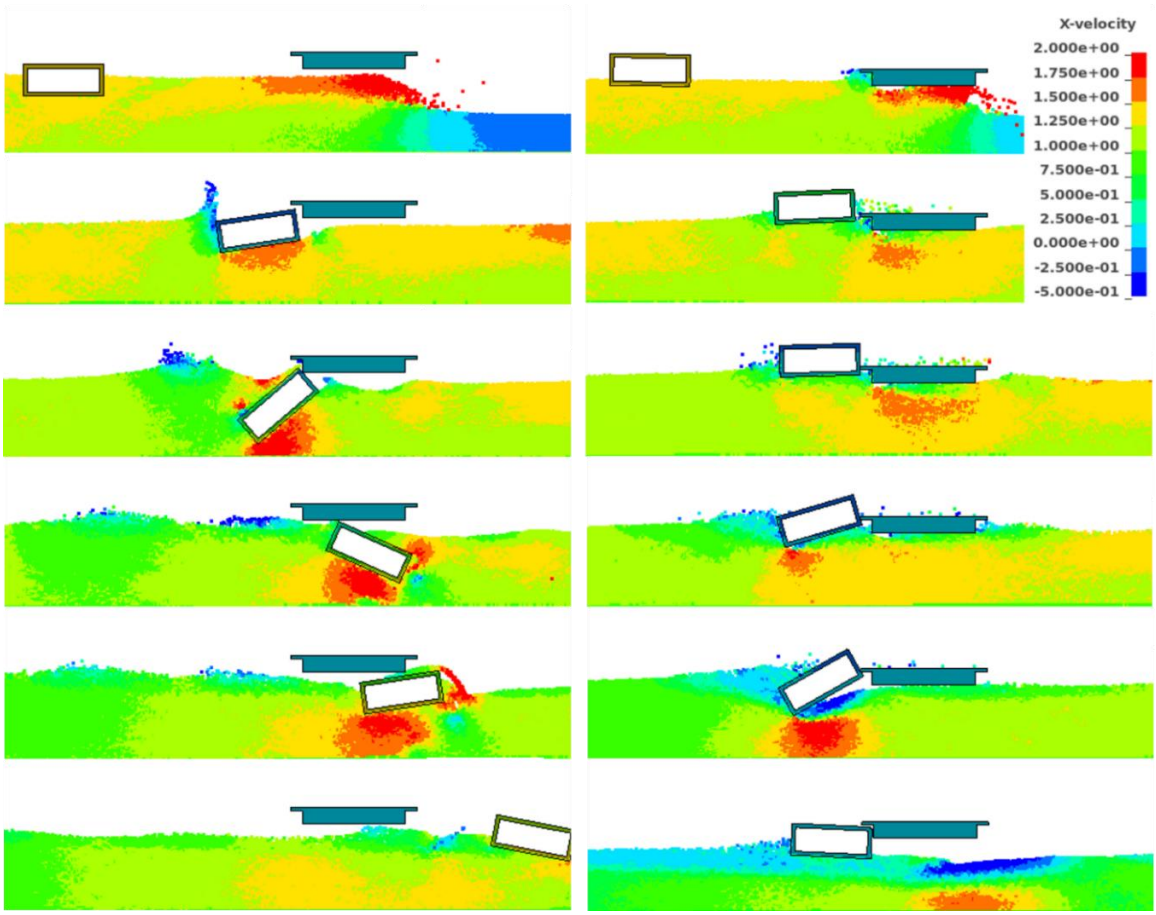

Figure 3-6 Tsunami-debris-deck interaction for a container in longitudinal direction and two bridge elevations, 0.60m (left) and 0.50m (right)

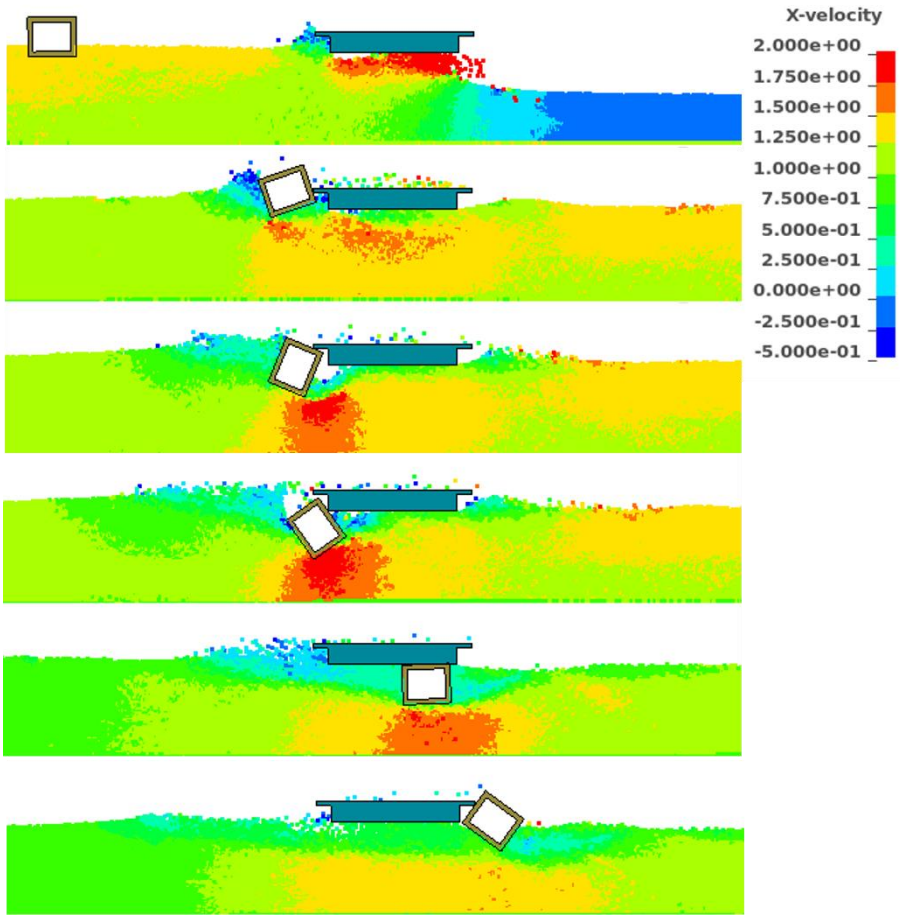

Figure 3-7 Tsunami-debris-deck interaction for a container in transverse direction and deck elevation 0.50m

Debris displacements, rotations, and velocities

In order to get a more quantitative view of the movement of the debris, Figures 3-8 and 3-9 plot the horizontal and vertical movements of the lower-right corner of the container and its rotation throughout the propagation inland, respectively. For this purpose, three different cases including (a) the longitudinal debris and the deck elevations of 0.5m and 0.6m (Long-0.5m, Long-0.6m) and (b) the transverse debris and the deck elevation of 0.5m (Transv-0.5m) are presented. This figure illustrates that despite the similar flow characteristics, the container flow is significantly dependent on the container orientation and the bridge elevation, with totally different movements being observed for the investigated cases. In fact, the longitudinal container exhibits the smallest upward

and the largest downward displacements as it impacts and moves below the deck with the highest elevation, with approximately 30% and 40% increase in upward and downward displacements relative to the initial position, respectively. However, the container with similar orientation does not have a downward displacement when it hits the deck with the lowest elevation (z_b=0.5m) and gets trapped below the offshore overhang. This case exhibits an upward displacement with approximately 38% increase in displacement relative to the initial position. This verifies quantitatively the significance role of the deck elevation on the container movement. Moreover, in addition to the difference in the translation of the container, it can be observed that the longitudinal container has different rotation trends as well. In case of the highest bridge elevation, the container shows a counter-clockwise rotation up to 180 degrees which is followed by a clockwise rotation up to 30 degrees. However, in case of the lowest deck elevation, a counter-clockwise rotation up to 70 degrees is observed. In contrast to the longitudinal debris, the transverse container exhibits upward and downward displacements as it impacts and moves below the lowest deck elevation, which highlights the effect of the container orientation on the debris flow. For this case, when the container impacts the offshore face, the upward displacement increases by approximately 42% relative to the initial position and as it moves below the deck it has downward displacement, without however moving to lower elevations than its initial one (i.e. y-displacement is always positive). Another interesting finding can be reached from the container rotation, according to which, the transverse container rotates more than 180 degrees (up to 400 degrees) which means that it rotates upside down, a fact that could potentially cause damage to the cargo. Therefore, it is important in future risk and damage assessment models, to predict the displacement and rotation of the floating container so that the designer can identify the structural components that are susceptible to debris impact.

The debris velocities in the horizontal and vertical directions for the three investigated cases are presented in Figure 3-10. Interestingly, all three cases exhibit similar horizontal impact velocities (about 1.4m/s), indicating that for two-dimensional analyses the debris acceleration and impact velocity is not a function of the container orientation. However, follow-up three-dimensional investigations should be conducted to evaluate if the 3D effects will not affect this finding. Moreover, after the primary impact on the bridge with the largest elevation (i.e., Long-0.6m), the debris moves below the deck and accelerates until it reaches similar horizontal velocity magnitudes with the one before the impact (about 86% of the peak velocity).

Moreover, the figure reveals that the debris has a vertical velocity at the instant of primary impact. The magnitude of the vertical velocity is in the range of (0.29-0.38) m/s, which is approximately (20-27) % of the horizontal impact velocity. The majority of previous work on debris impact on structures and available simplified equations have focused on the horizontal velocity. However, the present results demonstrate that the vertical velocity at the primary impact of a container on a bridge deck is significant and therefore should be considered in design guidelines. Furthermore, for the cases that the debris moves below the deck and accelerates, the vertical velocity increases significantly and can exceed the velocity of the initial impact. For example, for the longitudinal container with the largest deck elevation (i.e. Long-0.6m), after the initial impact the debris reaches similar horizontal velocity with the primary impact, but a vertical velocity that is about 2.06 time of the respective one at the instant of primary impact. Last but not least, for the cases that the tsunami bore reaches the deck, the debris velocity drops gradually, indicating the existence of a ‘cushioning effect’ from the fluid that is trapped between the debris and the deck at the instant of the impact.

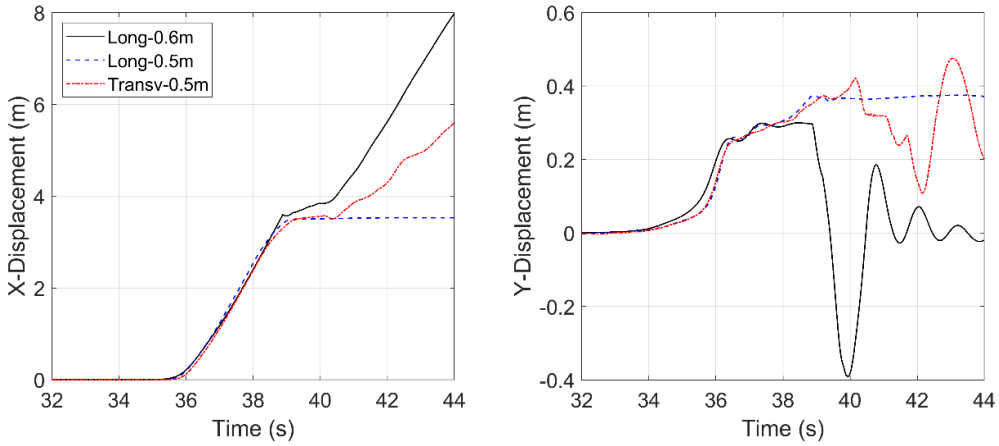

Figure 3-8 Debris horizontal and vertical displacement histories for three cases, including longitudinal and transverse container impact

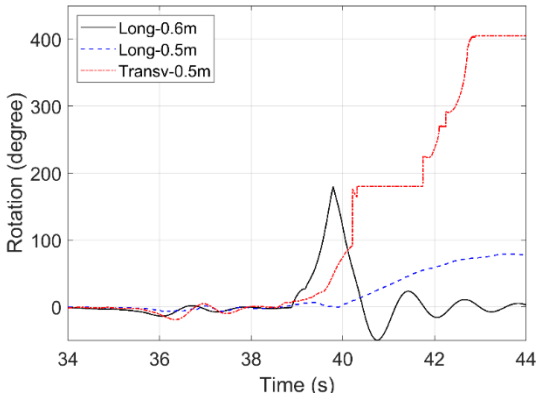

Figure 3-9 Debris rotations for three cases, including longitudinal and transverse container impact

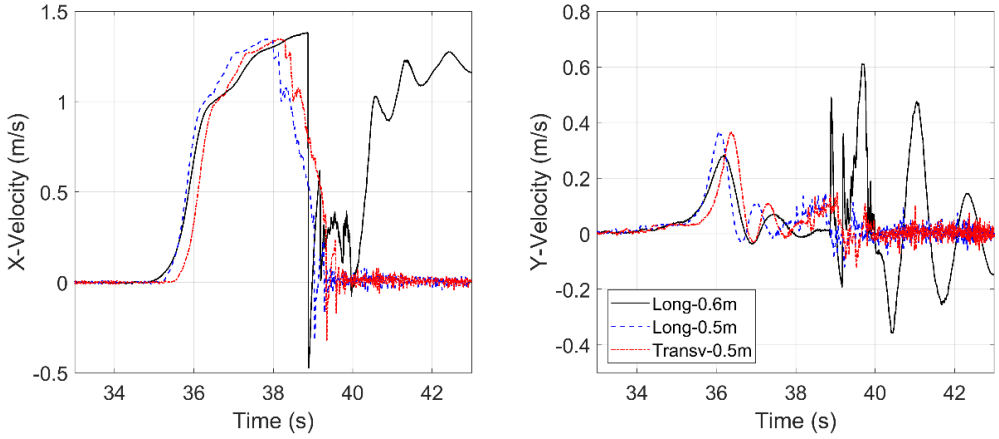

Figure 3-10 Debris velocities in the horizontal (left) and vertical (right) direction for three cases, including longitudinal and transverse container impact

3.3.2. Debris impact loads on bridge deck

Horizontal and vertical loads

Figure 3-11 shows the time histories of the total horizontal and vertical debris impact forces on the deck for the three selected cases. For, a deck elevation of 0.5m (i.e. two lower cases), the tsunami bore reaches the deck before the container, which exerts purely hydrodynamic loading in both directions. As the container propagates inland and impacts the deck for the first time, it applies impulsive loads in both directions. In case of the longitudinal container, the exerted impact load on the deck with the largest elevation in the horizontal direction is significantly higher the corresponding force in the vertical direction, e.g., about 4.8 times the vertical load. For the two other cases, the magnitude of the horizontal impact force is about 1.5 times the uplift force. In addition, for the cases where the tsunami reaches the deck and the fluid particles is trapped between the debris and the deck, i.e. cases Long-0.5 and Trans-0.5, the magnitude of the horizontal impact force is significantly smaller than for the deck at higher elevation than the tsunami (i.e., Long-0.6), which can be attributed to the cushioning effect of the fluid. Another interesting finding can be reached from the figure is that the deck experiences several vertical impact loads after the primary impact which could exceed the initial magnitude by up to about 290% (e.g. case Long-0.6). Overall, the horizontal impact force is always maximized at the primary impact but the vertical impact can be maximized either at the initial impact or as the debris moves below the soffit. This demonstrates the need to consider different load cases in the design of a new bridge, as was done by Istrati et al, (2018) [23] for clear-water conditions that will account also for different impact locations along the width of the superstructure.

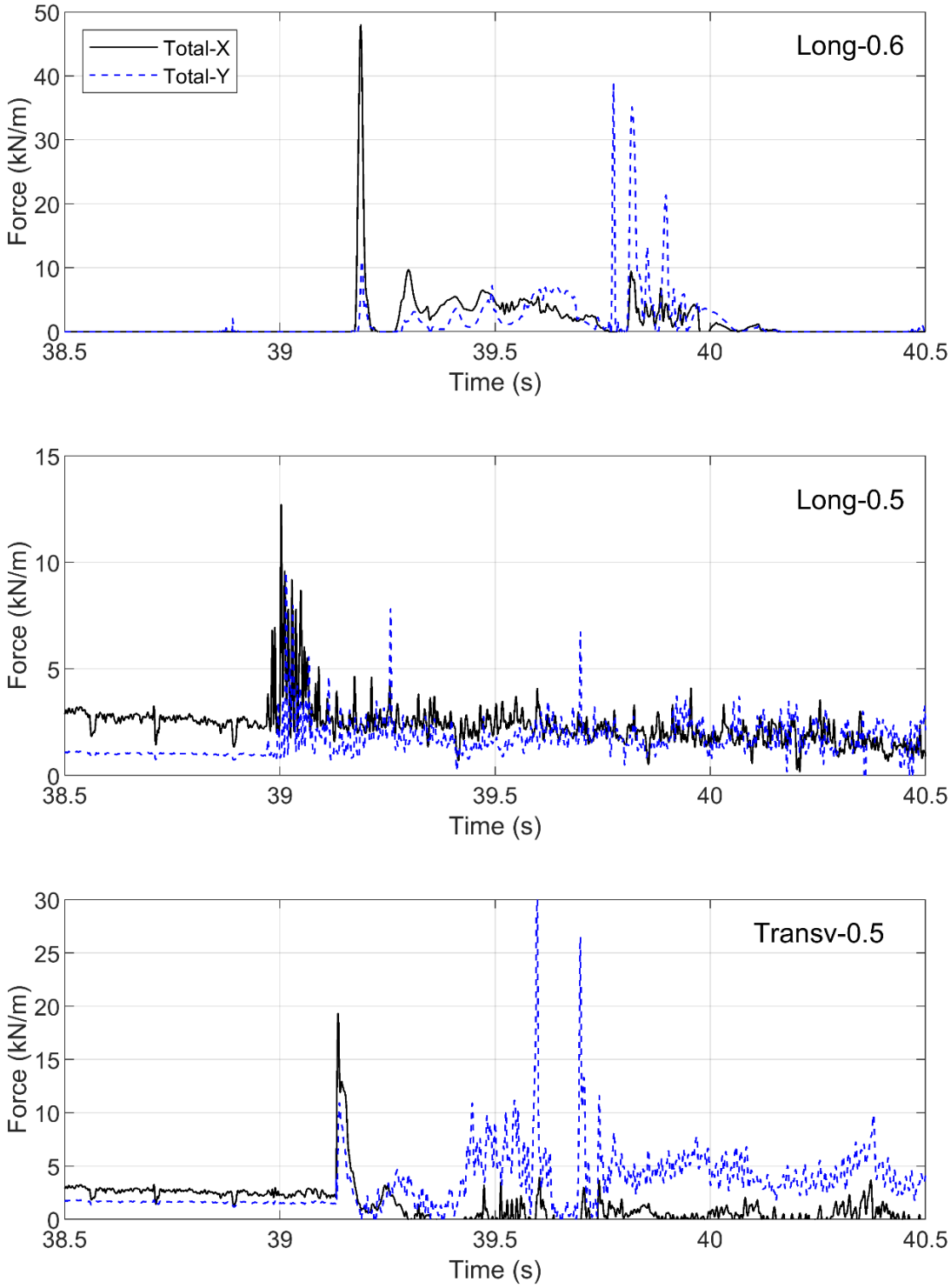

Figure 3-11 Applied horizontal and vertical force histories for three cases: Long_zb=0.6m (top), Long_zb= 0.5m (center) and Transv_zb =0.5m (bottom)

3.4. Conclusions

The present study conducted two-dimensional numerical simulations of the tsunami debris impact on a box-girder bridge deck using a multi-physics modeling approach, in which the fluid was modeled with particles via the SPH method and the debris, the bathymetry and the bridge deck were modeled as continuum elements via the FEM. In order to obtain a preliminary insight into the debris-tsunami-bridge interaction and the associated impact loads on the superstructure, two different orientations of a floating container and two deck elevations were investigated for a selected tsunami bore. While a much larger range of conditions is necessary for deciphering fully the complex interaction of floating debris with bridge decks, the multi-physics analyses presented herein provide preliminary evidence that:

- At least two different patterns exist in the debris-fluid-deck interaction: (i) the debris impacts the concrete slab of the offshore overhang or the web of the box-girder and remains there until the end of the inundation, while exerting several secondary impacts on different components of the offshore side of the superstructure, and (ii) the debris impacts the deck on the offshore face and then moves below the superstructure by exhibiting a complex flow pattern with significant rotation and multiple impacts on the soffit.

- The elevation of the deck and the initial orientation of the debris are the critical parameters that affect the movement of the debris below the deck and the debris-fluid-deck interaction. In fact, the transverse and longitudinal container exhibited a totally different debris-fluid-deck interaction and flow patterns around the deck for the same tsunami bore and initial water level. For example, the longitudinal container either remained trapped below the offshore overhang or it moved below the superstructure by initially rotating counter-clockwise up to 180 degrees and then rotating in the opposite direction as it passed below the soffit. On the other hand, the transverse debris kept rotating clockwise as it moved

below the superstructure exceeding the 180 degrees (total rotation of 400 degrees), which means that it rotates upside down, a situation that could cause damage to the non-structural components of the container.

- The debris has a vertical velocity at the instant of the primary impact on the deck, with a magnitude in the range of (20-27) % of the horizontal velocity at the same instant, resulting in a simultaneous application of both horizontal and uplift loads on the superstructure. The uplift load was in the range of (20-67) % of the horizontal impact load, highlighting the need to consider the impact in the vertical direction, which has not been done to date.

- When the debris moves below the deck, it can accelerate so much that it can reach (i) similar magnitudes of horizontal velocities as before the impact on the offshore face and (ii) vertical velocities that can be up to twice as large as the vertical velocity at the instant of the primary impact. This in turn can lead to the application of several vertical impact loads on the superstructure after the primary impact, the magnitude of which could exceed the initial magnitude by up to 290%.

- The horizontal impact force is always maximized at the primary impact on the offshore slab or web but the vertical one can be maximized either at the initial impact or at any other instant as the debris moves below the deck. This indicates the need to consider multiple load cases in future design guidelines, as was done in Istrati et al, (2018) [23] for clear-water conditions, in order to identify the critical case for the structure.

- For the situation where the tsunami reaches the deck and water is trapped between the debris and the deck, i.e. cases Long_zb=0.5 and Transv_zb=0.5, the magnitude of the horizontal impact load is much smaller than for decks at higher elevations which cannot be reached by the tsunami. In the former case the debris velocity drops gradually as it comes

in contact with the fluid and the deck, while in the latter case the debris velocity drops instantly, indicating that the trapped fluid has a ‘cushioning’ effect of the applied loads, which is beneficial for the structure.

In summary, the preliminary analyses reveal the complexity of the debris-tsunami-bridge interaction and associated loads on the superstructure, and highlight the need for further quantification and consideration in risk assessment frameworks of bridges. Follow-up studies should investigate a wider range of conditions (i.e. more water depths and bridge elevations) and include three-dimensional effects, in order to verify the validity of the presented findings or identify the range of their applicability.

3.5. Acknowledgements

This work was supported by the State of California through the Transportation System Research program of the Pacific Earthquake Engineering Research center (PEER). Any opinions, findings, and conclusions, or recommendations expressed in this paper are those of the authors and do not necessarily reflect those of the funding agency. The authors acknowledge Michael Scott from Oregon State University and Christos Papachristos from the University of Nevada, Reno for their support of the research project, and the Engineering Computing Team at the University of Nevada, Reno for providing computational support and resources that have contributed to the research results reported within this paper.

3.6. References

1. Azadbakht, Mohsen. (2013). Tsunami and hurricane wave load on bridge superstructures. PhD dissertation, Oregon State University, https://ir.library.oregonstate.edu/concern/graduate_thesis_or_dissertations/pg15bh86v
2. Saatcioglu, M., Ghobarah, A. and Nistor, I. (2006). Performance of structures in Indonesia during the 2004 Sumatra earthquake and tsunami, *Engineering Spectra, Earthquake Engineering Research Institute* (EERI), 22, 295-319. https://doi.org/10.1193/1.2209171
3. Rossetto, T., et al. (2007). “The Indian Ocean tsunami of December 26, 2004: Observations in Sri Lanka and Thailand.” *Nat. Hazards*, 42(1), 105–124.

4. Robertson, I., Chock, G., and Morla, J. (2010). “Tsunami effects of the February 27, 2010 Chile earthquake.” *EERI Preliminary Rep*., Earthquake Engineering Research Institute, Oakland, CA.
5. Araki, S.; Ishino, K.; Deguchi, I. (2010). Stability of girder bridge against tsunami fluid force. In Proceedings of the 32th International Conference on Coastal Engineering (ICCE), Shanghai, China, June 30- July 5, 2010.
6. Lau, T.L.; Ohmachi, T.; Inoue, S.; Lukkunaprasit, P. (2011). Experimental and Numerical Modeling of Tsunami Force on Bridge Decks; InTech: Rijeka, Croatia, 2011; pp. 105–130.
7. Hoshikuma, J.; Zhang, G.; Nakao, H.; Sumimura, T. (2013). Tsunami-induced effects on girder bridges. In Proceedings of the Inter-national Symposium for Bridge Earthquake Engineering in Honor of Retirement of Professor Kazuhiko Kawashima, Tokyo, Japan, March 2013.
8. P. Lomonaco, D. Istrati, T. Maddux, I.G. Buckle, S. Yim, T. Xiang (2016): “Large-scale testing of tsunami impact forces on bridges”. Proc. 6th Intl Conf on the Application of Physical Modelling in Coastal and Port Eng and Science (Coastlab16), Ottawa, Canada, May 10-13, 2016, DOI: 10.13140/RG.2.1.5184.2160
9. Istrati, D. (2017). Large-Scale Experiments of Tsunami Inundation of Bridges Including Fluid-Structure-Interaction. Ph.D. Thesis, University of Nevada, Reno, NV, USA, 2017. Available online: https://scholarworks.unr.edu//handle/11714/2030 (accessed in May 2020).
10. Zhu, M.; Elkhetali, I.; Scott, M.H. (2018). Validation of OpenSees for tsunami loading on bridge superstructures. J. Bridge Eng. 2018, 23, 04018015. https://doi.org/10.1061/(ASCE)BE.1943-5592.0001221
11. Bricker, J.D.; Nakayama, A. (2014). Contribution of trapped air deck superelevation, and nearby structures to bridge deck failure during a tsunami. *J. Hydraul. Eng*. 2014, 140, 05014002, https://doi.org/10.1061/(ASCE)HY.1943-7900.0000855
12. Istrati, D., Buckle, I.G. (2019): “Role of Trapped Air on the Tsunami-Induced Transient Loads and Response of Coastal Bridges”, *Geosciences journal*, MDPI, 9 (191), https://doi.org/10.3390/geosciences9040191
13. Istrati, D., Buckle, I. G., Lomonaco, P., Yim, S., & Itani, A. (2017a). Tsunami induced forces in bridges: large-scale experiments and the role of air-entrapment. Coastal Engineering Proceedings, (35), 30-30. https://doi.org/10.9753/icce.v35.structures.30
14. Istrati, D., Buckle, I., Lomonaco, P., Yim, S., & Itani, A. (2016). Large-scale experiments of tsunami impact forces on bridges: The role of fluid-structure interaction and air-venting. In The 26th International Ocean and Polar Engineering Conference. OnePetro.
15. Bradner, C.; Schumacher, T.; Cox, D.; Higgins, C. (2010). Experimental setup for a large-scale bridge superstructure model subjected to waves. *J. Waterw. Port Coast. Ocean* Eng. 2010, 137, 3–11. https://doi.org/10.1061/(ASCE)WW.1943-5460.0000059
16. Istrati D, Buckle IG (2014): Effect of fluid-structure interaction on connection forces in bridges due to tsunami loads. *Proc 30th US-Japan Bridge Engineering Workshop*, Washington DC, United States, https://www.pwri.go.jp/eng/ujnr/tc/g/pdf/30/30-10-2_Buckle.pdf (accessed in May 2020)
17. D. Istrati, I.G. Buckle, A. Itani, P. Lomonaco, S. Yim (2017b): “Large-scale FSI experiments on tsunami-induced forces in bridges”. 16th World Conf. Eq. Eng., Santiago, Chile, Jan. 9-13, 2017, https://www.wcee.nicee.org/wcee/article/16WCEE/WCEE2017-2579.pdf
18. Motley, M. R., Wong, H. K., Qin, X., Winter, A. O., & Eberhard, M. O. (2016). Tsunami-induced forces on skewed bridges. Journal of Waterway, Port, Coastal, and Ocean Engineering, 142(3), 04015025. https://doi.org/10.1061/(ASCE)WW.1943-5460.0000328
19. Istrati, D., & Buckle, I. G. (2021a). Tsunami Loads on Straight and Skewed Bridges–Part 1: Experimental Investigation and Design Recommendations (No. FHWA-OR-RD-21-12). Oregon. Dept. of Transportation. Research Section. https://rosap.ntl.bts.gov/view/dot/55988
20. Istrati, D.; Buckle, I.G. (2021b). Tsunami Loads on Straight and Skewed Bridges–Part 2: Numerical Investigation and Design Recommendations (No. FHWA-OR-RD-21-13). Oregon. Dept. of Transportation. Research Section, 2021. https://rosap.ntl.bts.gov/view/dot/55947

21. Azadbakht, M.; Yim, S.C. (2015). Simulation and estimation of tsunami loads on bridge superstructures. J. Waterw. Port Coast. Ocean Eng. 2015, 141, 04014031, https://doi.org/10.1061/(ASCE)WW.1943-5460.0000262.
22. Xiang, T.; Istrati, D.; Yim, S.C.; Buckle, I.G.; Lomonaco, P. (2020). Tsunami loads on a representative coastal bridge deck: Experi-mental study and validation of design equations. J. Waterw. Port Coast. Ocean Eng. 2020, 146, 04020022. https://doi.org/10.1061/(ASCE)WW.1943-5460.0000560.
23. Istrati, D., Buckle, I.G., A., Lomonaco, P., Yim, S. (2018): "Deciphering the Tsunami Wave Impact and Associated Connection Forces in Open-Girder Coastal Bridges", Journal of Marine Science and Engineering, 2018, MDPI, 6 (148). https://doi.org/10.3390/jmse6040148.
24. Como, A., and Mahmoud, H. (2013). "Numerical evaluation of tsunami debris impact loading on wooden structural walls." *Engineering. Structures*., 56, 1249–1261. https://doi.org/10.1016/j.engstruct.2013.06.023.
25. Ko, H.; Cox, D. (2012). OSU: 1-D Hydraulic Experiment, Aluminum, Water depth = 266.4 cm. DesignSafe-CI 2012. https://doi.org/10.4231/D3KH0DZ8Z.
26. Shafiei, S., Melville, B. W., Shamseldin, A. Y., Adams, K. N. and Beskhyroun S. (2016). "Experimental investigation of tsunami-borne debris impact force on structures: Factors affecting impulse-momentum formula." *Ocean Engineering* 127 (2016): 158-169. DOI: 10.1016/j.oceaneng.2016.09.008.
27. Goseberg, N.; Stolle, J.; Nistor, I.; Shibayama, T. (2016). Experimental analysis of debris motion due the obstruction from fixed obstacles in tsunami-like flow conditions. Coast. Eng. 2016, 118, 35–49, https://doi.org/10.1016/j.coastaleng.2016.08.012.
28. Hasanpour, A.; Istrati, D. (2021). Reducing extreme flooding loads on essential facilities via elevated structures, ASCE Lifelines Conference 2021-22, University of California, Los Angeles, 2021.
29. Yang, W. C. (2016). Study of Tsunami-Induced Fluid and Debris Load on Bridges using the Material Point Method. *Doctoral dissertation*, University of Washington. http://hdl.handle.net/1773/37064.
30. Oudenbroek, Kevin, Nader Naderi, Jeremy D. Bricker, Yuguang Yang, Cor Van der Veen, Wim Uijttewaal, Shuji Moriguchi, and Sebastiaan N. Jonkman. (2018). "Hydrodynamic and debris-damming failure of bridge decks and piers in steady flow." *Geosciences* 8, no. 11 (2018): 409. https://doi.org/10.3390/geosciences8110409.
31. Istrati, D., Hasanpour, A., Buckle, I.G. (2020): "Numerical investigation of tsunami-borne debris damming loads on a coastal bridge", 17th World Conf Earthq Engineering, Sendai, Japan.
32. Hasanpour, A.; Istrati, D.; Buckle, I. (2021). Coupled SPH–FEM Modeling of Tsunami-Borne Large Debris Flow and Impact on Coastal Structures. Journal of Marine Science and Engineering, 9(10), 1068. https://doi.org/10.3390/jmse9101068.
33. St-Germain, P.; Nistor, I.; Townsend, R.; Shibayama, T. (2014) Smoothed-particle hydrodynamics numerical modeling of structures impacted by tsunami bores. J. Waterw. Port Coast. Ocean Eng. 2014, 140, 66–81. https://doi.org/10.1061/(ASCE)WW.1943-5460.0000225.
34. Monaghan, J.J., & Kos, A., (1999). Solitary waves on a Cretan beach. J. Waterw. Port Coast. Ocean Eng. 125, 145–155. https://doi.org/10.1061/(ASCE)0733-950X(1999)125:3(145).
35. He, F., H. Zhang, C. Huang, and M. Liu. (2020). "Numerical Investigation of the Solitary Wave Breaking over a Slope by Using the Finite Particle Method." Coastal Engineering 156: 103617. doi: 10.1016/j.coastaleng.2019.103617.
36. Altomare, C., Crespo, A. J., Domínguez, J. M., Gómez-Gesteira, M., Suzuki, T., & Verwaest, T. (2015). Applicability of smoothed particle hydrodynamics for estimation of sea wave impact on coastal structures. *Coastal Engineering*, *96*, 1-12. https://doi.org/10.1016/j.coastaleng.2014.11.001.

37. Gómez-Gesteira, M., & Dalrymple, R.A., (2004). Using a three-dimensional Smoothed Particle Hydrodynamics method for wave impact on a tall structure. J. Waterw. Port Coast. Ocean Eng. 130, 63–69. https://doi.org/10.1061/(ASCE)0733-950X(2004)130:2(63).
38. Gingold, R. A., and Monaghan, J. J. (1977). "Smoothed particle hydrodynamics: Theory and application to non-spherical stars." Mon. Not. R. Astron. Soc., 181, 375–389. https://doi.org/10.1093/mnras/181.3.375.
39. Lucy, L. B. (1977). "A numerical approach to the testing of the fission hypothesis." Astron. J., 82, 1013–1024. DOI: 10.1086/112164.
40. Hallquist, J.O. LS-DYNA theory manual. Liverm. Software. Technol. Corp. 2006, 3, 25–31.
41. Monaghan, J. J. (1994). Simulating free surface flows with SPH. Journal Computational Physics, 110: 399-406. https://doi.org/10.1006/jcph.1994.1034.
42. Petschek, A.G.; Libersky, L.D. Cylindrical smoothed particle hydrodynamics. J. Comput. Phys. 1993, 109, 76–83, https://doi.org/10.1006/jcph.1993.1200.
43. Monaghan, J.J.; Gingold, R.A. Shock simulation by the particle method SPH. J. Comput. Phys. 1983, 52, 374–389, https://doi.org/10.1016/0021-9991(83)90036-0.
44. Xu, J.; Wang, J. Node to node contacts for SPH applied to multiple fluids with large density ratio. In Proceedings of the 9th European LS-DYNA Users' Conference, Manchester, UK, June 3, 2013; pp. 2–4.
45. Ko, H. (2013). Hydraulic Experiments on Impact Forces from Tsunami-Driven Debris. Master's Thesis, Oregon State University, Corvallis, OR, USA, 2013.
46. Thomas, S., & Cox, D. (2012). Influence of finite-length seawalls for tsunami loading on coastal structures. Journal of waterway, port, coastal, and ocean engineering, 138(3), 203-214. https://doi.org/10.1061/(ASCE)WW.1943-5460.0000125
47. FEMA P646. *Guidelines for Design of Structures for Vertical Evacuation from Tsunami*; Federal Emergency Management Agency: Washington, DC, USA, 2012.
48. American Society of Civil Engineers (ASCE). *Minimum Design Loads and Associated Criteria for Buildings and Other Structures; ASCE/SEI 7-16*; American Society of Civil Engineers (ASCE): Reston, VA, USA, 2016

Chapter 4

4. Three-Dimensional Investigation of Floating Debris Effects on Bridge Superstructures During Tsunamis

Abstract

As coastal communities continue to grow and catastrophic tsunamis continue to occur around the world, understanding the complex tsunami-structure-interaction and the induced effects on coastal structures becomes increasingly important. Despite the extremely valuable progress made towards advancing the understanding of tsunamis in the last decade, cascading effects like the impact of large water-borne debris on structures and especially on bridges, are still poorly understood. Therefore, the objective of the present study is to cover the existing knowledge gap and evaluate the effects of tsunami-borne floating containers on bridge superstructures. A coupled SPH-FEM modeling approach is first calibrated and validated with prior experiments of debris impact on a column, and then used for conducting an extensive three-dimensional investigation that sheds light on the debris-flow-bridge interaction phenomenon and the associated forces. The SPH-FEM numerical results demonstrate that the initial water level, the elevation of the bridge and the bore properties have a significant and complex effect on the debris trajectories, velocity and pitching, as well as, the loads on the deck. In fact, it is revealed that there exist three different patterns in the debris-flow-deck interaction of transverse containers; A) the container impacts the offshore side of the superstructure and moves below it, which in some cases can lead to secondary impacts below the soffit that generate uplift loads, B) the container moves above the deck, which could potentially impact the top surface of the deck and generate downward loads and C) the debris is trapped below the offshore overhang and remains there generating repetitive local impacts on the web or the overhang. It is noteworthy that in the cases that the bore is high enough to reach the superstructure, reflection occurs on the offshore side of the bridge, leading to significant reduction of the debris impact velocity. This explains why bridges with higher elevations that have phenomenally less exposure to tsunamis, witness larger impact loads than lower bridges, when the tsunami flow passes

below the superstructure but the debris can reach it. Interestingly, in addition to a horizontal velocity (Vx) the debris has also a vertical velocity (Vz) at the instant of impact, which can be up to 93% of the horizontal one, generating impulsive bridge forces in both directions, a fact that has not be recognized to date in the literature. Overall, the presence of the debris increased the total forces by a factor of 2.67 and 1.85 on average in the two directions, while the maximum observed increase was 550% and 450% respectively, demonstrating the need to consider such effects in future design guidelines and risk assessment frameworks.

Keywords: Tsunami; Debris; SPH; Wave; Deck; Coastal structure; Numerical modeling; Fluid-structure intercation

4.1. Introduction

Urban intensification of coastal zones has been continuously growing which increases the vulnerability of coastal structures to extreme hydrodynamic events such as tsunamis. Tsunami events can cause damage or failure of important infrastructure, such as bridges, which is critical due to the significant role of these structures in emergency services in the aftermath of the event. A total of 1,100 km of coastline was affected and 81 bridges were washed away as a result of the 2004 Indian Ocean tsunami [1]. The Great East Japan tsunami resulted in widespread damage of about USD211 billion and in the washout of about 252 bridges [2,3]. As a tsunami wave propagates inland, it could entrain and transport debris in different shapes and sizes which could lead to a significant increase in the impact and damming loads increasing consequently the likelihood of damage. According to post-surveys, coastal structures should be capable of withstanding the loads associated with water-borne debris such as shipping containers which affect their safety and serviceability [4-6]. Moreover, FEMA has also outlined the catastrophic effect of debris and reported that about 27% of the total disaster recovery costs in the United States are attributed to the existence of water-borne debris [7]. Therefore, developing an understanding of the tsunami-debris-

structure interaction and quantifying properly the associated loads is important in order to enhance the performance and resilience of coastal bridges and lessen the extent of damage during such extreme events.

To this end several experimental and numerical studies have been carried out to investigate the tsunami inundation mechanism of bridges and the corresponding hydrodynamic forces [8-15]. Some studies assessed (i) the role of the air-entrapment below the deck of open-girder bridges [16-18], revealing that it alters the fluid flow in the chambers and the fluid-structure interaction leading to a different pattern of horizontal and vertical pressures, and (ii) the efficiency of air-venting [11, 19], which was seen to be dependent on the number of venting holes. Moreover a few studies focused on the dynamic fluid-structure interaction of flexible bridges [20, 21], revealing the possibility of dynamic amplification, while others focused on the development of simplified predictive load equations [22, 23] and design methodologies with multiple load cases that can capture both the forces and the overturning moment [24]. Although the aforementioned studies focused on fundamental aspects and design procedures, some studies investigated the vulnerability, risk and resilience of bridges and transportation networks to tsunamis [25, 26] and other extreme flooding events [27-30].

The assumption in most of the past work was that the bridge was straight and the flow impacted the span at a normal angle, which enabled the simplification of the phenomenon as a two-dimensional problem. However, a few studies investigated more complex cases with significant three-dimensional effects, including skewed bridges [31, 32] and straight bridges impacted by oblique flows or waves [33, 34] revealing the generation of out-of-plane forces, as well as, roll and yaw moments that do not exist in simplified 2D conditions and can increase the risk of failure.

The majority of the past studies focused mainly on clear-water conditions, as shown above. However, field surveys conducted in the aftermath of major events including the 2004 Indian Ocean Tsunami and the 2011 Japan Tsunami revealed that the cause of damage to coastal structures in tsunami-prone areas is not limited to hydrodynamic loads but is affected by water-borne debris loads as well [35-38]. In recent years, several studies have been carried out to investigate the dynamics and impact of water-borne debris. According to experimental studies carried out by Haehnel and Daly (2004) [39] and Matsutomi (2009) [40], the maximum debris impact force depends on the debris mass, the impact velocity, and the effective stiffness. Arikawa et al., (2007) [41] carried out an experimental study to explore the impact of a 1:5 scale model of a shipping container under air and tsunami conditions and proposed an empirical formula based on the Hertz theory to calculate the impact force. The performance of RC columns against the impact loads from water-borne shipping containers was investigated by Madurapperuma and Wijeyewickrema (2012) [42] and a linear relationship between the maximum impact force and container velocity up to 2m/s was reported. Ko et al., (2015) [6] conducted a series of experiments to study the impact of a 1:5 scale shipping container on a column and concluded that the peak impact force in water was about 1.2 times the corresponding impact force in the air. However, in another experimental study, it was observed that the cushioning of trapped water between the debris and the vertical wall reduced the impact energy and force [43].

Shafiei (2016) [44] developed an equation to estimate the debris velocity based on the relative distance of debris pick-up location and the structure. Goseberg et al., (2016) [45] conducted an experimental study focusing on the motion of a 1:40 scaled model of a shipping container and observed that the debris tends to rotate toward an equilibrium position as it propagates inland with the long axis being perpendicular to the flow direction. Kennedy et al. (2017) [46] conducted a post-event field survey to identify the transport of blocks and boulders during Super Typhoon

Hayian and found that the movement of such large objects strongly exceeded the maximum values suggested in the literature. Derschum et al., (2018) [47] conducted a 1:40 scaled experimental study to investigate the impact of a shipping container on a vertical structure and reported that the initial orientation of the debris did not have a considerable effect on the debris impact load on the structure. More recently, Park et al (2021) [48] investigated experimentally the tsunami-driven debris spreading with different densities and debris elements, and found that the less dense debris had a higher probability of collision with the obstacles. Similarly, Hou et al. (2022) [49] investigated the influence of the layout of the shipping containers on the spreading and maximum propagation distance inland, and showed that the number of container rows, columns and stacking height are the critical parameters.

Although considerable amount of experimental work and field surveys related to water-borne debris have been conducted, the numerical studies are significantly fewer due to the associated computational challenges. For example, Como and Mahmoud (2013) [50] conducted a numerical assessment of the tsunami debris loading on wooden structural walls using the Arbitrary Lagrangian Eulerian (ALE) method. To overcome some of the existing challenges, a coupled approach between the Smoothed Particle Hydrodynamics (SPH) and the Discrete Element Method (DEM) was developed to simulate (i) the tsunami effects on a port with shipping containers in Portugal [51] and (ii) the block-fluid interaction during dam break bores [52], revealing the promising performance of such coupled methods. Similarly, Ruffini et al., (2021) [53] used a coupled approach between Duals Physics and Chrono and reported that the model is accurate to regenerate the floating debris dynamics (trajectory and velocity) of past experiments. In the same year a tsunami Hakathon was held in Japan [54], during which blind predictions of the transport of three container models under a tsunami-like bore were made. The results from four different numerical models were produced and compared to each other and the experiments, revealing considerable

differences and the need to (i) model accurately the flow field and (ii) use a two-way coupling in order to capture the interaction between the multiple debris. In addition to the two latter studies that focused mainly on simulating the debris dynamics, Hasanpour et al. (2021) [55] employed a numerical approach that coupled the SPH with the finite element method (SPH-FEM) and demonstrated its accuracy in simulating both the tsunami-borne debris transport and the impact on a coastal structure via comparison with two-dimensional large-scale experiments. Using the validated method, further insight into the tsunami debris effects was achieved, such as, the occurrence of a non-normal impact on the coastal structure and the existence of a non-linear force-velocity trend for small water depths. Despite these few successful numerical studies, Reis et al. (2022) [56] mentioned the challenging nature of simulating tsunami-borne debris and the importance of making progress in this field in order to be able to move towards an integrated framework for the risk assessment of coastal structures exposed to earthquake-induced tsunamis.

All the aforementioned studies focused either on the debris transport or on the debris impact on simplified vertical structures, building-like structures and walls. The number of studies that have investigated the debris effects on bridges is much lower. Yang (2016) [57] used the material point method to investigate the debris loads on bridge superstructures and reported that the debris impact forces in water could be up to 35% higher than the corresponding in-air cases. Oudenbroek et al., (2018) [58] conducted numerical and experimental investigations to study the damming of superstructures by wooden logs and the induced structural failure. It was reported that the bridge stability is affected by the presence of the logs via generation of additional drag and uplift forces. In addition, other studies have also focused on water-borne wooden logs during extreme floods, such as, the study of Majtan et al., (2021) [59] that investigated the impact forces on a masonry arch bridge using the SPH method and the studies of Panici and Alameida (2019) [60] and Zhang et al. (2021) [61] that evaluated experimentally the formation of woody debris jam at bridge piers.

Similarly, Istrati and Hasanpour (2022) [62] focused also on bridges piers but they investigated numerically the water-borne debris impact loads during dam break-induced extreme flows and reported that the debris impulsive loads are 6 to 10 times larger than the fluid force. In regards to tsunamis, Istrati et al., (2020) [63] carried out a three-dimensional FEM-based computational fluid dynamic analyses to investigate the container-induced damming loads on a coastal bridge and demonstrated that although the damming does not have a significant effect on the applied horizontal and vertical forces, it has a major effect on the overturning moment, yaw and roll moments, which lead to concentration of the forces in individual structural components increasing consequently the likelihood of damage. Last but not least, the most recent study of tsunami-borne debris impact on bridge superstructures was conducted by Hasanpour et al. (2022) [64], which documented a very complex debris-flow-bridge interaction with multiple impulsive loads applied at different locations around the deck, however, the study was limited to two dimensions.

Despite the availability of plethora of studies on clear water tsunami conditions and on the effect of wood logs and large debris impact on building-like structures, the available investigations of tsunami-borne container impact on coastal bridges is extremely limited. Considering the catastrophic consequences and disruptions of past tsunami events with entrained debris, and the critical role of transportation networks, it is essential to decipher the complex debris-flow-bridge interaction and quantify the associated loads. Therefore, the main objective of this manuscript is to shed light on the latter topics via advanced three-dimensional numerical simulations of a transverse debris impacting a box-girder bridge, which is a common type of superstructure in coastal areas, such as the West Coast of the United States.

4.2. Methodology

4.2.1. Description of numerical method

The Smoothed Particle Hydrodynamics, which is the numerical method used in the current study, was originally invented to deal with astronomical problems [65]. SPH is a Lagrangian meshless technique, in which the fluid domain is represented by a set of non-connected particles. The particles carry individual material properties and move and interact with others within the computational domain according to conservation governing equations derived from the Navier-Stokes equations (NS). The SPH technique employed in this investigation is available in LS-DYNA [66] and is based on weakly compressible smoothed particle hydrodynamics. This computational method can deal with problems of large deformations and distorted free-surface making it suitable for modeling highly non-linear free-surface motions [67]. Using a coupled SPH-FEM approach even more complex multi-physics problems can be investigated, such the debris-flow-structure interaction (Hasanpour et al., 2021). The SPH formulation is made up of two parts. The first part is the Kernel approximation which presents the integral form of the governing equations and has the following form [66, 67]:

$$< f(x) >= \int_{\Omega} f(x')W(x - x', h)dx' \qquad \text{Equation 4.1}$$

where $f(x)$ is a continuous function of the three-dimensional position vector x; $W(x - x', h)$ is the smoothing function and h is the smoothing length.

The second part is the particle approximation, which represents the entire computational domain Ω by finite number of particles. The Kernel approximation is transformed to the Equation 4.2, using the weighted average of the neighboring particles in its discretized form [66]:

$$< f(x_i) >= \sum_{j=1}^{n} \frac{m_j}{\rho_j} f(x_i)\, W(\, x_i - x_j, h) = \sum_{j=1}^{n} \frac{m_j}{\rho_j} f(x_j)\, W_{ij,} \quad \text{Equation 4.2}$$

where $f(x_j)$ is the physical value at the *j*th position, i is the number of any particle in the domain; n is the total number of particles within the influence area of the particle at i; and m_j and ρ_j are the mass and density associated with particle *j*.

The implemented SPH method in LS-DYNA is based on weakly compressible smoothed hydrodynamics (WCSPH). For the weakly compressible fluids, according to the variation in density and internal energy of fluid particles, the dynamic fluid pressures are calculated using an equation of state (EOS) given in Equation (3) [66]:

$$P = k_0[(\frac{\rho}{\rho_0})^{\Upsilon} - 1] \quad \text{Equation 4.3}$$

where ρ_0 denotes the reference water density, ρ is the current density, Υ is equal to 7 for water, and k_0 is used to control the maximum fluctuations of pressure, and is usually taken as follows [67]:

$$c_0 = \sqrt{\frac{\Upsilon k_0}{\rho_0}} \geq 10\, v_{max} \quad \text{Equation 4.4}$$

where c_0 is the speed of sound in water at the reference density.

Penalty-based contact algorithms are utilized to define the interface between the SPH and FE parts, in which the particles are treated as the slave and other elements as the master. To treat the interaction between SPH and FE parts, the particles are considered as nodes, and the FE parts as surface. When the fluid particles come into contact with the surface,

each slave node is searched for penetration and if the slave node penetrates, a resisting force is applied to eliminate further penetration. The resisting force is stated by [66]:

$$f=kdn \qquad \text{Equation 4.5}$$

where d is the penetration distance, n is the surface normal vector and k is a penalty factor. The stiffness factor k for master segment s_i is given in terms of the bulk modulus K_i, the volume V_i, and the face area A_i of the element that contains s_i as

$$k_i = \frac{A_i K_i f_{si}}{max\ (shell\ diagonal)} \qquad \text{Equation 4.6}$$

where f_{si} is a scale factor for the interface stiffness and is defined equal 10. The constant k should be set large to minimize penetration and instabilities, but it should not be too large that it generates artificially large forces. As the contact location and the direction may be difficult to predict, the automatic contacts are recommended, since they can detect the penetration at each time step, irrespective of whether it is coming from the slave or master part. The automatic contacts determine the contact surface by projecting normally from the shell mid-plane to a distance equal to half of the contact thickness. It must be noted that the solver can simulate the contact between flexible structures, rigid and flexible structures, or between rigid bodies only. Interestingly, even in the case of rigid bodies where the deformations are not calculated, it is possible to define a bulk modulus at the material level, which enables the user to adjust the contact parameters (e.g., contact stiffness) and avoid numerical spikes in the contact forces.

The interaction between the FE elements with each other is defined through a two-way treatment of contact in which both slave and master segments are checked for penetration. This type of contact is symmetric and the definition of the slave and master surfaces are arbitrary. As the prediction of the contact location and the direction may be difficult to conclude, the automatic contacts are recommended, since they can detect the penetration at each time-step, irrespective of whether it is

coming from the slave or master part. The automatic contacts determine the contact surface by projecting normally from the shell mid-plane to a distance equal to half of the contact thickness.

4.2.2. Validation with experiments of container impact on coastal structure

To evaluate the accuracy of the SPH-FE numerical method, the experimental investigation of Shafiei (2016) [68] was selected as a benchmark. The experiments were carried out at a 14 m long, 1.2 m wide, and 0.8 m deep wave flume. The volume of water released during an experiment was from 1 up to 3 m^3. For the experiments, three different bores were generated, namely a "weak" bore (B1) with a water depth of 400 mm, a "moderate" bore (B2) with a water depth of 500 mm, and a "strong" bore (B3) with a water depth of 600 mm were generated. The coastal structure was represented by a 0.3 m×0.3 m×0.6 m square prism located 10m downstream from the gate. Rigid disk and box-shaped devices were used as floating debris. The disk had an outer diameter of 0.2 m, the thickness of 0.05 m, the mass of 500 g and the density of 318 kg/m^3 and the box has a cross-section of 0.1 m×0.1m×0.3 m, the mass of 510g and, density of 170 kg/m^3. The debris devices were placed 2m upstream of the structure, on the flume floor and were free to move in all directions.

To measure the bore heights five wave gauges were used. The first wave gauge was positioned 2.5 m downstream from the gate, with the remaining wave gauges equally spaced 1.75 m apart from each other over a total distance of 9.5 m downstream from the gate. The average bore velocity was calculated using the recorded time at which the bore front reached each wave gauge.

A three-dimensional (3D) numerical model of the experimental setup was generated, using particles (SPH) for the fluid, and finite elements (FE) for the flume walls, the debris, and the structure. In the numerical model the length of the reservoir was selected to be 4.2m in order to match the maximum volume of water (3 m^3) released during the experiment when the water level in the reservoir was 0.6m. Therefore, the 3D numerical flume with a total length of 18.2 m was developed

as shown in Figure 1. It must be mentioned that although the experimental work had a wide range of debris objects, the current paper presents selected results of the disk debris, because it was the debris shape with the most characteristic 3D effects due to its circular shape. The final 3D numerical model had a 1 cm particle size and 1cm FE mesh size, consisted of 632,848 shell elements and 3,049,163 SPH particles.

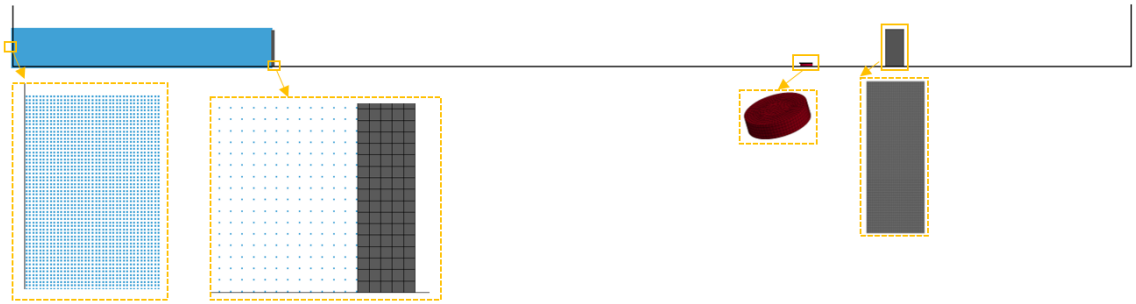

Figure 4-1 Cross section of the computational domain (top), numerical models with the gate, the debris, and the column

The accuracy of the numerical approach is evaluated by comparing the results of free-surface and fluid particle velocities at different locations along the flume with experimental data measured by Shafiei (2016) [68]. Figure 4-2 demonstrates the variation of the free-surface and fluid velocity and the corresponding average velocity at every experimental wave gauge position. It can be observed that the numerically calculated free-surface at each wave gauge position is in good agreement with experimental data and the overall trends are reproduced with good accuracy. The average deviation from the maximum value is 5% and the over predictions do not exceed 4% for the selected bore height. In terms of the fluid velocity, for the selected bore, the average velocity is 2.45m/s and 2.5 m/s for the experimental and numerical simulations, respectively. By comparing the measured and calculated velocity percentage errors of about 2% are found. The encouraging thing is that at each wave gauge location, the numerical model gives a close match with the experimental data in terms of the instant of the bore arrival, which is an important factor for the initiation of the debris entrainment and transport in the dam break flow. The observed trend verifies the ability of the

three-dimensional coupled SPH-FEM technique to capture the interaction of the fluid with the flume wall and predict the free-surface and the average fluid velocity during the bore propagation with good accuracy.

Figure 4-3 shows time-series of the disk velocity and impact force on the column Good agreement with the experimental was achieved, with the maximum deviation from the measured maximum disk velocity being 3%. In terms of the disk impact force, the agreement between the computations and the physical test is reasonable. Although there exist noticeable differences in the temporal evolution of the force histories before the arrival of the debris at the structural location, i.e. when the column is impacted only by the bore (time between 2.85s and 2.95s), the agreement is surprisingly good when the debris starts interacting with the column and the deviation of the maximum values is only 2.26%. The observed trends reinforce our confidence in the three-dimensional coupled SPH-FEM modeling approach to simulate and capture the bore propagation, debris velocity and debris-structure interaction with good accuracy.

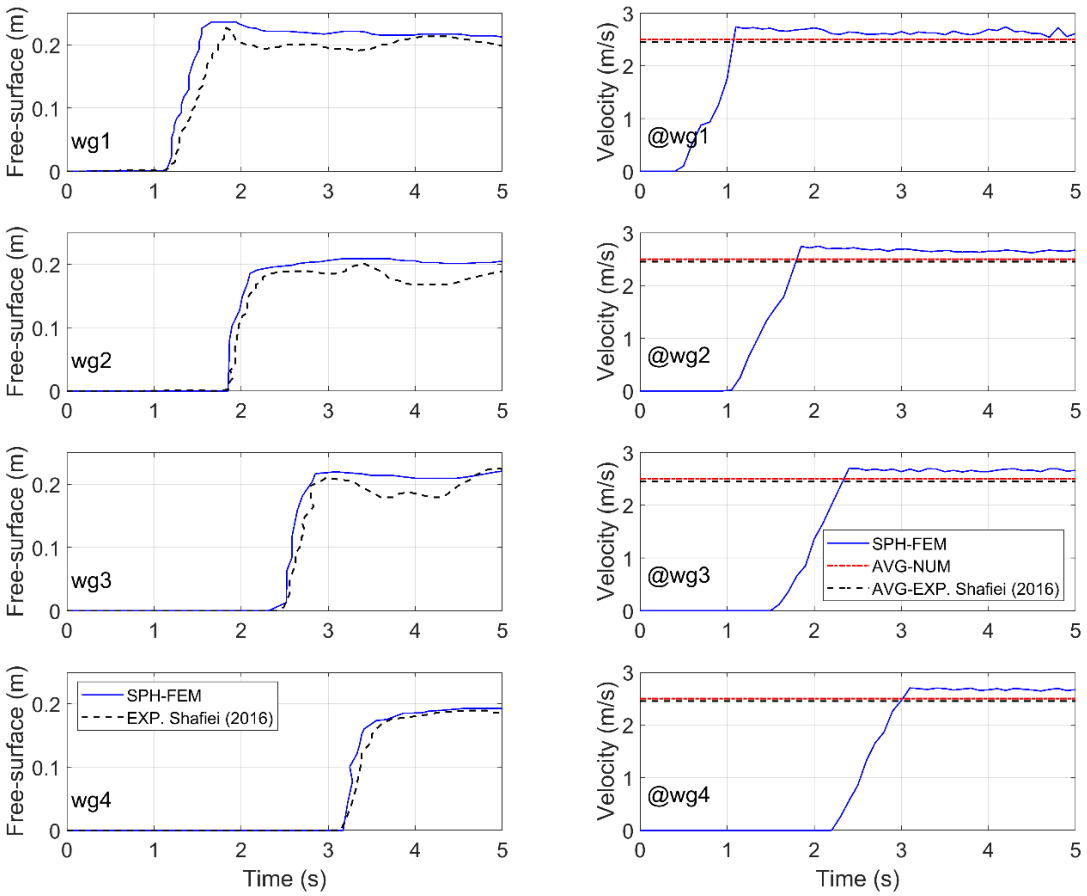

Figure 4-2 Variation of the free surface and fluid velocity at different locations along the flume. Experimental [68] and numerical results for the strong bore (B3)

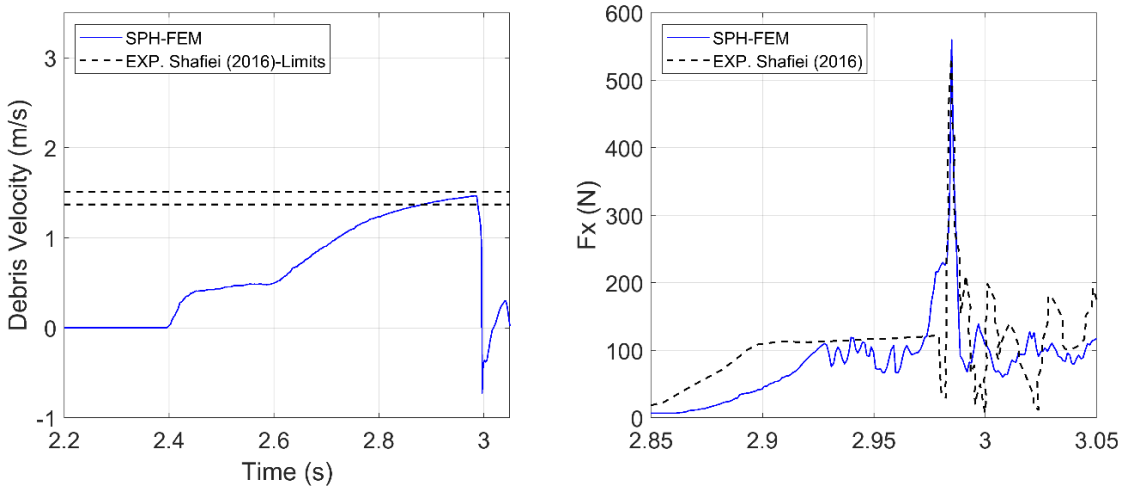

Figure 4-3 Comparison of the disk debris velocity and impact force: experimental test [68]and numerical simulation for the strong bore (B3)

4.2.3. Three-dimensional numerical model of single debris impact on a box-girder bridge

In order to quantify large debris impact on bridge decks subjected to extreme hydrodynamic events such as tsunamis, the validated numerical model of the previous section was considered as a baseline model and additional modifications were made. First, the coastal structure was replaced by a bridge deck with a scaled-down length of 0.5 m, and height of 0.13 m, which follows the dimensions of the deck used in the previous large-scale hydrodynamic tests [14]. Second, the floating debris was represented by a standard shipping container with typical full-scale dimensions of 6.1 m long, 2.6 m wide and 2.6 m tall. Based on the length scale of 1:20, the dimensions of the model container are 0.30 m long, 0.13 m wide and 0.13 m tall. Moreover, in order to ensure the availability of an adequate volume of water to pick up and transport the floating debris and to achieve a steady-state condition before the water in the reservoir finishes, the length of the reservoir for the numerical investigation was increased from 4.2m to 10m. Lastly, in order to avoid potential boundary effects from the outlet (e.g. distorted velocities or reflected bores, which could be large enough to generate subsequent motion to the debris and affect both the debris dynamics and the debris-wave-bridge interaction), the outlet was moved 2 m towards the right elongating the flume further. Also, an artificial beach with a 1:12th slope was added for energy dissipation, followed by an empty reservoir that gathered the released water after it passed the bridge. Therefore, the final numerical model had a total length of 36 m (including the end reservoir) and a width of 1.2 m. Figure 4 illustrates the cross-section of the three-dimensional developed numerical model. The model consisted of 969,908 shell elements and 4,203,331 SPH particles. All the computational analyses were run on the “Multihaz” high-performance computing (HPC) cluster at the University of Nevada, Reno using up to 80 cores per analysis. The analysis time ranged between 78 and 110hrs depending on the hydrodynamic characteristics.

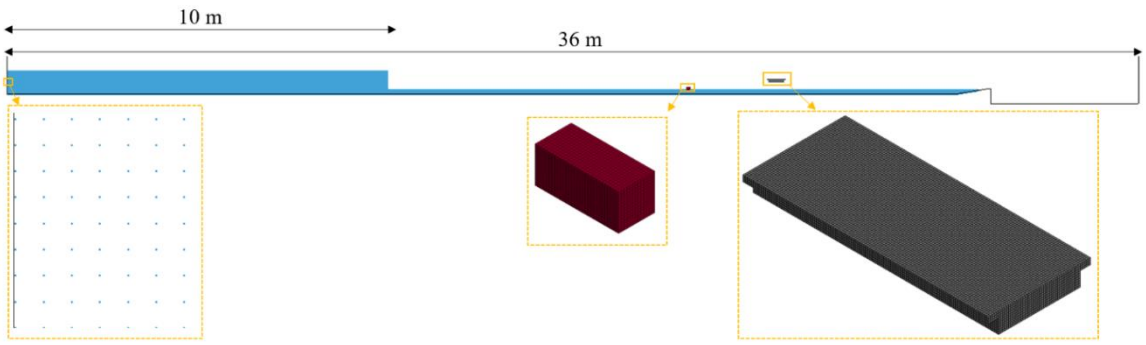

Figure 4-4 Cross section of the computational domain (top), numerical models with the debris and the bridge

The maximum full-scale weight of a 6.1m standard shipping container is 245.2 kN. According to Ko et al., (2015) [6], the typical empty weight of a standard shipping container is about 9.2% of the maximum full-scale weight. For this research study, by matching 50% of the total weight of a standard shipping container including 9.2% of the full-scale weight representing the empty container plus 40.8% as the nonstructural mass/cargo, a total weight of 0.0153 kN was considered. Based on the Froude similarity law, the debris specimen at the 1:20 scale corresponds to a prototype weight of 122.6 kN. Nonstructural mass was added to the debris to model shipping container cargo and was treated as the mass that was attached to the specimen and homogeneously distributed along the bottom slab of the debris. The resultant draft of the debris for the numerical simulations was 3.9 cm. It has to be mentioned that for the purpose of this study, the transverse orientation of the debris was defined in which the major axis of the debris was perpendicular to the direction of wave propagation and the minor axis of the debris is parallel to the flume horizontal axis.

According to the Federal Highway Administration the weight per deck area of a two-span continuous CIP concrete box bridge, three-span continuous steel girder bridge, single-span precast girder bridge, three-span continuous CIP concrete bridge, three-span continuous CIP concrete box bridge and twelve span viaduct precast concrete bridge are 13.04kN/m^2, 9.75kN/m^2, 12.31kN/m^2, 16.66kN/m^2, 15.59kN/m^2 and 11.80kN/m^2, respectively [69-73]. Therefore, for the parametric

investigation, the average weight of a hypothetical single span bridge was considered to be 0.40kN/m^2 which corresponds to a prototype average weight of 13.19kN/m^2 at the 1:20 length scale. For the purpose of numerical investigations, three different deck elevations including 0.20 m (Z_a), 0.30 m (Z_b), and 0.35 m (Z_c) were considered to compare different scenarios.

A wide range of hydrodynamic conditions which could occur in extreme events was considered and reported in Table 4-1. Similar bores were used in previous studies [10, 68].

Table 4-1 Hydrodynamic conditions

Bore cases	**d: Initial water level (m)**	**H_r: Reservoir level (m)**	**Bore strength**
B1	0.10	0.40	Weak
B2	0.15		
B3	0.10	0.60	Strong
B4	0.15		
B5	0.20		
B6	0.25		

4.3. Tsunami flow characteristics

Figure 4-5 shows the variation of the free-surface and fluid particle velocities (V_f) for strong bores including B3, B4, B5, and B6. The free-surface time-histories are plotted at a location close to the offshore side of the debris, while the fluid particle velocities are plotted at the same x coordinate at the level of the maximum initial free-surface for the weakest bore (B1), i.e. Z=0.25 m. The figure shows that the tsunami bores at the debris location have a relatively long duration, which should be enough for the debris to transport from its initial location, impact the bridge superstructure and interact with it, and have reasonable velocities for tsunami-like conditions.

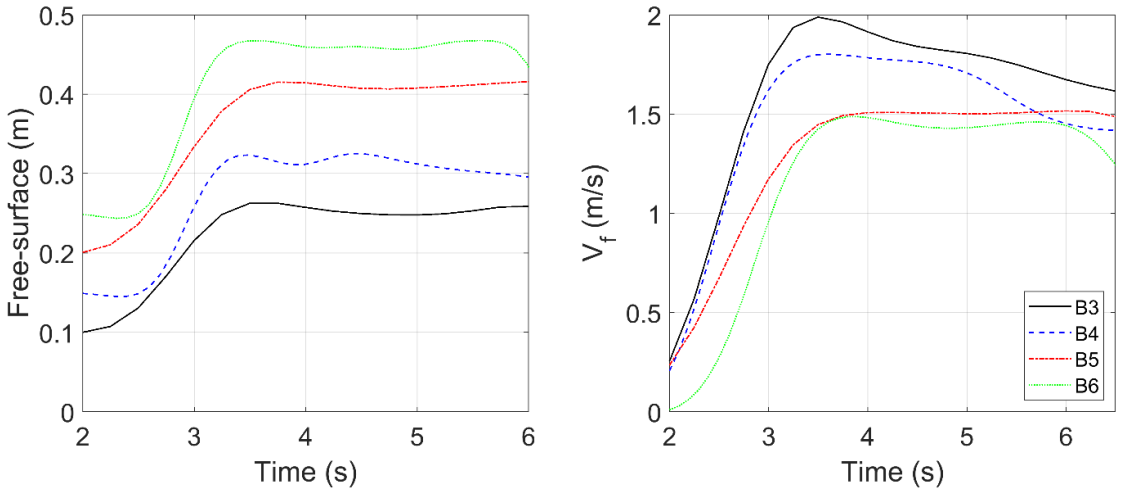

Figure 4-5 Free-surface (left) and fluid particle velocity histories (right) of tsunami flow in front of the debris location for strong bores and Z=0.25 m

Figure 4-6 presents the numerically predicted maximum values of the free-surface and bore height at the aforementioned location and maximum values of the fluid velocities at three elevations (Z=0.15, 0.20, and 0.25 m) for all bore cases. The figure shows that while a higher level of the free-surface and bore height is achieved for the stronger bore, a smaller value of the fluid velocity is recorded. As expected, fluid velocity reaches the maximum magnitude at the free-surface level and there is a reduction in fluid velocity over the vertical coordinate (depth). Reduction in fluid velocity along the depth is more significant for the weaker bores.

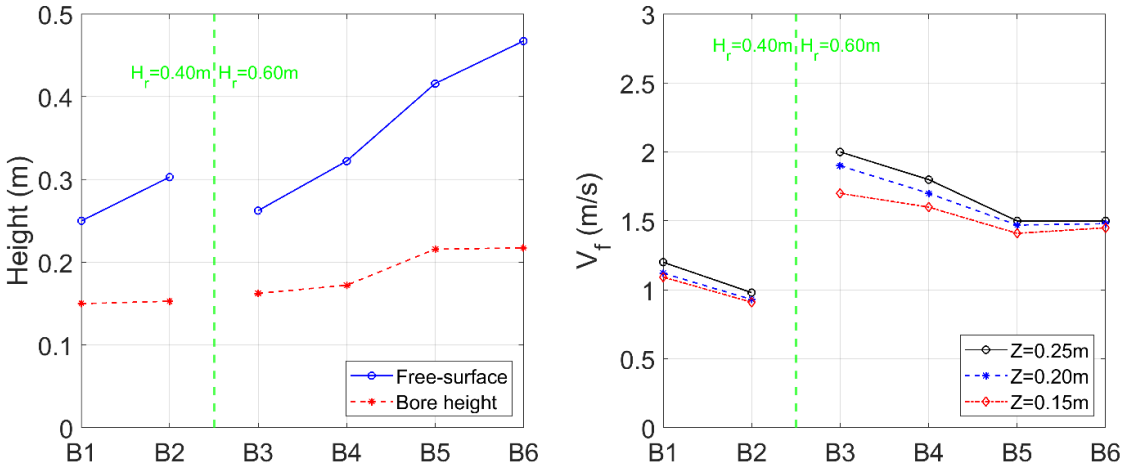

Figure 4-6 Maximum free-surface values (left) and fluid velocities (right) of tsunami flow in front of the debris location for all the investigated bores and three elevations with Z=0.15, 0.20 and 0.25 m

4.4. Debris movement and debris-fluid-bridge intercation

4.4.1. General trends

In order to visualize the tsunami-debris-bridge interaction, Figure 4-7 shows some selected snapshots of the x-velocities representing the sequence of tsunami-debris-deck interaction for case $B4Z_b$ (strong bore and bridge elevation of 0.30 m). The figure demonstrates that as the floating container moves inland and starts to interact with the deck, it impacts the offshore overhang which is followed by several impacts on the offshore web. Then, the debris moves below the bridge and applies multiple impacts on the soffit, and resurfaces again. The snapshots highlight the complexity of the tsunami flow pattern around the deck and flow-debris-bridge interaction. Moreover, the observed three-dimensional trends agree with the two-dimensional trends reported in the previous research study by Hasanpour et al., (2022) [64].

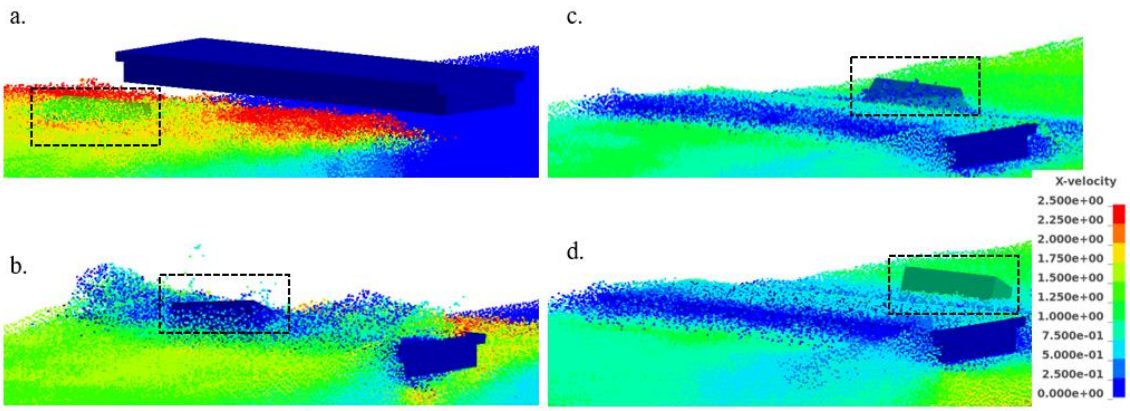

Figure 4-7 Tsunami-debris-bridge interaction for case B4Zb; strong bore and bridge elevation of 0.30 m

To serve the purpose of the flow-debris-bridge interaction well, Figure 4-8 shows some selected snapshots of the x-velocities for three different representative cases including $B2Z_b$ (weak bore and bridge elevation of 0.30 m), $B3Z_b$ (strong bore and bridge elevation of 0.30 m), and $B5Z_a$ (strong bore and bridge elevation of 0.20 m), as the container moves inland and impacts the bridge superstructure. The visual presentation of the phenomena reveals that for the selected cases, the

tsunami bore reaches the deck before the debris, which implies that the impulsive tsunami bore forces will not coincide with the debris impact forces. For the same bridge elevation ($B2Z_b$ and $B3Z_b$ and different bore strength), bore properties play a significant role in the debris transport and debris-tsunami-bridge interaction. In the case of the weak bore ($B2Z_b$), as the container reaches the offshore side of the deck, it impacts the offshore web and then moves below the deck. However, in the case of the strong bore ($B3Z_b$), after the primary impact on the offshore web, the container becomes trapped below the offshore overhang until the end of the inundation. For the last case ($B6Z_a$), as the debris propagates inland, it moves above the deck without any interaction with it. The snapshots clearly demonstrate the complex debris-tsunami and debris-tsunami-deck interactions and reveal that the elevation of the bridge and bore properties are critical parameters that affect the movement of the debris around the deck which determines the sequence of the loadings on the bridge superstructure.

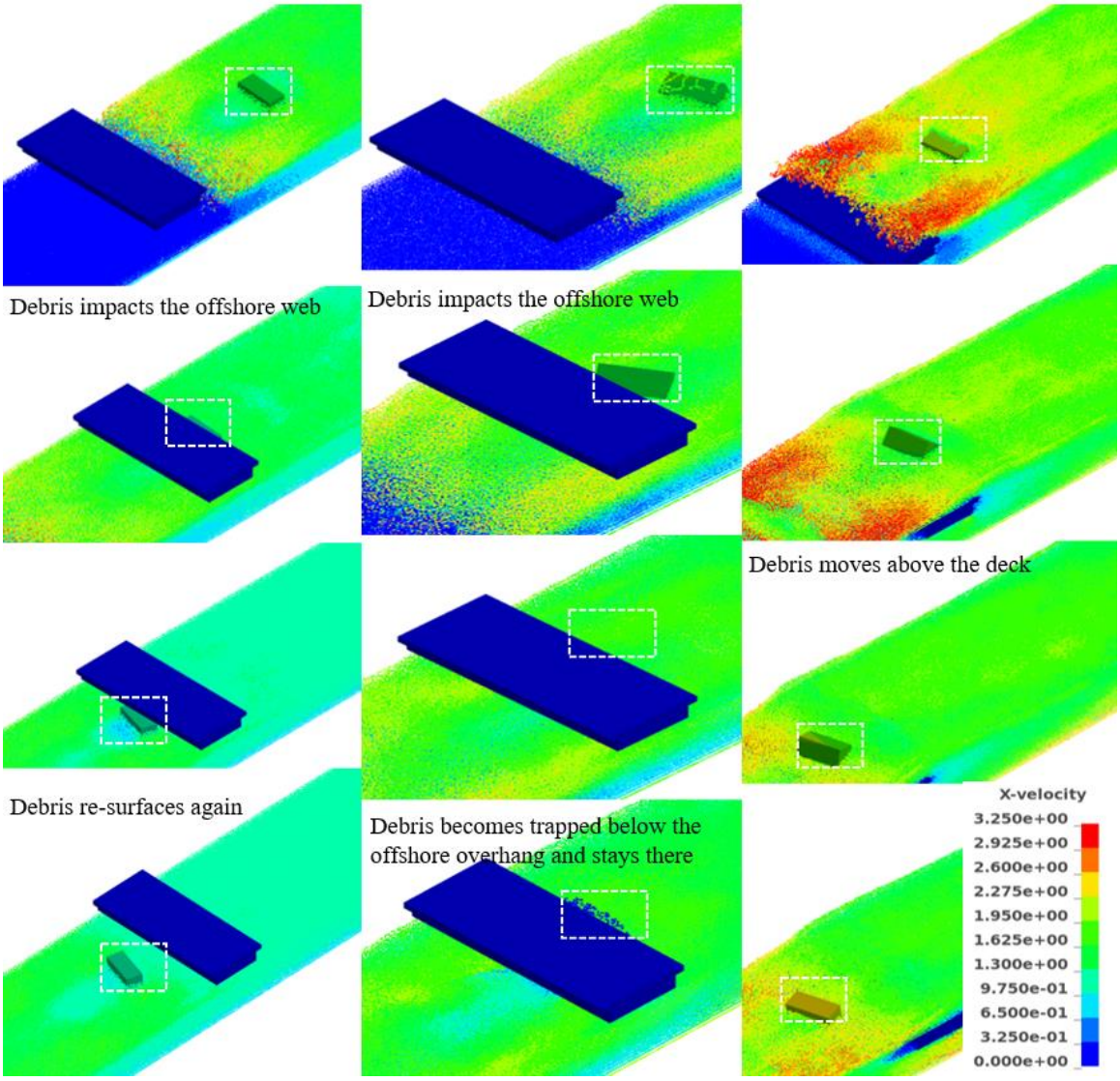

Figure 4-8 Debris-tsunami and debris-tsunami-bridge interaction for three scenarios: B2Zb (left, weak bore and bridge elevation of 0.30 m), B3Zb (center, strong bore and bridge elevation of 0.30 m), and B5Za (right, strong bore and bridge elevation of 0.20 m)

To explore the debris-tsunami and debris-tsunami-bridge interactions, different bore properties and bridge elevations were investigated in this study A total of thirteen cases were analyzed. In terms of the debris-tsunami-deck interaction, three different trends (A, B, and C) were observed. The most frequent trend is trend A and is happened when the debris impacts the offshore side of the bridge superstructure and moves below it. Eight cases out of thirteen show trend A. Trend B occurs

when the debris moves above the deck, with or without interaction with it. In four cases, trend B governs the debris interaction with the deck. The infrequent trend is trend C in which the debris impacts the offshore side of the bridge superstructure and becomes trapped below the offshore overhang until the end of inundation. One of the cases exhibits trend C. Table 4-2 illustrates that the movement of the debris is a function of both the bore properties and the bridge elevation. For example, in case B6, for similar flow characteristics, the container could either propagates below the bridge or moves above the deck which is determined by the bridge elevation. In the case of similar bridge elevation such as B3Zb, B4Zb, B5Zb, and B6Zb, depending on the bore properties, the debris can move below or above the bridge or becomes trapped below the offshore overhang until the end of inundation. Overall, the movement of the container and its interaction with the tsunami flow and the deck is a complex multi-physics phenomenon. Table 4-2 summarizes the observed flow-debris-bridge interaction for all investigated cases.

Table 4-2 Debris-deck interaction for the investigated bore cases

Bore Cases	**H_r (m)**	**d (m)**	**Bridge Elevation (m)**		
			0.20 **(Z_a)**	0.30 **(Z_b)**	0.35 **(Z_c)**
B1	0.40	0.10	Impacts the offshore side and moves below the bridge **(A)**		
B2		0.15	Impacts the offshore side and moves below the bridge **(A)**	Impacts the offshore side and moves below the bridge **(A)**	
B3	0.60	0.10	Impacts the offshore side and moves above the deck **(B)**	Impacts the offshore side and gets trapped below the offshore overhang **(C)**	
B4		0.15	Impacts the offshore side and moves above the deck **(B)**	Impacts the offshore side and moves below the bridge **(A)**	Impacts the offshore side and moves below the bridge **(A)**
B5		0.20	Impacts the offshore side and moves above the deck- **NO CONTACT (B)**	Impacts the offshore side and moves below the bridge **(A)**	Impacts the offshore side and moves below the bridge **(A)**
B6		0.25		Impacts the offshore side and moves above the deck **(B)**	Impacts the offshore side and moves below the bridge **(A)**

4.4.2. Debris displacements and rotations

In order to get a more quantitative view of the movement of the debris, Figure 4-9 plots the average vertical displacement (D_z) of the offshore and and onshore corners of the container and its trajectory (D_x vs. D_z) throughout the propagation inland. For this purpose, nine different cases based on (i) two different bridge elevations including 0.20m (Z_a) and 0.30m (Z_b) and (ii) different bore properties are presented. This figure illustrates that the container flow is significanltly dependent on the bore properties and the bridge elevation, with totally different movements being observed for the investigated cases. The stronger bore elevates the container up to three times more than the weaker bore which consequently affects the tsunami-debris-deck interaction. For instance, in case of B2Za (weak bore and bridge elevation of 0.20m) the debris moves below the deck, while for the same bridge elevation and the stronger bore, i.e., $B4Z_a$, the debris propagates above the deck. Interestingly, in case of the stronger bores, the debris exhibits the upward and downward dispalcements (except case $B6Z_b$, in which the debris moves above the deck), while when the debris picks up by the weaker bores, nearly a consistent movement of the debris is observed. Moreover, the figure highlights the effect of bridge elevation on the debris movement as well. For example, for the same bore properties and different deck elevation such as cases $B3Z_a$ and $B3Z_b$, the debris could either moves below the bridge or becomes trapped in front of the deck, depending on the bridge elevation.

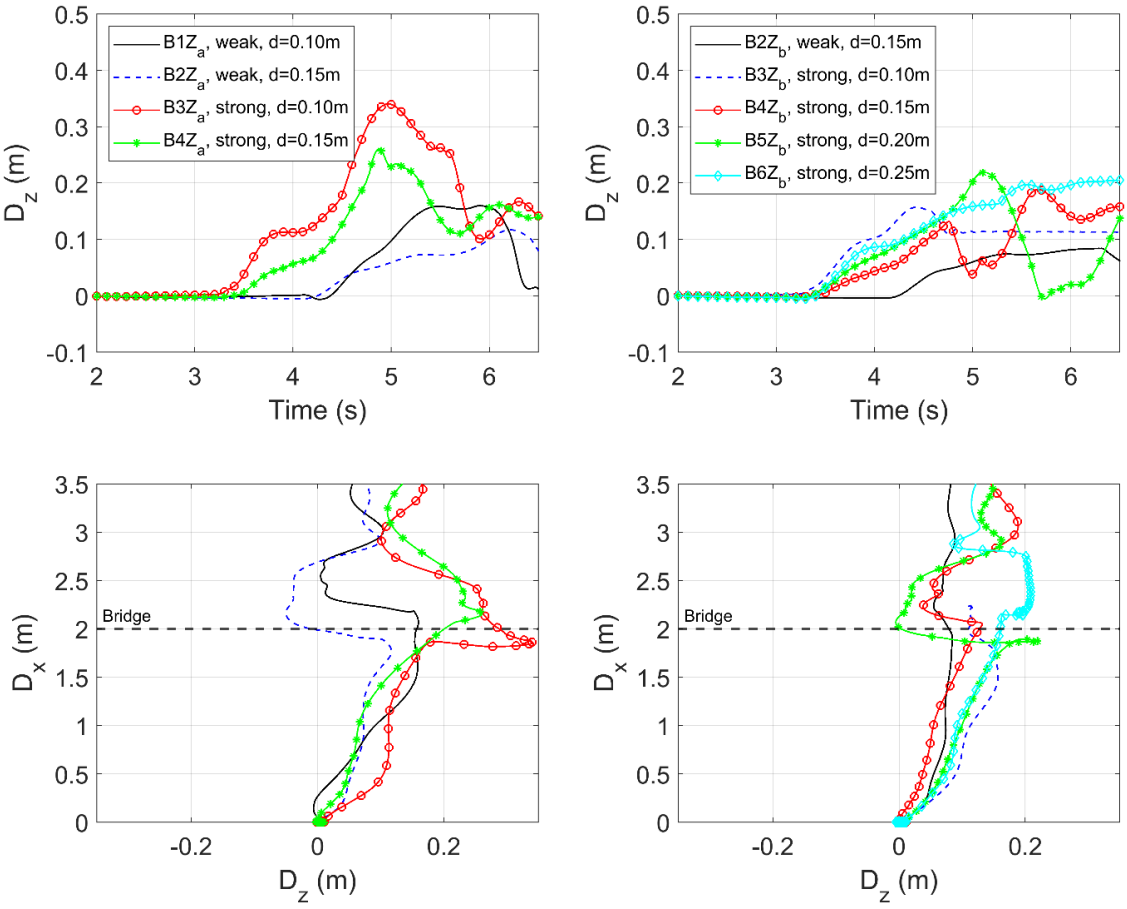

Figure 4-9 Debris vertical displacement histories (top) and trajectories (bottom) for two bridge elevations (0.20 m (Za) and 0.30 m (Zb)) and different bore strengths

The above time-histories gave an insight into the debris vertical displacement and trajectory. To get a better view of the debris displacement, Figure 4-10 presents the debris maximum vertical displacement for all the tested tsunami flows and bridge elevations. It is critical predicting the vertical displacement and location of the debris impact on the bridge. In fact, vertical displacement of the debris determines the range of interactions with the bridge superstructure that is a function of the bore properties and the deck elevation. This figure verifies the observed trends. For instance, in cases of $B3Z_a$, $B4Z_a$, and $B5Z_a$ in which the debris moves above the deck, maximum vertical displacement (relative to the center of gravity) of 0.33 m, 0.25 m, and 0.23 m are reported, respectively. Furthermore, for the highest bridge elevations, i.e., cases $B4Z_c$, $B5Z_c$, and $B6Z_c$, the

debris moves below the deck and exhibits vertical displacement of 0.16 m, 0.17 m, and 0.15 m, respectively.

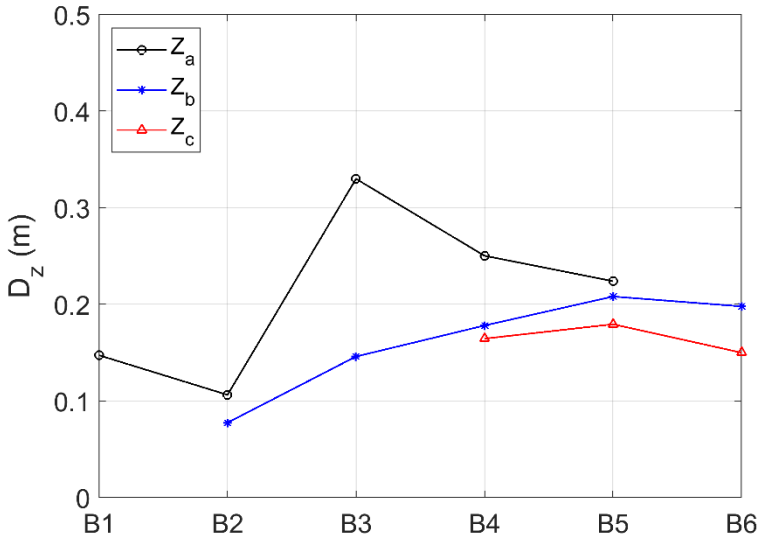

Figure 4-10 Debris maximum vertical displacement for all the investigated cases

Figure 4-11 shows time-histories of the debris rotations relative to the initial position for two different bridge elevations including 0.20 m (Z_a) and 0.30 m (Z_b) and different bore properties. The figure reveals that both bore properties and bridge elevation play a significant role in the debris rotation throughout the propagation and impact on the bridge superstructure. As shown, for the similar bridge elevation and bore strength, such as cases $B1Z_a$ and $B2Z_a$, higher initial water levels results in approximately a 36% reduction in debris rotation. Furthermore, in case of similar bridge elevation and initial water level such as cases $B2Z_b$ and $B4Z_b$, the stronger bore induces an approximately 3-fold larger maximum pitching angle relative to the weaker case of $B2Z_b$. These trends verify quantitatively the significant role of bore properties on the debris flow. However, for the same bore properties, the bridge elevation could play a critical role and affects the movement of the debris around the deck and the debris-fluid-deck interaction. For instance, in the case of $B4Z_a$, the debris rotates up to 480 degrees and moves above the deck, while for the higher deck elevation, i.e., $B4Z_b$, rotation of the debris reduces by approximately 31%, and the debris moves

below the deck. Another interesting finding can be reached from the container rotation, according to which, in some cases such as B4Za, B4Zb, and B5Zb the debris rotates more than 180 degrees (up to 480 degrees) which means that it rotates upside down, a fact that could potentially cause damage to cargo. Therefore, it is important in future risk assessment models, to predict the displacement and rotation of the floating container so that the designer can identify the structural components that are susceptible to debris impact.

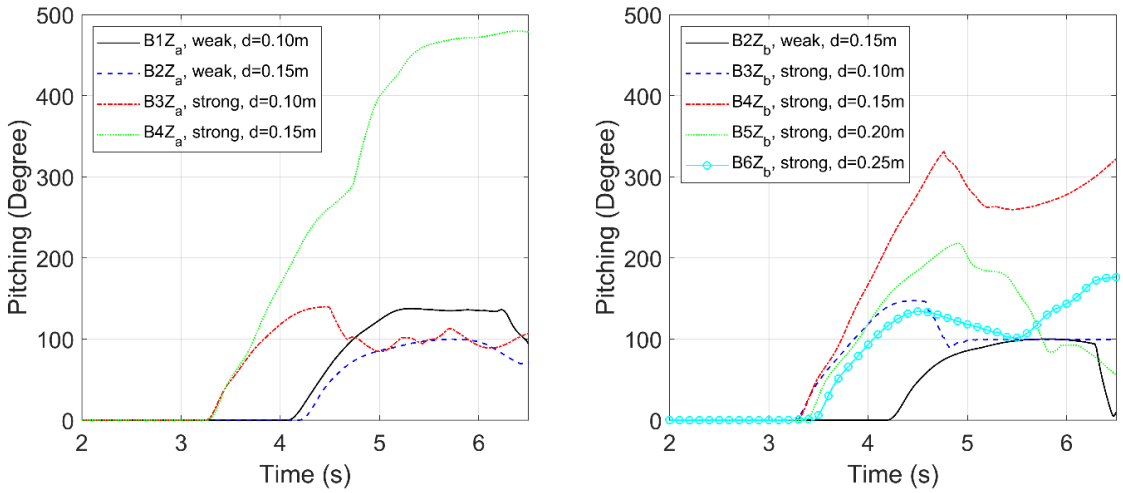

Figure 4-11 Debris rotation histories for two bridge elevations (0.20 m (Za) and 0.30 m (Zb)) and different bore strengths

4.4.3. Debris velocities

To provide further explanations for the observed trends in the previous figure, the debris offshore and onshore corners velocities in the horizontal (Vx_d) and vertical (Vz_d) directions for three selected cases including $B3Z_a$ (strong bore and bridge elevation of 0.20 m), $B4Z_b$ (strong bore and bridge elevation of 0.30 m), and $B5Z_c$ (strong bore and bridge elevation of 0.35 m) are presented in Figure 4-12. The figure demonstrates that while at the instant of primary impact, the offshore and onshore corners exhibit similar velocities (horizontal and vertical), throughout the entrainment process the velocities (horizontal and vertical) significantly differ for the offshore and onshore corners of the debris. Based on the figure, when the debris is picked up by the approaching bore and its motion is

initiated, the horizontal and vertical velocities of the offshore corners of the debris are higher than the respective velocities of the onshore corners. For instance, the maximum horizontal offshore velocity prior to the primary impact is about 6%, 25%, and 10% higher than the respective velocity of the onshore corners for cases $B3Z_a$, $B4Z_b$, and $B5Z_c$, respectively. In terms of the maximum vertical velocity before the first impact on the bridge superstructure, the SPH-FEM models predict higher offshore velocity than the onshore velocity by approximately 27%, 96%, and 17%, for cases $B3Z_a$, $B4Z_b$, and $B5Z_c$, respectively. The differences in the offshore and onshore velocities could be attributed to the presence of debris pitching and verifying the previously observed trends. For example, in the case of $B4Z_b$, the debris rotates more than 180 degrees (up to 330 degrees) which cause significant differences in the offshore and onshore velocities. The presence of the debris pitching causes the floating container impacts the structure with an angle to the horizontal plane. The importance of the debris pitching and non-normal impact on the structures is reported by past studies as well [55, 68].

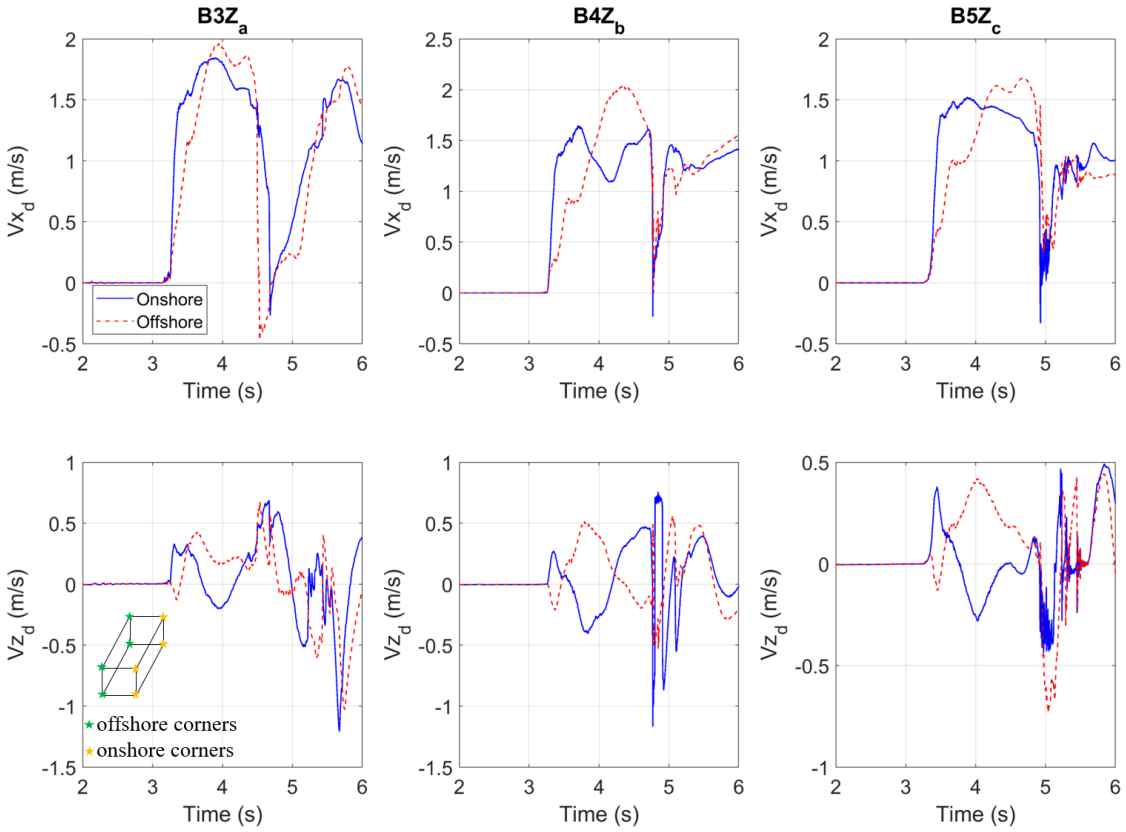

Figure 4-12 Debris offshore and onshore corners velocities in the horizontal (top) and vertical (bottom) directions for three strong bore cases and different bridge elevation, including B3Za (bridge elevation of 0.20 m), B4Zb (bridge elevation of 0.30 m), and B5Zc (bridge elevation of 0.35 m)

To evaluate the effect of bore strength on the debris velocities, Figure 4-13 presents time-histories of the average debris velocities in the horizontal and vertical directions for two selected cases, including $B1Z_a$ (weak bore and bridge elevation of 0.20 m) and $B3Z_a$ (strong bore and bridge elevation of 0.20 m). As expected, a strong bore transfers more momentum to the container which results in a higher debris velocities. In fact, strong bore causes an increase of about 62% and 400% in the horizontal and vertical velocities, respectively. Moreover, a higher level of velocity affects the debris-flow-bridge interaction. For instance, in the case of $B3Z_a$, the debris propagates above the deck, while in the case of $B1Z_a$, the container impacts the offshore side of the bridge and moves below it.

Figure 4-14 shows time-series of the average horizontal and vertical debris velocities for different cases with similar bore strength (strong bore) and bridge elevation (0.30 m) and different initial water levels, including $B3Z_b$ (d=0.10 m), $B4Z_b$ (d=0.15 m), $B5Z_b$ (d=0.20 m) and $B6Z_b$ (d=0.25 m). This figure reveals that initial water level plays a significant role in the debris velocities which affects tsunami-debris-deck interaction. For example, in the case of the shallower water depth, i.e, $B3Z_b$, as the container propagates inland, it impacts the offshore side of the bridge and becomes trapped below the offshore overhang until the end of inundation (debris velocities drop significantly and becomes almost zero). However, in the case of the deepset water level, i.e, $B6Z_b$, the debris impacts the deck and moves above it. In this case, after the primary impact, as the debris moves above the deck, it accelerates and reaches about 60% and 17% of the horizontal and vertical impact velocities, respectively. Regarding the two other cases, i.e., $B4Z_b$ and $B5Z_b$, where the debris impacts the offshore side and moves below the bridge, a larger initial water level leads to an increase of about 70% in the horizontal velocity. In the aforementioned cases, after the primary impact on the bridge, the debris accelerates and, the horizontal velocity increases and reaches approximately 87% and 120% of the horizontal impact velocities, respectively. In terms of the vertical velocity, as the debris moves below the soffit, the vertical velocity increases significantly and can exceed even the velocity of the initial impact. For instance, an increase of about 163% and 80% in the debris vertical velocity relative to the impact velocity is reported for cases $B4Z_b$ and $B5Z_b$, respectively. Another interesting finding can be reached from the figure is that in the cases that the debris moves below the bridge and accelerates and re-surfaces with significant velocities (equal or greater than the primary impact velocity) if there are a set of bridges running parallel to each other, i.e., twin bridges, the second bridge experiences similar or worsening situation. Follow-up studies should investigate the tsunami-borne debris impact loads on twin bridges to quantify the impact forces for future risk assessment frameworks of bridges.

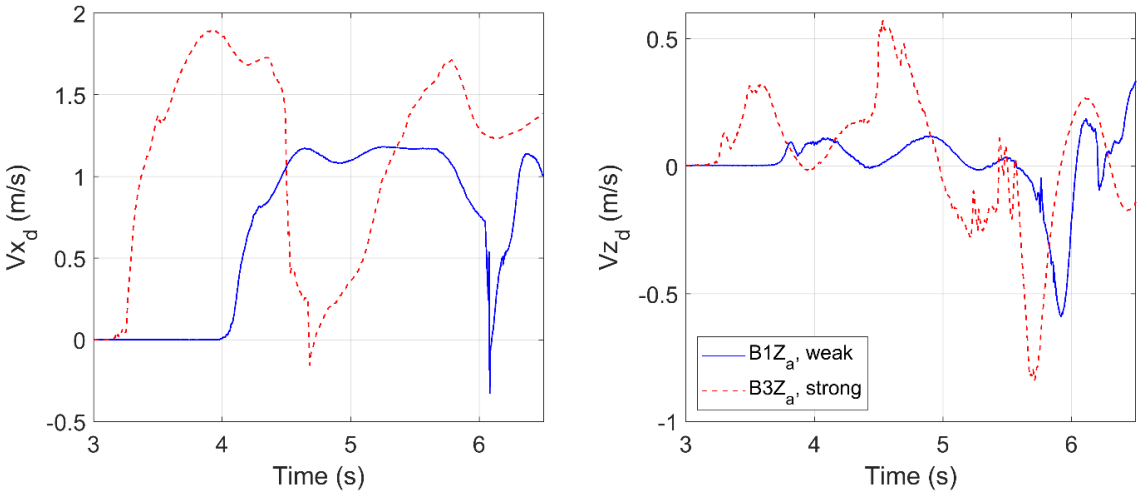

Figure 4-13 Debris velocities in the horizontal (left) and vertical (right) directions for two selected cases with similar bridge elevation (0.20 m) and different bore strengths, including B1Za (weak bore), and B3Za (strong bore) generate

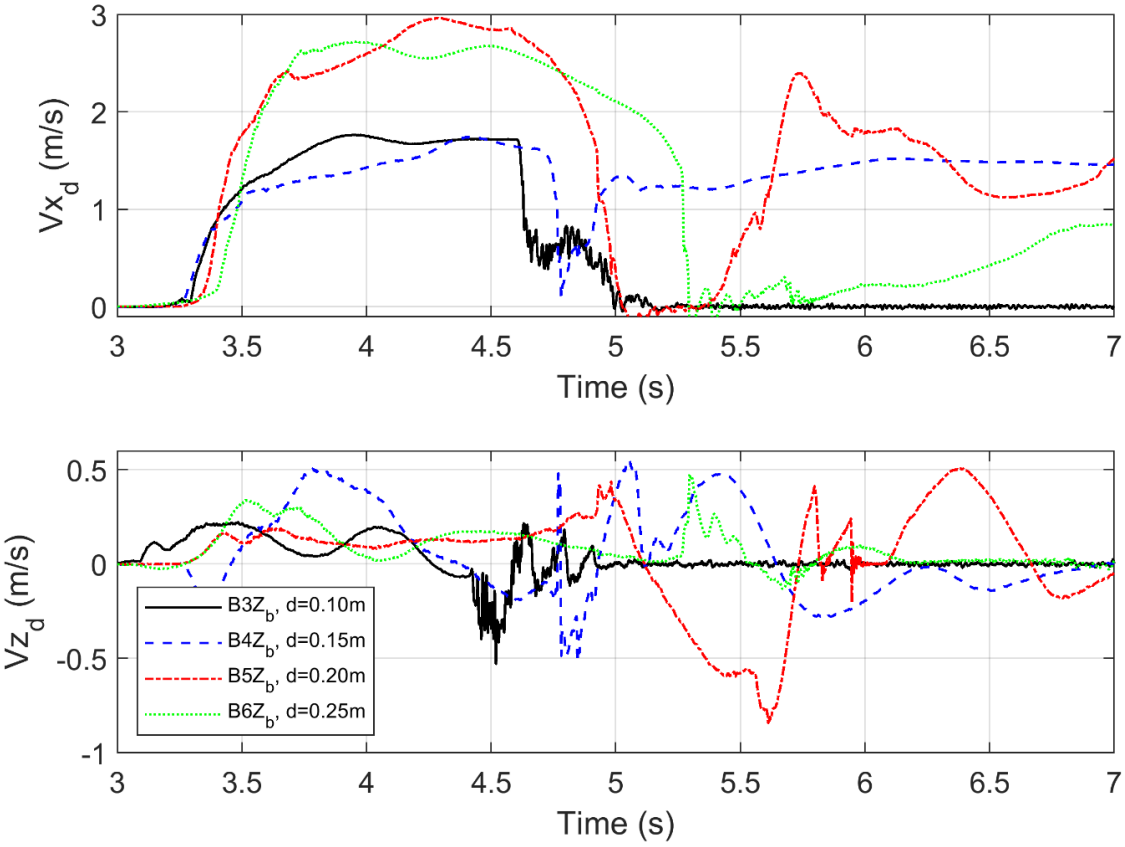

Figure 4-14 Debris velocities in the horizontal (top) and vertical (bottom) directions for four selected strong bores with similar bridge elevation (0.30 m) and different initial water levels, including B3Zb (d=0.10 m), B4Zb (d=0.15 m), B5Zb (d=0.20 m), and B6Zb (d=0.25 m)

Time-histories of the debris horizontal and vertical velocities for similar bore properties and different bridge elevations are plotted in Figure 4-15. For this purpose, three different cases including $B4Z_a$ (bridge elevation of 0.20 m), $B4Z_b$ (bridge elevation of 0.30 m), and $B4Z_c$ (bridge elevation of 0.35 m) are presented. In the case of the lowest bridge elevation, after the primary impact on the deck, the debris horizontal velocity drops gradually. However, for the two other cases, more abrupt decreases in the debris horizontal velocity are observed. The trends could be attributed to the (i) different debris-flow-deck interactions and (ii) cushioning effect from the trapped fluid between the debris and the deck at the instant of impact. While the debris moves below the soffit when it hits the bridge with higher elevations, i.e., 0.30 m and 0.35 m, it moves above the deck with the lowest elevation. Furthermore, fluid-structure interaction is more significant for the deck at a lower elevation than the deck at a higher elevation. Therefore, the smoothing role of fluid particles becomes more evident which causes a gradual decrease in the debris velocity. Moreover, the figure demonstrates that for the cases where the debris moving below the bridge, it exhibits approximately similar horizontal impact velocities irrespective of the bridge elevation, with about 4% higher velocity associated with the deck elevation of 0.35 m.

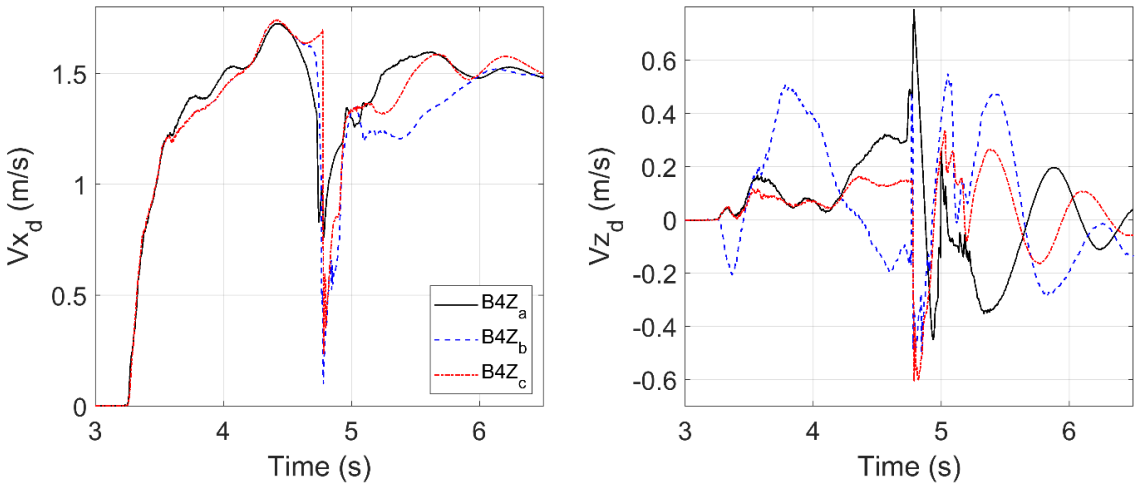

Figure 4-15 Debris velocities in the horizontal (left) and vertical (right) directions for three selected cases with similar bore properties and different bridge elevations, including B4Za (bridge elevation of 0.20 m), B4Zb (bridge elevation of 0.30 m), and B4Zc (bridge elevation of 0.35 m)

Figure 4-16 illustrates maximum values of the debris velocities in the horizontal and vertical directions throughout the propagation before the primary impact on the bridge superstructure, i.e., maximum velocity, and at the instant of impact, i.e., impact velocity, for all the investigated cases. This figure reveals that the debris primary impact velocity is not necessarily the maximum velocity. In other words, the primary impact velocity is equal to or smaller than the maximum velocity throughout the propagation before the first impact. After the approaching bore entrains the debris, due to the transfer of tsunami flow momentum to the container, there is a transient effect, therefore, the container accelerates promptly and reaches the peak velocity. This effect is more significant in terms of horizontal velocity. However, when the debris impacts the bridge superstructure, the reflection of the wave from the offshore side of the bridge mitigates the debris energy and slows down the debris velocity. The reflection of the bore is more significant for cases in which the larger height of the bridge becomes inundated. The debris maximum horizontal velocity is 2.64, 1.82, and 1.69 times higher than the impact velocity for the bridge elevation of 0.20 m (Z_a), 0.30 m (Z_b), and 0.35 m (Z_c), respectively. In terms of the vertical velocity, the maximum velocity is 1.25, 1.12, and 4.2 times higher than the associated impact velocity, respectively. The results presented herein raise the question of the future predictive equations of the debris impact forces on the bridges, the designer should consider the maximum velocity of the debris throughout the propagation with reduction coefficients, or the primary impact velocity.

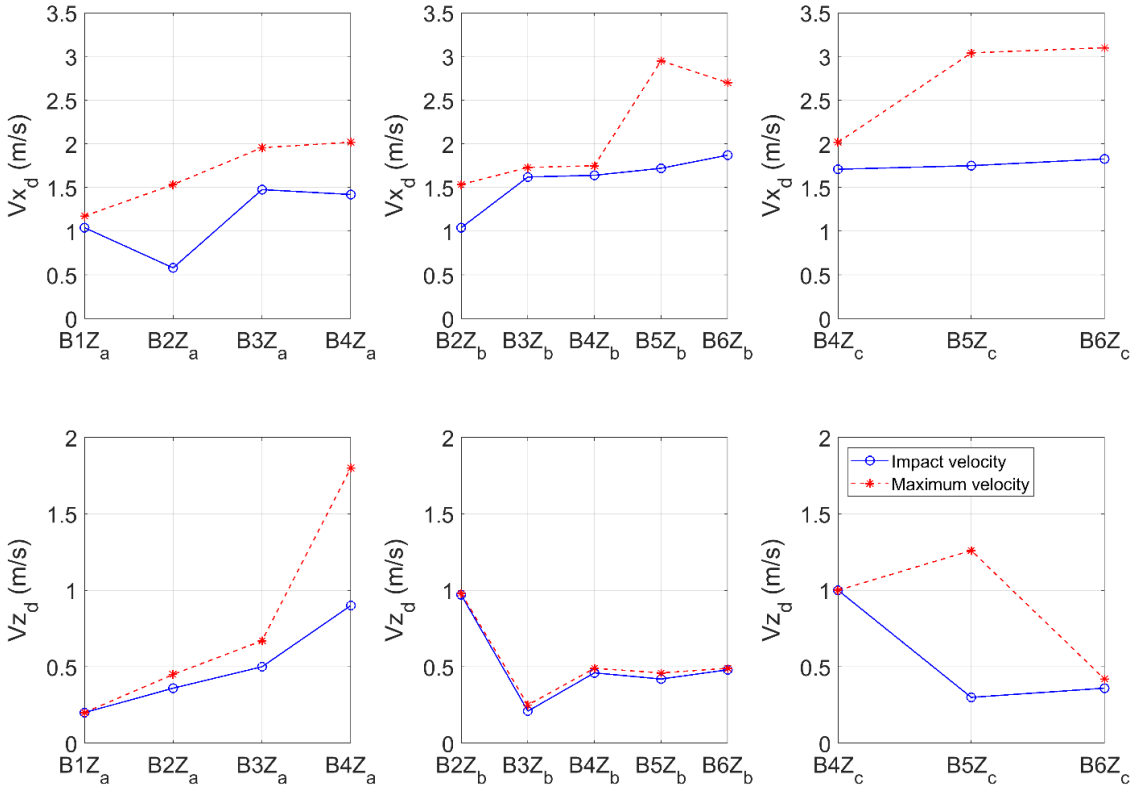

Figure 4-16 Maximum values of the debris velocities in the horizontal (top) and vertical (bottom) directions at the instant of primary impact and throughout propagation

To gain further insight into the debris impact velocities in the horizontal and vertical directions, Figure 4-17 presents the ratio of the primary vertical impact velocity relative to the respective horizontal velocity for all the investigated cases. As presented in previous figures, the debris has a primary vertical impact velocity. The magnitude of the vertical velocity for the bridge elevation of 0.20m (Z_a) is in the range of (0.36-1.5)m/s which is approximately (42-70)% of the horizontal impact velocity. In the case of the bridge elevation of 0.3m (Z_b), the debris vertical velocity lies between (0.44-0.97) m/s which is about (25-93)% of the respective horizontal velocity. For the highest bridge elevation, i.e., 0.35 m (Z_c), the container exhibits a vertical velocity between 0.3 m/s up to 1m/s which is approximately (20-58)% of the horizontal impact velocity. Furthermore, for some cases in which the debris moves below the bridge, the magnitude of the follow-up vertical impact velocity is significant and is approximately 17%, 42%, 135%, 35%, and 30% of the primary

horizontal impact velocity for cases $B2Z_a$, $B2Z_b$, $B4Z_b$, $B5Z_b$, and $B4Z_c$, respectively. As mentioned by Hasanpour et al., (2022), the main focus of the majority of previous studies on debris impact on the structure and available simplified equations are on the horizontal velocity. However, the results of two-dimensional and three-dimensional numerical investigations demonstrate that the vertical velocity at the instant of primary impact is significant and should be considered in design guidelines.

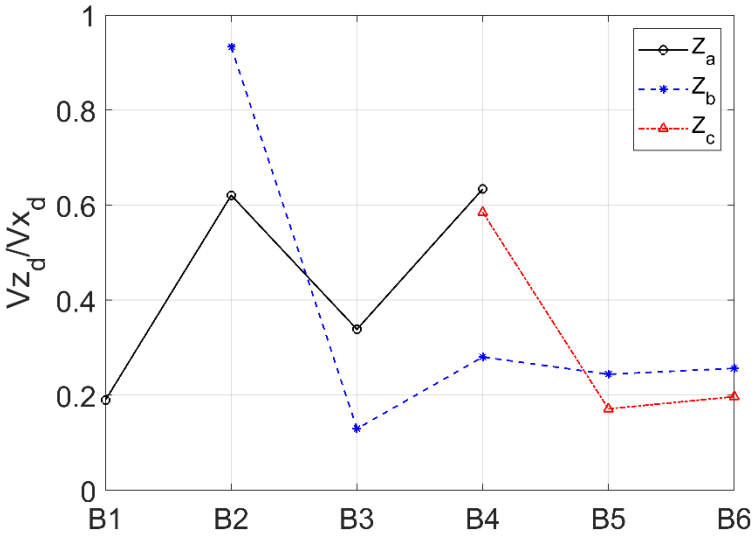

Figure 4-17 Ratio of the primary impact velocities for all investigated cases

4.5. Impact force on bridge superstructure

Figure 4-18 shows time histories of the horizontal and vertical debris (F_d) and fluid (F_f) forces applied on the bridge superstructure with an elevation of 0.30 m for strong bores and different initial water levels including $B3Z_b$ (d=0.10 m), $B4Z_b$ (d=0.15 m), $B5Z_b$ (d=0.20 m), and $B6Z_b$ (d=0.25 m). As mentioned previously, the initial water level is one of the parameters that govern the flow-debris-deck interaction and causes different movements of the debris around the deck which consequently determines the sequence of loadings. In the case of the shallowest water depth ($B3Z_b$) where the debris becomes trapped below the offshore overhang (trend C), the applied hydrodynamic forces are negligible and the container induces up to 2 and 1.2 times larger horizontal

and vertical forces, respectively. For the intermediate initial water levels ($B4Z_b$ and $B5Z_b$) in which the debris impacts the offshore side and moves below the deck (trend A), the bridge exposes to higher debris and fluid impact forces in both directions. While the primary debris horizontal impact force is about 1.5 and 2 times the maximum fluid force in cases of $B4Z_b$ and $B5Z_b$, respectively, similar uplift forces are applied on the bridge (debris and fluid). For these two cases, the magnitude of the primary horizontal debris impact force is about 1.75 times the uplift force. Another interesting finding that can be reached from this figure is that the soffit experiences several uplift forces after the primary impact as the debris moves below the bridge, which agrees with the observations made by Hasanpour et al., (2022). The magnitude of the secondary uplift force is about 76% and 82% of the initial impact for cases $B4Z_b$ and $B5Z_b$, respectively. It should be mentioned that in the case of $B4Z_b$, according to previous figures, the debris secondary vertical impact velocity overcomes the primary respective velocity with approximately 1.63 times higher velocity. However, the magnitude of the secondary impact force is smaller than the primary one which could be attributed to the presence of the debris pitching and non-linear force-velocity relation as reported by Hasanpour et al., (2021) [55]. For the deepest initial water depth ($B6Z_b$) that the debris moves above the deck, the magnitude of the debris horizontal impact force is about 1.6 times the fluid force. Moreover, as the debris propagates over the deck, it applies a downward force with a magnitude of about 40% of the respective horizontal force. Furthermore, in some cases, the debris and the fluid forces do not get maximized at the same instant during the inundation process, highlighting the need to consider different load cases in the design of new bridges to identify the governing scenario, as was done by Istrati et al., (2018) [24] for the clear-water condition that will account for different impact locations along the width of the superstructure.

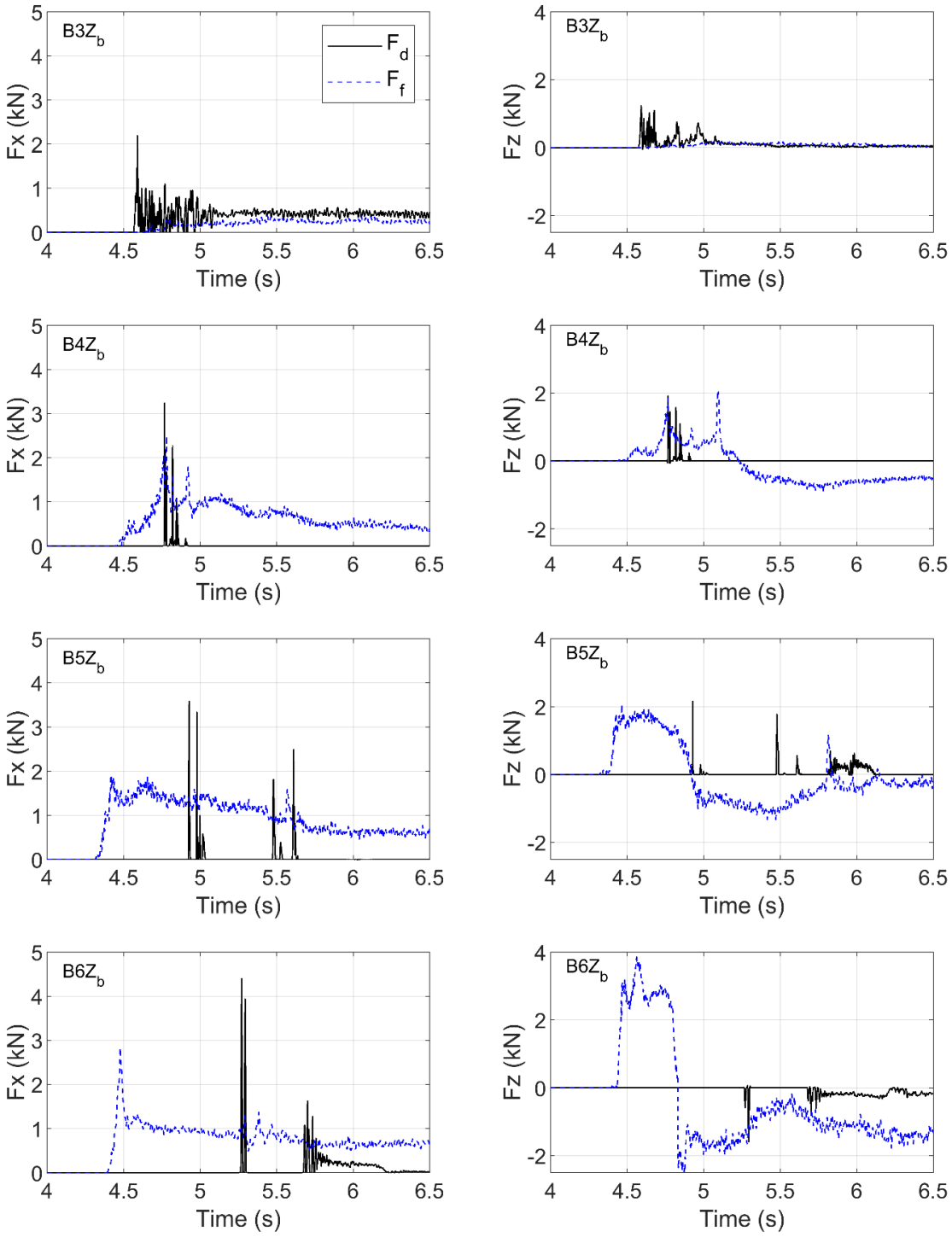

Figure 4-18 Applied horizontal and vertical force histories for four cases with similar bridge elevation of 0.30m and bore strength and different initial water depths, including B3Zb (d=0.10 m), B4Zb (d=0.15 m), B5Zb (d=0.20 m), and B6Zb (d=0.25 m)

To get further insight into the applied loading on the bridge superstructure, Figure 4-19 illustrates the time histories of the (a) debris horizontal impact force (Fx_d), (b) debris vertical impact force (Fz_d), (c) total horizontal force (Fx_t), (d) total uplift force (Fz_t), the maximum magnitude of the (e) debris impact force in the two directions and (f) peak values of the total applied loads in the two directions for strong bores and different initial water levels including $B3Z_b$ (d=0.10 m), $B4Z_b$ (d=0.15 m), $B5Z_b$ (d=0.20 m), and $B6Z_b$ (d=0.25 m). It is observed that as the initial water depth increases, the debris impact forces in the two directions increase as well. For example, by increasing the initial water level from 0.10 m to 0.25 m, the debris horizontal impact force increases by approximately 100%. For the initial water level of 0.20 m, the debris applies uplift force with approximately a 75% increase relative to the shallowest water depth (0.10 m). In the case of the deepest water depth, the container moves above the deck and induces downward force. In terms of the total horizontal applied loads, the largest bore applies up to about 140% higher force relative to the smallest one. For the total uplift force, in the case of $B5Z_b$, when the bridge superstructure becomes fully inundated and the tsunami bore induces downward force, the debris applies the primary impact force. Therefore, the maximum total uplift force for the case decreases by up to 50% relative to the $B4Z_b$. In the case of the largest bore ($B6Z_b$), the increase in hydrodynamic force is compensated by the debris downward force and the bridge superstructure experiences almost similar total vertical forces to the $B4Z_b$. Overall, the observed trends reveal the complexity of the phenomena and indicate that more complex predictive equations should be developed accounting for both horizontal and uplift forces for the future risk assessment framework.

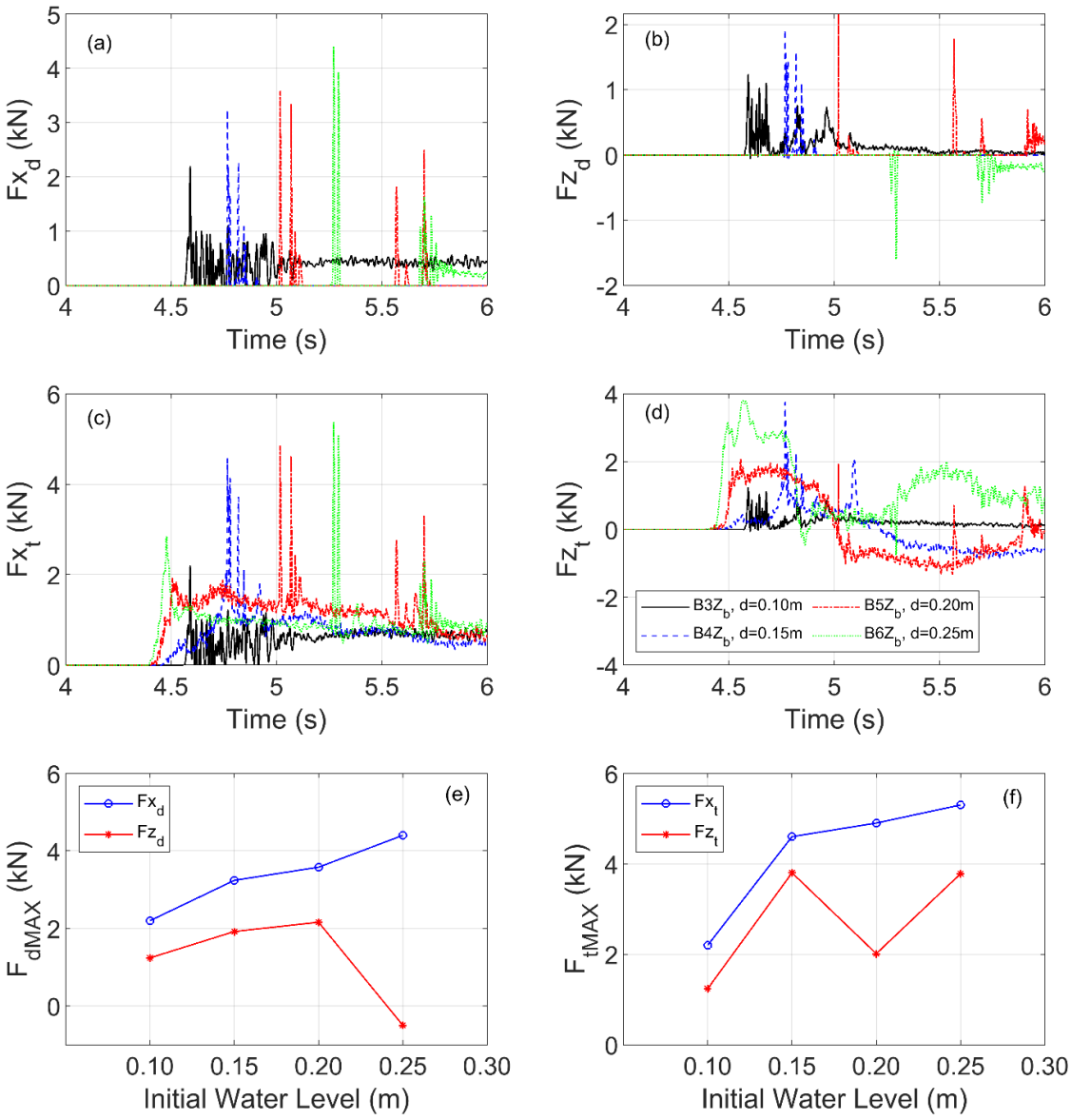

Figure 4-19 Time histories of the debris horizontal and vertical forces, total horizontal and vertical forces, and the maximum values of the debris and total horizontal and vertical forces for four cases with similar bridge elevation of 0.30 m and bore strength and different initial water depth, including B3Zb (d=0.10 m), B4Zb (d=0.15 m), B5Zb (d=0.20 m), and B6Zb (d=0.25 m)

To evaluate the effect of the bridge elevation on the applied loadings, time-histories of the debris forces in the two directions for three cases with similar bore properties and different deck elevations including $B4Z_a$ (bridge elevation of 0.20 m), $B4Z_b$ (bridge elevation of 0.30 m), and $B4Z_c$ (bridge elevation of 0.35 m) are presented in Figure 4-20. For the lower bridge elevation (Z_a), the horizontal

force caused by the tsunami bore overcomes the debris impact force with the fluid force being approximately 3 times larger than the debris impact forces. In this case, the debris moves above the deck (trend B) and applies downward force. On the other hand, for the highest deck elevation (Z_c), the fluid forces become negligible (there is no significant fluid-deck) and the debris-deck interaction plays an important role. In this case, the debris exerts significant forces on the deck and the magnitude of the horizontal force is about 1.7 times the vertical load. However, as the debris propagates below the deck, it applies secondary impact force on the soffit which is about 8% of the respective initial magnitude. For the intermediate bridge elevation (Z_c), the magnitude of the debris horizontal impact force is about 1.3 times the fluid force, while the debris and the bore apply approximately similar uplift forces.

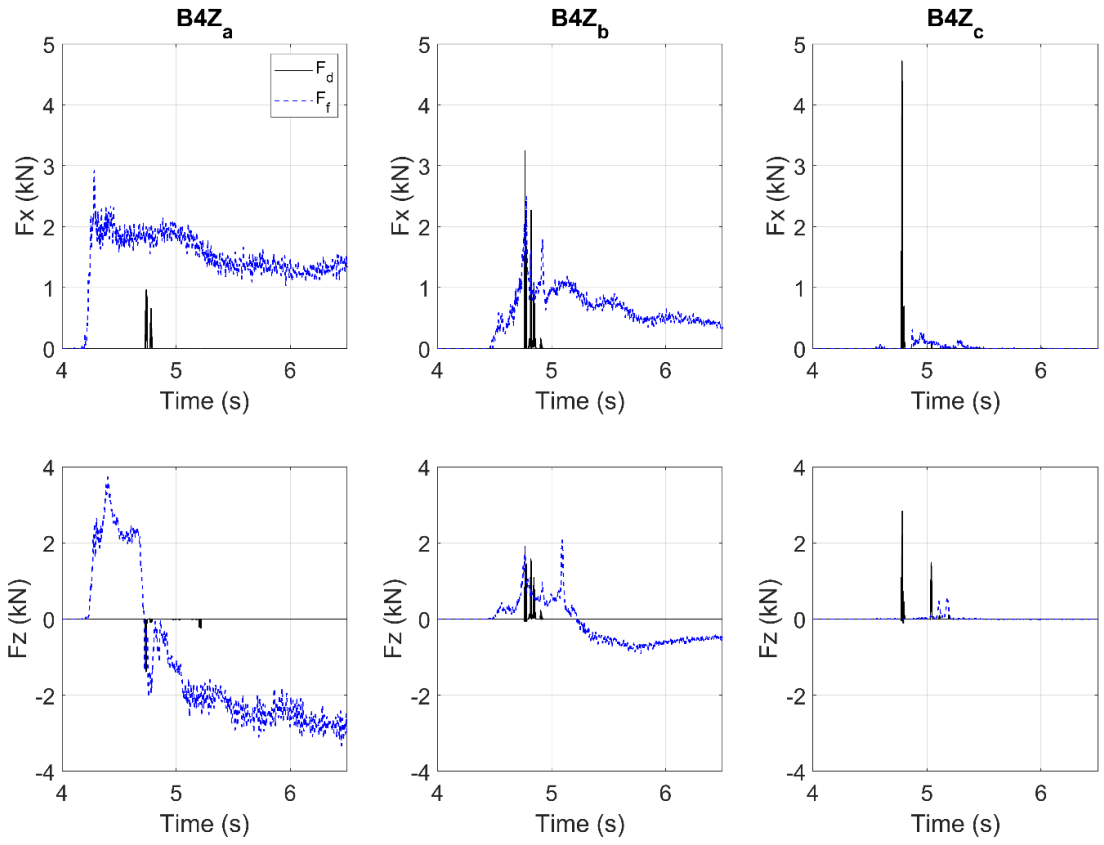

Figure 4-20 Applied horizontal and vertical force histories for three cases with similar bore properties and different bridge elevations, including B4Za (bridge elevation of 0.20 m), B4Zb (bridge elevation of 0.30 m), and B4Zc (bridge elevation of 0.35 m)

Figure 4-21 presents the numerically calculated maximum values of the debris, fluid, and total impact forces in the two directions for three cases with similar bore properties and different deck elevations including $B4Z_a$ (bridge elevation of 0.20 m), $B4Z_b$ (bridge elevation of 0.30 m), and $B4Z_c$ (bridge elevation of 0.35 m). This figure reveals that by increasing the deck elevation, the debris-induced forces are increased as well. For instance, an increase of about 385% and 106% in the horizontal and vertical loads for the highest deck elevation relative to the lowest one are observed, respectively. However, in terms of the hydrodynamic forces, a reduction of about 90% and 85% in the horizontal and uplift forces are reported. This trend could be attributed to the fluid-structure interaction. As mentioned in the previous section, for the higher deck elevation, the tsunami bore barely reaches the deck, and the smoothing effect of fluid particles on the debris-deck interaction decreases. Therefore, debris has a significant contribution to the applied loadings and structural integrity. In terms of the total applied forces, the bridge with the highest elevation experiences up to 62% larger horizontal force relative to the lowest deck elevation. However, the lowest deck elevation exposes to approximately 27% larger uplift force relative to the highest bridge elevation.

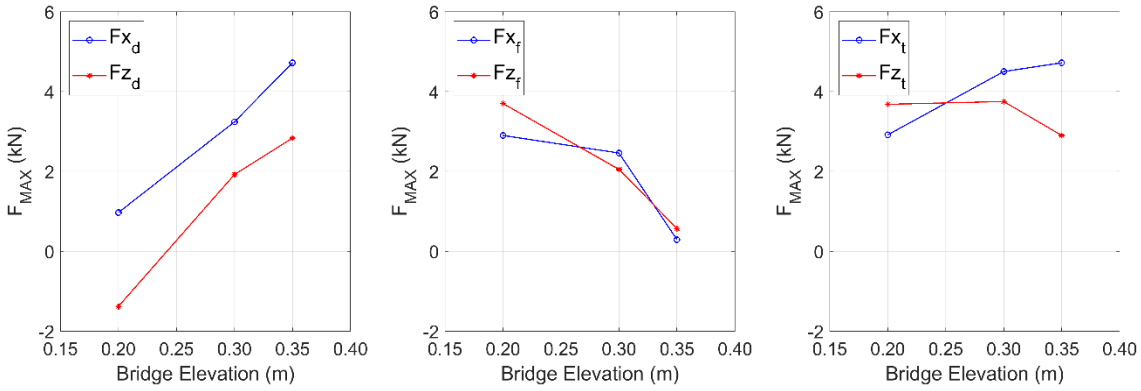

Figure 4-21 Maximum values of the debris, fluid, and total horizontal and vertical forces for three cases with similar bore properties and different bridge elevations, including B4Za (bridge elevation of 0.20 m), B4Zb (bridge elevation of 0.30 m), and B4Zc (bridge elevation of 0.35 m)

4.6. Role of debris

In order to decipher the role of debris on the hydrodynamic and total applied loads (combination of the hydrodynamic loading and the debris impact force), the selected cases were re-analyzed considering clear-water condition (no debris). Figure 4-22 depicts numerically calculated maximum values of the hydrodynamic forces for all the investigated tsunami flows and two scenarios; with and without debris. As shown, in the case of the lowest bridge elevation, i.e., Z_a, the presence of the debris has a negligible effect on the exerted horizontal hydrodynamic forces on the deck. In the case of $B5Z_a$, in which the debris propagates above the deck without any interaction with it, similar fluid forces are applied on the deck for both configurations. However, for the higher bridge elevation, the role of debris in the fluid-bridge interaction becomes more significant. For instance, the presence of the debris leads to an increase up to about 38% and 43% for the bridge elevation of 0.30 m (Z_b) and 0.35 m (Z_c) in the horizontal hydrodynamic force, respectively. In terms of the uplift force, an increasing rate of the applied load due to the presence of debris is observed. Similarly, the increase in peak uplift force appears to be significant for the higher deck elevation with an increase of about 23% and 57% for the elevation of 0.30 m and 0.35 m, respectively. For the higher deck elevation and clear-water conditions, tsunami bore barely reaches the deck. However, the presence of the debris leads to an increase in flow particle velocities around the deck (flow is constricted around the debris) and affects the flow-bridge interaction. Therefore, the approaching bore could inundate the bridge at a higher elevation and impose higher hydrodynamic loads on the bridge.

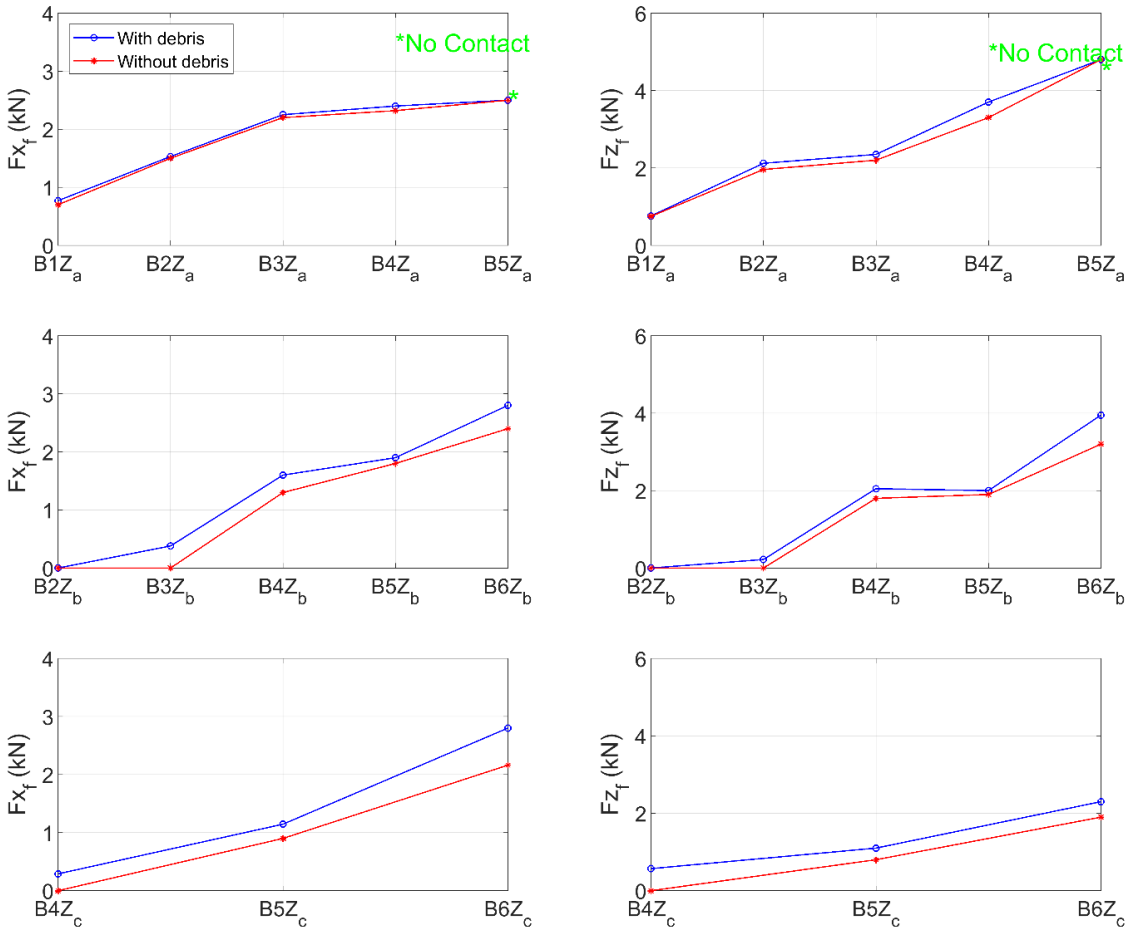

Figure 4-22 Maximum values of the hydrodynamic forces in the horizontal and vertical directions on the bridge superstructure for the investigated cases and two scenarios; with and without debris

To provide further insight into the role of debris on the applied loadings, Figure 4-23 presents numerically predicted maximum values of the total forces for all the tested tsunami waves and two scenarios; with and without debris. This figure reveals that the presence of the debris leads to an increase in the total imposed loads (as expected). However, in the case of $B5Z_a$, the presence of the debris does not affect the magnitude of the total applied loads, since the debris does not interact with the bridge. For some cases in which the tsunami bore does not reach the bridge superstructure such as $B2Z_b$, $B3Z_b$, and $B4Z_c$, the presence of the container plays an important role and has a significant contribution to the induced loadings. In fact, the bridge superstructure experiences about

3.1, 2.2, and 2.8 times larger horizontal force and approximately 1.01, 1.24, and 4.72 times larger uplift force, respectively. Overall, the increase in total horizontal impact force ranged between (0-208) % for Z_a, (112-310) % for Z_b, and (200-550) % for Z_c. In terms of the total uplift loads, the increase in the force ranged between (0-12) % for Z_a, (0-110) % for Z_b, and (70-470) % for Z_c. For some cases where the debris moves above the deck, the increase in the hydrodynamic uplift force is canceled out by the downward debris impact force. For instance, in the case of B3Za, the bridge superstructure exposes to a similar uplift load.

Overall, in terms of the total horizontal impact force, the mean measured force with debris impact is 1.53, 3.57, and 4.91 times larger than the case without debris for the bridge elevation of Z_a, Z_b, and Z_c, respectively, equating to a higher level of impact load. In terms of the total uplift load, the bridge superstructure should withstand 1.88, and 4.26 times larger forces compared to the clear-water condition for Z_b, and Z_c, respectively. However, in the case of the lower elevation (Z_a), the bridge experiences approximately similar total uplift load, which could be attributed to the debris-deck interaction. The observed trends confirmed that for higher bridge elevations, the contribution of the debris to the total impact force is more significant. As stated, in the case of the elevation equal to 0.35 m (Z_c), the bridge exposes to 4.91 and 4.26 times larger horizontal and vertical total impact forces, respectively, compared to the clear-water condition. For higher elevations, it sounds improbable that the tsunami bore reaches the bridge to fully inundate it, therefore, debris-induced forces could govern the failure mechanism of the bridge superstructure.

To improve the understanding of the role of debris on structural demand furthermore, Table 4-3 presents the ratio of the total horizontal (Rx) and vertical (Rz) forces for the models with the debris versus the clear-water condition (with debris/without debris). This table supports the previous figures and shows that for the higher Rx and Rz that the tsunami bore barely reaches the deck, the debris plays an important role and applies significant impact loads on the bridge. For example, in

the case of the highest deck elevation (0.35 m), the presence of the debris causes an increase of up to 6.5 and 4.7 times in the total horizontal and uplift forces, respectively. Furthermore, for case $B3Z_a$ that the debris moves above the deck (trend B), and Rz becomes less than 1, meaning that the total uplift is reduced relative to the clear-water condition. Overall, the observed trends in the previous figures and the reported data in Table 4-3 demonstrate that role of debris on horizontal impact force is more significant than the vertical load.

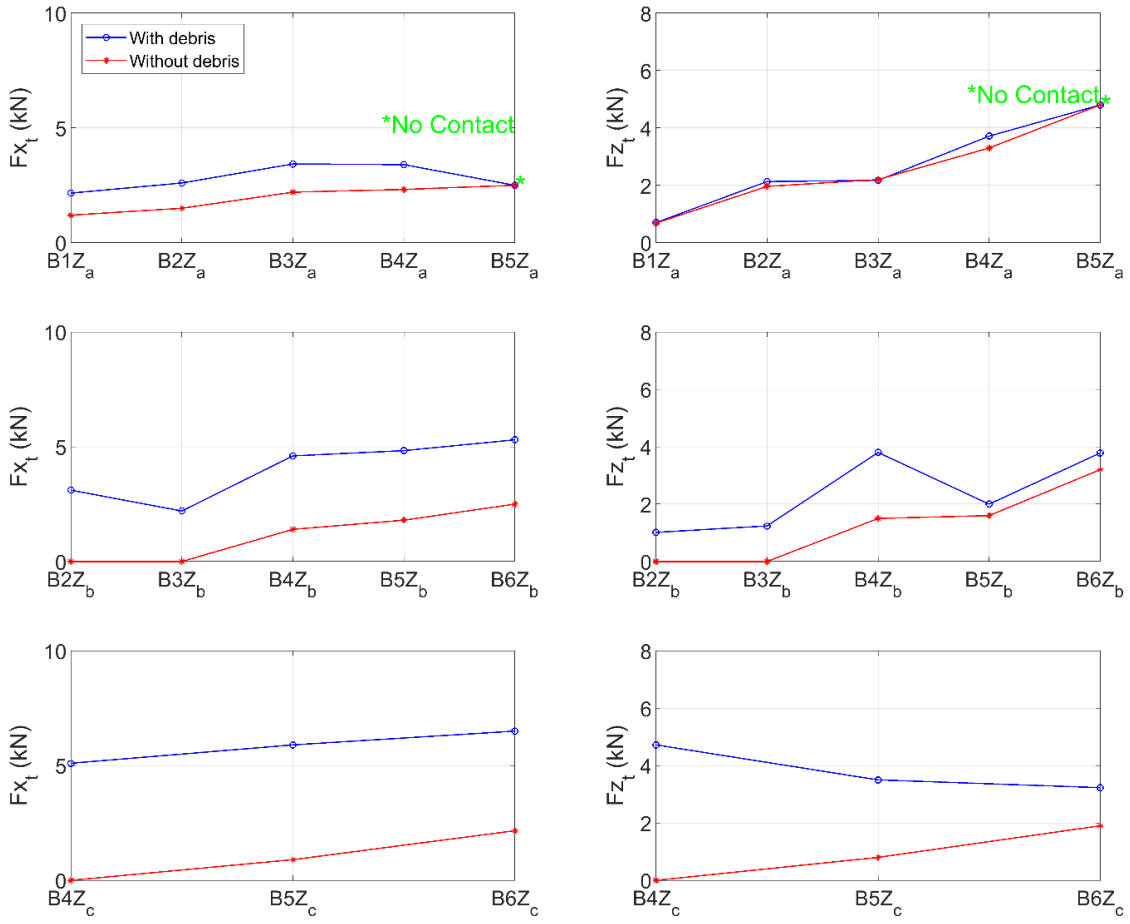

Figure 4-23 Maximum values of the total impact forces in the horizontal and vertical directions on the bridge superstructure for the investigated cases and two scenarios; with and without debris

Table 4-3 Ratio of the total forces with and without debris in the two directions

Bore Cases	H_r (m)	d (m)	Bridge Elevation (m)		
			0.20 (Z_a)	0.30 (Z_b)	0.35 (Z_c)
B1	0.40	0.10	Rx=1.8, Rz=1.1		
B2		0.15	Rx=1.7, Rz=1.1	Rx=3.1, Rz=1.1	
B3	0.60	0.10	Rx=1.5, Rz=0.9	Rx=2.2, Rz=1.2	
B4		0.15	Rx=1.5, Rx=1.1	Rx=3.2, Rz=2.5	Rx=2.8, Rz=4.7
B5		0.20	Rx=1, Rz=1 **(NO CONTACT)**	Rx=2.6, Rz=1.3	Rx=6.5, Rz=4.4
B6		0.25		Rx=2.1, Rz=1.2	Rx=3, Rz=1.7

4.7. Conclusions and recommendations

Numerical simulations using a coupled SPH-FEM method have been performed in order to investigate the three-dimensional debris-flow-bridge interaction. First, the numerical method was validated with an experimental study carried out by Shafiei (2016), revealing the ability to capture the debris dynamics and impact forces on coastal structures. Following the validation, another three-dimensional model was developed, which included a single container with a transverse orientation and a box-girder superstructure and was used to explore the effect of the bore properties, the initial water depth and the bridge elevation on the debris movement and the impact forces. The numerical results provided the following insights:

- **Debris-flow-bridge interaction patterns**: Three different patterns A, B, C were observed in the movement of the debris around the deck, which were affected by the elevation of the bridge, initial water depth and bore properties. The most frequent pattern is A, which can be described by the debris impact on the offshore side of the bridge superstructure followed by the movement below the soffit until it resurfaces again on the onshore side. As the debris passes below the deck, in some cases it impacts the soffit generating uplift loads that can

even exceed the maximum horizontal ones. In pattern B the debris moves above the deck, with or without interacting with the top surface. The least frequent pattern is C, in which the debris impacts the offshore side of the superstructure and becomes trapped below the offshore overhang generating repetitive impulsive loads and long-duration damming loads until the end of the inundation.

- **Debris pitching:** In most cases debris pitching was observed, which tended to reduce in the case of higher initial water levels by up to 36% and increase with the bore strength. In fact, the strongest bore introduced an approximately 3-fold larger maximum debris pitching angle relative to the weaker bore. Interestingly, in some case the debris rotated more than 180 degrees (up to 480 degrees) which means that it turned upside down, a fact that could potentially damage the cargo and would indicate the need for appropriate support systems inside the container to protect the cargo.

- **Debris velocities:** In some cases, after the primary impact on the bridge, as the debris moves below the deck it accelerates and the horizontal velocity increases up to approximately 120% of the horizontal impact velocity, while the vertical velocity can increase up to 163% of the respective value at the primary impact. For the lowest bridge elevations, the debris tends to slow down as it approaches the bridge due to the reflection of the bore on the offshore face of the deck, which means that in these cases the debris impact velocity is smaller that the maximum debris velocity. The latter tends to occur when the approaching tsunami entrains the debris and starts moving it inland. Therefore, this indicates the need to develop methodologies that will be able to account for the bore reflection in order to predict accurately the debris impact velocities that are so essential for estimating the forces on bridges and the associated risk of damage.

Regarding the forces applied on the bridge superstructure, in the case of the shallowest water depth, the applied hydrodynamic (fluid) forces were negligible and the debris impact forces were up to 2 and 1.2 times larger in the two directions respectively. As the initial water level increases, the bridge becomes exposed to higher debris and hydrodynamic forces in both directions. Interestingly, the horizontal debris forces seem to increase consistently with the increase of the water level, however, for the uplift forces this is true only up to a certain water level, after which the trend changes due to the dramatic changes in the debris movement patterns (e.g. debris moves above the deck instead of below the deck). Moreover, as expected the increase of the bore strength increased the loads on the deck, with the stronger tsunami bore exerting 140% larger horizontal forces than the weaker bore.

Another parameter that has a governing effect on the total bridge forces is the deck elevation because it affects the ratio between the debris forces and fluid forces. For example, for small deck elevations the fluid forces can be up to 3 times larger than the debris forces, however, for larger deck elevations the trends are reversing and the debris forces are much larger than the fluid ones, dominating the total demand. Interestingly, as the bridge elevation increases, the debris impact forces increase in both directions, with the bridge at the highest elevation witnessing 385% and 106% larger horizontal and vertical forces respectively than the lowest bridge. On the other hand, for the hydrodynamic forces, an opposite trend seems to occur, with a reduction of about 90% and 85% in the horizontal and uplift forces between the bridge with the highest and lowest elevation. This finding is important for design and risk assessment purposes, because intuitively bridges with higher elevations are less exposed to direct tsunami loads, however, in certain conditions they can witness larger debris loads and consequently larger total loads than lower bridges, which would lead to a higher risk of failure. However, more work is required in the future in order to identify these conditions and the exact risk.

In comparison to the SPH-FEM analyses of clear-water tsunami conditions (no debris) it was found that the presence of the debris tends to affect also the fluid forces on the bridge, which could increase by up to 43% in the horizontal direction. This is because the existence of the debris affects spatially and temporally the flow velocities and consequently the pressures on the bridge. More importantly, for all the investigated cases the debris increased consistently the total horizontal forces, with the ratio of the total forces with debris to the total forces without the debris (Rx) being between 1.5 and 6.5 and having an average value of 2.67. Respectively the same ratio in the vertical direction (Ry) was between 0.9 and 4.7, with an average value of 1.85.

In summary, the presented results reveal the complexity of the phenomena and indicate that appropriate predictive equations should be developed in order to predict both the horizontal and uplift forces at the instant of the primary debris impact on the bridges. Moreover, given the fact that in some cases the soffit experienced several uplift forces after the primary impact as the debris moved below the bridge, it might be necessary to consider multiple load cases that will apply the debris loads at different locations of the deck. Follow up studies with a wider range of hydrodynamic conditions, debris orientations and preferably at prototype scale should be conducted in order to quantify accurately all the aforementioned parameters.

4.8. Acknowledgments

The work described in this paper was supported by the State of California through the Transportation System Research Program of the Pacific Earthquake Engineering Research Center (PEER). Any opinions findings, and conclusion or recommendations expressed in this material are those of the author(s) and do not necessarily reflect those of the funding agency.

4.9. References

1. Unjoh S. (2007). Bridge damage caused by tsunami. B Japan Assoc Earthquake Eng, 2007, 6: 6–28.
2. Aglipay, M.R.I., Kyokawa, H., Konagai, K., 2011. Bridges washed away by tsunami in minamisanriku, miyagi prefecture in the March 11th 2011 Great East Japan earthquake. Seisan Kenkyu 63 (6), 723–727.
3. Kajitani Y, Chang S, Tatano H (2013): Economic Impacts of the 2011 Tohoku-Oki Earthquake and Tsunami.Earthquake Spectra, 29 (S1), S457-S478. [https://doi.org/10.1193%2F1.4000108]
4. Ghobarah, A.; Saatcioglu, M.; Nistor, I. The impact of the 26 December 2004 earthquake and tsunami on structures and infrastructure. Eng. Struct. 2006, 28, 312–326.
5. Naito, C.; Cercone, C.; Riggs, H.R.; Cox, D. Procedure for site assessment of the potential for tsunami debris impact. J. Waterw. Port Coast. Ocean Eng. 2014, 140, 223–232.
6. Ko, H., Cox, D., Riggs, H., and Naito, C. (2015). "Hydraulic experiments on impact forces from tsunami-driven debris." J. Waterway, Port, Coastal, Ocean Eng., 10.1061/(ASCE)WW.1943-5460.0000286, 04014043.
7. U. FEMA, Public Assistance—Debris Management Guide, Dept. of Homeland Security, Washington, DC, 2007.
8. Araki, S.; Ishino, K.; Deguchi, I. (2010). Stability of girder bridge against tsunami fluid force. In Proceedings of the 32th International Conference on Coastal Engineering (ICCE), Shanghai, China, June 30- July 5, 2010.
9. Lau, T.L.; Ohmachi, T.; Inoue, S.; Lukkunaprasit, P. (2011). Experimental and Numerical Modeling of Tsunami Force on Bridge Decks; InTech: Rijeka, Croatia, 2011; pp. 105–130.
10. Nakao, H., Zhang, G., Sumimura, T., & Hoshikuma, J. I. (2013, November). Numerical assessment of tsunami-induced effect on bridge behavior. In Proceedings of the 29th US-Japan Bridge Engineering Workshop, Tsukuba, Japan (pp. 11-13).
11. Azadbakht, Mohsen. (2013). Tsunami and hurricane wave load on bridge superstructures. PhD dissertation, Oregon State University
12. P. Lomonaco, D. Istrati, T. Maddux, I.G. Buckle, S. Yim, T. Xiang (2016): "Large-scale testing of tsunami impact forces on bridges". Proc. 6th Intl Conf on the Application of Physical Modelling in Coastal and Port Eng and Science (Coastlab16), Ottawa, Canada, May 10-13, 2016, DOI: 10.13140/RG.2.1.5184.2160
13. Nakamura, T., Sawa, Y., & Mizutani, N. (2016). Study on the evaluation of temporal change in horizontal and vertical tsunami forces acting on a bridge superstructure. Coastal Engineering Journal, 58(4), 1640020-1. [https://doi.org/10.1142/S0578563416400209]
14. Istrati, D. 2017. "Large-scale experiments of tsunami inundation of bridges including fluid-structure-interaction." Ph.D. dissertation, Dept. of Civil Engineering and Environmental Engineering, Univ. of Nevada, Reno.
15. Zhu, M.; Elkhetali, I.; Scott, M.H. (2018). Validation of OpenSees for tsunami loading on bridge superstructures. J. Bridge Eng. 2018, 23, 04018015.
16. Bricker, J.D.; Nakayama, A. "Contribution of trapped air, deck superelevation, and nearby structures to bridge deck failure during a tsunami". J. Hydraulic Eng. 2014, 140, 05014002. [https://doi.org/10.1061/(ASCE)HY.1943-7900.0000855]
17. Istrati, D., Buckle, I. G., Lomonaco, P., Yim, S., & Itani, A. (2017a). Tsunami induced forces in bridges: large-scale experiments and the role of air-entrapment. Coastal Engineering Proceedings, (35), 30-30. https://doi.org/10.9753/icce.v35.structures.30
18. Istrati, D., Buckle, I.G. (2019): "Role of Trapped Air on the Tsunami-Induced Transient Loads and Response of Coastal Bridges", Geosciences journal, MDPI, 9 (191), doi: 10.3390/geosciences9040191

19. Istrati, D., Buckle, I., Lomonaco, P., Yim, S., & Itani, A. (2016). Large-scale experiments of tsunami impact forces on bridges: The role of fluid-structure interaction and air-venting. In The 26th International Ocean and Polar Engineering Conference. OnePetro.
20. Bradner, C.; Schumacher, T.; Cox, D.; Higgins, C. (2010). Experimental setup for a large-scale bridge superstructure model subjected to waves. J. Waterw. Port Coast. Ocean Eng. 2010, 137, 3–11.
21. Istrati, D. and Buckle, IG. (2014): "Effect of fluid-structure interaction on connection forces in bridges due to tsunami loads," Proc. 30th US-Japan Bridge Eng Workshop, Washington D.C., USA, https://www.pwri.go.jp/eng/ujnr/tc/g/pdf/30/30-10-2_Buckle.pdf
22. Xiang T., Istrati, D., T., Yim, S., Buckle, I.G., Lomonaco, P. (2020): "Tsunami loads on a representative coastal bridge deck – experimental study and validation of design equations", ASCE Journal of Waterway, Port, Coastal, and Ocean Engineering, https://doi.org/10.1061/(ASCE)WW.1943-5460.0000560
23. Xiang, T.; Istrati, D. (2021): Assessment of Extreme Wave Impact on Coastal Decks with Different Geometries via the Arbitrary Lagrangian-Eulerian Method. Journal of Marine Science and Engineering, 2021, MDPI, 9(12), 1342
24. Istrati, D., I. Buckle, P. Lomonaco, and S. Yim. 2018. "Deciphering the tsunami wave impact and associated connection forces in open-girder coastal bridges." J. Mar. Sci. Eng. 6 (4): 148.
25. Akiyama, M., Frangopol, D. M., Arai, M., & Koshimura, S. (2013). Reliability of bridges under tsunami hazards: Emphasis on the 2011 Tohoku-oki earthquake. *Earthquake Spectra*, *29*(1_suppl), 295-314.
26. Burns, P. O., Barbosa, A. R., Olsen, M. J., & Wang, H. (2021). Multihazard damage and loss assessment of bridges in a highway network subjected to earthquake and tsunami hazards. Natural Hazards Review, 22(2), 05021002.
27. Greco, F., Lonetti, P., & Blasi, P. N. (2021). Impact mitigation measures for bridges under extreme flood actions. *Journal of Fluids and Structures*, *106*, 103381.
28. Pregnolato, M., Gavriel, G., & Lopane, F. D. (2021). A risk-based taxonomy for bridges at risk of flooding. In Bridge Maintenance, Safety, Management, Life-Cycle Sustainability and Innovations (pp. 3282-3285). CRC Press.
29. Mitoulis, S. A., Argyroudis, S. A., Loli, M., & Imam, B. (2021). Restoration models for quantifying flood resilience of bridges. Engineering structures, 238, 112180.
30. Loli, M., Kefalas, G., Dafis, S., Mitoulis, S. A., & Schmidt, F. (2022). Bridge-specific flood risk assessment of transport networks using GIS and remotely sensed data. Science of the Total Environment, 850, 157976.
31. Motley, M. R., Wong, H. K., Qin, X., Winter, A. O., & Eberhard, M. O. (2016). Tsunami-induced forces on skewed bridges. Journal of Waterway, Port, Coastal, and Ocean Engineering, 142(3), 04015025.
32. Istrati, D., & Buckle, I. G. (2021a). Tsunami Loads on Straight and Skewed Bridges–Part 1: Experimental Investigation and Design Recommendations (No. FHWA-OR-RD-21-12). Oregon. Dept. of Transportation. Research Section. https://rosap.ntl.bts.gov/view/dot/55988
33. Istrati, D., Buckle, I.G. (2021b): Tsunami Loads on Straight and Skewed Bridges–Part 2: Numerical Investigation and Design Recommendations (No. FHWA-OR-RD-21-13). Oregon. Dept. of Transportation. Research Section, https://rosap.ntl.bts.gov/view/dot/55947
34. Jia, L., Zhang, Y., Zhu, D., & Dong, Y. (2022). 3D Numerical Modeling and Quantification of Oblique Wave Forces on Coastal Bridge Superstructures. Journal of Marine Science and Engineering, 10(7), 860.
35. Rossetto, T., et al., 2007. The Indian Ocean tsunami of December 26, 2004: observations in Sri Lanka and Thailand. Nat. Hazards 42 (1), 105–124.
36. Robertson, I., Chock, G., and Morla, J. (2010). "Tsunami effects of the February 27, 2010 Chile earthquake." EERI Preliminary Rep., Earthquake Engineering Research Institute, Oakland, CA.

37. Yeh, H., Sato, S., & Tajima, Y. (2013). The 11 March 2011 East Japan earthquake and tsunami: Tsunami effects on coastal infrastructure and buildings. Pure and Applied Geophysics, 170(6), 1019-1031.
38. Esteban, M., Takagi, H., & Shibayama, T. (Eds.). (2015). Handbook of coastal disaster mitigation for engineers and planners. Butterworth-Heinemann.
39. Haehnel, R. B., & Daly, S. F. (2004). Maximum impact force of woody debris on floodplain structures. Journal of Hydraulic Engineering, 130(2), 112-120.
40. Matsutomi, H. (2009). Method for estimating collision force of driftwood accompanying tsunami inundation flow. Journal of Disaster Research, 4(6), 435-440.
41. ARIKAWA, T., OHTSUBO, D., Nakano, F., SHIMOSAKO, K., & ISHIKAWA, N. (2007). Large model tests of drifting container impact force due to surge front tsunami. In Proceedings of coastal engineering, JSCE (Vol. 54, pp. 846-850). Japan Society of Civil Engineers.
42. Madurapperuma, M. A. K. M., and Wijeyewickrema, A. C. (2012). "Inelastic dynamic analysis of an RC building impacted by a tsunami water-borne shipping container." J. Earthquake Tsunami, 6, 1250001. [https://doi.org/10.1142/S1793431112500017]
43. Ikeno, M., Takabatake, D., Kihara, N., Kaida, H., Miyagawa, Y., & Shibayama, A. (2016). Improvement of collision force formula for woody debris by airborne and hydraulic experiments. Coastal Engineering Journal, 58(04), 1640022.
44. Shafiei, S., Melville, B. W., Shamseldin, A. Y., Adams, K. N., & Beskhyroun, S. (2016). Experimental investigation of tsunami-borne debris impact force on structures: Factors affecting impulse-momentum formula. Ocean Engineering, 127, 158-169.
45. Goseberg, N., Stolle, J., Nistor, I., & Shibayama, T. (2016). Experimental analysis of debris motion due the obstruction from fixed obstacles in tsunami-like flow conditions. Coastal Engineering, 118, 35-49. [https://doi.org/10.1016/j.coastaleng.2016.08.012]
46. Kennedy, A. B., Mori, N., Yasuda, T., Shimozono, T., Tomiczek, T., Donahue, A., ... & Imai, Y. (2017). Extreme block and boulder transport along a cliffed coastline (Calicoan Island, Philippines) during Super Typhoon Haiyan. Marine Geology, 383, 65-77.
47. Derschum, C., Nistor, I., Stolle, J., & Goseberg, N. (2018). Debris impact under extreme hydrodynamic conditions part 1: Hydrodynamics and impact geometry. Coastal Engineering, 141, 24-35. [https://doi.org/10.1016/j.coastaleng.2018.08.016]
48. Park, H., Koh, M. J., Cox, D. T., Alam, M. S., & Shin, S. (2021). Experimental study of debris transport driven by a tsunami-like wave: Application for non-uniform density groups and obstacles. Coastal Engineering, 166, 103867.
49. Hou, Y., Nakamura, T., Cho, Y. H., Mizutani, N., & Tomita, T. (2022). Influence of Tsunami-Driven Shipping Containers' Layout on Their Motion. Journal of Marine Science and Engineering, 10(12), 1911.
50. Como, A., and Mahmoud, H. (2013). "Numerical evaluation of tsunami debris impact loading on wooden structural walls." Engineering. Structures., 56, 1249–1261.
51. Canelas, R., Ferreira, R. M. L., Domínguez, J. M., & Crespo, A. J. C. (2014). Modelling of wave impacts on harbour structures and objects with SPH and DEM. In Proc. 9th SPHERIC Int. Workshop (pp. 313-320).
52. Canelas, Ricardo B., Alejandro JC Crespo, Jose M. Domínguez, Rui ML Ferreira, and Moncho Gómez-Gesteira. "SPH–DCDEM model for arbitrary geometries in free surface solid–fluid flows." Computer Physics Communications 202 (2016): 131-140.
53. Ruffini, G., Briganti, R., De Girolamo, P., Stolle, J., Ghiassi, B., & Castellino, M. (2021). Numerical Modelling of Flow-Debris Interaction during Extreme Hydrodynamic Events with DualSPHysics-CHRONO. Applied Sciences, 11(8), 3618.
54. Takabatake, Tomoyuki, Jacob Stolle, Koji Hiraishi, Naoto Kihara, Kazuya Nojima, Yoshinori Shigihara, Taro Arikawa, and Ioan Nistor. "Inter-model comparison for tsunami debris simulation." Journal of Disaster Research 16, no. 7 (2021): 1030-1044.

55. Hasanpour, A., Istrati, D., & Buckle, I. (2021). Coupled SPH–FEM Modeling of Tsunami-Borne Large Debris Flow and Impact on Coastal Structures. Journal of Marine Science and Engineering, 9(10), 1068. [https://doi.org/10.3390/jmse9101068]
56. Reis, C., Lopes, M., Baptista, M. A., & Clain, S. (2022). Towards an integrated framework for the risk assessment of coastal structures exposed to earthquake and tsunami hazards. Resilient Cities and Structures, 1(2), 57-75.
57. Yang, W.C. Study of Tsunami-Induced Fluid and Debris Load on Bridges using the Material Point Method. Ph.D. Thesis, University of Washington, Seattle, WA, USA, 2016. Available online: http://hdl.handle.net/1773/37064 (accessed on 15 July 2021).
58. Oudenbroek, Kevin, Nader Naderi, Jeremy D. Bricker, Yuguang Yang, Cor Van der Veen, Wim Uijttewaal, Shuji Moriguchi, and Sebastiaan N. Jonkman. "Hydrodynamic and debris-damming failure of bridge decks and piers in steady flow." Geosciences 8, no. 11 (2018): 409. [https://doi.org/10.3390/geosciences8110409]
59. Majtan, E., Cunningham, L. S., & Rogers, B. D. (2021). Flood-induced hydrodynamic and debris impact forces on single-span masonry arch bridge. Journal of Hydraulic Engineering, 147(11), 04021043.
60. Panici, D., & de Almeida, G. A. (2018). Formation, growth, and failure of debris jams at bridge piers. Water Resources Research, 54(9), 6226-6241.
61. Zhang, W., Nistor, I., Rennie, C. D., & Almansour, H. (2022). Influence of Dynamic Woody Debris Jam on Single Bridge Pier Scour and Induced Hydraulic Head. Journal of Marine Science and Engineering, 10(10), 1421.
62. Istrati, D., & Hasanpour, A. (2022). Advanced numerical modelling of large debris impact on piers during extreme flood events. In Proceedings of the 7th IAHR Europe Congress, Athens, Greece (pp. 7-9).
63. Istrati, D.; Hasanpour, A.; Buckle, I. (2020) Numerical Investigation of Tsunami-Borne Debris Damming Loads on a Coastal Bridge. In Proceedings of the 17 World Conference on Earthquake Engineering, Sendai, Japan, 13–18 September 2020.
64. Hasanpour, A., Istrati, D., & Buckle, I. G. (2022). Multi-Physics Modeling of Tsunami Debris Impact on Bridge Decks. In Proceedings of the 3rd International Conference on Natural Hazards & Infrastructure, Athens, Greece (pp. 5-7). EID: 2-s2.0-85137813076, ISSN: 26234513
65. Monaghan, J.J. Simulating free surface flows with SPH. J. Comput. Phys. 1994, 110, 399–406.
66. Hallquist, J.O. LS-DYNA theory manual. Liverm. Softw. Technol. Corp. 2006, 3, 25–31.
67. St-Germain, Philippe, Ioan Nistor, Ronald Townsend, and Tomoya Shibayama. "Smoothed-particle hydrodynamics numerical modeling of structures impacted by tsunami bores." Journal of Waterway, Port, Coastal, and Ocean Engineering 140, no. 1 (2014): 66-81.
68. Shafiei Amraei, S (2016). Tsunami Inland Structures Interaction and Impact of Floating Debris (Doctoral dissertation, University of Auckland).
69. Mast, R., Marsh, L., Spry, C., Johnson, S., Griebenow, R., Guarre, J., & Wilson, W. (1996). Seismic design of bridges-design example no. 1: Two-span continuous CIP concrete box bridge (No. FHWA-SA-97-006).
70. Mast, R., Marsh, L., Spry, C., Johnson, S., Griebenow, R., Guarre, J., & Wilson, W. (1996). SEISMIC DESIGN OF BRIDGES-DESIGN EXAMPLE NO. 2: THREE-SPAN CONTINUOUS STEEL GIRDER BRIDGE (No. FHWA-SA-97-007).
71. Mast, R., Marsh, L., Spry, C., Johnson, S., Griebenow, R., Guarre, J., & Wilson, W. (1996). SEISMIC DESIGN OF BRIDGES-DESIGN EXAMPLE NO. 3: SINGLE SPAN AASHTO PRECAST GIRDER BRIDGE (No. FHWA-SA-97-008).
72. Mast, R., Marsh, L., Spry, C., Johnson, S., Griebenow, R., Guarre, J., & Wilson, W. (1996). SEISMIC DESIGN OF BRIDGES-DESIGN EXAMPLE NO. 4: THREE-SPAN CONTINUOUS CIP CONCRETE BRIDGE (No. FHWA-SA-97-009).

73. Mast, R., Marsh, L., Spry, C., Johnson, S., Griebenow, R., Guarre, J., & Wilson, W. (1996). SEISMIC DESIGN OF BRIDGES-DESIGN EXAMPLE NO. 7: TWELVE-SPAN VIADUCT AASHTO PRECAST CONCRETE BRIDGE (No. FHWA-SA-97-012).

Chapter 5

5. Effect of Debris Orientation on the Debris-Tsunami-Bridge Interaction and Induced Forces

Abstract

Natural hazard events such as tsunamis pose a significant threat to coastal communities and infrastructure. These events can result in significant environmental destruction and damage to coastal infrastructure, including bridges, and can endanger human lives. The vulnerability of near-shore bridges to both the hydrodynamic power of the tsunami and the impact forces of water-borne debris has been demonstrated by major earthquakes in the past. Field surveys have shown that the presence of debris carried by tsunami flow such as shipping containers, can lead to a significant increase in the peak forces impacting structures and potentially cause severe structural failure. In light of the potential consequences of natural hazards events, it is crucial to advance the understanding of tsunami-borne debris loadings on coastal bridges. The goal of this study is to utilize the coupled SPH-FEM molding technique to gain a deeper understanding of the fundamental physics behind three-dimensional (3D) debris-wave and debris-wave-bridge interactions. A comprehensive numerical investigation was conducted to examine the role of various parameters in these interactions. The findings of this study showed the debris can remain on the offshore side, travel above the deck, or move below it. The three-dimensional nature of flow can affect the debris movement and results in significant yaw rotation. The presence of debris pitching was also attributed to variations in the velocities of offshore and onshore corners. Interestingly, in some cases, after the initial impact, the container may accelerate and reach velocities that are similar to or greater than those at the instant of initial impact and consequently applied follow-up impacts. Furthermore, the longitudinal debris reaches higher velocities compared to the transverse debris which in turn leads to on average about 1.48 and 1.5 times greater horizontal and vertical debris forces, respectively. Last but not least, the presence of debris results in average about 3.64 and 2.13 times larger horizontal and vertical forces, respectively, compared to cases without debris.

Keywords: tsunami; wave; bore; flooding; debris; SPH; numerical modeling; SPH-FEM coupling; fluid structure interaction, bridge

5.1. Introduction

In response to climate change and adverse consequences of population growth, natural hazard events like tsunamis, bring significant environmental destruction and devastation to coastal infrastructure such as bridges and endanger lives. As observed during the recent major earthquakes which took place in the Indian Ocean (2004) and Japan (2011), near-shore bridges located in tsunami-prone areas are increasingly vulnerable to not only the destructive hydrodynamic power of tsunamis, but also water-borne debris impact loads. The Indian Ocean tsunami caused about 350,000 causalities which is considered the deadliest natural disaster of the 21st century [1]. A total of 1,100 km of coastline was affected and 81 bridges were washed away [2]. The Great East Japan resulted in widespread damages of about USD211 billion which made it the costliest natural disaster on record [3]. More than 119,000 residential buildings collapsed and 252 bridges were damaged [3, 4] and a total loss of life of over 19,000 occurred [5]. Post-tsunami reconnaissance surveys revealed that the induced forces by tsunami waves, debris, and floating objects led to a significant lateral displacement or washout of the bridge deck [6, 7]. The results derived from these surveys also showed that the presence of debris carried by tsunami flow is responsible for a drastic increase in the peak forces impacting the structures, which could lead to severe structural failure [8, 9]. Therefore, it is of extreme importance to advance the understanding of tsunami-borne debris loadings and the effects on coastal bridges to reduce casualties and improve the performance of these structures that may be subject to future earthquake and tsunami events.

The documented extensive damage to coastal bridges in recent tsunamis provoked the research community around the world to focus on the tsunami inundation mechanism and contribute to the development of a better understanding of the tsunami forces on coastal bridges. Guo et al. (2015)

[10] proposed an analytical method to estimate the applied wave forces on submerged bridge superstructure. Nakamura et al. (2016) [11] experimentally and numerically evaluated the performance of bridge superstructure against tsunami and concluded that drag and Morisons' equation are able to predict the steady-state component of the applied forces. Araki et al. (2010) [12] and Istrati (2017) [13] experimentally assessed the performance of bridge superstructure against different types of waves including unbroken, breaking, and post-breaking waves and bore, and observed different patterns of loadings. In fact, Istrati (2017) [13] demonstrated that the horizontal forces exceed the uplift forces by a factor of 2.2 for the turbulent bore, while in the case of the unbroken waves, the vertical forces were larger than the horizontal forces by up to a factor of 1.85. Some studies evaluated the effects of air entrapment on wave-induced forces on bridge deck and exhibited via small-scale [14] and large-scale experiments [15] or numerical simulations [16, 17] that bridge decks with solid diaphragms at the supports trapped significant amount of air in the chambers, increasing substantially the buoyancy and the total wave-induced uplift forces. More recently, it was revealed by Istrati and Buckle (2019) [15], that this trapped air does not only increase the total uplift loads but it has a complex role that modifies the fluid flow in the chambers and the wave-structure interaction, introduces a different pattern of horizontal and vertical pressures. Although the main focus of the past studies is on the maximum horizontal and uplift forces, some of them [13, 15, 18-21] highlighted the importance of the wave-induced overturning moment in combination with the uplift and horizontal forces which leads to increase demand in specific bearings and connections. More specifically, the large-scale experimental conducted by Istrati et al. (2018) [18] revealed that the force combination of the overturning moment generated at the time of the initial impact and large forces transfers to the significant uplift forces in the offshore bearings that are larger than the forces in the onshore bearings by up to a factor of 5.9 for turbulent bore.

In recent years, quantifying the impact forces caused by water-borne debris attracted the attention of researchers and several studies were gone into the evaluation of these loading conditions. Haehnel and Daly (2004) [22] and Matsutomi (2009) [23] studied the maximum induced force by woody debris and reported that the peak impact force is a function of impact velocity, the mass of the debris, and the effective stiffness between the floating object and the structure. The performance of RC columns against the impact loads from water-borne shipping containers was investigated by Madurapperuma and Wijeyewickrema (2012) [24] and a linear relationship between the maximum impact force and container velocity up to 2m/s was reported. Farahmandpour et al. (2016) [25] experimentally investigated debris impact forces on structures. Goseberg et al. (2016) [26] conducted 1:40 experimental studies to analyze floating container motion. Canelas et al., (2017) [27] employed the SPH-DCDEM numerical approach and the results showed the capability of this technique to capture the debris flow. In an experimental effort, Nistor et al. (2017) [28] studied debris motion over a horizontal apron and a linear relationship between the spreading angles and total inland displacement was reported. In another study by Roohparvar et al. (2018) [29], the transient motion of floating debris was evaluated and a model to predict the debris motion was proposed. Derschum et al. (2018) [30] carried out a 1:40 scaled experimental study to evaluate the impact of a shipping container on a vertical structure and reported that the hydraulic condition has a significant effect on impact geometry. Some research studies focused on the role of structural stiffness and demonstrated that the debris impact forces can be significantly decreased by increasing the deformability of the debris [31] or the structural flexibility [32].

Despite the major contribution to the damage or failure mechanism of coastal bridges during tsunami inundation, significantly limited research studies addressed the water-borne debris impact and damming on bridge decks. Using the material point method, the debris impact loading on the bridge deck was investigated by Yang (2016) [33] and it was revealed that the presence of debris

leads to a drastic increase in the peak forces impacting the structures, with the in-water analyses resulting up to 35% higher debris impact forces than the in-air scenarios. Oudenbroek et al. (2018) [34] experimentally and numerically studied the debris damming loads on a bridge deck and found that debris accumulation played a major role in the failure of the bridge by increasing the demands on structural components. More recently, tsunami-borne debris damming load on coastal bridges was investigated by Istrati et al. (2020) [35] through a three-dimensional numerical investigation. The results of the analyses revealed that while the debris damming does not affect the horizontal and vertical loads significantly, it has a major effect on the overturning moment which could introduce an additional uplift force and lead to the failure of the offshore bearings and connections. Moreover, if the container is trapped close to the supports of the span, due to the 3D effects, additional yow and roll moments are generated, which should be accounted for the design of the structural components to avoid potential damage or collapse. Ruffini et al., (2021) [36] employed the open-source DualSPHysics and it was shown that the model is able to re-generate the floating debris dynamics (trajectory and velocity) with good accuracy. Hasanpour et al. (2021) [37] used the coupled SPH-FEM to investigate the complex wave-debris-structure interaction and loads on coastal structures. The results of the analyses demonstrated that coupled SPH-FEM is able to capture the non-linear transformation of the tsunami wave as it propagates inland, debris-fluid interaction, and the impact on the coastal structure. Moreover, a high level of debris pitching which transferred to the non-normal impact on the coastal structure, and the resultant reduced contact area and impact force was observed. It was reported that the level of debris pitching is a function of tsunami flow characteristics and initial water depth and a non-linear force-velocity trend for small water depth was documented. More recently, Hasanpour et al., (2022) [38] studied the tsunami debris impact on bridge deck using the coupled SPH-FEM and reported that the debris shows both a horizontal and vertical velocity at the instant of the primary impact and applies impulsive loads simultaneously in both directions, and the debris-fluid-deck interaction is quite complex and can

accelerate the debris as it moves below the bridge, causing follow up impacts on the soffit with significant magnitudes much larger than the ones of the initial. In another study, Istrati and Hasanpour (2022) [39] carried out numerical investigation to study the water-borne debris impact loads on piers and the results revealed that the debris impulsive loads are 6 to 10 times larger than the fluid force.

Considering the rapid growth of coastal communities, it is of utmost significance to increase the resiliency of coastal communities against extreme natural hazards such as tsunamis and the catastrophic effects of tsunami-borne debris loading to lessen the associated damages. In recent years, while extremely valuable progress was made towards developing and designing resilient coastal infrastructure to withstand the impact of natural disasters, a quite limited number of studies addressed tsunami-borne debris loading on coastal bridges. The objective of the present study is to utilize the coupled three-dimensional SPH-FEM technique to investigate tsunami-borne debris applied loadings on a bridge superstructure.

5.2. Methodology

The SPH technique employed in this research was implemented in the LS-DYNA software and is based on weakly compressible smoothed particle hydrodynamics (WCSPH). LS-DYNA enables the coupling of mesh-based (FEM) and mesh-less methods (SPH). Extensive details of the method could be found in Hasanpour et al., (2021) [37].

Validation

This paper is the continuation of another study [40]. The coupled SPH-FEM modeling technique was validated against experimental data of tsunami inland structures interaction and the impact of floating debris found in Shafiei (2016) [41]. Details of the numerical settings and the results could be found in Hasanpour et al., (2023) [40].

Numerical models of longitudinal debris impact on a box-girder bridge

In order to quantify the large debris impact on bridge decks subjected to extreme hydrodynamic events, the developed numerical model of the validation study was used with some modifications. First, the coastal structure was replaced with a scaled-down bridge deck that is 0.50 m long and 0.13m tall, based on the dimensions used in previous large-scale hydrodynamic tests [13]. Second, a standard shipping container with dimensions of 6.1m by 2.6m by 2.6m was used to represent the floating debris. The dimensions of the model container are scaled down to 0.30m long, 0.13m wide, and 0.13m tall based on a length scale of 1:20. Third, the length of the reservoir in the numerical model was increased from 4.2m to 10m to ensure a steady-state condition and an adequate volume of water to transport the debris. Finally, the outlet was moved 2 m upstream and an artificial beach with a slope of 1:12 and an end reservoir was added to the model to avoid boundary conditions that could affect the debris-wave and debris-wave-bridge interactions. The resulting numerical model was 36 m long, 1.2 m wide, and consisted of 969,908 shell elements and 4,203,331 SPH particles. Figure 5-1 shows the cross-section (top), three-dimensional, and top views (bottom) of the numerical model. It should be noted that to generate the snapshot of the three-dimensional view, the SPH part was deactivated. The computational analyses run on a high-performance computing cluster at the University of Nevada, Reno, with analysis times ranging from 78 to 110 hours depending on the hydrodynamic characteristics.

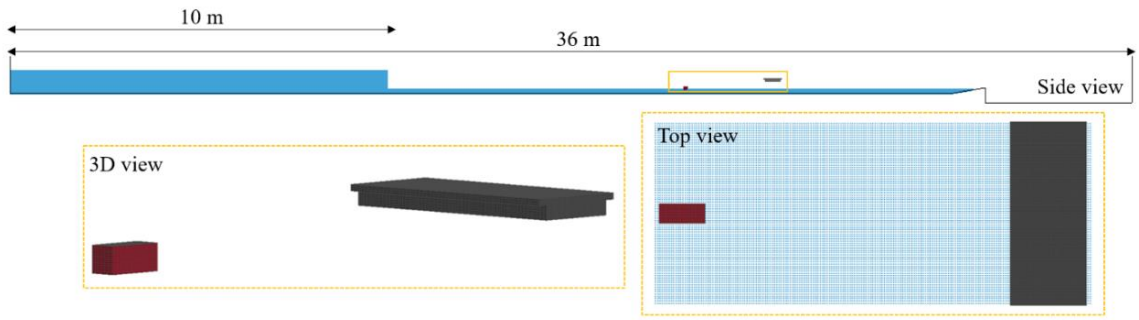

Figure 5-1 Cross section of the computational domain (top), three-dimensional and top views of numerical models with the debris and the bridge (bottom)

A standard shipping container with a maximum full-scale weight of 245.2 kN was used in this research study. According to Ko et al., (2015) [42], the typical empty weight of a standard shipping container is approximately 9.2% of the maximum full-scale weight. For this study, a total weight of 0.0153 kN was considered, which included 50% of the total weight of a standard shipping container (9.2% representing the empty container weight and 40.8% representing nonstructural mass/cargo). The debris specimen was scaled down to 1:20 using the Froude similarity law, resulting in a prototype weight of 122.6 kN. Nonstructural mass was added to the debris to simulate shipping container cargo, which was distributed uniformly along the bottom slab of the debris. For the purpose of this study, the longitudinal orientation of the debris was defined such that the major axis is parallel to the direction of wave propagation and the minor axis is perpendicular to the horizontal axis of the flume. The resulting draft of the debris for the numerical simulations is 3.9 cm.

The Federal Highway Administration has determined the weight per deck area for various types of bridges, including two-span continuous CIP concrete box bridges (13.04 kN /m^2), three-span continuous steel girder bridges (9.75 kN /m^2), single-span precast girder bridges (12.31 kN /m^2), three-span continuous CIP concrete bridges (16.66 kN /m^2), three-span continuous CIP concrete box bridges (15.59 kN /m^2), and twelve span viaduct precast concrete bridges (11.80 kN /m^2) [43-

47]. For this parametric investigation, the average weight of a hypothetical single-span bridge is taken to be 0.40 kN /m^2, which corresponds to a prototype average weight of 13.19 kN /m^2 at a 1:20 scale. In the numerical investigations, three different deck elevations (0.20 m, 0.30 m, and 0.35 m) were considered to compare different scenarios.

5.3. Tsunami flow characteristics

A range of hydrodynamic conditions, as shown in Table 5-1, were considered to study the debris-wave and debris-wave-bridge interactions. The initial water level is varied from 0.10m to 0.25m in the analysis. The selected range of the reservoir depth is similar to that used by Shafiei (2016) [41]. The numerically predicted maximum values of the bore height, free-surface, maximum velocity at the level of the maximum initial free-surface for the weakest bore (B1), i.e. Z=0.25m, and maximum velocity at free-surface are reported in Table 5-1. As expected, the fluid velocity reaches its maximum magnitude at the free-surface level and decreases with depth.

Figure 5-2 displays the variation of the bore height and fluid particle velocity (V_f) for strong bores (B3, B4, B5, and B6). The bore height time-histories are plotted along with the fluid particle velocities, which are measured at the same x coordinate and at the level of the maximum free-surface for the weakest bore (B1, Z=0.25 m). The figure shows that the tsunami bores at the debris location have a relatively long duration, which allows the debris to be transported, impact the bridge, and interact with it. The figure also indicates that the velocities of the tsunami bores are appropriate for tsunami-like conditions.

Table 5-1 Hydrodynamic conditions and maximum magnitude of bore height, free-surface and fluid velocity at Z=0.25m and at free-surface

Bore cases	d: Initial water level (m)	H_r: Reservoir level (m)	Bore strength	Bore height (m)	Free-surface (m)	Max. velocity @ Z=0.25m (m/s)	Max. velocity @ free-surface (m/s)
B1	0.10	0.40	Weak	0.15	0.25	1.2	1.25
B2	0.15			0.153	0.303	0.98	1.51
B3	0.10	0.60	Strong	0.163	0.263	2	2.10
B4	0.15			0.172	0.322	1.8	2.52
B5	0.20			0.216	0.416	1.5	3.1
B6	0.25			0.217	0.467	1.5	3.25

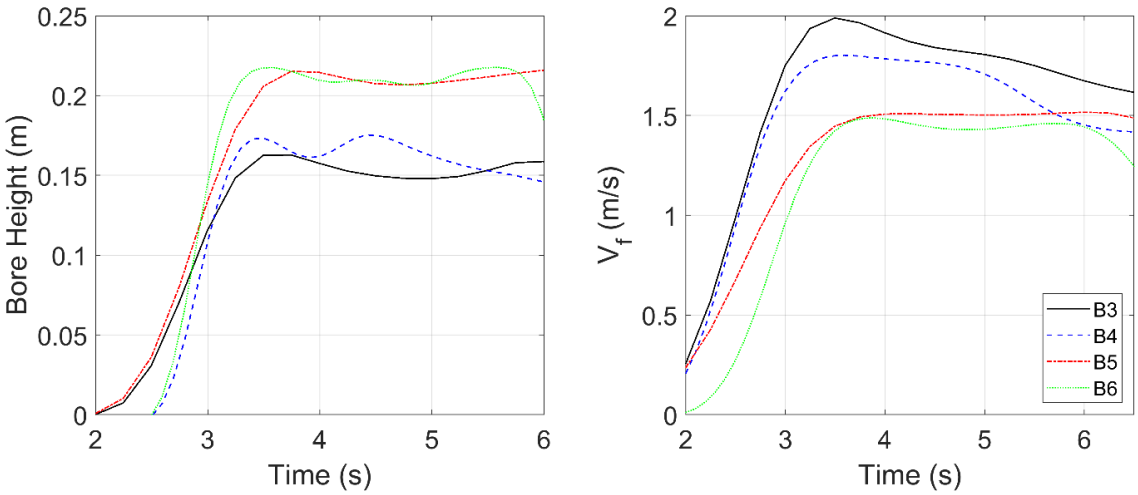

Figure 5-2 Bore height (left) and fluid particle velocity histories (right) of tsunami flow in front of the debris location for the strong bores and Z=0.25 m

5.4. Debris movement and debris-flow-bridge interaction

General trends

Figure 5-3 presents selected snapshots of the x-velocities that show the sequence of debris-flow-interaction for case B6Z_b (strong bore and bridge elevation of 0.30m). The sequence of interaction comprises a series of temporal instants, including (a) slightly before the initial impact, (b) after the primary impact, (c) and (d) yaw rotation of the debris around the z-axis, (e) the maintenance of transverse orientation by the debris, (f) the emergence of the transverse debris upon re-surfacing. These snapshots demonstrate the impact of flow in the movement of the debris, highlighting the

three-dimensional nature of this effect. Additionally, the snapshots show the intricate nature of the tsunami flow patterns surrounding the bridge and the ways in which the flow, debris, and bridge interact with one another. These interactions are likely to be complex and dynamic, as the flow of the tsunamis and the movement of the debris can significantly impact the stability and integrity of the bridge.

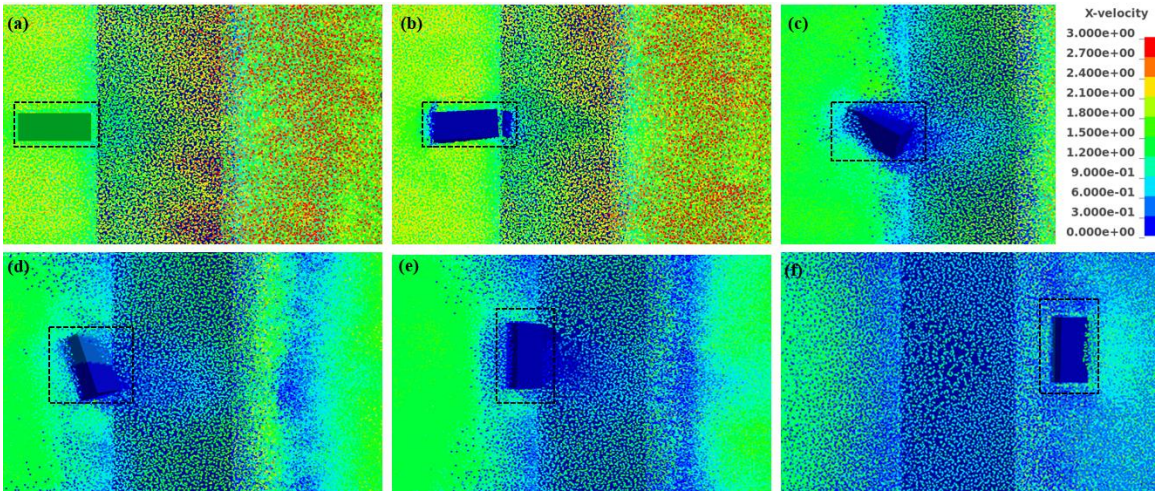

Figure 5-3 Top view of tsunami-debris-bridge interaction for case B6Zb; strong bore and bridge elevation of 0.30m

To enhance understanding of the debris-flow-bridge interaction, Figure 5-4 presents selected snapshots of the x-velocities for three representative cases. These cases are as follows: (a) debris impacts the offshore side of the bridge and remains there till the end of inundation process, (b) debris impacts the offshore side and travels above the deck, and (c) debris impacts the bridge and moves below it. These snapshots provide insight into the various ways in which the debris can interact with the bridge and flow during a tsunami event. In the first case, the debris remains on the offshore side of the bridge, suggesting that the forces acting on the bridge are insufficient to move it further inland. In the second case, the debris moves above the deck after impact, possibly due to the combined effects of the flow and the debris momentum. In the third case, the acting forces propel the debris to move below the bridge. These snapshots demonstrate the complexity and

dynamics of the debris-flow-bridge interaction and underscore the importance of considering these interactions in the design of bridge superstructures in tsunami-prone areas.

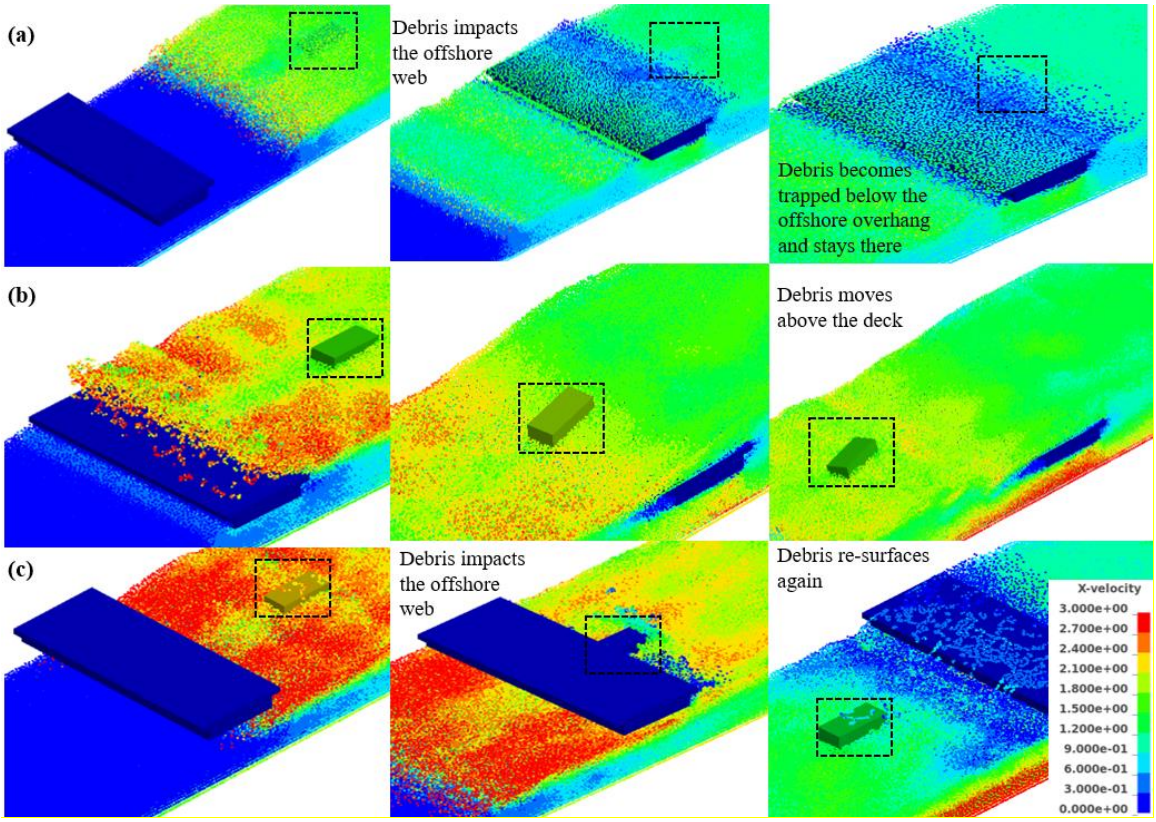

Figure 5-4 Debris-tsunami and debris-tsunami-bridge interaction for three scenarios: (a): top, debris becomes trapped below the offshore overhang, (b): center, debris moves above the deck, (c): bottom, debris moves below the bridge

To gain a more quantitative understanding of the movement of debris, Figure 5-5 plots the average vertical displacement (D_z) of the container and its trajectory (D_x vs. D_z) throughout inland propagation, with various cases analyzed based on different bore properties and bridge elevations. The figure illustrates that the container flow is significantly influenced by the bore properties and bridge elevation, leading to a diverse movement for the various cases. Estimating the vertical displacement of debris is crucial for future risk assessment and the prediction of potential impacts on the bridge. By understanding the likelihood of debris impact and the location of the impact, it is possible to assess the potential risks posed by tsunami events and take the appropriate measures to

mitigate them. This is particularly important for the design of bridge superstructures in tsunami-prone areas, as it helps to ensure their structural integrity and safety.

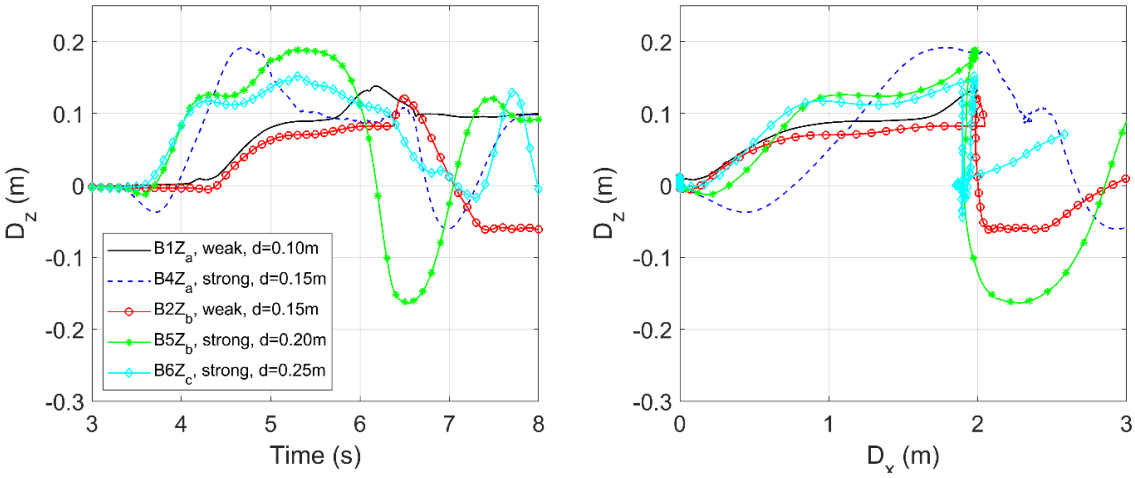

Figure 5-5 Debris vertical displacement histories (left) and trajectories (right) for selected cases

To further understand the role of bore properties and bridge elevation on debris rotation, Figure 5-6 presents time-histories of the debris rotations around the y-axis and the z-axis for the aforementioned cases. The results indicate that these factors significantly affect the rotational behavior of the debris during the propagation and impact the bridge superstructure. For example, in cases of $B4Z_a$ and $B5Z_b$, the debris rotates more than 180 degrees around the y-axis, resulting in an upside-down orientation that could potentially cause damage to cargo. This rotation around the y-axis is often referred to as pitch, and it can have significant implications for the stability and trajectory of the debris.

In terms of the rotation around the z-axis, case B5Zb, rotates about 90 degrees, resulting in a shift in the longitudinal orientation of the debris to a transverse orientation. This rotation around the z-axis is often referred to as yaw, and it can also have significant effects on the movement of the debris. For example, the change in debris orientation due to yaw can affect the flow field by increasing constriction, which can alter the fluid velocity and sequence of loadings. Additionally, in the case of a twin bridge, the resurfaced-transverse debris will likely impact the second bridge

differently compared to the first bridge. Overall, the rotational behavior of the debris is a complex phenomenon that is influenced by various factors.

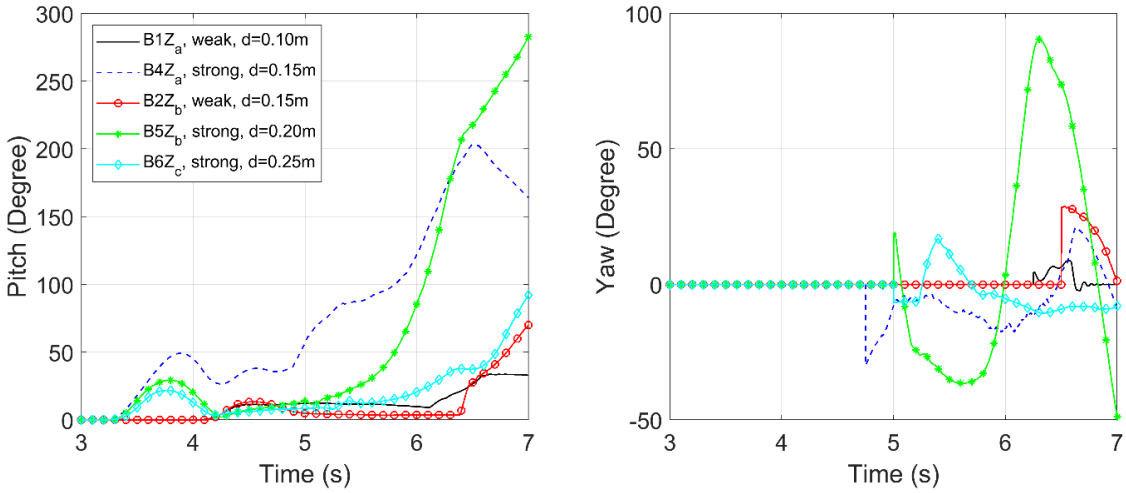

Figure 5-6 Debris pitch rotation and yaw rotation time-histories for selected cases

Debris velocities

The data presented in Figure 5-7 provide further insight into the trends observed in the previous figure by examining the offshore and onshore corner velocities of the debris in the horizontal (Vx_d) and vertical directions (Vz_d) for two selected cases with the same bridge elevation (0.35m) and different bore properties: $B3Z_c$ (d=0.10 m) and $B4Z_c$ (d=0.15 m). In the case of $B4Z_c$, the results indicate that both offshore and onshore corners exhibit similar horizontal and vertical velocities during the propagation and impact on the bridge. However, in the case of $B3Z_c$, while the offshore and onshore corners exhibit approximately similar velocities at the instant of primary impact, the velocities significantly diverge throughout the entrainment process. Specifically, the horizontal and vertical velocities of the offshore corners are generally higher than those of the onshore corners. The maximum horizontal and vertical offshore velocities prior to the primary impact is approximately 10% and 42% higher than the respective velocity of the onshore corners.

The variation in offshore and onshore velocities may be the result of debris pitching, which can cause the floating container to collide with the bridge at an angle relative to the horizontal plane. Previous research has emphasized the significance of debris pitching and non-normal impact angle [37, 41]. These findings suggest that the rotational behavior of the debris can significantly impact its velocity and collision with structures.

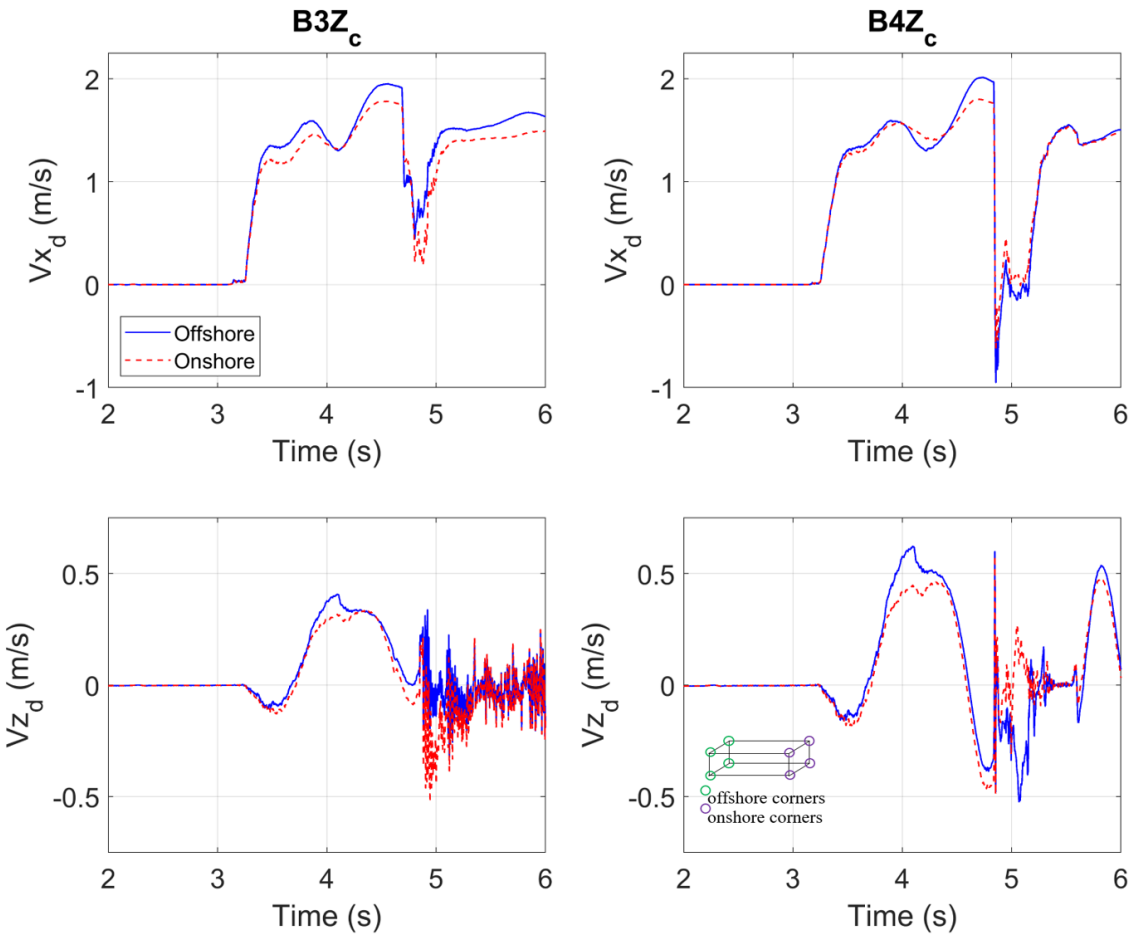

Figure 5-7 Debris offshore and onshore corners velocities in the horizontal (top) and vertical (bottom) directions for the same bridge elevation and bore strength but initial water level, including B3Zc (d=0.10 m), B4Zc (0.15 m)

The results presented in Figure 5-8 demonstrate the effect of initial water level on the horizontal and vertical debris velocities in cases with comparable bore strength (strong bore) and bridge elevation (0.30 m). It is apparent that the initial water level has a notable impact on the tsunami-

borne debris-bridge interaction. In the case of shallow water (B3Zb, d=0.10 m), the container impacts the offshore side of the bridge and becomes trapped below the offshore overhang until the end of the inundation process. This results in a drastic reduction in debris velocities and minimal movement. In cases with deeper initial water levels (B4Zb, d=0.15 m, B5Zb, d=0.20 m, and B6Zb, d=0.25 m), the container impacts the offshore side of the bridge and moves below it. Following the initial impact, the container may accelerate and reach approximately similar impact velocities or exceed them. In certain cases such as B4Zb, B5Zb, and B6Zb, the horizontal velocity reaches approximately 81%, 110%, and 115% of the initial impact velocity, respectively. The vertical velocity of the debris may also increase significantly as it moves below the soffit and may even exceed the velocity of the initial impact. This is observed in the case of B5Zb, where the vertical velocity of the debris increases by approximately 275% relative to the impact velocity.

It is essential to consider the potential impact of debris on multiple bridges in close proximity, as the behavior of the debris may have significant consequences for the structural integrity and stability of these structures. In cases where the debris moves below the bridge, accelerates, and re-surfaces with velocities equal to or greater than the primary impact velocity, a second bridge running parallel to the first (i.e., a twin bridge) may be subjected to similar or even more severe conditions. Further research is needed to evaluate the impact of tsunami-borne debris on twin bridges in order to accurately quantify the impact forces and assess the potential risks to these structures. This information can be used to develop risk assessment frameworks for the design and evaluation of bridge systems exposed to tsunami hazards.

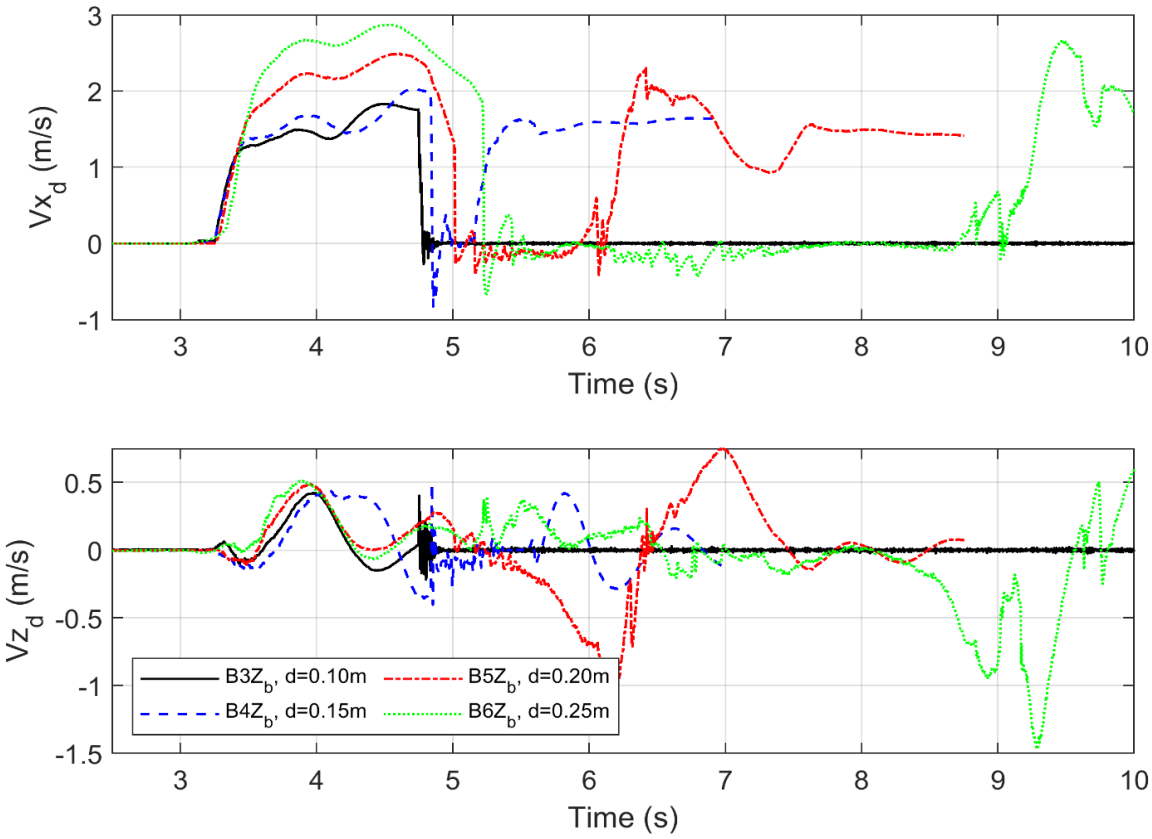

Figure 5-8 Debris velocities in the horizontal (top) and vertical (bottom) directions for four selected strong bores with the same bridge elevation (0.30 m) but different initial water level, including B3Zb (d=0.10 m), B4Zb (d=0.15 m), B5Zb (d=0.20 m), and B6Zb (d=0.25 m)

The time-histories of the horizontal and vertical velocities of the debris for different bridge elevations and the same bore properties are presented in Figure 5-9. Two cases are considered, including $B2Z_a$ (bridge elevation of 0.20 m) and $B2Z_b$ (bridge elevation of 0.30 m). The results indicate that the bridge elevation plays a significant role in the debris velocity. In particular, the horizontal velocity of the debris may decrease gradually after the primary impact on the deck in cases with lower bridge elevations, while more abrupt decreases in horizontal velocity are observed for higher bridge elevations. This difference in trend may be attributed to the interaction between the debris and the bridge, as well as the cushioning effect of trapped fluid at the moment of impact. Additionally, the results show that the primary impact velocity of the debris is not necessarily the maximum velocity experienced by the debris during its propagation prior to the impact on the

bridge. In other words, as the approaching bore entrains the debris, there is a transient effect where the container experiences a sudden acceleration due to the transfer of tsunami flow momentum. However, when the debris impacts the bridge superstructure, the reflection of the wave from the offshore side of the bridge can mitigate the energy of the debris, causing a slowdown in velocity.

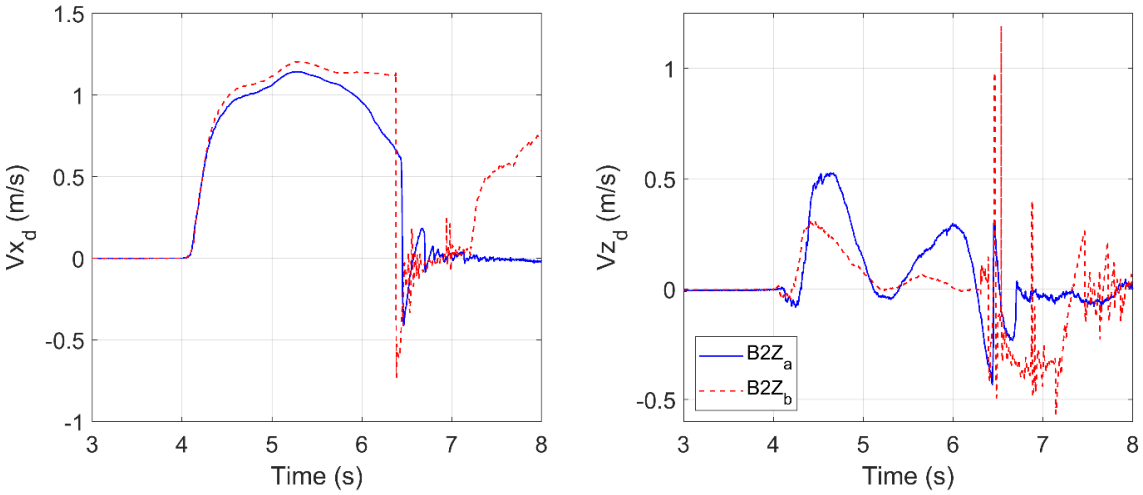

Figure 5-9 Debris velocities in the horizontal (left) and vertical (right) directions for selected cases with the same bore properties but different bridge elevation, including B2Za (bridge elevation of 0.20 m) and B2Zb (bridge elevation of 0.30 m)

5.5. Impact force on bridge superstructure

Understanding the temporal evolution of the applied loadings on the bridge by debris and tsunami bores is critical for designing structures that can effectively resist these forces and remain safe. To this end, Figure 5-10 illustrates the time-histories of the horizontal and vertical forces applied on the bridge by both debris (F_d) and tsunami bore (F_f) at an elevation of 0.30 m. The forces are shown for strong bores and a range of initial water levels including $B3Z_b$ (d=0.10 m), $B4Z_b$ (d=0.15 m), $B5Z_b$ (d=0.20 m), and $B6Z_b$ (d=0.25 m). As discussed previously, the initial water level plays a crucial role in influencing the debris-flow-bridge interaction and can result in different movements of the debris around the deck, which in turn affects the sequence of loadings.

For the initial water level with the shallowest depth ($B3Z_b$), where the debris becomes trapped below the offshore overhang, the applied hydrodynamic forces are negligible and the magnitude of the debris horizontal impact force is about 2.3 times the debris uplift force. For the other initial water levels, where the debris impacts the offshore side and moves below the bridge, the bridge is subjected to higher debris and impact forces in both directions. The magnitude of the primary horizontal debris impact force is approximately 1.85, 1.91, and 2.16 times the magnitude of the uplift force for cases $B4Z_b$, $B5Z_b$, and $B6Z_b$, respectively. In the $B5Z_b$ and $B6Z_b$ cases, the bridge experiences successeive patterns of loadings in both directions, which can affect its stability and worsen the situation. It is important to note that in these two cases, the debris and fluid forces do not reach their maximum at the same instant during the inundation process, emphasizing the need to consider different load cases in the design of new bridges to identify the governing scenario, as was done by Istrati et al., (2018) [18] for clear-water condition. This approach takes into account the possibility of different impact locations along the width of the superstructure.

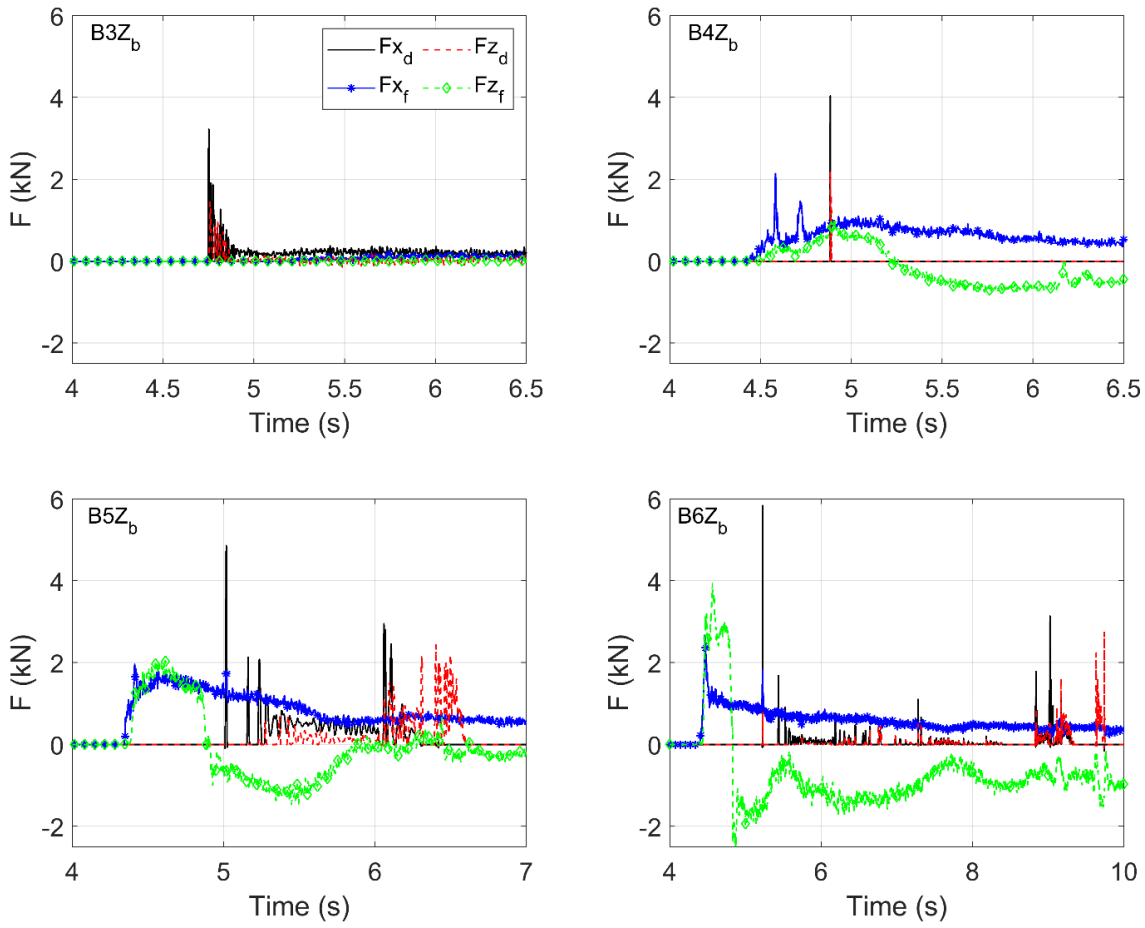

Figure 5-10 Applied horizontal and vertical debris and fluid force histories for four cases with similar bridge elevation of 0.30 m and bore strength and different initial water depths, including B3Zb (d=0.10 m), B4Zb (d=0.15 m), B5Zb (d=0.20 m), and B6Zb (d=0.25 m)

To gain a deeper understanding of the loadings applied to the bridge superstructure, Figure 5-11 presents the maximum magnitude of the debris and total impact forces in the two directions, for the aforementioned cases. It is observed that as the initial water depth increases, the debris and total impact forces in the two directions also increase. For instance, when the initial water level is increased from 0.10 m to 0.25 m, the horizontal and vertical impact forces exerted by the debris increases by approximately 77% and 88%, respectively. Similarly, the total applied forces in the horizontal and vertical directions increase by approximately 127% and 176%, respectively. These findings highlight the importance of considering the initial water level in the design process of

bridges in order to design structures that are able to withstand the force they will encounter during their lifetime.

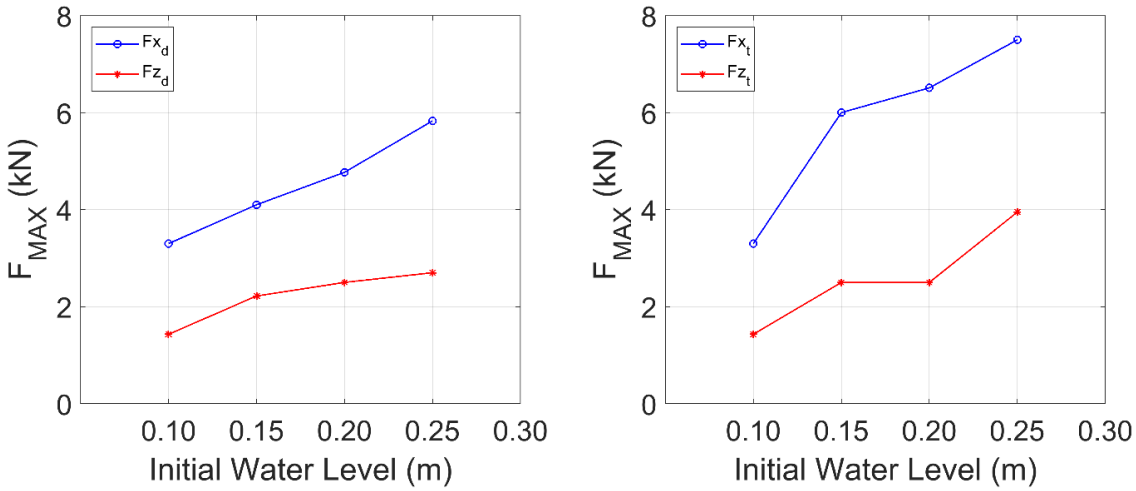

Figure 5-11 Maximum values of the debris and total horizontal and vertical forces for four cases with the same bridge elevation of 0.30m and bore strength, but different initial water depths, including B3Zb (d=0.10 m), B4Zb (d=0.15 m), B5Zb (d=0.20 m), and B6Zb (d=0.25 m)

To evaluate effect of bridge elevation on the applied loadings, Figure 5-12 presents time-histories of the debris, fluid, and total applied forces in the two directions for two cases with the same bore properties but different bridge elevations: $B2Z_a$ (bridge elevation of 0.20 m) and $B2Z_b$ (bridge elevation of 0.30 m). The bridge with the lower elevation experiences both fluid and debris impact forces. In the horizontal direction, the debris force is relatively larger and it applies a force that is 1.48 times larger than the fluid force. In contrast, in the vertical direction, the fluid force is larger than the debris force, with the fluid force being approximately 3 times larger. On the other hand, for the higher deck elevation, the tsunami bore barely touches the deck and the bridge is subjected to the debris force only. The magnitude of the debris horizontal impact force is about 2.8 times the vertical force. Additionally, as the debris moves below the deck, it applies several uplift loads to the soffit with magnitudes that are greater than the primary impact. For instance, the magnitude of the vertical follow-up impact is about 1.26 times the primary one. These findings are in agreement with the conclusions reached by Hasanpour et al., (2022) [38]. Overall, the observed trends

highlight the need for the development of more comprehensive design equations that take into account both horizontal and vertical loads. This is essential in order to accurately predict and design for the forces experienced by a structure under debris impact.

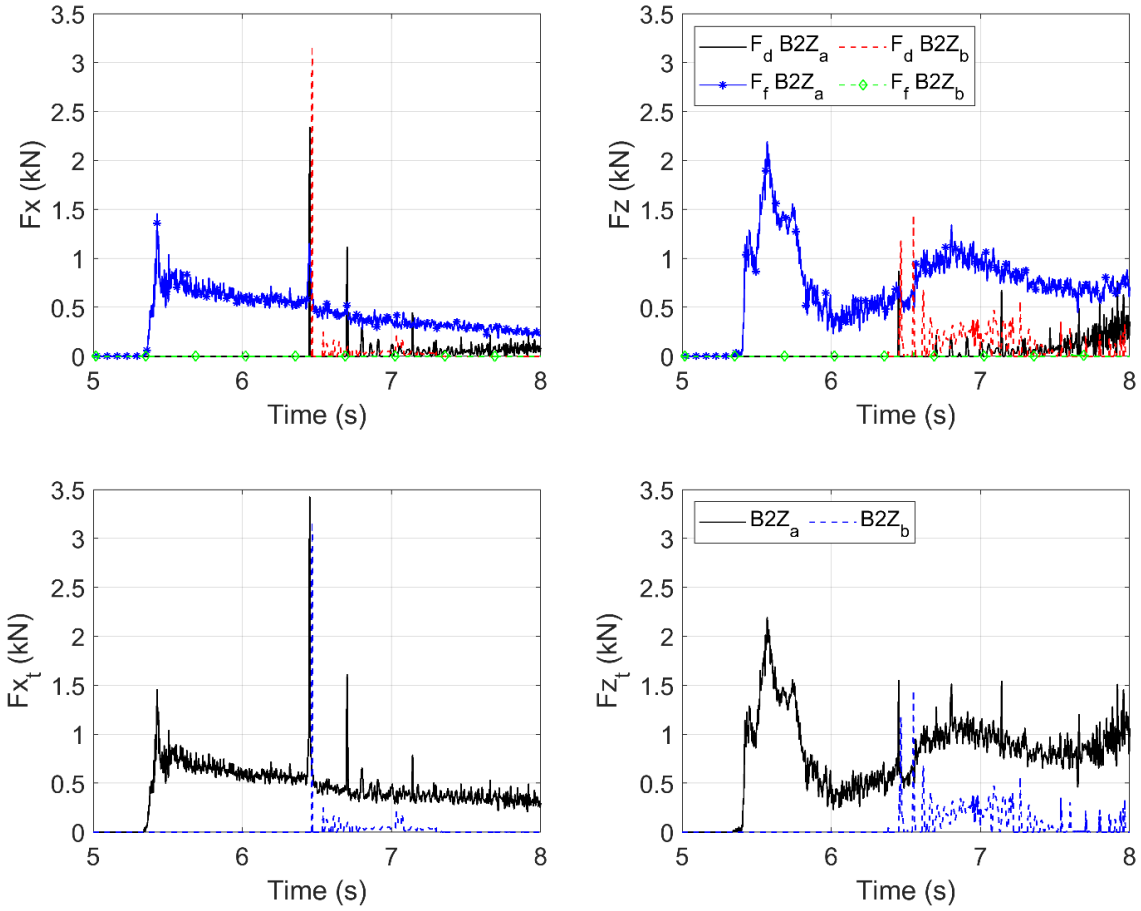

Figure 5-12 Applied horizontal and vertical debris, fluid, and total force histories for cases with the same bore properties but different bridge elevations, including B2Za (bridge elevation of 0.20 m) and B2Zb (bridge elevation of 0.30 m)

5.6. Role of debris orientation

To further investigate the influence of initial debris orientation prior to entrainment on its movement and interaction of the debris with the bridge during debris flow, a reanalysis was conducted in all previously studied cases where the debris was oriented transversely relative to the

Table 5-2 Debris-tsunami-bridge interaction for transverse debris [40] and longitudinal debris

Bore Cases	H_r (m)	d (m)	Bridge Elevation (m)					
			0.20 (Z_a)		0.30 (Z_b)		0.35 (Z_c)	
			Debris Orientation					
			Transv.	Long.	Transv.	Long.	Transv.	Long.
B1	0.40	0.10	Impacts and moves below **(A)**	Impacts and gets trapped below the offshore overhang **(C)**				
B2		0.15	Impacts and moves below **(A)**	Impacts and gets trapped below the offshore overhang **(C)**	Impacts and moves below **(A)**	Impacts and moves below **(A)**		
B3	0.60	0.10	Impacts and moves above **(B)**	Impacts and moves above **(B)**	and gets trapped below the offshore overhang **(C)**	Impacts and gets trapped below the offshore overhang **(C)**		
B4		0.15	Impacts and moves above **(B)**	Impacts and moves above **(B)**	Impacts and moves below **(A)**	Impacts and moves below **(A)**	Impacts and moves below **(A)**	Impacts and moves below **(A)**
B5		0.20	Impacts and moves above **(B)- NO CONTACT**	Impacts and moves above **(B)- NO CONTACT**	Impacts and moves below **(A)**	Impacts and moves below **(A)**	Impacts and moves below **(A)**	Impacts and moves below **(A)**
B6		0.25			Impacts and moves above **(B)**	Impacts and moves below **(A)**	Impacts and moves below **(A)**	Impacts and moves below **(A)**

direction of wave propagation. In general, three distinct trends in the movement of the debris around the bridge during tsunami flow were observed. The first trend involves debris impacting the offshore side of the bridge and moving beneath the soffit (A). The second trend involves debris impacting the offshore and traveling above the deck (B). The third trend involves debris impacting the bridge and remaining trapped below the offshore overhang till the end of the inundation process (C). Table 5-2 presents the results of the investigation into the debris-tsunami-bridge interaction for both longitudinal and transverse debris orientations. As shown, in the majority of the cases, similar movement of the debris around the bridge is observed for both orientations. However, there are three cases- $B1Z_a$, $B2Z_a$, and $B6Z_b$, that display different trends. Specifically, in the $B1Z_a$ and $B2Z_a$ cases, the transverse debris impacts the bridge and moves below it, while the longitudinal debris remains there after the initial impact. In the case of $B6Z_b$, the transverse debris impacts, and travels above the deck, while the longitudinal debris impacts the bridge and moves below it.

In order to gain a deeper understanding of the debris displacement, Figure 5-13 presents the maximum vertical displacement of debris for all studied cases and two debris orientations. The figure illustrates that the vertical displacement of the transverse debris is generally greater than that of the longitudinal debris. Accurate estimation of debris vertical displacement is essential for future risk assessment and the development of effective protection measures against the potential impact of debris flows on bridges. This is because the range of debris-flow-bridge interaction is mainly determined by the vertical displacement of the debris.

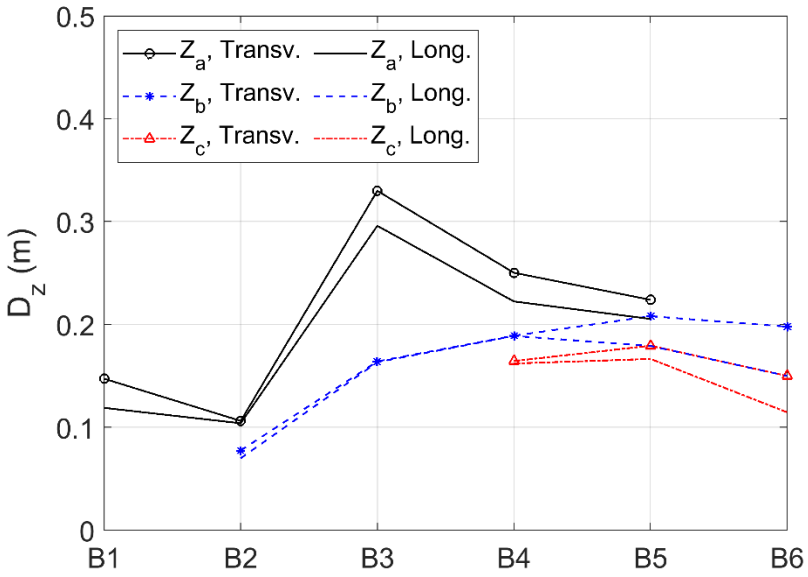

Figure 5-13 Debris maximum vertical displacement for two debris orientations; transverse and longitudinal

Figure 5-14 shows the time-series of the debris velocities and impact forces in the two directions for case B1Za and two debris orientations. The debris exhibits two different trends when it interacts with the deck, with the longitudinal debris getting trapped and the transverse debris moving below the deck. The data indicate that the longitudinal debris reaches higher velocities compared to the transverse debris, with the horizontal and vertical velocities being approximately 1.54 and 1.19 times those of the transverse debris, respectively. The results also demonstrate that the longitudinal debris exerts higher impact forces on the bridge compared to the transverse debris. Specifically, the peak horizontal and vertical impact forces induced by the longitudinal orientation are found to be approximately 1.47 and 1.29 times greater, respectively, than those exerted by the transverse orientation. This observation has also been reported in the literature [22,48-49].

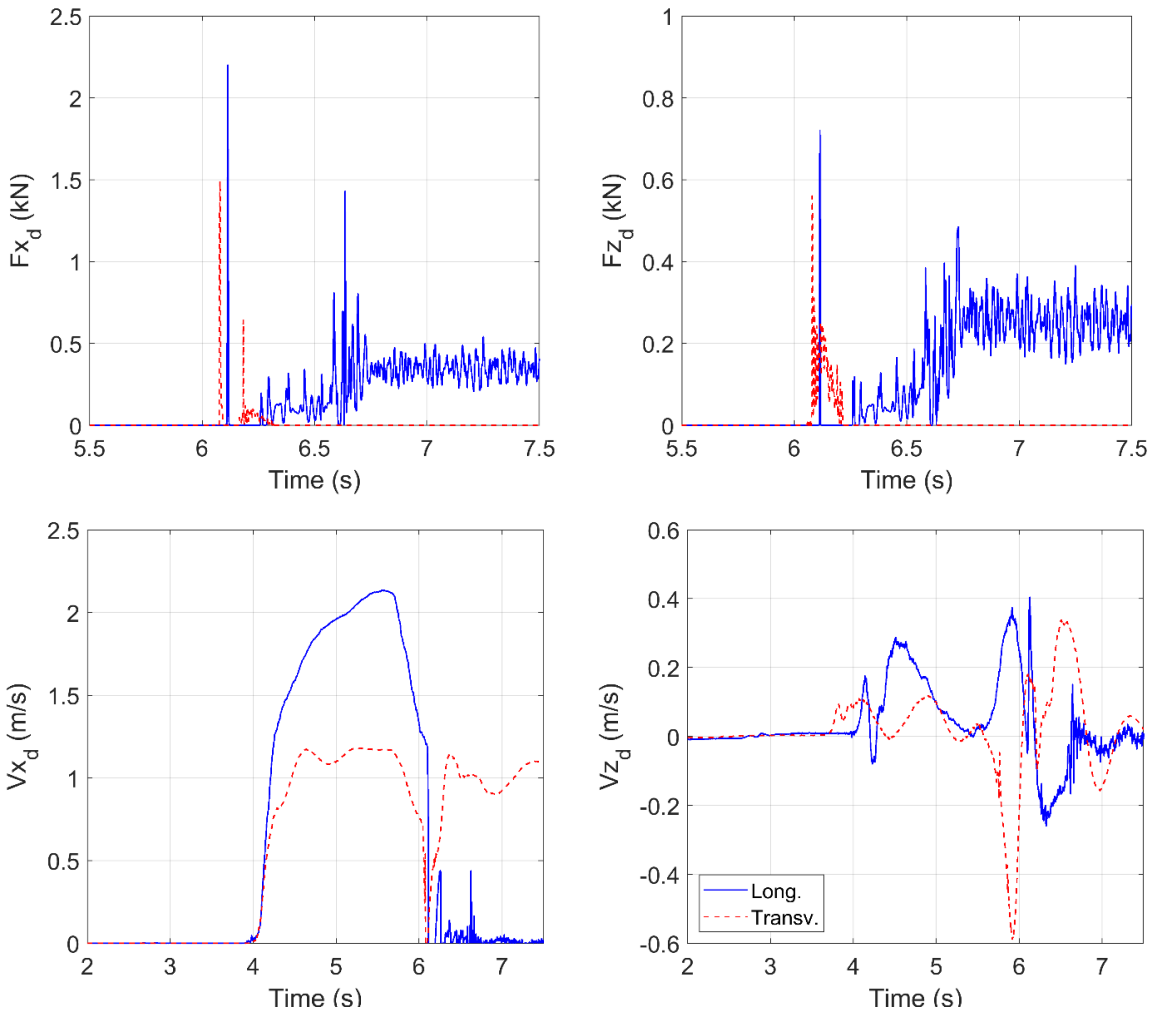

Figure 5-14 Time histories of the horizontal (top left) and vertical (top right) debris velocities, horizontal (bottom left) and vertical (bottom right) debris forces for case B1Za and two different debris orientations

In order to further evaluate the effect of the initial orientation of the debris on the impact forces and velocities in the two directions, Figure 5-15 shows the numerically calculated maximum values of the impact forces and velocities in the two directions for both the longitudinal and transverse orientations. The green rectangle represents the cases in which the debris exhibits different movement trends for the two orientations. As demonstrated, the longitudinal debris reaches higher velocities compared to the transverse debris, which in turn leads to higher impact forces on the bridge in the two directions. This trend is observed in most cases, with the exception of case B6Z_b,

in which the transverse debris experiences higher velocities due to the different debris-flow-bridge interactions.

According to Table 5-3 which presents the ratio of the debris impact forces in the longitudinal direction to those in the transverse direction, the longitudinal debris applies on average approximately 1.48 and 1.5 times greater horizontal and vertical forces, respectively.

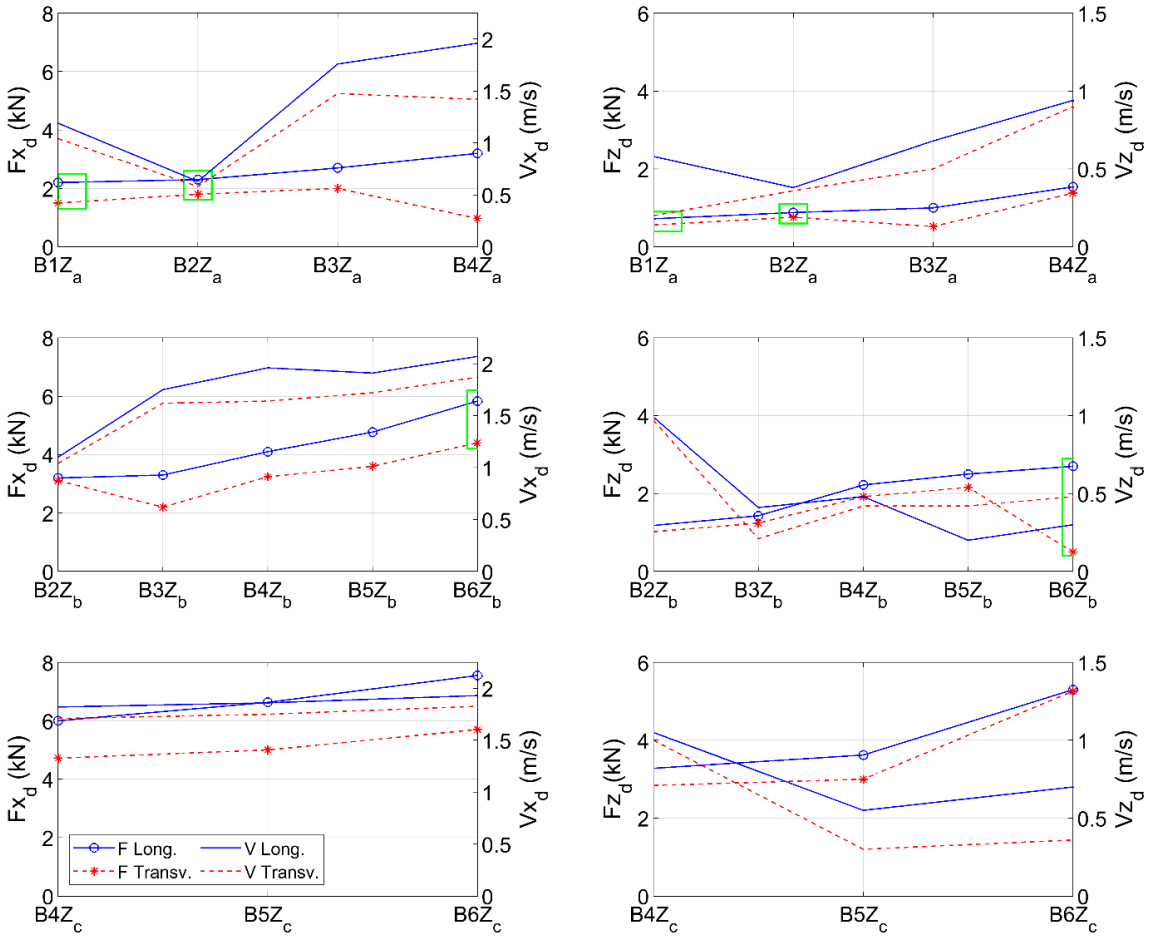

Figure 5-15 Maximum values of the debris impact forces and velocities in the horizontal and vertical directions on the bridge superstructure for the investigated cases and two debris orientations

Table 5-3 Ratio of the debris forces: longitudinal and transverse orientations in the two directions

Bore Cases	H_r (m)	d (m)	Bridge Elevation (m)					
			0.20 (Z_a)		0.30 (Z_b)		0.35 (Z_c)	
			Rx_d	Rz_d	Rx_d	Rz_d	Rx_d	Rz_d
B1	0.40	0.10	1.47	1.29				
B2		0.15	1.28	1.16	1.03	1.16		
B3	0.60	0.10	1.35	1.92	1.50	1.15		
B4		0.15	3.30	1.12	1.27	1.18	1.27	1.16
B5		0.20			1.33	1.16	1.33	1.21
B6		0.25			1.35	5.40	1.32	1.01
Mean			Rx=1.48				Rz=1.50	
SD			0.32				0.45	

Figure 5-16 presents the maximum values of the total forces on the bridge that are predicted numerically for two debris orientations. The results demonstrate that, in terms of the horizontal force, cases with longitudinal debris apply a great total force. However, the orientation that contributes higher total forces in the vertical direction is dependent on the moment of maximum debris and fluid force during the inundation process, with either longitudinal or transverse configurations potentially exerting a greater impact.

Table 5-4 illustrates the ratio of the total forces applied by longitudinal debris to transverse debris. The results indicate that. On average, longitudinal orientation applies horizontal and vertical forces that are 1.27 and 1.19 times larger. These findings suggest that the longitudinal orientation has a greater influence on the forces acting on the bridge, particularly in the horizontal direction.

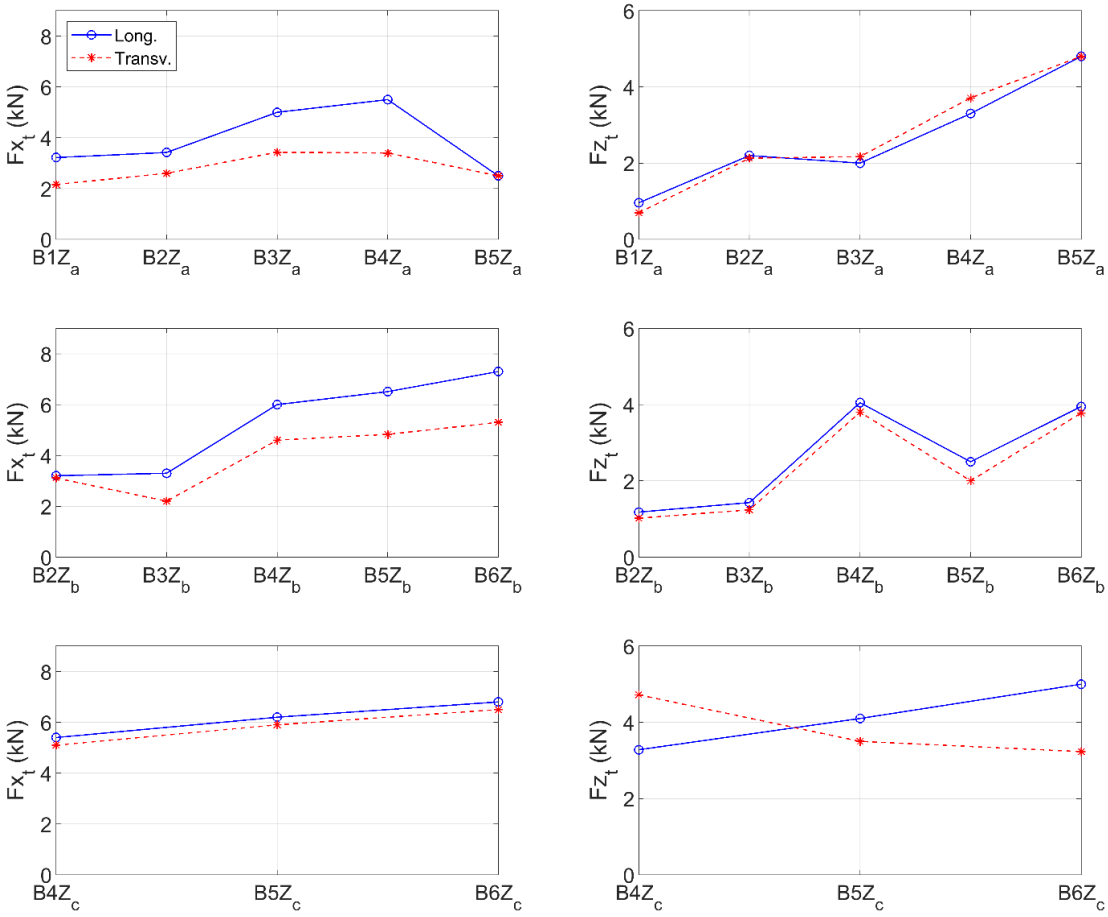

Figure 5-16 Maximum values of the total forces in the horizontal and vertical directions on the bridge superstructure for the investigated cases and two debris orientations

Table 5-4 Ratio of the total forces: longitudinal and transverse orientations in the two directions

Bore Cases	H_r (m)	d (m)	Bridge Elevation (m)					
			0.20 (Z_a)		0.30 (Z_b)		0.35 (Z_c)	
			Rx_t	Rz_t	Rx_t	Rz_t	Rx_t	Rz_t
B1	0.40	0.10	1.49	1.37				
B2		0.15	1.32	1.03	1.03	1.16		
B3	0.60	0.10	1.46	1.02	1.50	1.15		
B4		0.15	1.62	1.03	1.30	1.07	1.06	1.02
B5		0.20			1.35	1.25	1.05	1.17
B6		0.25			1.38	1.34	1.04	1.64
Mean			Rx=1.27				Rz=1.19	
SD			0.21				0.08	

5.7. Role of debris

The effect of debris on hydrodynamic and total applied loads was analyzed by comparing simulations with and without debris under the same hydrodynamic conditions. Figure 5-17 shows the numerically calculated maximum magnitudes of the tsunami bore and total forces in the two directions. The results indicate that the presence of the debris has a negligible effect on the fluid impact forces. However, as expected, the total applied loadings are significantly higher when the debris is present.

According to Figure 5-18, which displays the ratio of the total forces between the cases with and without debris in the two directions, on average, the presence of debris increases the total horizontal force by a factor of 2.4, 3.4, and 5.14 for the bridge elevation of 0.20 m, 0.30 m, and 0.35 m, respectively. In terms of the total uplift force, the presence of debris increases the total force by a factor of 1.11, 1.62, and 3.68 for the bridge elevation of 0.20m, 0.30m, and 0.35m, respectively. This data clearly demonstrates that the impact of debris on the applied loadings becomes more significant for the bridge at higher elevations, where the tsunami bore barely comes into contact with the deck.

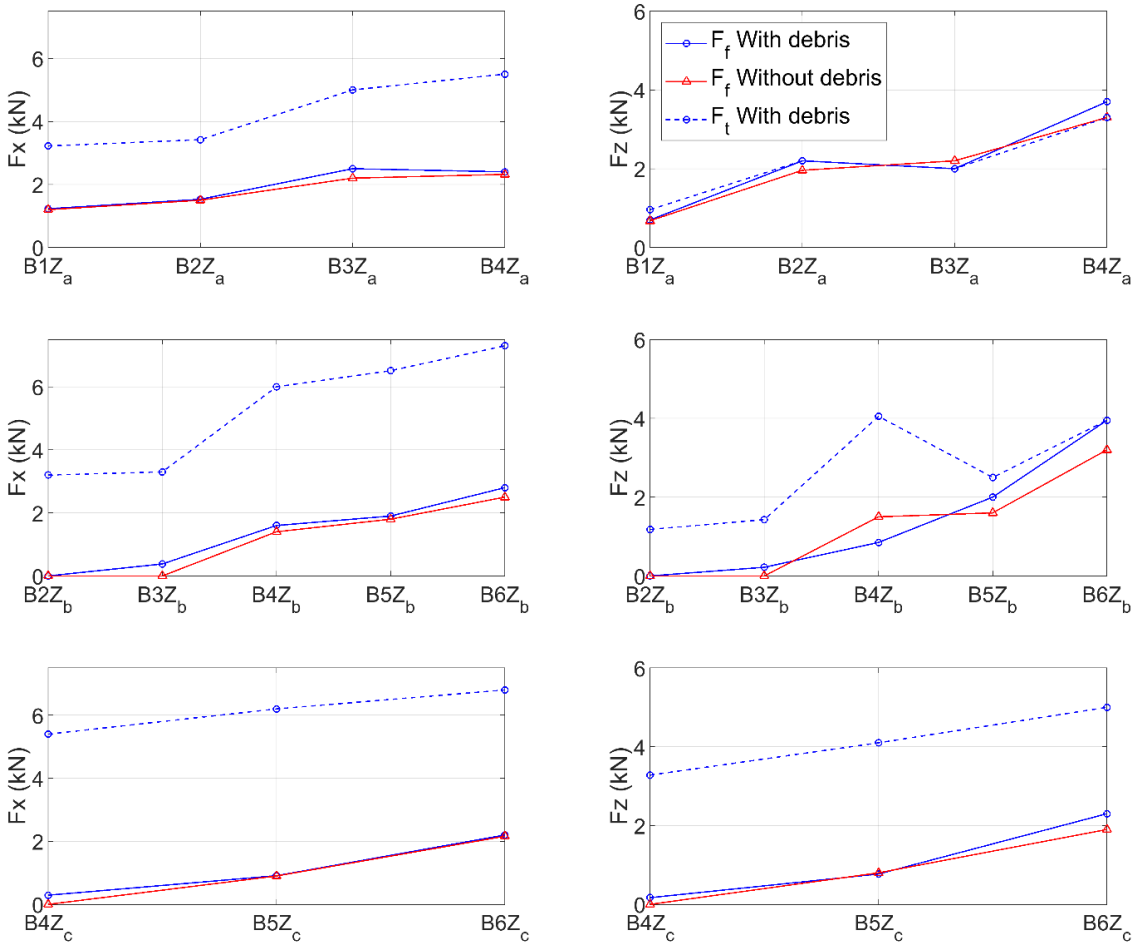

Figure 5-17 Maximum values of the hydrodynamic and total forces in the horizontal and vertical directions on the bridge superstructure for the investigated cases and two scenarios; with and without debris

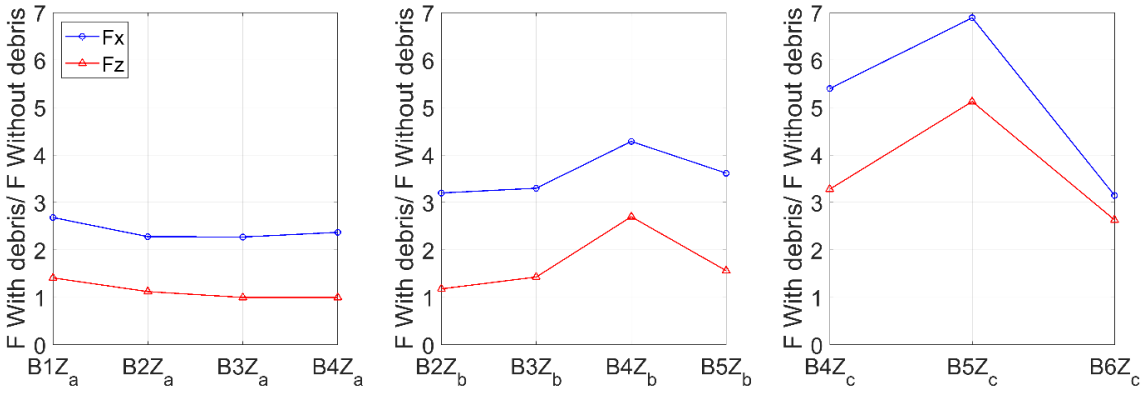

Figure 5-18 Ratio of the maximum total force with and without debris in the two directions

5.8. Conclusions

The purpose of this study is to advance the understanding of the tsunami-borne debris impact loadings on a box-girder bridge. To achieve this goal, a novel coupled SPH-FEM modeling technique was employed. To ensure the accuracy of the approach, it was first validated through comparison with the experimental study conducted by Shafiei (2016) [41]. The validation results indicated that this approach is capable of accurately reproducing the three-dimensional debris dynamics and impact forces on coastal structures. Following this, a comprehensive parametric investigation was carried out to assess the effect of bore properties (bore strength and initial water level) and bridge elevation on debris-flow and debris-flow-bridge interactions.

From the research that was undertaken, it is concluded that during the inundation process, three possible scenarios may occur with regard to the movement of the debris: (i) debris impacts the offshore side of the bridge and remains there until the end of the inundation process, (ii) debris impacts the offshore side and travels over the deck, or (ii) debris impacts the bridge and moves beneath it. In the majority of cases, the initial orientation of debris does not significantly affect the movement of debris around the bridge. Despite the similarities observed in the movement of debris with respect to the bridge, the vertical displacement of the transverse debris was generally greater than that of the longitudinal debris. Estimating the vertical displacement of debris, prediction of potential impacts on the bridge and the location of impact are crucial for future risk assessment frameworks.

Furthermore, it was observed that the three-dimensional effect of fluid caused the debris to rotate around the z-axis. In some cases, the debris exhibited yaw rotation up to 90 degrees, resulting in a shift in the longitudinal orientation of the debris to a transverse orientation. This change in debris orientation due to yaw can alter the flow field by increasing constriction, which can subsequently affect fluid velocity and the sequence of loadings on the bridge. These findings highlight three-

dimensional fluid-debris interaction in the analysis and design of coastal bridges subjected to tsunami flow.

Evaluation of the debris velocities in the two directions revealed that:

- In some cases, the maximum horizontal and vertical offshore velocities prior to the primary impact were found to be approximately 10% and 42% higher than the respective velocities of the onshore corners, respectively. This variation in velocities may be the result of debris pitching, which can cause a floating container to collide with the bridge at an angle relative to the horizontal plane.

- In some cases, the container may accelerate after the initial impact and reach velocities that are similar to or even higher than the initial impact velocities. For instance, in the case $B5Z_b$, the horizontal and vertical velocities increased to approximately 110% and 275% of the initial impact velocity, respectively.

- It was demonstrated that the reflection of the wave from the offshore side of the bridge can reduce the velocity of the debris upon impact, such that the primary impact is not necessarily the maximum velocity experienced by the debris during its propagation.

- The results showed that the longitudinal debris reached higher velocities compared to transverse debris.

One of the main objectives of this study is to draw attention to the applied loadings on coastal bridges. The initial water level was found to have a significant impact on the impact forces. Specifically, when the initial water level was increased from 0.10 m to 0.25 m, the horizontal and vertical impact forces exerted by the debris increased by approximately 77% and 88%, respectively.

Similarly, the total applied forces in the horizontal and vertical directions increased by approximately 127% and 176%, respectively.

The findings of this study suggest that, on average, the longitudinal debris applies approximately 1.45 and 1.5 times greater horizontal and uplift forces, respectively, compared to the transverse debris. In terms of the total applied loadings, the longitudinal orientation results in about 1.27 and 1.19 times larger horizontal and vertical forces, respectively.

Evaluation of the role of debris on impact forces revealed that the presence of debris has a negligible effect on fluid impact forces, but as expected, the total applied loadings are significantly higher when the debris is present. On average, the presence of debris leads to 3.64 and 2.13 times larger horizontal and vertical forces, respectively, compared to cases without debris.

5.9. Acknowledgement

The work described in this paper was supported by the State of California through the Transportation System Research Program of the Pacific Earthquake Engineering Research Center (PEER). Any opinions findings, and conclusion or recommendations expressed in this material are those of the author(s) and do not necessarily reflect those of the funding agency.

5.10. References

1. Athukorala, P. C., & Resosudarmo, B. P. (2005). The Indian Ocean tsunami: Economic impact, disaster management, and lessons. *Asian economic papers*, *4*(1), 1-39. [https://doi.org/10.1162/asep.2005.4.1.1]
2. Unjoh S. (2007). Bridge damage caused by tsunami. B Japan Assoc Earthquake Eng, 2007, 6: 6–28.
3. Kajitani Y, Chang S, Tatano H (2013): Economic Impacts of the 2011 Tohoku-Oki Earthquake and Tsunami.*Earthquake Spectra*, **29** (S1), S457-S478. [https://doi.org/10.1193%2F1.4000108]
4. Suppasri, A., Koshimura, S., Imai, K., Mas, E., Gokon, H., Muhari, A., & Imamura, F. (2012). Damage characteristic and field survey of the 2011 Great East Japan tsunami in Miyagi prefecture. *Coastal Engineering Journal*, *54*(1), 1250005-1. [https://doi.org/10.1142/S0578563412500052]
5. Mimura, N., Yasuhara, K., Kawagoe, S., Yokoki, H., & Kazama, S. (2011). Damage from the Great East Japan Earthquake and Tsunami-a quick report. *Mitigation and adaptation strategies for global change*, *16*(7), 803-818. [https://doi.org/10.1142/S0578563412500052]

6. Saatcioglu, M., Ghobarah, A. and Nistor, I. (2006). Performance of structures in Indonesia during the 2004 Sumatra earthquake and tsunami, *Engineering Spectra, Earthquake Engineering Research Institute* (EERI), 22, 295-319.
7. Yeh, H., Sato, S. and Tajima., Y. (2013). The 11 March 2011 East Japan Earthquake and Tsunami: Tsunami Effects on Coastal Infrastructure and Buildings. *Pure Appl. Geophys*., 170, 1019-1031.
8. Rossetto, T., Peiris, N., Pomonis, A., Wilkinson, S. M., Del Re, D., Koo, R., & Gallocher, S. (2007). the Indian Ocean tsunami of december 26, 2004: observations in Sri Lanka and Thailand. *Natural Hazards*, *42*(1), 105-124.
9. Robertson, I. N., Carden, L., Riggs, H. R., Yim, S., Young, Y. L., Paczkowski, K., & Witt, D. (2010). Reconnaissance following the September 29, 2009 tsunami in Samoa. *Research Rep. UHM/CEE/10*, *1*.
10. Guo, A., Fang, Q., & Li, H. (2015). Analytical solution of hurricane wave forces acting on submerged bridge decks. *Ocean Engineering*, *108*, 519-528. [https://doi.org/10.1016/j.oceaneng.2015.08.018]
11. Nakamura, T., Sawa, Y., & Mizutani, N. (2016). Study on the evaluation of temporal change in horizontal and vertical tsunami forces acting on a bridge superstructure. *Coastal Engineering Journal*, *58*(4), 1640020-1. [https://doi.org/10.1142/S0578563416400209]
12. Araki, S.; Ishino, K.; Deguchi, I. Stability of girder bridge against tsunami fluid force. In Proceedings of the 32th International Conference on Coastal Engineering (ICCE), Shanghai, China, 30 June–5 July 2010.
13. Istrati, D. 2017. "Large-scale experiments of tsunami inundation of bridges including fluid-structure-interaction." Ph.D. dissertation, Dept. of Civil Engineering and Environmental Engineering, Univ. of Nevada, Reno.
14. Seiffert, B. R.; Cengiz Ertekin, R.; Robertson, I. N. Effect of entrapped air on solitary wave forces on a coastal bridge deck with girders. *Journal of Bridge Engineering* **2016**, *21*(2), 04015036. [https://doi.org/10.1061/(ASCE)BE.1943-5592.0000799]
15. Istrati, D., Buckle, I.G. (2019): "Role of Trapped Air on the Tsunami-Induced Transient Loads and Response of Coastal Bridges", *Geosciences journal*, MDPI, 9 (191), doi: 10.3390/geosciences9040191
16. Bricker, J.D.; Nakayama, A. "Contribution of trapped air, deck superelevation, and nearby structures to bridge deck failure during a tsunami". J. Hydraulic Eng. 2014, 140, 05014002. [https://doi.org/10.1061/(ASCE)HY.1943-7900.0000855]
17. Bozorgnia, M.; Lee, J.J.; Raichlen, F. Wave structure interaction: Role of entrapped air on wave impact and uplift forces. In Proceedings of the International Conference on Coastal Engineering, 30 June–5 July 2010.
18. Istrati, D., I. Buckle, P. Lomonaco, and S. Yim. 2018. "Deciphering the tsunami wave impact and associated connection forces in open-girder coastal bridges." J. Mar. Sci. Eng. 6 (4): 148.
19. Denson, K.H. Wave forces on causeway-type coastal bridges. NASA STI/Recon Technical Report N. 79 1978.
20. Cai, Y.; Agrawal, A.; Qu, K., and Tang, H.S. Numerical Investigation of Connection Forces of a Coastal Bridge Deck Impacted by Solitary Waves. *J. Bridge Eng*. **2018**, *23(1)*, 04017108. https://doi.org/10.1061/(ASCE)BE.1943- 5592.0001135
21. Lehrman, J. B., C. Higgins, and D. Cox. 2012. "Performance of highway bridge girder anchorages under simulated hurricane wave-induced loads." J. Bridge Eng. 17 (2): 259–271. https://doi.org/10.1061 /(ASCE)BE.1943-5592.0000262.
22. Haehnel, R. B., & Daly, S. F. (2004). Maximum impact force of woody debris on floodplain structures. *Journal of Hydraulic Engineering*, *130*(2), 112-120. [https://doi.org/10.1061/(ASCE)0733-9429(2004)130:2(112)]

23. Matsutomi, H. (2009). Method for estimating collision force of driftwood accompanying tsunami inundation flow. *Journal of Disaster Research*, *4*(6), 435-440. [https://doi.org/10.20965/jdr.2009.p0435]
24. Madurapperuma, M. A. K. M., and Wijeyewickrema, A. C. (2012). "Inelastic dynamic analysis of an RC building impacted by a tsunami water-borne shipping container." *J. Earthquake Tsunami*, 6, 1250001. [https://doi.org/10.1142/S1793431112500017]
25. Farahmandpour, O., Marsono, A. K., Tap, M. M., & Forouzani, P. (2016). Experimental investigation of tsunami waterborne debris impact on structures. *GEOMATE Journal*, *10*(22), 2030-2035.
26. Goseberg, N., Stolle, J., Nistor, I., & Shibayama, T. (2016). Experimental analysis of debris motion due the obstruction from fixed obstacles in tsunami-like flow conditions. *Coastal Engineering*, *118*, 35-49. [https://doi.org/10.1016/j.coastaleng.2016.08.012]
27. Canelas, R. B., Domínguez, J. M., Crespo, A. J. C., Gómez-Gesteira, M., & Ferreira, R. M. L. (2017). Resolved simulation of a granular-fluid flow with a coupled SPH-DCDEM model. *Journal of Hydraulic Engineering*, *143*(9), 06017012.
28. Nistor, I., Goseberg, N., Stolle, J., Mikami, T., Shibayama, T., Nakamura, R., & Matsuba, S. (2017). Experimental investigations of debris dynamics over a horizontal plane. *Journal of Waterway, Port, Coastal, and Ocean Engineering*, *143*(3), 04016022. [https://doi.org/10.1061/(ASCE)WW.1943-5460.0000371]
29. Roohparvar, H. G., Lopez, D., Riviere, N., Piegay, H., & Mignot, E. (2018). Experimental study of the transient motion of floats reproducing floating wood in rivers. In *E3S Web of Conferences* (Vol. 40, p. 02041). EDP Sciences.
30. Derschum, C., Nistor, I., Stolle, J., & Goseberg, N. (2018). Debris impact under extreme hydrodynamic conditions part 1: Hydrodynamics and impact geometry. *Coastal Engineering*, *141*, 24-35. [https://doi.org/10.1016/j.coastaleng.2018.08.016]
31. Shafiei, S., Melville, B. W., Shamseldin, A. Y., Adams, K. N. and Beskhyroun S. (2016). "Experimental investigation of tsunami-borne debris impact force on structures: Factors affecting impulse-momentum formula." *Ocean Engineering* 127 (2016): 158-169. [https://doi.org/10.1016/j.oceaneng.2016.09.008]
32. Stolle, J., C. Derschum, N. Goseberg, I. Nistor, and Emil Petriu. "Debris impact under extreme hydrodynamic conditions part 2: Impact force responses for non-rigid debris collisions." *Coastal Engineering* 141 (2018): 107-118. [https://doi.org/10.1016/j.coastaleng.2018.09.004]
33. Yang, W.C. Study of Tsunami-Induced Fluid and Debris Load on Bridges using the Material Point Method. Ph.D. Thesis, University of Washington, Seattle, WA, USA, 2016. Available online: http://hdl.handle.net/1773/37064 (accessed on 15 July 2021).
34. Oudenbroek, Kevin, Nader Naderi, Jeremy D. Bricker, Yuguang Yang, Cor Van der Veen, Wim Uijttewaal, Shuji Moriguchi, and Sebastiaan N. Jonkman. "Hydrodynamic and debris-damming failure of bridge decks and piers in steady flow." *Geosciences* 8, no. 11 (2018): 409. [https://doi.org/10.3390/geosciences8110409]
35. Istrati, D.; Hasanpour, A.; Buckle, I. Numerical Investigation of Tsunami-Borne Debris Damming Loads on a Coastal Bridge. In Proceedings of the 17 World Conference on Earthquake Engineering, Sendai, Japan, 13–18 September 2020.
36. Ruffini, G., Briganti, R., De Girolamo, P., Stolle, J., Ghiassi, B., & Castellino, M. (2021). Numerical Modelling of Flow-Debris Interaction during Extreme Hydrodynamic Events with DualSPHysics-CHRONO. *Applied Sciences*, *11*(8), 3618.
37. Hasanpour, A., Istrati, D., & Buckle, I. (2021). Coupled SPH–FEM Modeling of Tsunami-Borne Large Debris Flow and Impact on Coastal Structures. *Journal of Marine Science and Engineering*, *9*(10), 1068. [https://doi.org/10.3390/jmse9101068]

38. Hasanpour, A., Istrati, D., & Buckle, I. G. (2022, July). Multi-Physics Modeling of Tsunami Debris Impact on Bridge Decks. In *Proceedings of the 3rd International Conference on Natural Hazards & Infrastructure, Athens, Greece* (pp. 5-7).
39. Istrati, D., & Hasanpour, A. (2022, September). Advanced numerical modelling of large debris impact on piers during extreme flood events. In *Proceedings of the 7th IAHR Europe Congress, Athens, Greece* (pp. 7-9).
40. Hasanpour, A., Istrati, D., & Buckle, I. (2023). Three-Dimensional Investigation of Floating Debris Effects on Bridge Superstructures During Tsunamis. *Has been submitted to Coastal Engineering*.
41. Amraei, S. S. (2016). *Tsunami Inland Structures Interaction and Impact of Floating Debris* (Doctoral dissertation, University of Auckland).
42. Ko, H. S., Cox, D. T., Riggs, H. R., & Naito, C. J. (2015). Hydraulic experiments on impact forces from tsunami-driven debris. *Journal of Waterway, Port, Coastal, and Ocean Engineering*, *141*(3), 04014043.
43. Mast, R., Marsh, L., Spry, C., Johnson, S., Griebenow, R., Guarre, J., & Wilson, W. (1996). *Seismic design of bridges-design example no. 1: Two-span continuous CIP concrete box bridge* (No. FHWA-SA-97-006).
44. Mast, R., Marsh, L., Spry, C., Johnson, S., Griebenow, R., Guarre, J., & Wilson, W. (1996). *SEISMIC DESIGN OF BRIDGES-DESIGN EXAMPLE NO. 2: THREE-SPAN CONTINUOUS STEEL GIRDER BRIDGE* (No. FHWA-SA-97-007).
45. Mast, R., Marsh, L., Spry, C., Johnson, S., Griebenow, R., Guarre, J., & Wilson, W. (1996). *SEISMIC DESIGN OF BRIDGES-DESIGN EXAMPLE NO. 3: SINGLE SPAN AASHTO PRECAST GIRDER BRIDGE* (No. FHWA-SA-97-008).
46. Mast, R., Marsh, L., Spry, C., Johnson, S., Griebenow, R., Guarre, J., & Wilson, W. (1996). *SEISMIC DESIGN OF BRIDGES-DESIGN EXAMPLE NO. 4: THREE-SPAN CONTINUOUS CIP CONCRETE BRIDGE* (No. FHWA-SA-97-009).
47. Mast, R., Marsh, L., Spry, C., Johnson, S., Griebenow, R., Guarre, J., & Wilson, W. (1996). *SEISMIC DESIGN OF BRIDGES-DESIGN EXAMPLE NO. 7: TWELVE-SPAN VIADUCT AASHTO PRECAST CONCRETE BRIDGE* (No. FHWA-SA-97-012).
48. Ko, H.T., 2013. Hydraulic Experiments on Impact Forces from Tsunami-driven Debris. Oregon State University, Corvallis, Oregon.
49. Piran Aghl, P., Naito, C. J., & Riggs, H. R. (2014). Full-scale experimental study of impact demands resulting from high mass, low velocity debris. *Journal of Structural Engineering*, *140*(5), 04014006.

Chapter 6

6. SPH-FEM Investigation of Floating Container Impact on Bridge Superstructures: Role of Debris Mass

Abstract

Coastal structures, particularly bridges, are highly susceptible to the destructive forces of tsunamis which can lead to the failure of their integrity and stability. Past tsunamis have resulted in significant damage to infrastructure, with bridges being particularly vulnerable. The importance of bridges in post-disaster response and recovery cannot be overstated, as damage to them can greatly impede rescue efforts and impede access to affected areas. One of the major causes of damage to coastal bridges during tsunamis is the impact of floating debris, such as shipping containers. These debris can cause washout or loss of decks. Despite the significant contribution of tsunami-borne debris to the applied loadings on bridges, there is a lack of research on the impact forces of floating debris on coastal bridges, which can be attributed to the challenging multi-physics nature of the phenomena. Therefore, the main goal of this paper is to employ the coupled SPH-FEM numerical approach to evaluate the role of debris mass on its dynamic and impact forces on coastal bridges. To accomplish this, two different orientations of the debris with varying masses were examined. The results of the analysis indicated that debris mass has a substantial impact on its movement with lighter debris displacing, on average, up to 1.75 times more than the heavier debris, depending on its orientation. Additionally, the findings demonstrated that as the mass of debris increases, there is a decrease in velocities and an increase in impact forces in the horizontal and vertical directions.

Keywords: tsunami; wave; bore; flooding; debris; debris mass; SPH; numerical modeling; SPH-FEM coupling; fluid structure interaction, bridge

6.1. Introduction

Tsunamis are one of the most devastating natural disasters, with the potential to cause severe damage to coastal infrastructure such as transportation networks and bridges and compromise their

integrity and stability. Past tsunamis, notably the 2004 Indian Ocean and the 2011 Great East Japan tsunamis, led to unprecedented destruction of infrastructure. An estimated 1,500 km of coastline was affected and out of 186 damaged bridges, 81 of them were completely washed away during the Indian tsunami [1-2]. Similar damage occurred during the Tohoku tsunami, in which more than 300 bridges received massive damage and a loss of $235 billion [3]. Transportation assets play a crucial role in post-disaster response and recovery and rescue process can be impeded by roads and bridges that are damaged or have a reduced level of serviceability. According to Williams et al. (2020) [4], bridges are more vulnerable to tsunami loads than roads and several studies have been conducted to study the tsunami-bridge interaction and the associated loads. Field surveys after the 2004 tsunami revealed that tsunami-driven debris pose significant threats and a number of key bridges were impacted by debris and floating objects such as shipping containers; resulting in washout of the structure or loss of their decks [5-7]. While an appropriate quantification of the forces involved with water-borne debris is vital to design tsunami-resistant bridges, a very limited number of studies have addressed the floating debris impact forces on coastal bridges which can be attributed to the challenging multi-physics nature of the phenomena.

To improve the safety of coastal bridges, several numerical and experimental research works have been carried out to study the wave-bridge interaction. After Hurricane Katrina, Robertson et al., (2007) [8] surveyed the damaged bridges and reported that hydrostatic and hydrodynamic loading played a major role in structural failure. Bradner et al., (2008) [9] conducted a large-scale experimental study of a concrete bridge deck under regular and irregular waves and presented predictive equations for applied pressures and forces. Araki et al. (2010) [10] investigated the performance of a bridge model against breaking and nonbreaking waves and concluded that the bridge experienced a higher level of impact forces in the case of a breaking wave. Kosa et al. (2010) [11] carried out an experimental investigation on a 1:50 scale bridge and reported that in contrast

to the broken wave, the bridge superstructure has to resist a higher level of uplift force than the horizontal force in the case of an unbroken wave. The three-dimensional effects of the skew angle of the bridge relative to the incoming wave during the tsunami impact were investigated by Motley et al., (2016) [12] and Istrati and Buckle (2021b) [13] and it was reported that as the angle of skew increases, the magnitude of the applied loadings decreases. Azadbakht and Yim (2015) [14] and Xiang et al., (2020) [15] conducted numerical simulation to investigate tsunami-induced loadings on coastal bridges and proposed simplified predictive equations. More specifically, Xiang et al., (2020) [15] assessed the effect of bridge elevation and wave height on the quasi-static and slamming phases of the loading and proposed an improved predictive equation that can capture both forces and moments. Istrati (2017) [16] carried out a large-scale experimental study on a 1:5 scale model of a single-span bridge with different configurations using solitary waves and bores. The results showed that the total applied forces highly depend on the deck type and the wave type [16, 17]. Moreover, other critical aspects affecting the hydrodynamic demands on coastal bridges include role of trapped air below the deck [18, 19] and the demand on individual structural components [20] have been studied as well. Loli et al., (2022) [21] developed a framework that combines field-based and theoretical research for efficient evaluation of flood risk to bridge.

A proper characterization of debris-fluid-structure interaction is crucial for evaluating the contribution of water-borne debris to the impact forces to design resilient infrastructure that can withstand the demand. Haehnel and Daly (2002) [22] and Matsutomi (2009) [23] investigated the maximum debris impact force on the structures and stated that the impact force is a function of debris mass, impact velocity and effective stiffness. Madurapperuma and Wijeyewickrema (2012) [24] evaluated the induced impact force from shipping containers on the RC columns and reported that the impact force is a linear function of the impact velocity up to 2m/s. Como and Mahmoud (2013) [25] carried out fluid-structure interaction analyses to study the debris impact on interior

and exterior wood structural panels and concluded that the impact force decreases for an interior panel. The impact on a column by a 1:5 scale model of a shipping container was investigated by Ko et al., (2015) [26]. The results showed that the impact force in water is larger than the impact force in the air by a factor of 1.2. Derschum et al., (2018) [27] performed a 1:40 dam-break test to investigate the shipping container impact force on a vertical structure and concluded that the initial impoundment depth plays a significant role in the impact force.

In an experimental effort, Haehnel and Daly (2004) [28] used logs with varying mass to evaluate the impact forces on a structure and reported that impact force depends on the mass of the debris. Nouri et al., (2010) [29] utilized logs with different masses ranging between 0.474 kg to 1.479 kg and made a similar observation. Shafiei et al., (2016) [30] conducted an experimental study using two different debris types including box and disk with varying masses to evaluate the impact force on a cylindrical structure. The extra masses were firmly attached to the debris. The results revealed the dependency of the impact force on the debris mass. However, Paczkowski et al., (2012) [31] carried out an experimental study to investigate the in-air impact of a projectile with different masses and concluded that the impact force does not depend on the total mass of the debris. A similar observation was reported by Ko et al., (2015) [26] for the in-water impact. They found that the unattached extra masses inside the debris do not have an effect on the maximum impact force.

While the majority of the past works mainly focused on investigating water-borne debris impact force on vertical structures, very limited studies addressed the debris impact force on bridge superstructures. For example, Yang (2016) [32] studied debris impact force on bridge superstructures using the material point method and stated that the existence of water-borne debris causes a drastic increase in the peak impact forces. Oudenbroek et al., (2018) [33] experimentally and numerically investigated the debris damming failure of bridge decks and piers and concluded that debris impact forces affect bridge functionality and integrity. Tsunami-borne debris damming

loads on a coastal bridge were evaluated by Istrati et al., (2020) [34] through three-dimensional computational fluid dynamic analyses. The results demonstrated that while the applied horizontal and vertical forces do not influence by the debris damming loads, it significantly affects the overturning moment which increases the vertical forces and demands on structural components. Moreover, it was shown that if the container is trapped close to the supports, as a result of the 3D effects, additional yow and roll moments are generated, highlighting the importance of the container location for designing the structural components. Hasanpour et al. (2021) [35] used the smoothed particle hydrodynamic coupled finite element method (SPH-FEM) modeling approach to investigate tsunami-borne debris transport and its impact on the coastal structure. The results demonstrated the accuracy of this technique to regenerate the debris transport and impact. In addition, a high level of debris pitching which lead to the non-normal impact and consequently reduced contact area and impact force was reported. They concluded that the level of debris pitching depends on tsunami flow characteristics and initial water depth and a non-linear force-velocity trend for small water depth was documented. In a study conducted by Majtan et al, (2021) [36] the SPH method was utilized to investigate the debris impact forces on a masonry arch bridge. More recently, Hasanpour et al., (2022) [37] evaluated the tsunami debris impact on a bridge deck utilizing the two-dimensional coupled SPH-FEM. The results showed that at the instant of primary impact, the debris has both a horizontal and vertical velocity and applies impact forces in both directions. The debris-fluid-deck interaction exhibits a quite complex trend and the debris accelerates as it propagates below the deck, leading to secondary impacts on the soffit with magnitudes much larger than the ones of the primary impact on the offshore side of the deck. In another study, Istrati and Hasanpour (2022) [38] carried out numerical investigation to study the water-borne debris impact loads on piers and the results revealed that the debris impulsive loads are 6 to 10 times larger than the fluid force.

A review of past studies revealed that extremely limited experimental and numerical investigations have been carried out to explore the debris-fluid-bridge interaction. Moreover, contradictory observations were made regarding the effect of debris mass on the peak impact forces, highlighting the complex nature of the phenomena and the necessity of exploring the debris impact forces. Given the critical role of bridges in the economic prosperity of the coastal communities and post-disaster recovery of the affected areas, it is extremely important to quantify the debris impact forces with varying masses on coastal bridges to develop resilient coastal infrastructure that can deal with the structural demands and remain operational against extreme events such as tsunamis. To this end, this study investigates the role of tsunami-borne debris mass on induced forces on coastal bridges, utilizing a three-dimensional coupled finite element and smoothed particle hydrodynamics modeling approach (SPH-FEM).

6.2. Methodology

In this paper, the coupled SPH-FEM numerical method was utilized. The accuracy of the numerical technique was validated against experimental results from a study conducted by Shafiei (2016) [30]. A detailed explanation of the numerical technique and results of the validation study can be found in Hasanpour et al., (2023) [39-41].

6.2.1. Numerical models of debris impact with varying masses on a box-girder bridge

This paper is a continuation of the study presented in Hasanpour et al., (2023) [39] and Hasanpour et al., (2023) [40] and applied the same numerical settings and assumptions. However, in terms of the debris mass, a range of masses including 9.2%, 50% and, 75% of the total weight of a standard shipping container was considered. As a result, two different debris orientations were analyzed, each based on three different mass values. According to ko et al., (2015) [26], 9.2% represents the typical empty weight of a standard shipping container. It is worth noting that, for the purpose of this paper, the bridge elevation of 0.30 m was only considered. In this study, only strong bores (as

defined by [39,40]) including B3 (H_r=0.60 m, d=0.10 m), B4 (H_r=0.60 m, d=0.15m), B5 (H_r=0.60 m, d=0.20 m), and B6 (H_r=0.60 m, d=0.25 m) were considered for the tsunami flow, where H_r is the depth of water in the reservoir and d is the standing water level.

6.3. Debris-bore-bridge interaction

6.3.1. General trends

Figure 6-1 presents a visualization of the debris-flow-bridge interaction for the transverse debris and bore properties of case B6, with a debris mass of (a) 9.2% and (b) 75%. It is evident from these snapshots that, in addition to the initial orientation of the debris, bridge elevation, bore strength, and standing water level which was discussed in detail in previous publications [39-41], the mass of the debris also has a significant impact on its movement around the bridge. For instance, in this case, the lighter debris (9.2% mass) impacts the bridge and moves above the deck, while the heaviest container (75% mass) impacts the offshore side and travels below the soffit.

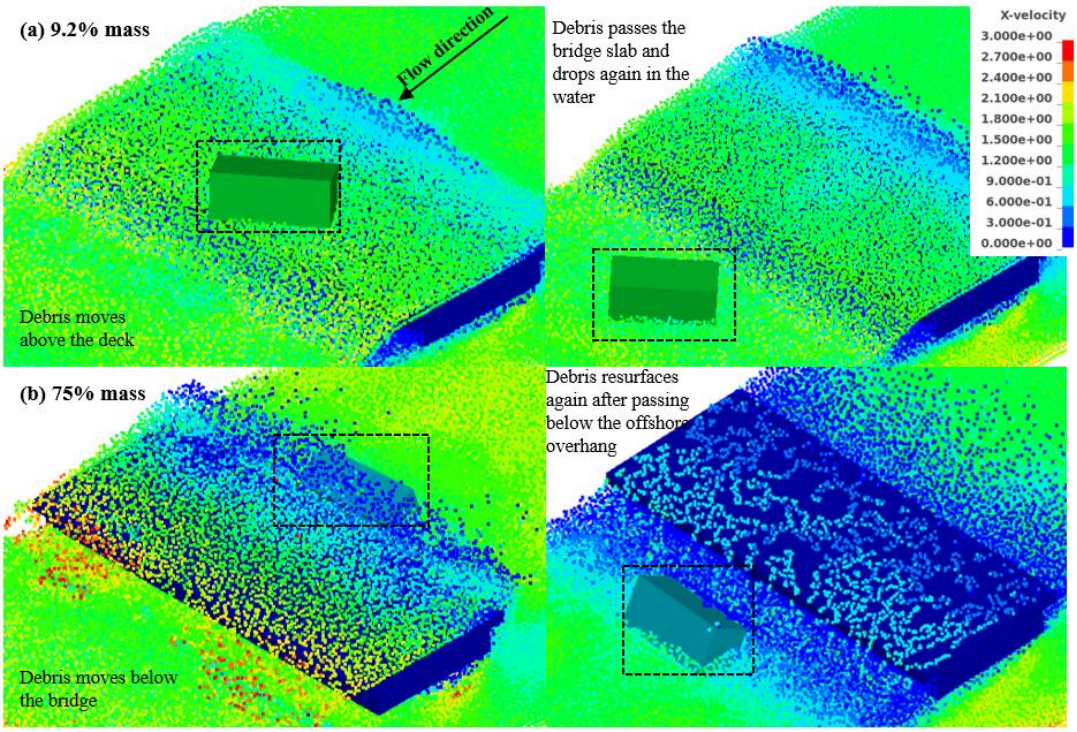

Figure 6-1 Debris-flow-bridge interaction for transverse debris and case B6: (a) 9.2% mass, (b) 75% mass

To better comprehend the effect of debris mass on the debris-flow-bridge interaction, Table 6-1 presents information on the movement of debris for all cases studied in this study. This table is organized based on the mass of the debris and its initial orientation, with Table 6-1a displaying the results of longitudinal debris movement and Table 6-1b displaying the results of transverse debris movement. Different trends in debris movement are observed based on the mass of the debris. For example, in the cases of B5 and B6, the longitudinal debris with 9.2% mass, moves above the deck without any interaction with it, while debris with other masses (50% and 75%) impacts the offshore side of the bridge and moves below it. However, for the transverse debris and case B4, debris of different masses all impact the bridge and move below it, indicating that debris mass does not seem to affect the movement of the debris in this case.

Table 6-1 Debris-tsunami-bridge interaction

a) Longitudinal orientation

Bore Cases	**H_r (m)**	**d (m)**	**Debris mass (%)**		
			9.2	**50**	**75**
B3	0.60	0.10	Impacts and gets trapped below the offshore overhang	Impacts and gets trapped below the offshore overhang	Moves below- NO interaction
B4		0.15	Impacts and gets trapped below the offshore overhang	Impacts and moves below	Impacts and moves below
B5		0.20	Moves above the deck- NO interaction	Impacts and moves below	Impacts and moves below
B6		0.25	Moves above the deck- NO interaction	Impacts and moves below	Impacts and moves below

b) Transverse orientation

Bore Cases	H_r (m)	d (m)	Debris mass (%)		
			9.2	50	75
B3	0.60	0.10	Impacts and moves below	Impacts and gets trapped below the offshore overhang	Impacts and moves below
B4		0.15	Impacts and moves below	Impacts and moves below	Impacts and moves below
B5		0.20	Impacts and moves above	Impacts and moves below	Impacts and moves below
B6		0.25	Impacts and moves above	Impacts and moves above	Impacts and moves below

6.3.2. Debris displacements and rotations

To gain a quantitative understanding of the movement of the container with varying masses as it propagates inland and impacts the bridge, Figure 6-2 presents the time-histories of the vertical displacement and trajectory of the debris for case B5. This figure demonstrates the significant effect of debris mass on its movement. As expected, the tsunami bore elevated debris with a mass of 9.2% more than debris with masses of 50% and 75%, resulting in different interactions with the deck.

According to Figure 6-3 which displays the maximum vertical displacement of the debris for all the studied cases, on average, the maximum vertical displacement of longitudinal debris with 9.2% mass is 1.33 and 1.52 times larger than debris with masses of 50% and 75%., respectively. The transverse debris with the mass of 9.2% also shows a larger average vertical displacement, 1.36 and 2 times larger than debris with masses of 50% and 75%, respectively.

The accurate estimation of the vertical displacement of debris is essential for predicting the effects of impact on the bridge and for identifying the location of impact. It is feasible that a container applies multiple impacts on the bridge which could potentially deteriorate the structural integrity of the bridge.

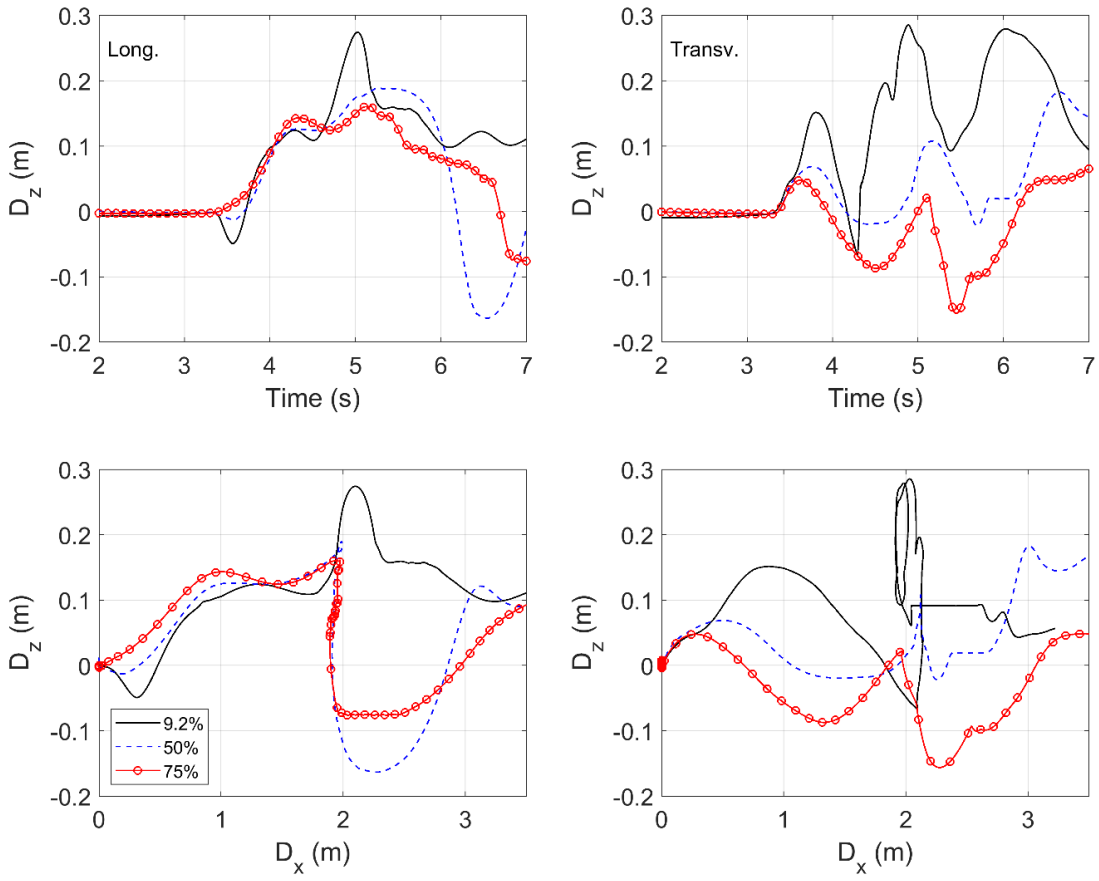

Figure 6-2 Debris vertical displacement histories (top) and trajectories (bottom) for case B5 for two orientations with variable masses

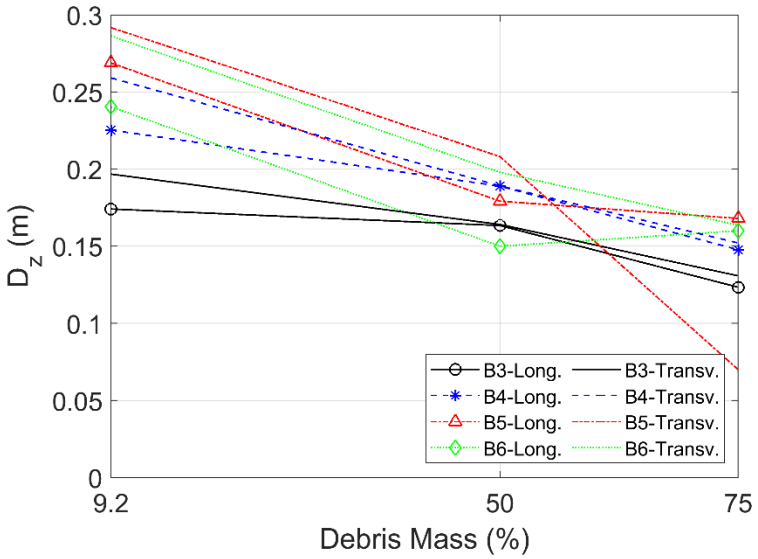

Figure 6-3 Debris maximum vertical displacement for two orientations with variable masses

Figure 6-4 demonstrates the rotation of the debris around the y-axis (pitch) for case B5, which includes two different orientations of the debris and a range of masses. In this figure, the vertical lines show the instant of initial impact for each case. The data demonstrate that the mass of the debris significantly affects its rotational movement. In the depicted cases, for both orientations of the debris, the debris with a mass of 9.2% moves above the deck. However, the longitudinal debris does not come into contact with the deck, while the transverse debris impacts the bridge and propagates above it. This difference in movement explains the significant variation in the pitching rotation of the transverse debris. The debris with masses of 50% and 75% in both orientations impacts the bridge and travels beneath it. However, the longitudinal debris continues to rotate after the primary impact and even when it resurfaces, while the transverse debris experiences a reduction in pitch rotation following the initial impact. This discrepancy in rotational behavior could potentially be attributed to the differences in the initial orientation of the debris.

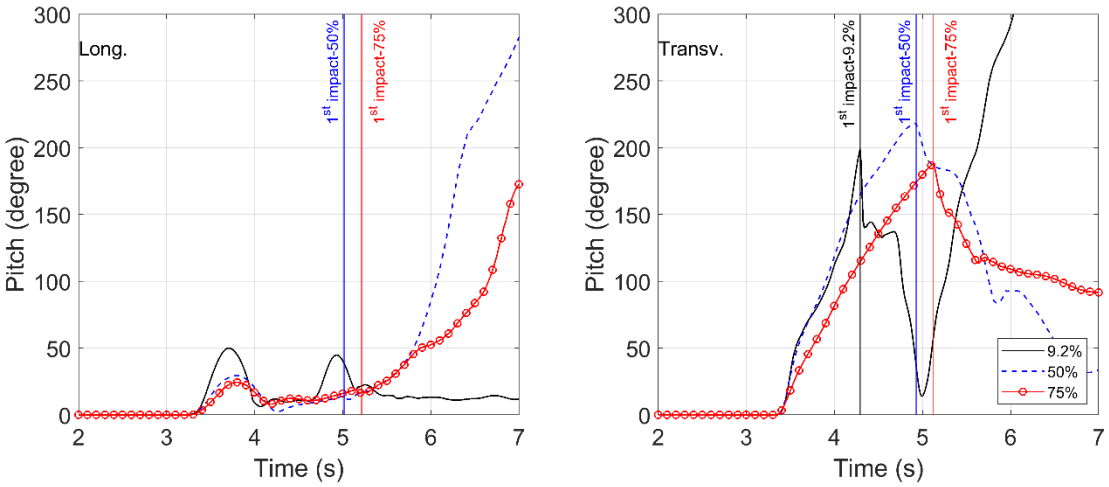

Figure 6-4 Time histories of debris pitch rotation for case B5 and two orientations with variable masses

6.3.3. Debris velocities

Figure 6-5 demonstrates the time-series of horizontal (Vx_d) and vertical (Vz_d) velocities of debris in case B5 for two different debris orientations and varying masses. The results, as reported by Hasanpour et al., (2023) [40], show that the longitudinal debris reaches higher velocities in all scenarios. As shown in Table 6-1, the longitudinal debris with 9.2% impacts the bridge and becomes trapped below the offshore overhang till the end of the inundation process. That is why the debris velocity drops significantly and becomes almost zero after the initial impact. As expected, increasing the mass of the debris leads to a decrease in velocity. In this case, increasing the mass of the debris from 9.2% to 75% results in decrease in the maximum velocity of the longitudinal debris by 35% and 80% in the horizontal and vertical directions, respectively. The transverse debris also experiences a decrease in velocity of about 25% and 86% in the horizontal and vertical directions, respectively.

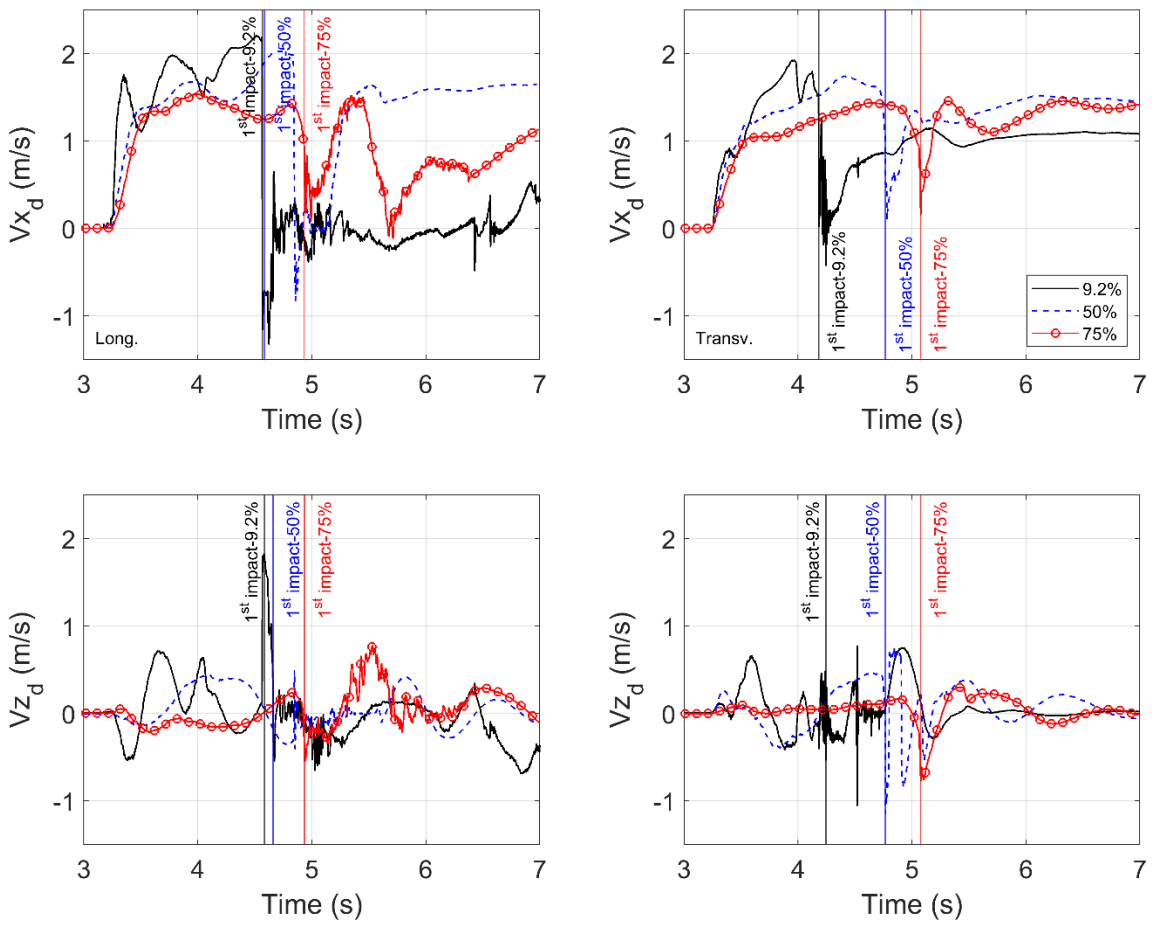

Figure 6-5 Debris velocities in the horizontal (top) and vertical (bottom) directions for case B4 for two debris orientations and variable masses

Figure 6-6 displays the debris impact velocities in the horizontal and vertical directions for all studied cases. It is worth noting that for the longitudinal debris in cases B5 and B6 with 9.2% mass and case B3 with 75%, debris does not interact with the deck and the debris impact velocities are zero. The results presented in this figure indicate that increasing the mass of the longitudinal debris from 9.2% to 75% leads to an average reduction of approximately 25% and 65% in the horizontal and vertical velocities, respectively. Additionally, when the mass is increased from 50% to 75%, there is a reduction of approximately 17% and 12% in the horizontal and vertical velocities, respectively. For the transverse debris, increasing the mass from 9.2% to 75% results in an average reduction of approximately 21% and 75% in the horizontal and vertical velocities, respectively.

Furthermore, increasing the mass from 50% to 75% results in a reduction of approximately 20% and 23% in the horizontal and vertical velocities, respectively. These observations are consistent with the findings presented by Shafiei (2016) [30].

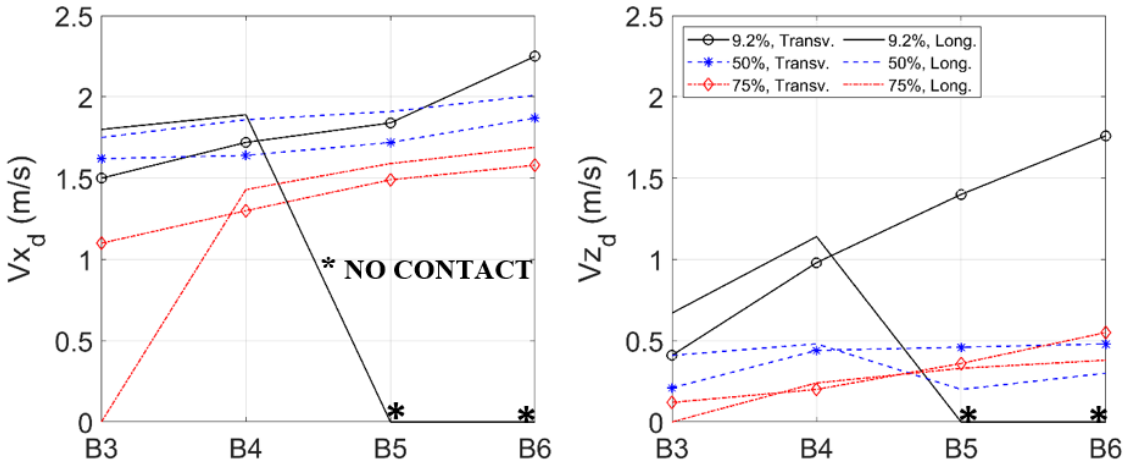

Figure 6-6 Maximum values of debris velocities in the horizontal (left) and vertical (right) directions for all studied cases including two different orientations and variable masses

6.4. Impact forces on bridge superstructures

The temporal progression of the loadings applied to the bridges as a result of debris and tsunami bores is essential in designing structures that can effectively resist and withstand these forces to ensure their safety. Figure 6-7 presents the time-histories of the debris horizontal (Fx_d) and vertical (Fz_d) impact forces applied on the bridge superstructure by case B6 for two debris orientations with variable masses. In the case of longitudinal debris, debris with 9.2% mass moves above the deck without interacting with it, while debris with higher masses (50% and 75%) impacts the offshore side of the bridge and moves beneath it. As expected, impact forces increase with the mass of the debris. In the aforementioned cases, the primary impact forces applied by the debris with 75% mass are up to 1.5 and 2 times larger than the respective horizontal and vertical forces applied by the debris with 50% mass, respectively. In the case of the transverse debris, debris with 9.2% and 50% masses impact the offshore side and travel above the deck, applying downward vertical forces. The heaviest debris impacts the offshore side and moves below the bridge. A similar trend in terms of

the impact forces is observed, with the greatest impact force being exerted by debris with 75% mass. Furthermore, the analysis of the impact force reveals that as the mass of debris increases from 9.2% to 75%, there is a fourfold increase in horizontal impact force. Additionally, a comparison of impact forces from debris with 50% and 75% mass indicates that the latter exerts 1.4 times larger horizontal force.

As seen in Figure 6-8, the impact forces of debris in both horizontal and vertical directions are analyzed for all scenarios under examination. It is noteworthy that for longitudinal debris in cases B5 and B6 with 9.2% mass, and case B3 with 75% mass, there is no interaction with the bridge. The data presented in this figure demonstrate that an increase in mass of longitudinal debris from 9.2% to 75% results in an average increase of approximately 4.8 and 6 times in the horizontal and vertical impact forces, respectively. Furthermore, when the mass is increased from 50% to 75%, there is an average increase of approximately 1.4 and 2.4 times in the horizontal and vertical impact forces, respectively. In the case of transverse debris, increasing mass from 9.2% to 75% leads to an average increase of approximately 6.1 and 3.8 times in the horizontal and vertical forces, respectively. Furthermore, increasing mass from 50% to 75% results in an average increase of approximately 1.6 and 1.5 times in the horizontal and vertical forces, respectively.

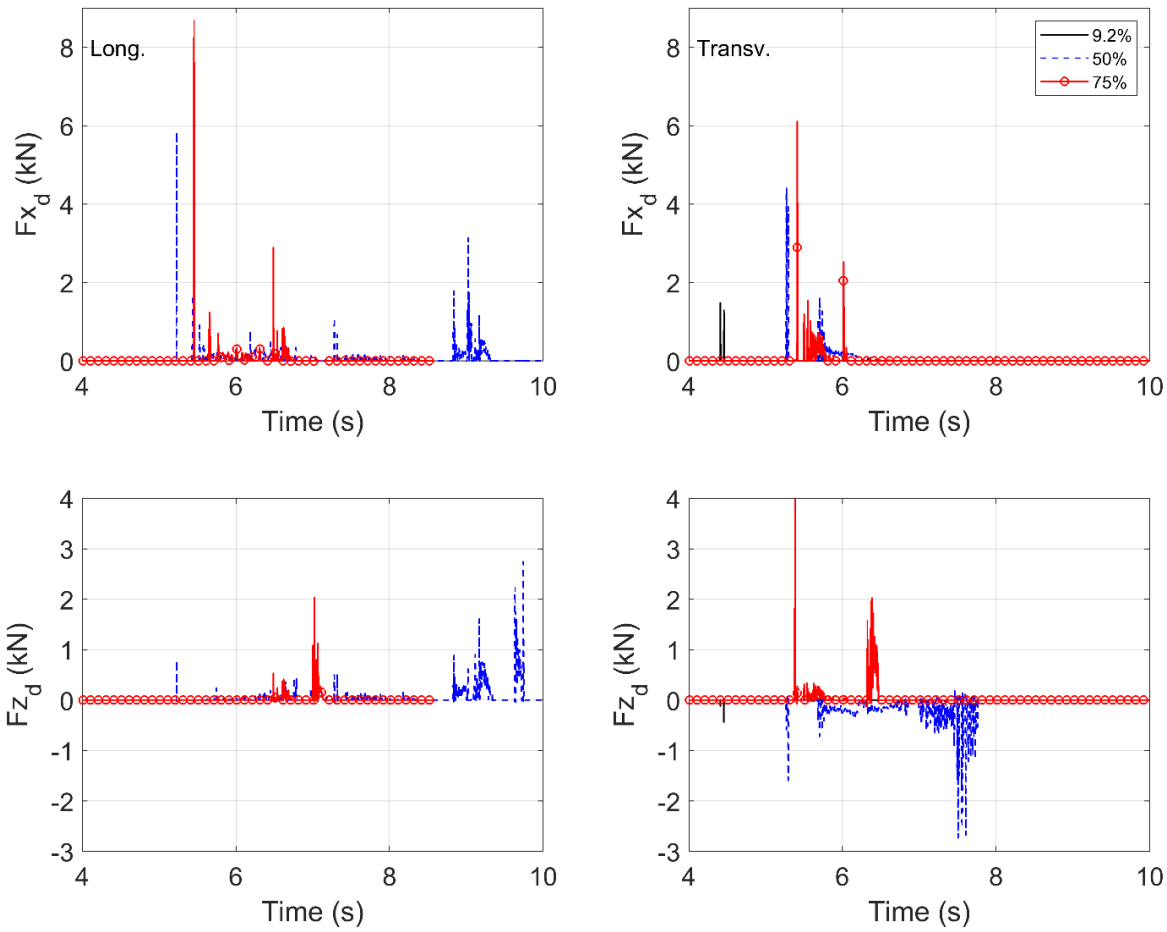

Figure 6-7 Time histories of debris impact forces in the horizontal (top) and vertical (bottom) directions for case B6 for two debris orientations and variable masses

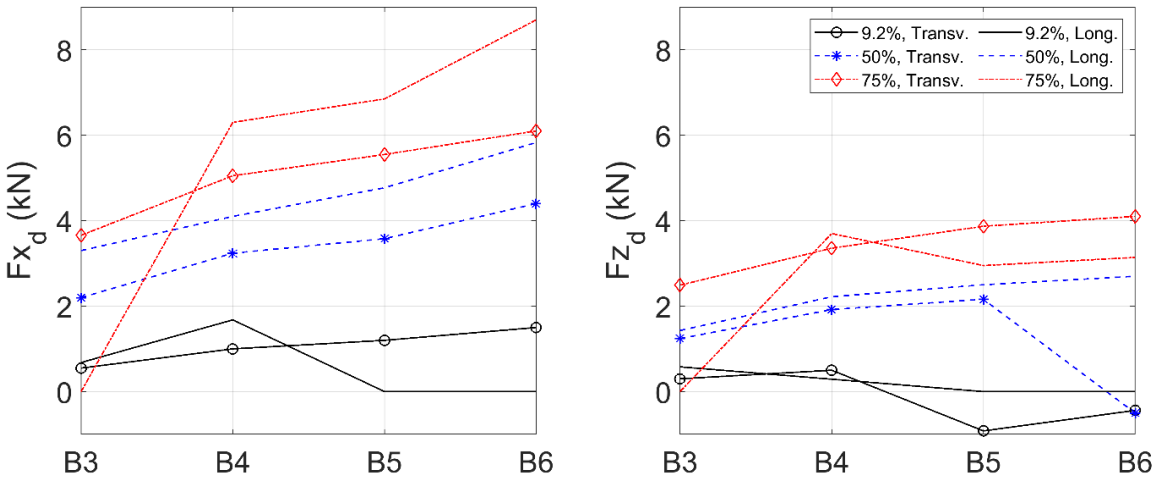

Figure 6-8 Maximum values of debris impact forces in the horizontal (left) and vertical (right) directions for all studied case including two different orientations and variable masses

Figure 6-9 shows the time-histories of the total horizontal (Fx_t) and vertical (Fz_t) impact forces applied on the bridge superstructure by case B6 for two debris orientations with varying masses. The results demonstrate that, as expected, the total impact forces increase with the mass of the debris. It is important to note that, in the case of longitudinal debris with 9.2% mass, the total impact force is solely a result of the tsunami-bridge interaction. The analysis of the total horizontal impact force applied in the case of the longitudinal debris with 75% mass reveals that it is up to 1.31 and 2.73 times larger than the respective horizontal forces applied in cases of debris with 50% and 9,2% mass, respectively. Additionally, a comparison of the total horizontal impact forces in cases of debris with 9.2% and 50% mass indicates that the latter exerts 2.07 times larger force. In contrast, the bridge experiences the largest total uplift force in the case of debris with 9.2% mass which is 1.06 and 1.03 times the cases with 50% and 75% mass, respectively.

In the case of the transverse debris, a similar trend in terms of the total impact forces is observed, with the highest total impact force being exerted by debris with 75% mass, which is 1.33 and 2.71 times the cases with 50% and 9.2% mass, respectively. Furthermore, the analysis of the impact force reveals that as the mass of debris increases from 9.2% to 50%, there is a twofold increase in the total uplift impact force. Additionally, a comparison of the vertical impact forces from debris indicates that the heaviest debris exerts 1.4 and 1.2 times larger force than the debris with 50% and 9.2% mass, respectively.

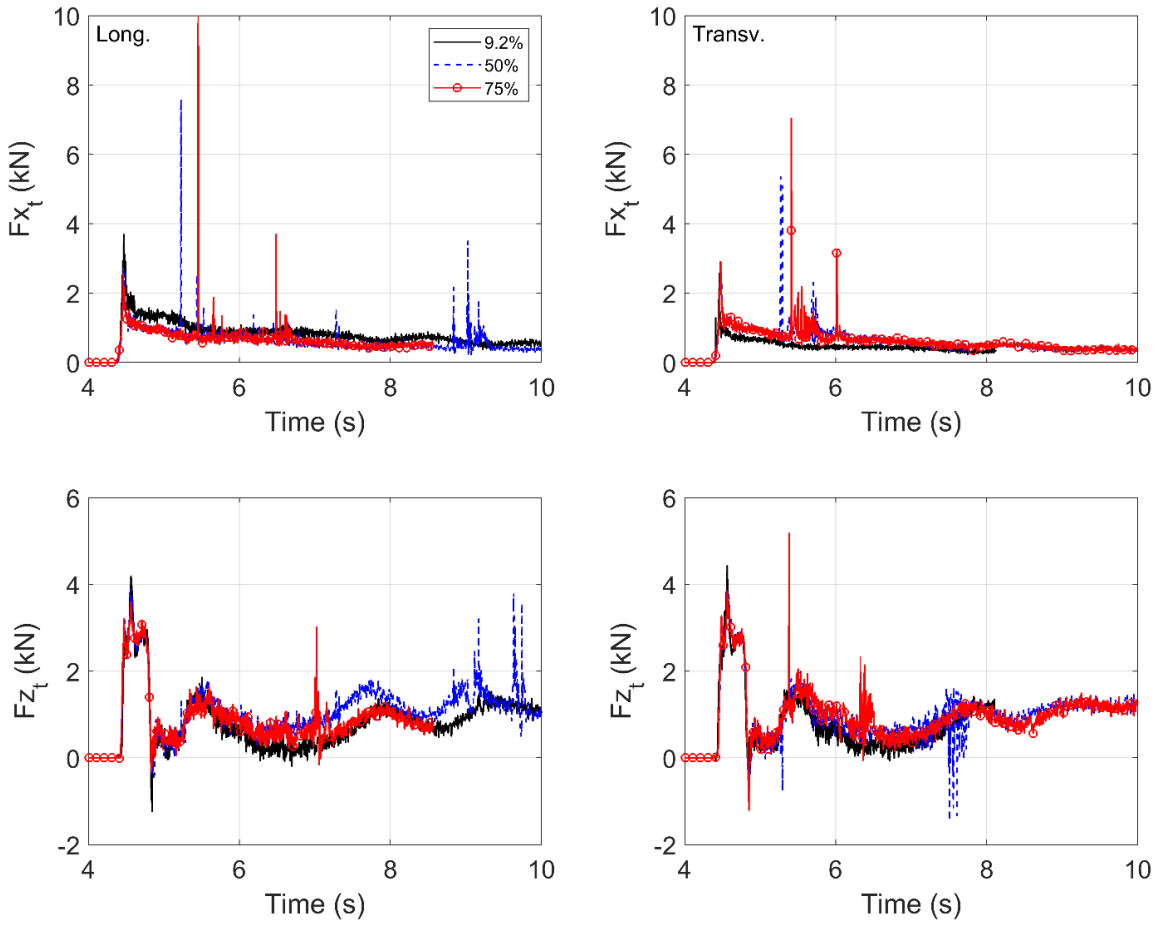

Figure 6-9 Time histories of total impact forces in the horizontal (top) and vertical (bottom) directions for case B6 for two debris orientations and variable masses

The total impact forces in both horizontal and vertical directions are analyzed for all the studied cases and presented in Figure 6-10. The data demonstrate that an increase in the mass of longitudinal debris from 9.2% to 75% results in an average increase of approximately 2.9 and 1.4 times in the horizontal and vertical impact forces, respectively. Additionally, when the mass is increased from 50% to 75%, there is an average increase of approximately 1.09 and 1.03 times in the horizontal and vertical impact forces, respectively. Furthermore, when it comes to transverse debris, In the case of transverse debris, an increase in mass from 9.2% to 75% leads to an average increase of approximately 4 and 1.9 times in the horizontal and vertical forces, respectively.

Furthermore, an increase in mass from 50% to 75% results in an average increase of approximately 1.44 and 1.47 times in the horizontal and vertical forces, respectively.

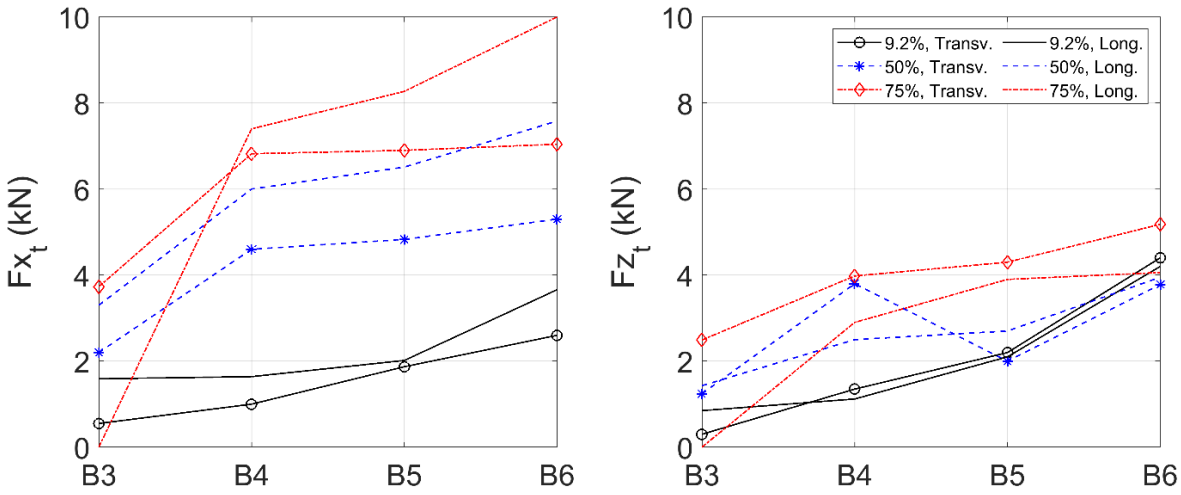

Figure 6-10 Maximum values of total.3 impact forces in the horizontal (left) and vertical (right) directions for all studied case including two different orientations and variable masses

6.5. Summary and conclusions

The objective of this study was to examine the influence of debris mass on the debris-flow and debris-flow-bridge interactions by employing the coupled SPH-FEM numerical technique. The study considered two orientations of the debris, with mass variations ranging from 9.2% to 75% of the total mass of standard shipping container and a spectrum of hydrodynamic conditions. Based on the results of the current study, the following conclusions were drawn:

- Mass of the debris has a significant impact on its movement. The maximum vertical displacement of longitudinal debris with a mass of 9.2% was found to be 1.33 and 1.52 times larger, on average, than debris with masses of 50% and 75%, respectively. Similarly, transverse debris with the mass of 9.2% also showed a larger average vertical displacement, 1.36 and 2 times larger than debris with masses of 50% and 75%.

- The data show that as the mass of debris increases, the velocity of debris decreases. Specifically, as the mass of the longitudinal debris increases from 9.2% to 75%, there is an average reduction of 25% and 65% in the horizontal and vertical velocities, respectively. Additionally, an increase in mass of the transverse debris from 9.2% to 75% results in an average reduction of 21% and 75% in horizontal and vertical velocities, respectively.

- The study found a correlation between the mass of debris and impact forces, where an increase in mass leads to a corresponding increase in impact forces. The data revealed that as the mass of the longitudinal debris increases from 9.2% to 75%, there is an average increase of 4.8 and 6 times in horizontal and uplift forces, respectively. Similarly, when the mass of the transverse debris increases from 9.2% to 75%, there is an average increase of 6.1 and 3.8 times in horizontal and vertical impact forces, respectively.

- The results indicated that an increase in the mass of longitudinal debris from 9.2% to 75% results in an average increase of approximately 2.9 and 1.4 times in the horizontal and vertical total impact forces, respectively. Additionally, an increase in debris mass from 9.2% to 75% for the transverse debris is found to result in an average increase of approximately 4 and 1.9 times in the horizontal and vertical total impact forces, respectively.

In conclusion, the findings of the three-dimensional analyses conclusively demonstrate the significant effect of debris mass on its dynamic and impact forces experienced by bridge superstructure. Further research should expand upon the current study by incorporating a more diverse range of hydrodynamic conditions and debris masses in order to verify the validity of these results and to determine the range of their applicability.

6.6. Acknowledgment

The work described in this paper was supported by the State of California through the Transportation System Research Program of the Pacific Earthquake Engineering Research Center (PEER). Any opinions findings, and conclusion or recommendations expressed in this material are those of the author(s) and do not necessarily reflect those of the funding agency.

6.7. References

1. Ghobarah, A., Saatcioglu, M., & Nistor, I. (2006). The impact of the 26 December 2004 earthquake and tsunami on structures and infrastructure. *Engineering structures*, *28*(2), 312-326.
2. Unjoh, S., & Endoh, K. (2006, May). Damage investigation and the preliminary analyses of bridge damage caused by the 2004 Indian Ocean tsunami. In *Proceedings of the 38th UJNR joint panel meeting*.
3. Kosa, K. (2011). Damage analysis of bridges affected by tsunami due to Great East Japan Earthquake. In *Proceedings of the international symposium on engineering lessons learned from the* (pp. 1-4).
4. Williams, J. H., Wilson, T. M., Horspool, N., Paulik, R., Wotherspoon, L., Lane, E. M., & Hughes, M. W. (2020). Assessing transportation vulnerability to tsunamis: utilising post-event field data from the 2011 Tōhoku tsunami, Japan, and the 2015 Illapel tsunami, Chile. *Natural Hazards and Earth System Sciences*, *20*(2), 451-470.
5. Saatcioglu, M., Ghobarah, A. and Nistor, I. (2006). Performance of structures in Indonesia during the 2004 Sumatra earthquake and tsunami, *Engineering Spectra, Earthquake Engineering Research Institute* (EERI), 22, 295-319. https://doi.org/10.1193/1.2209171
6. Rossetto, T., et al. (2007). "The Indian Ocean tsunami of December 26, 2004: Observations in Sri Lanka and Thailand." *Nat. Hazards*, 42(1), 105–124.
7. Robertson, I., Chock, G., and Morla, J. (2010). "Tsunami effects of the February 27, 2010 Chile earthquake." *EERI Preliminary Rep*., Earthquake Engineering Research Institute, Oakland, CA.
8. Robertson, I.N., Riggs, H.R., Yim, S.C., Young, Y.L., 2007. Lessons from hurricane Katrina storm surge on bridges and buildings. J. Waterw. Port, Coast. Ocean Eng. 133, 463–483. https://doi.org/10.1061/(ASCE)0733-950X(2007)133:6(463).
9. Bradner, C. Large-Scale Laboratory Observations of Wave Forces on a Highway Bridge Superstructure. Master's Thesis, Oregon State University, Corvallis, OR, USA, 2008.
10. Araki, S., K. Ishino, and I. Deguchi. 2010. "Stability of girder bridge against tsunami fluid force." In Proc., 32nd Int. Conf. on Coastal Engineering, 2. Red Hook, NY: Curran Associates.
11. Kosa, K., Nii, S., Miyahara, K., & Shoji, M. (2010, September). Experimental study for estimating tsunami forces acting on bridge girders. In *Proc., 26th US–Japan Bridge Engineering Workshop* (pp. 1-14). Tsukuba, Japan: Public Works Research Institute.
12. Motley, M. R., Wong, H. K., Qin, X., Winter, A. O., & Eberhard, M. O. (2016). Tsunami-induced forces on skewed bridges. Journal of Waterway, Port, Coastal, and Ocean Engineering, 142(3), 04015025. https://doi.org/10.1061/(ASCE)WW.1943-5460.0000328
13. Istrati, D.; Buckle, I.G. (2021b). Tsunami Loads on Straight and Skewed Bridges–Part 2: Numerical Investigation and Design Recommendations (No. FHWA-OR-RD-21-13). Oregon. Dept. of Transportation. Research Section, 2021. https://rosap.ntl.bts.gov/view/dot/55947

14. Azadbakht, M.; Yim, S.C. (2015). Simulation and estimation of tsunami loads on bridge superstructures. J. Waterw. Port Coast. Ocean Eng. 2015, 141, 04014031, https://doi.org/10.1061/(ASCE)WW.1943-5460.0000262
15. Xiang, T.; Istrati, D.; Yim, S.C.; Buckle, I.G.; Lomonaco, P. (2020). Tsunami loads on a representative coastal bridge deck: Experi-mental study and validation of design equations. J. Waterw. Port Coast. Ocean Eng. 2020, 146, 04020022. https://doi.org/10.1061/(ASCE)WW.1943-5460.0000560.
16. Istrati, D. Large-Scale Experiments of Tsunami Inundation of Bridges Including Fluid-Structure-Interaction. Ph.D. Thesis, University of Nevada, Reno, NV, USA, 2017. Available online: https://scholarworks.unr.edu//handle/11714/2030
17. Istrati, D.; Buckle, I.; Itani, A.; Lomonaco, P.; Yim, S. Large-Scale FSI Experiments on Tsunami-Induced Forces in Bridges. In Proceedings of the 16th World Conference on Earthquake Engineering, Santiago, Chile, 9–13 January 2017; Available online: https://www.wcee.nicee.org/wcee/article/16WCEE/WCEE2017-2579.pdf
18. Bozorgnia, M.; Lee, J.J.; Raichlen, F. Wave structure interaction: Role of entrapped air on wave impact and uplift forces. In Proceedings of the International Conference on Coastal Engineering, 30 June–5 July 2010.
19. Istrati, D.; Buckle, I. Role of trapped air on the tsunami-induced transient loads and response of coastal bridges. Geosciences **2019**,9, 191.
20. Istrati, D., I. Buckle, P. Lomonaco, and S. Yim. 2018. "Deciphering the tsunami wave impact and associated connection forces in open-girder coastal bridges." J. Mar. Sci. Eng. 6 (4): 148
21. Loli, M., Kefalas, G., Dafis, S., Mitoulis, S. A., & Schmidt, F. (2022). Bridge-specific flood risk assessment of transport networks using GIS and remotely sensed data. *Science of the Total Environment*, *850*, 157976.
22. Haehnel, R. B., & Daly, S. F. (2002). *Maximum impact force of woody debris on floodplain structures*. ENGINEER RESEARCH AND DEVELOPMENT CENTER HANOVER NH COLD REGIONS RESEARCH AND ENGINEERING LAB.
23. Matsutomi,H. (2009).Method for estimating collision force of drift wood accompanying tsunami inundation flow. J. Disaster Res. 4, 435–440. doi:10.20965/jdr. 2009.p0435
24. Madurapperuma, M. A. K. M., and Wijeyewickrema, A. C. (2012). "Inelastic dynamic analysis of an RC building impacted by a tsunami water-borne shipping container." J. Earthquake Tsunami, 6,1250001.
25. Como, A., and Mahmoud, H. (2013). "Numerical evaluation of tsunami debris impact loading on wooden structural walls." Eng. Struct., 56, 1249–1261.
26. Ko, H., Cox, D., Riggs, H., and Naito, C. (2015). "Hydraulic experiments on impact forces from tsunami-driven debris." J. Waterway, Port, Coastal, Ocean Eng., 10.1061/(ASCE)WW.1943-5460.0000286, 04014043.
27. Derschum, C.; Nistor, I.; Stolle, J.; Goseberg, N. Debris impact under extreme hydrodynamic conditions part 1: Hydrodynamics and impact geometry. Coast. Eng. **2018**, 141, 24–35.
28. Haehnel, R.B.; Daly, S.F. Maximum impact force of woody debris on floodplain structures. J. Hydraul. Eng. **2004**, 130, 112–120.
29. Nouri, Y., Nistor, I., Palermo, D. A. N., & Cornett, A. (2010). Experimental investigation of tsunami impact on free standing structures. *Coastal Engineering Journal*, *52*(1), 43-70.
30. Shafiei, S., Melville, B. W., Shamseldin, A. Y., Adams, K. N., & Beskhyroun, S. (2016). Experimental investigation of tsunami-borne debris impact force on structures: Factors affecting impulse-momentum formula. *Ocean Engineering*, *127*, 158-169.
31. Paczkowski, K., Riggs, H. R., Naito, C. J., & Lehmann, A. (2012). A one-dimensional model for impact forces resulting from high mass, low velocity debris. *Structural Engineering and Mechanics*, *42*(6), 831-847.

32. Yang,W.C. Study of Tsunami-Induced Fluid and Debris Load on Bridges using the Material Point Method. Ph.D. Thesis, University of Washington, Seattle, WA, USA, 2016.
33. Oudenbroek, K.; Naderi, N.; Bricker, J.D.; Yang, Y.; Van der Veen, C.; Uijttewaal, W.; Moriguchi, S.; Jonkman, S.N. Hydrodynamic and debris-damming failure of bridge decks and piers in steady flow. Geosciences **2018**, 8, 409.
34. Istrati, D.; Hasanpour, A.; Buckle, I. Numerical Investigation of Tsunami-Borne Debris Damming Loads on a Coastal Bridge. In Proceedings of the 17 World Conference on Earthquake Engineering, Sendai, Japan, 13–18 September 2020.
35. Hasanpour, A.; Istrati, D.; Buckle, I. (2021). Coupled SPH–FEM Modeling of Tsunami-Borne Large Debris Flow and Impact on Coastal Structures. Journal of Marine Science and Engineering, 9(10), 1068. https://doi.org/10.3390/jmse9101068
36. Majtan, E., Cunningham, L. S., & Rogers, B. D. (2021). Flood-induced hydrodynamic and debris impact forces on single-span masonry arch bridge. *Journal of Hydraulic Engineering*, *147*(11), 04021043.
37. Hasanpour, A., Istrati, D., & Buckle, I. G. (2022, July). Multi-Physics Modeling of Tsunami Debris Impact on Bridge Decks. In *Proceedings of the 3rd International Conference on Natural Hazards & Infrastructure, Athens, Greece* (pp. 5-7).
38. Hasanpour, A., Istrati, D., & Buckle, I. G. (2022, July). Multi-Physics Modeling of Tsunami Debris Impact on Bridge Decks. In *Proceedings of the 3rd International Conference on Natural Hazards & Infrastructure, Athens, Greece* (pp. 5-7).
39. Hasanpour, A., Istrati, D., & Buckle, I. (2023). Three-Dimensional Investigation of Floating Debris Effects on Bridge Superstructures During Tsunamis. *Has been submitted to Coastal Engineering*.
40. Hasanpour, A., Istrati, D., & Buckle, I. (2023). Effect of Debris Orientation on the Debris-Tsunami-Bridge Interaction and Induced Forces. *In press*.
41. Hasanpour, A., Istrati, D., & Buckle, I. (2023). Three-dimensional numerical simulation of tsunami-borne debris-loads on bridges. New Zealand Society of Earthquake Engineering (NZSEE) Annual Technical Conference 2023: *Facing the Seismic Challenge*, April 19-21, 2023, Auckland, New Zealand.

Chapter 7

7. Prescriptive Design Equations

7.1. Background

The impact of tsunami-borne debris on coastal structures is an important issue because the likelihood of severe damage caused by large and heavy objects carried in the bore must be anticipated. Further these loads are in addition to the hydrodynamic forces of the bore itself. Although sophisticated numerical modeling using high-performance computing gives insight into these forces, this approach is not suitable for everyday design-office use and prescriptive design equations are required. Such equations have been proposed for buildings but there are none for bridges at this time. Developing such equations is a significant challenge given the diverse size, orientation, and stiffness of potential debris objects, and the hydrodynamic conditions of the bore (velocity and height), still-water conditions, and bridge elevation. This chapter summarizes the equations for buildings, compares their application to bridges against rigorous numerical modelling, and then makes recommendations for bridge-specific equations.

7.2. Prescriptive equations for debris impact loads on buildings

Three simplified prescriptive equations have been proposed and adopted in various codes for the estimation of horizontal debris forces on buildings. They are as follows:

(a) ASCE (2007) [1] proposed a single DOF model to study the impact of two rigid bodies. The model, referred to as the Contact Stiffness Approach, gives the following value for the debris impact force, F_d

$$F_d = u_d\sqrt{m_d K_d} \qquad \text{Equation 7.1}$$

where u_d is debris velocity, m_d is debris mass, and K_d is debris stiffness.

(b) In their design guidelines for structures and infrastructure subject to flood impact, ASCE (2010) [2] and FEMA (2011) [3] recommended the following equation for F_d, which is based on Impulse Momentum and two rigid bodies:

$$F_d = \frac{\pi\, m_d u_d}{2\Delta t} \qquad \text{Equation 7.2}$$

where Δt is the contact duration. The term $\frac{\pi}{2}$ is included to estimate the maximum impact force rather than the average force, assuming a sinusoidal variation of force with time [4]. FEMA (2011) [4] recommends a range of values for Δt from 0.1 to 1s, while ASCE suggests a value of 0.03s. The choice of Δt can significantly affect the calculated impact force and the wide range of recommended values may lead to significant differences in the estimated force.

(c) FEMA P464 (2012) [5] and ASCE (2016) [6] uses a more generalized form of Equation 7.1 as below:

$$F_d = 1.3\, u_d \sqrt{m_d K_d C_{add}} \qquad \text{Equation 7.3}$$

where C_{add} is the added mass coefficient of 1 and 2 for the longitudinal and transverse debris orientation, respectively. The 1.3 multiplier is an importance coefficient for 'essential' structures, as specified in ASCE/SEI 7-10.

Review of these prescriptive equations shows a lack of consistency, but apparently, they are acceptable for buildings. Application to bridges is explored below.

7.3. Comparison of results from simplified equations for buildings with numerical simulations of bridges

7.3.1. Results

A comparison of results from the numerical investigation of bridges (debris horizontal impact force) with the values from the three simplified equations for buildings noted above, is presented

in this section. For this purpose, three different debris masses, (9.2%, 50%, and 75% of the maximum weight of a shipping container), three scaled bridge elevations (0.20 m, 0.30 m, and 0.35 m), two debris orientations (longitudinal and transverse), and a range of hydrodynamic conditions are considered. It is important to consider the elevation of the bridge as a factor in determining the accuracy of impact force calculations using simplified equations, as it can have a significant effect on the debris velocities at the point of impact. Figures 7-1 through 7-3 present comparisons of the numerical data for longitudinal debris with 50% mass, and bridge elevations of 0.20 m, 0.30 m, and 0.35 m, respectively. The results of the comparative analysis for the longitudinal debris with masses of 9.2% and 75% for the bridge elevation of 0.30 m are displayed in Figures 7-4 and 7-5, respectively.

Figures 7-6 through 7-8 depict the comparison of data for the transverse debris with 50% mass for the bridge elevations of 0.20 m 0.30 m, and 0.35 m, respectively. The results of the transverse debris with masses of 9.2% and 75% and the bridge elevation of 0.30m are presented in Figures 7-9 and 7-10, respectively.

A summary of the average values of the debris impact force for the studied cases with different debris orientations, masses, and bridge elevations is presented in Table 7-1.

7.3.2. Discussion

The analysis revealed that for the longitudinal debris with 50% mass and the bridge elevation of 0.20 m, both Equation 7.1 and Equation 7.3 result in an overestimation of the impact force, with Equation 7.1 overestimating by 12% and Equation 7.3 overestimating by 66%. Similar results were found for the transverse debris, with Equation 7.1 overpredicting by 36% and Equation 7.3 overpredicting by 137%. The results of the analysis indicated that the lightest debris and the bridge elevation of 0.30 m display a similar trend of overestimation for both orientations. Specifically, Equation 7.1 overestimates the impact force by 19% for the longitudinal debris and 97% for the

transverse debris, while Equation 7.3 overestimates by 75% for the longitudinal debris and 155% for the transverse debris.

Furthermore, the analysis demonstrated that for the debris with 50% mass in both longitudinal and transverse orientations and the bridge elevation of 0.30 m, only Equation 7.3 results in an overestimation of the peak impact force. The overestimation is 17% for the longitudinal debris and 18% for the transverse debris.

The data also indicated that for the highest bridge elevation (0.35 m) and the debris with 50% mass in both directions, all three equations tend to underestimate the peak impact force. For example, Equation 7.3 underestimated the impact of longitudinal debris by 33% and transverse debris by 23%. A similar trend is observed for the heaviest debris and the bridge elevation of 0.30m in both directions, with Equation 3 underestimating longitudinal debris by 65% and transverse debris by 30%.

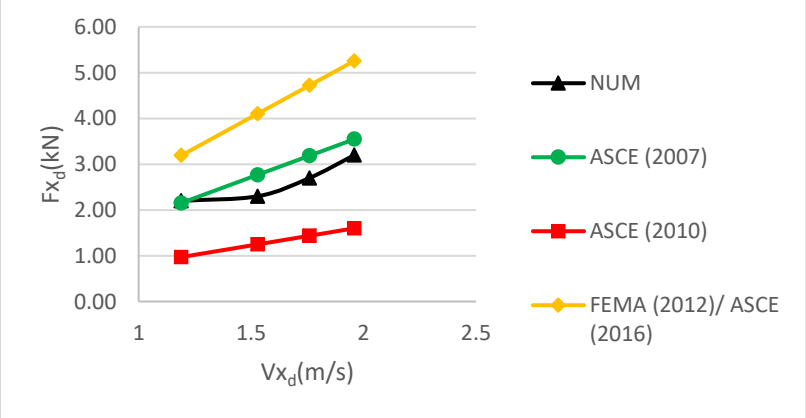

Figure 7-1 Comparison of longitudinal debris impact force for 50% mass and bridge elevation of 0.20m (Z_a)

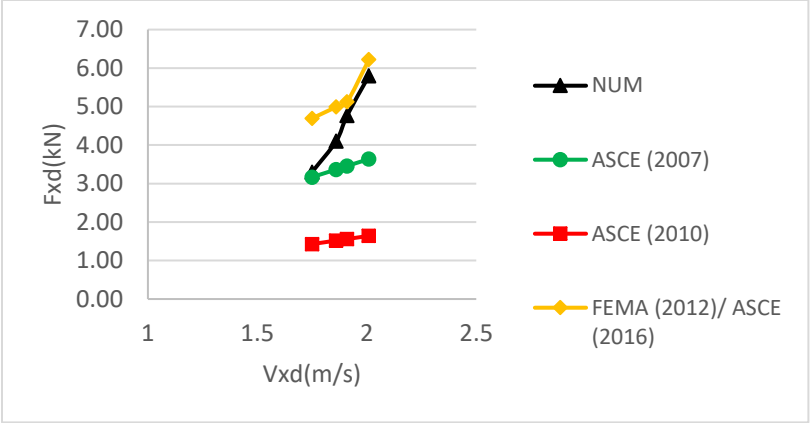

Figure 7-2 Comparison of longitudinal debris impact force for 50% mass and bridge elevation of 0.30 m (Z_b)

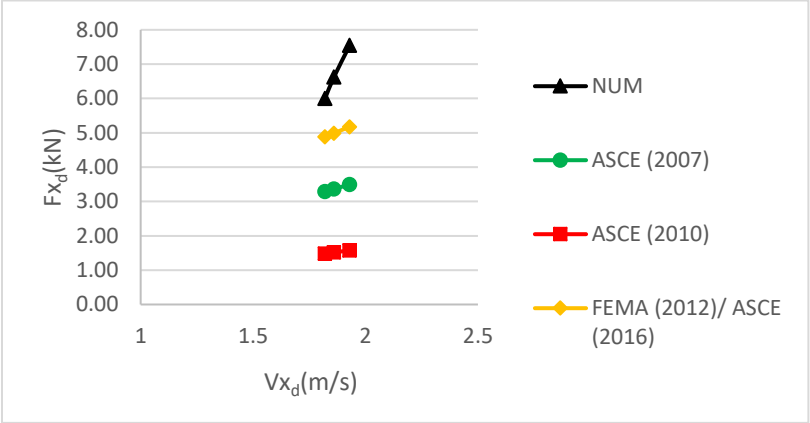

Figure 7-3 Comparison of longitudinal debris impact force for 50% mass and bridge elevation of 0.35 m (Z_c)

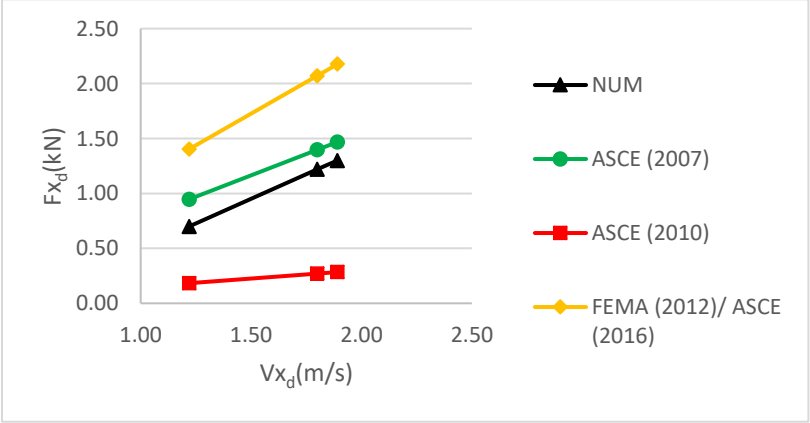

Figure 7-4 Comparison of longitudinal debris impact force for 9.2% mass and bridge elevation of 0.30 m (Z_b)

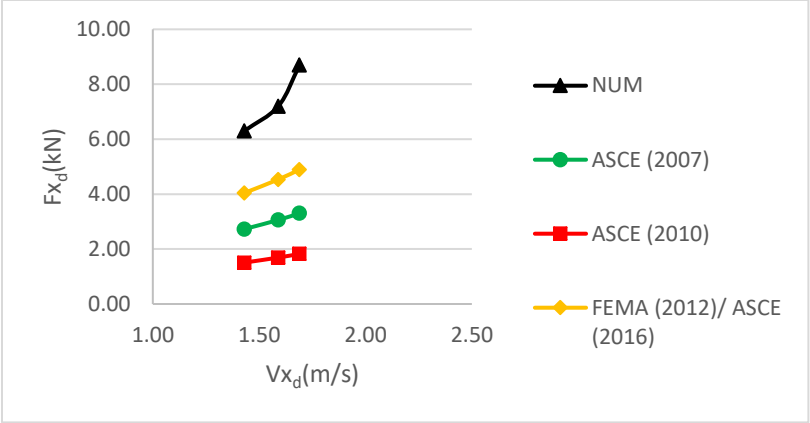

Figure 7-5 Comparison of longitudinal debris impact force for 75% mass and bridge elevation of 0.30 m (Z_b)

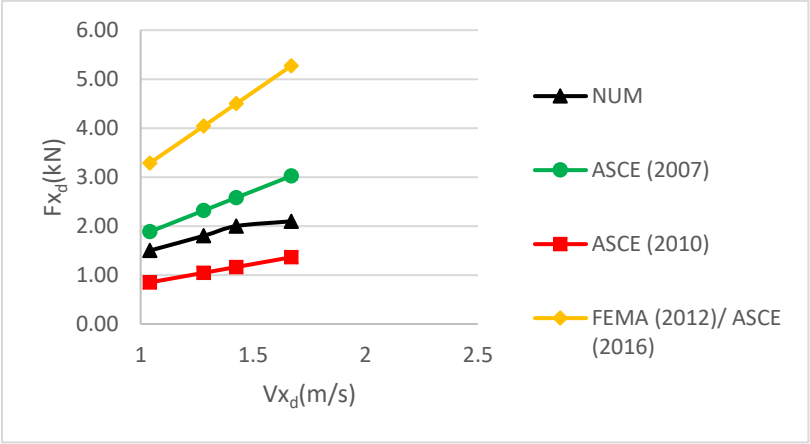

Figure 7-6 Comparison of transverse debris impact force for 50% mass and bridge elevation of 0.20 m (Z_a)

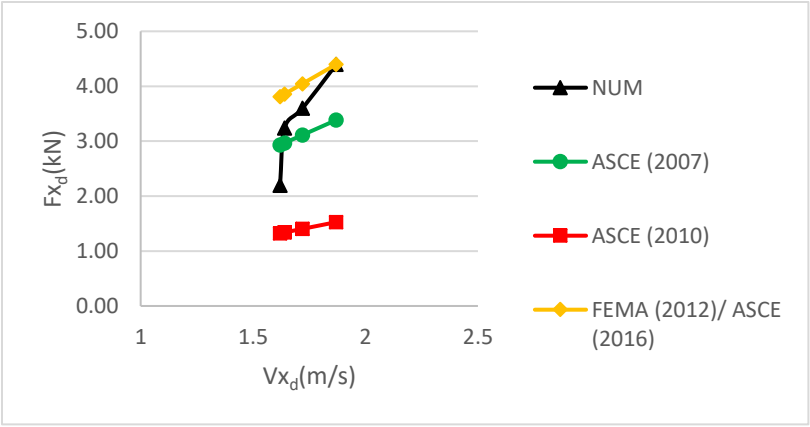

Figure 7-7 Comparison of transverse debris impact force for 50% mass and bridge elevation of 0.30 m (Z_b)

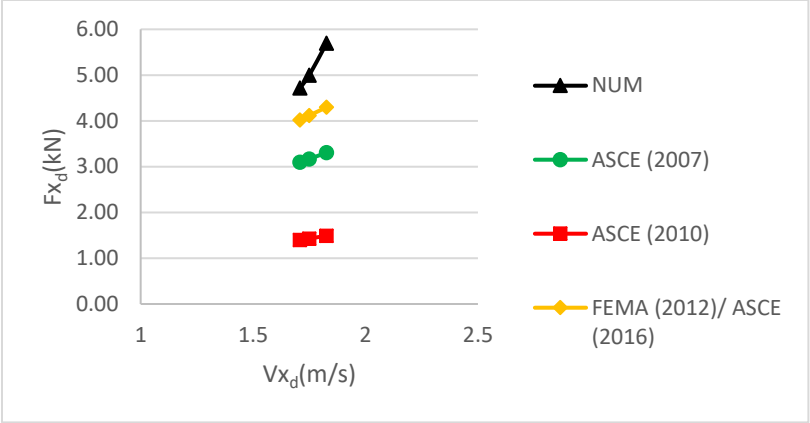

Figure 7-8 Comparison of transverse debris impact force for 50% mass and bridge elevation of 0.35 m (Z_c)

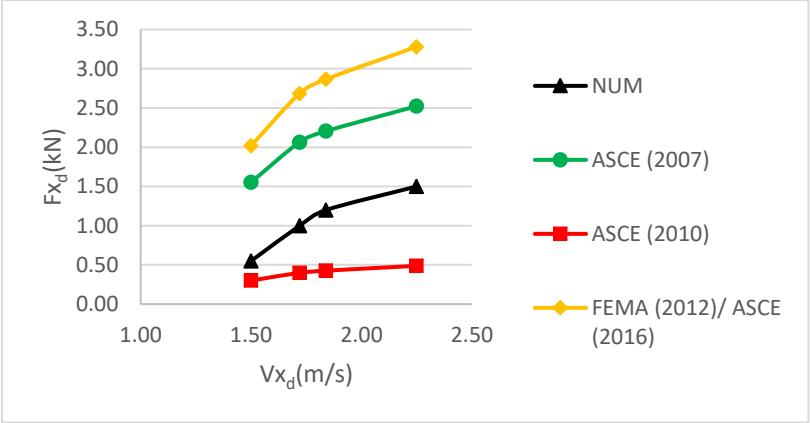

Figure 7-9 Comparison of transverse debris impact force for 9.2% mass and bridge elevation of 0.30 m (Z_b)

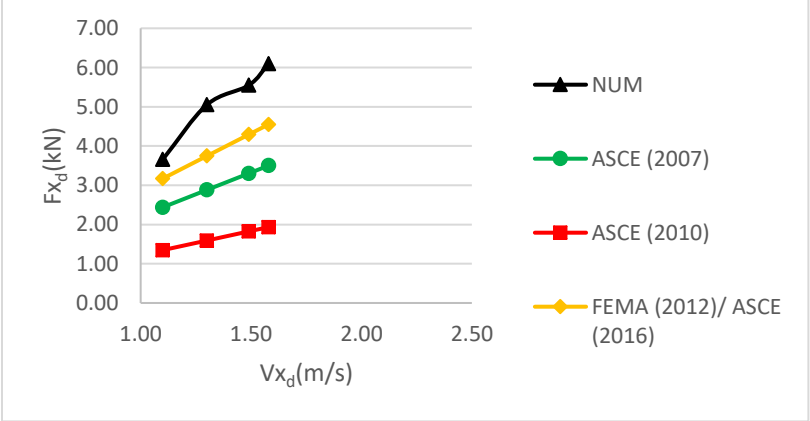

Figure 7-10 Comparison of transverse debris impact force for 75% mass and bridge elevation of 0.30 m (Z_b)

Table 7-1 Average values of the debris horizontal impact force calculated by numerical simulations and estimated by the simplified equations

a. Debris mass=50%

		Longitudinal orientation				Transverse orientation			
		NUM	Eq.7.1	Eq.7.2	Eq.7.3	NUM	Eq.7.1	Eq.7.2	Eq.7.3
Bridge elevation	0.20 m	2.6	2.91	1.31	4.32	1.8	2.45	1.11	4.28
	0.30 m	4.5	3.41	1.54	5.26	3.4	3.1	1.4	4.03
	0.35 m	6.7	3.38	1.53	5.02	5.1	3.2	1.44	4.15

b. Debris mass=9.2%

		Longitudinal orientation				Transverse orientation			
		NUM	Eq.7.1	Eq.7.2	Eq.7.3	NUM	Eq.7.1	Eq.7.2	Eq.7.3
Bridge elevation	0.30 m	1.07	1.27	0.25	1.88	1.06	2.09	0.4	2.71

c. Debris mass=75%

		Longitudinal orientation				Transverse orientation			
		NUM	Eq.7.1	Eq.7.2	Eq.7.3	NUM	Eq.7.1	Eq.7.2	Eq.7.3
Bridge elevation	0.30 m	7.4	3.03	1.67	4.49	5.1	3.03	1.67	3.94

7.4. Recommendations for bridges

It may be concluded from the results in the previous section that the prescriptive equations for horizontal loads on buildings might be used for estimating horizontal loads on bridges. In particular Equation 7.3 ([5,6]) appears to provide an upper limit on horizontal load in many cases. However, a major difference between a building and a bridge is that debris may pass under a bridge causing vertical impact forces at the same time as horizontal impacts. Such behavior is not seen in a building.

Based on the numerical simulations described in previous chapters (see chapters 4-6), the maximum vertical debris force can be correlated to factors such as debris mass, initial orientation, and magnitude of horizontal impact force. For the scenarios where the maximum impact forces in the two directions applied simultaneously, which is observed in the majority of the cases, the maximum vertical debris impact force on a bridge (F_v) may be approximated by:

$$F_v = 0.5 * F_d$$ Equation 7.4

where F_d is given by Equation 7.3. It is noted that this force acts upward on the bridge superstructure.

7.5. References

1. ASCE, 2007. Minimum design loads for buildings and other structures. American Society of Civil Engineers, Reston, Virginia, USA, ASCE/SEI 7–10.
2. ASCE, 2010. Minimum design loads for buildings and other structures. American Society of Civil Engineers, Reston, Virginia, USA, ASCE/SEI 7–10.
3. FEMA, 2011. Coastal Construction Manual: Principles and Practices of Planning, Siting, Designing, Constructing, and Maintaining Residential Buildings in Coastal Areas (4th Edition), FEMA P-55. Federal Emergency Management Agency.
4. Haehnel, R.B., Daly, S.F., 2004. Maximum impact force of woody debris on floodplain structures. J. Hydraul. Eng. 130, 112–120.
5. FEMA, 2012. P646 Guidelines for Design of Structure for Vertical Evacuation from Tsunamis. Federal Emergency Management Agency.
6. ASCE. 2016. Minimum design loads for buildings and other structures. American Society of Civil Engineers, Reston, Virginia, USA, ASCE/SEI 7–16.

Chapter 8

8. Summary, Conclusions, and Future Work

8.1. Summary

Tsunamis are one of the most devastating natural disasters, with the potential to cause significant damage to coastal infrastructure, such as transportation networks and bridges, and compromise their stability. The 2004 Indian Ocean and 2011 Great East Japan tsunamis are notable examples of the destruction that can be caused by these events, with approximately 1,500 km of coastline affected and numerous bridges damaged or destroyed in each instance. Bridges are particularly vulnerable to tsunami damage, and field surveys following past disasters have demonstrated that tsunami-driven debris, including shipping containers, can wash out or damage bridge superstructures. Despite the importance of understanding the impact of floating debris on coastal bridges, there have been relatively few studies on this topic, due to the complex multi-physics nature of the phenomena. Accurate quantification of the forces involved is essential for the design of tsunami-resistant bridges, as transportation infrastructure is vital for post-disaster response and recovery efforts. The main objective of this dissertation and doctoral work is to improve our fundamental understanding of the physics involved in the debris-flow-bridge interaction and the associated loads, with the ultimate aim of improving the design of bridge superstructures that are more resistant to damage and more resilient in the face of natural disasters.

To achieve the stated goal above, a novel coupled method of Smoothed Particle Hydrodynamics (SPH) and Finite Element (FE) was employed to investigate the impact loading of tsunami-borne debris on coastal bridges. The validity of the numerical approach was verified through comparison with the results of a large-scale experimental study found in the literature. The two-dimensional investigation revealed that this technique is capable of accurately capturing the flow propagation, as well as the debris-flow and the debris-flow-structure interaction. Following the validation, a two-

dimensional investigation was conducted to assess the impact of a shipping container on a box-girder bridge under various tsunami flows, bridge elevations, and initial debris orientations.

In the next step, the three-dimensional validity of the numerical technique was tested by comparing the results to an experimental study of debris impact on the coastal structure. Two types of debris, including a box and a disk, were used in the study. The results of the three-dimensional evaluations showed that this method is able to accurately capture the tsunami flow, as well as the debris-flow and the debris-flow-structure interactions. Following the successful validation of the three-dimensional numerical technique, an extensive numerical investigation was conducted using a 1/20 scale model to analyze the effect of different parameters on the debris impact loadings on coastal bridges during a tsunami event. The model included a scaled-down version of a standard shipping container with dimensions of 0.30m long, 0.13m wide, and 0.13m tall and a box-girder bridge with dimensions of 0.50m (length) by 0.13m (height). The parameters examined included the tsunami flow characteristics, the elevation of the bridge, the initial orientation of the debris, and the mass of the debris.

8.2. Conclusions

The dissertation is presented in standalone paper format, as outlined in Chapter 1. For detailed conclusions of each section of the study, the reader is directed to the respective chapters. In summary, the simulation results obtained through the application of coupled SPH-FEM numerical technique have provided insight into the effect of tsunami flow characteristics, the initial orientation of the debris, the debris mass, and the bridge elevation on the movement, velocity, and impact forces of debris. The findings have shown that the debris can become trapped below the offshore overhang, travel above the deck, or move below it, depending on the aforementioned parameters. Additionally, the study has demonstrated that variations in the velocities of the offshore and onshore corners can result in significant debris pitching, which in turn leads to non-normal impact

angles and could potentially result in a non-linear force-velocity trend that has not been considered to date. Furthermore, it was found that the debris has both a horizontal and vertical velocity at the instant of the initial impact on the offshore side of the bridge, exerting impulsive loads simultaneously in both directions. The complexity of the debris-fluid-bridge interaction was also highlighted with some cases resulting in secondary impacts of greater magnitude than the primary impact. The study also found that the longitudinal debris reaches higher velocities compared to the transverse debris, which leads to an average increase of 1.48 and 1.5 times greater horizontal and vertical forces, respectively. Additionally, presence of the longitudinal debris results in an average of 3.64 and 2.13 times larger horizontal and vertical forces, respectively, in comparison to cases without debris. Similarly, presence of the transverse debris results in an average increase of 3.33 and 3.07 times larger horizontal and vertical forces, respectively, compared to the cases without debris. It was also found that the debris mass has a significant impact on its movement, with lighter debris typically elevating up to 1.75 times more than heavier debris, depending on debris orientation. Additionally, as the debris mass increases, there is a corresponding decrease in the debris velocities. Specifically, as the longitudinal debris mass increases from 9.2% to 75%, there is an average reduction of 25% and 65% in the horizontal and vertical velocities, respectively. Similarly, an increase in the mass of transverse debris from 9.2% to 75% results on an average reduction of 21% and 75% in the horizontal and vertical velocities, respectively. Furthermore, it was found that as the mass of longitudinal debris increases from 9.2% to 75%, there is an average increase of 4.8 and 6 times in the horizontal and uplift forces, respectively. Similarly, as the mass of transverse debris increases from 9.2% to 75%, there is an average increase of 6.1 and 3.8 times in the horizontal and vertical impact forces, respectively.

8.3. Recommendations for future work

The coupled SPH-FEM numerical analyses presented in this dissertation have given an insight into the role of hydrodynamic parameters, bridge elevation, debris orientation, and debris mass and have advanced our understanding of the debris-wave-structure interaction during the tsunami inundation. At the same time, the work has highlighted the complexity of certain phenomena and identified topics that merit further investigation. Potential topics for future research include:

- Mitigation strategies for new and existing bridges for reducing tsunami demand
- Examine other types of bridges, such as open-girder, under a broad range of hydrodynamic conditions
- Investigate the impact forces if the debris interacts with the substructure
- Conduct full-scale analyses to confirm that there is no significant scale effect
- Examine the effect of multiple debris impact forces on coastal bridges
- Study effect of bridge and debris flexibility on response